



**HAL**  
open science

# Magnetic field responsive nano-platforms composed of magnetic nanoparticle-loaded metal-organic frameworks for anticancer targeted drug delivery

Ahmed Gamal Ali Abdelhamid

► **To cite this version:**

Ahmed Gamal Ali Abdelhamid. Magnetic field responsive nano-platforms composed of magnetic nanoparticle-loaded metal-organic frameworks for anticancer targeted drug delivery. Cancer. Université Paul Sabatier - Toulouse III, 2023. English. NNT : 2023TOU30231 . tel-04551550

**HAL Id: tel-04551550**

**<https://theses.hal.science/tel-04551550>**

Submitted on 18 Apr 2024

**HAL** is a multi-disciplinary open access archive for the deposit and dissemination of scientific research documents, whether they are published or not. The documents may come from teaching and research institutions in France or abroad, or from public or private research centers.

L'archive ouverte pluridisciplinaire **HAL**, est destinée au dépôt et à la diffusion de documents scientifiques de niveau recherche, publiés ou non, émanant des établissements d'enseignement et de recherche français ou étrangers, des laboratoires publics ou privés.



# THÈSE

**En vue de l'obtention du  
DOCTORAT DE L'UNIVERSITÉ DE TOULOUSE  
Délivré par l'Université Toulouse 3 - Paul Sabatier**

---

**Présentée et soutenue par  
Ahmed Gamal Ali ABDELHAMID**

Le 21 novembre 2023

**Nano-plateformes composées de réseaux métallo-organiques  
chargés de nanoparticules magnétiques pour le ciblage et le  
relargage contrôlé magnétiquement de médicaments  
anticancéreux**

---

Ecole doctorale : **BSB - Biologie, Santé, Biotechnologies**

Spécialité : **CANCEROLOGIE**

Unité de recherche :  
**CRCT - Centre de Recherche en Cancérologie de Toulouse**

Thèse dirigée par  
**Véronique GIGOUX et Julian CARREY**

Jury

**M. Robert MOREL**, Rapporteur  
**Mme Lucie SANCEY**, Rapporteur  
**M. Nicolas TSAPIS**, Rapporteur  
**Mme Véronique GIGOUX**, Directrice de thèse  
**M. Julian CARREY**, Co-directeur de thèse  
**M. Fabien DELPECH**, Président

## Summary

Metal-organic frameworks (MOFs) are hybrid materials composed of inorganic metal ions coordinated with organic linkers, which are interesting carriers for anticancer drug delivery applications. Due to the considerable flexibility in choosing their structural building units, MOFs with large tunable porosity, high drug loading capacity and biocompatibility could be synthesized. However, they commonly suffer from off-target uncontrolled drug release and accumulation. In order to overcome these challenges, this study aimed to use MOF-based magnetic nanocomposites composed of magnetic nanoparticles (MNPs) core and MOF shell. So that, the cargo release from the nanocomposites could be induced thermally or mechanically in response to the applied magnetic fields (MF). In addition, the MNPs embedded into the MOF platform could enable their targeting to the tumor tissues through magnetic forces.

The two major aims of this study were: 1) to provide a proof-of-concept for the ability to control the cargo release from the nanocomposites by MF, and 2) to investigate the design of a setup that could enable targeting MNP-based nanocarriers to deep-seated tumors.

The first aim was investigated using nanocomposites consisted of iron oxide nanoparticles cores and zeolitic imidazolate frameworks-8 MOF shells, which were loaded with cresyl violet (CV) fluorescent probe. The synthesized nanocomposites had a core-shell structure with a hydrodynamic diameter of  $229.5 \pm 1.9$  nm. The nanocomposites were biocompatible on MiaPaCa2 cancer cells and cancer-associated fibroblasts (CAF) used model cells, up to 1 pM and 72 h of incubation with main accumulation inside the lysosomes. Both the alternating high-frequency MF (AMF) or rotating low-frequency MF (RMF) exposures significantly increased the CV release from the nanocomposite in MiaPaCa2 and CAF cells. In addition, an enhanced CV release in both cells was observed after a second AMF exposure. The CV release was associated with a decrease in cell viability in MiaPaCa2 exposed to AMF or RMF, and in CAF exposed to AMF, due to the CV cytotoxicity. Moreover, the CV release from the nanocomposites in MiaPaCa2/CAF spheroids was also induced via AMF or RMF, and decreased the spheroid size.

For the second aim, we presented a design of a novel setup that could enable the accumulation of MNP-based carriers into deep-seated tumors and not only superficial ones. The proposed setup relies on using two permanent magnet blocks in order to generate a strong and low-gradient MF in the gap between them. Ordinary coils were added in the gap to generate a weaker but high-gradient MF in the opposite direction to the MF generated by the permanent magnets. Therefore, the net MF distribution in the gap would have the highest intensity in a middle area away from the MF sources

where the magnetic-based nanocarriers could preferentially accumulate. In addition, tuning the MF generated by the coils with different currents could enable changing the MNP focusing area. COMSOL Multiphysics® simulations were used to optimize the setup parameters and to provide a proof-of-concept for the setup design. Afterwards, the ordinary coils were fabricated in the lab and allowed to generate MF intensity up to 158 mT at the center of their surface, thanks to developed water-cooling coil supports. At this MF intensity, the coils would be able to reverse the MF distribution of the permanent magnets on the lab-designed setup support.

In conclusion, this work allowed the development of biocompatible MOF-based magnetic nanocomposites of high porosity that could allow pulsatile on-demand MF-cargo release inside cells. Also, we presented a strategy for targeting MNP-based delivery systems specifically to deep-seated tumors. Both could allow spatiotemporal control over the accumulation and drug release from the magnetic nanocomposites to enhance their efficiency as targeted cancer nanomedicine formulations.

## Acknowledgments

First, I want to thank my thesis director Véronique Gigoux for her dedicated time, help, guidance and support while supervising me during the thesis. Her guidance enabled me to be in track on the complex, yet, very interesting cancer biology and tumor microenvironment fields. In addition, she was always meticulous going on with the project and the thesis requirements and formalities. She was also highly supportive towards my professional and personal development as for the French language courses. Thanks also for her support and the amazing time I was lucky to have while attending conferences together and presenting our results. Thanks also for her time and effort in helping me writing the thesis manuscript.

I want also to thank my labmates Justine Journaux, Pascal Clerc, Loubna Kehal, Angela Agaësse and Doha Zorkot for the wonderful time we had together as a team. It was wonderful three years that I was very glad that we shared this journey together with all of its scientific and life events. Thanks for the time of the whole team in making every event special and celebrating it as the birth of Mousa, it was a very happy day when we celebrated it. Thanks also to Hidaya M'COLO-MARI, my first and only, till now, master student that I had the opportunity to work with her. It was an enriching experience for me.

The thanks also extends to Corinne Bousquet for welcoming me within team 6 (MICROPANC: Microenvironment & Therapeutic Resistance in Pancreatic Neoplasms) in Toulouse Cancer Research Center (CRCT) and her constructive comments and helps during the thesis. Also thanks a lot to all MICROPANC team: Yvan Martineau, Christine Jean, Morgane Le Bras, Petnoi Petsophons, Ludmila Recoules, Marjorie Fanjul, Alexia Brunel, Ismahane Belhabib, Jacobo Solorzano, Claire Lac, Mehdi Liauzun, Hippolyte Audureau, Chloé Bazile, Evangelia Papadopoulou, Delphine Vezzosi, Maxime Boyer, Ossama Kohil and Cédric Fabre; for both their valuable enriching comments raised on my work during our meetings and for their welcoming spirit and the wonderful time I spent with them.

Also, thanks a lot to Elodie Riant, Alexia Zakaroff and Rémy Flores-Flores from Metabolic and Cardiovascular Research Institute (I2MC) for their help in introducing the flow cytometry and confocal microscopy to me and for providing great technical help when needed.

Now, on the other side of the téléphérique, I want to thank my thesis co-director Julian Carrey for his help and support during the thesis both on professional as well as personal levels. I learned a lot from him as a university professor and also as a mentor and a team leader. He was always motivating and helping me to go into the nanomagnetism physics field and as he says, “to be in part a physicist”. Thanks a lot for him always being supportive towards my professional and personal development with great guidance and points of views. Thanks a lot also for his time and effort helping me in writing the thesis manuscript.

Also, thanks a lot to Touati Douar and Géraldine Ballon for their efforts especially for developing the 3D magnetic focusing set-up. The thanks also extend to all nanomagnetism teammates: Bastien Sanglard, Lionel Petit, Ilona Lecerf, Marion Luu, Tom Fournier, Danny Petty Gweha Nyoma, Abraao-Cefas Torres-Dias, Benjamin Lassagne, Thomas Blon and Anne Bernard-Mantel; it was really a great time I spent with them and they were always welcoming for help and explaining to me the physics and engineering related subjects that I asked them about. Thanks also to all friends and colleagues from other teams in LPCNO (Laboratory of Physics and Chemistry of Nano-objects) for the wonderful time being with them during these 3 years. Thanks a lot to Brice Altman, Lucie Marpinard and Assia Khodja (administrative team in LPCNO), Célia Vigée (from INSA-Toulouse human resources team), Guillaume Viau (LPCNO director) and Bertrand Raquet (Director of INSA Toulouse) for their time and tremendous efforts with the administrative part and making life easier for me towards the realization of our collaborative thesis project.

Thanks also to Maria Pozzi, Wolfgang J. Parak and all group members in Institute for Nanostructure and Solid State Physics (INF) and Center for Hybrid Nanostructures (CHyN) (University of Hamburg, Germany) for welcoming me and for the amazing enriching secondment. It opened a window for me at the light-sensitive drug delivery systems as well as at the 3D cellular spheroids world. Thanks also to AnaMaria Panaite, Aleksandra Predeina and Teresa Pellegrino and all the Nanomaterials for biomedical application group members in Italian institute of technology (Genova, Italy) for welcoming me and for the amazing, enriching secondment. It expanded my horizons on the inorganic magnetic nanoparticle synthesis, characterization and biomedical applications. Also, thanks a lot to Anil Misra, Alejandro Peña, Ash Alavijeh, Mo Alavijeh and all Pharmidex company team members (London, United Kingdom) for the amazing enriching experience I had during my secondment. It was a great add-on to have a flavor of private pharmaceutical company perspective and get hands-on experience with its working protocols and culture.

Thanks a lot also to Elena Solera, Maialen López, Radoslava Metodieva, Eva García and Patricia Horcajada, all HeatNMof EU project members for their efforts and time in organizing and help implementing the project. Thanks also for the project funding from the European Union's Horizon 2020 research and innovation program under grant agreement No 860942.

Thanks also to Anne-Francoise Mingotaud and Daniel Cussac for their time and efforts being the thesis supervision committee. Thanks also to the jury members (Robert Morel, Lucie Sancey, Nicolas Tsapis and Fabien Delpech) for their time and efforts in evaluating my thesis and for traveling to come to the thesis defense.

Finally, I should also say thanks a lot to my family where words won't in anyway suffice to express here but would give it a try.

Thanks my mother (Awatef) and my father (Gamal) for all your efforts in supporting me. You were role models in the support and in paving the road for me to be able to learn, grow up and develop. Thanks also to my brother (Abd-Elrahman) and my sister (Omnia) for all "funny" moments we shared together and for the "meaningless" challenges that we passed together in our games when we were young. Wishing you the best in your personal and professional lives. Although we were far from each other, you were always motivating and supporting me with all what you can do, I'm very happy and proud of you all!

Thanks also to my wife (Gehad) who shared with me this progress in all the postgraduate studies way started 8 years ago! Yes, 8! Thanks for your strong support and also sacrifice in difficult times. I hope that you are enjoying our nomad-like life with the journey around Europe. Thanks for the amazing food and sweets you make for us! I'm very glad and proud of you being my other half!

Thanks for my older son (Yehia) who although having less than 6-years was able to realize and accept that I'm "almost always" doing work! Thanks for your always smile and trying to play and laugh. Thanks for sharing together all moments with my masters and PhD studies. Thanks also for my younger son (Mousa) for doing your best to let me sleep in the night to finish the PhD although you had less than 6 months! Thanks also to my father-in-law (Mustafa), my mother-in-law (Eptsam) and my brother-in-law (Omar), they were always supportive and helping us to go through our life journey. Thanks also for your care to celebrate our success moments together.

Without the unconditional support and help of all of my family, I would not have been able to do many things since the start of my Erasmus master's and Marie-Curie PhD's mobility, journey and life experience abroad started back in 2018.

# Table of Content

Introduction.....	1
State of the art .....	5
Part I. Targeted nanomedicines for cancer treatment .....	5
I.1. Cancer.....	5
I.2. Traditional treatments .....	6
I.3. Cells, targeted and ablation therapies .....	6
I.4. Nanomedicine .....	8
I.4.1 Introduction and nanomedicine definition .....	8
I.4.2. Passive and active targeting .....	12
I.4.3. Stimuli-responsive nanomedicines.....	16
I.4.3.1. Internal stimuli-responsive nanomedicines.....	17
I.4.3.1.1. pH-responsive nanomedicines .....	17
I.4.3.1.2. Redox responsive nanomedicines .....	18
I.4.3.1.3. Reactive oxygen species-responsive nanomedicines.....	19
I.4.3.1.4. Hypoxia-responsive nanomedicines.....	20
I.4.3.1.5. Enzyme-responsive nanomedicine.....	21
I.4.3.1.6. Conclusion on internal stimuli-responsive nanomedicines.....	21
I.4.3.2. External stimuli-responsive nanomedicines .....	23
I.4.3.2.1. Ultrasound (US)-responsive nanomedicines .....	23
I.4.3.2.2. Light-responsive nanomedicines .....	24
I.4.3.2.3. Magnetic fields (MF)-responsive nanomedicines .....	25
I.4.3.2.4. Heat (thermal)-responsive nanomedicines .....	26
I.4.3.1.5. Conclusion on external stimuli-responsive nanomedicines .....	30
I.4.3.3. Conclusion on stimuli-responsive nanomedicines.....	31
Part II. The magnetic stimulus for targeting the nanomedicines to the tumor tissue and triggering cell death and/or cargo release .....	32
II.1. Magnetic nanoparticle properties (physicochemical properties and biological interactions) .	32
II.1.1. Magnetic nanoparticle physical properties .....	32
II.1.2. Magnetic nanoparticle chemical composition for biomedical applications.....	35
II.1.3. Biological interaction of magnetic nanoparticles .....	36
II.2. Magnetic nanoparticle biomedical applications .....	37
II.2.1. Magnetic nanoparticle focusing/targeting to tumor tissues under magnetic field gradient guidance .....	37
II.2.2. Magnetic imaging using magnetic resonance imaging (MRI) and magnetic particle imaging (MPI) .....	41
II.2.3. Magnetic nanoparticles as antitumor nanomedicines .....	46

II.2.3.1. Hyperthermia .....	46
II.2.3.2. Magneto-mechanical destruction.....	50
II.2.3.3. Photothermal applications.....	51
II.2.4. Magnetic nanoparticles based nanomedicines for drug delivery .....	51
II.2.5. Conclusion on magnetic nanoparticles biomedical applications .....	59
Part III. Metal-organic frameworks (MOFs) as drug delivery systems.....	61
III.1. MOF structure, synthesis and characterization .....	61
III.2. Naming and classification of MOF families .....	64
III.3. Drug loading and encapsulation into MOFs.....	65
III.4. Drug release from MOFs .....	68
III.5. MOF biocompatibility.....	69
III.6. MOF cellular uptake and interactions.....	71
III.7. MOF antitumor applications .....	72
III.7.1. Antitumor MOFs .....	73
III.7.2. MOFs as antitumor delivery systems .....	75
III.7.3. MOFs as stimuli-responsive antitumor delivery systems.....	76
III.8. Conclusions.....	83
Part IV. Pancreatic tumor treatment using magnetic stimulus-responsive drug delivery systems....	84
IV.1. PDAC development and its treatment challenges .....	84
IV.2. PDAC stages and their standard of care treatment options.....	86
IV.3. New PDAC treatment strategies .....	88
IV.3.1. PDAC stroma modulation .....	88
IV.3.2. Targeting PDAC stem cells.....	89
IV.3.3. Targeting the PDAC immune cells .....	89
IV.3.4. Tailoring the nanomedicine formulations properties .....	90
IV.4. Conclusions .....	93
V. References .....	95
Objectives.....	119
Results .....	121
First part of results: Magnetic field-induced cargo release from magnetic nanoparticles@metal-organic frameworks nanocomposites through heating or mechanical actuation .....	121
Second part of results: Synthesis of chemotherapeutic drug loaded metal-organic frameworks magnetic nanocomposites .....	163
Third part of results: Development of magnetic nanoparticles focusing setup with tunable targeting area.....	179
Conclusions and perspectives .....	219

# List of Abbreviations

5-FU	5-Fluorouracil
ALA	Aminolevulinic Acid
AMF	Alternating magnetic field
APCs	Antigen-presenting cells
BET	Brunauer–Emmett–Teller
BTC	1,3,5-Denzenetricarboxylate
CaCO <sub>3</sub>	Calcium carbonate
CAF	Cancer-associated fibroblasts
cal	Calcein
CaP	Calcium phosphate
CAR	Chimeric antigen receptor
cDNA	Complementary DNA
Chol	Cholesterol
CPE	PEG-conjugated polyelectrolyte
CPT	Camptothecin
CT	Computed tomography
CTAB	Cetyltrimethylammonium bromide
CTLs	Cytotoxic T cells
CUSs	Coordinatively unsaturated sites
Cy5	Cyanine5
DBA	2,5-Di(p-benzoato)aniline
DLS	Dynamic light scattering
DM1	Mertansine
DM-ACMSs	DOX-loaded MNPs alginate-chitosan microspheres
DMEM	Dulbecco's Modified Eagle Medium
DOX	Doxorubicin
DPPC	Dipalmitoylphosphatidylcholine
DSPE	1,2-Diacyl-SN-glycero-3-phosphoethanolamine
DUT	Dresden University of Technology
EC	European commission
EE	Encapsulation efficiency
ELF-AMF	Extremely low-frequency AMF

EMA	European medical agency
EPR	Enhanced permeability and retention
EtOH	Ethanol
F127	Pluronic® F-127
FBS	Fetal bovine serum
FC	Folic acid-chitosan conjugate
FDA	Food and Drug Administration
FFR	Field free region
FOLFIRINOX	5-fluorouracil with leucovorin, irinotecan, and oxaliplatin
FTIR	Fourier transform infra-red
Gd	Gadolinium
GdNCT	Gd neutron capture therapy
GelMA	Gelatin methacryloyl
GNPs	Gold nanoparticles
GOx	Glucose oxidase
GSH	Glutathione
HA	Hexanoate
HCC	Hepatocellular carcinoma
HF-US	High-frequency ultrasound
HIFU	High intensity focused ultrasound
HKUST	Hong Kong University of Science and Technology
HOE	Hoechst
HPC	Hydroxypropyl cellulose
HPLC	High-performance liquid chromatography
i.v.	Intravenous
IFP	Interstitial fluid pressure
IONCs	Iron oxide nanocubes
IONFs	Iron oxide nanoflowers
IONPs	Iron oxide nanoparticles
iPSCs	Induced pluripotent stem cells
iRGD	Internalizing arginyl-glycyl-aspartic acid
$K_{eff}$	Magnetic anisotropy
LCST	Lower critical solution temperature
LD 50	Median lethal dose

LF-US	Low-frequency ultrasound
LNCaP	Lymph node carcinoma of the prostate
LPSR	Local plasmon surface resonance
mAb	Monoclonal antibody
MagTSLs	Magneto-thermosensitive-liposomes
Melm	Methyl imidazole
MeOH	Methanol
MF	Magnetic fields
MH	Magnetic hyperthermia
MIL	Materials of Institute Lavoisier
MMPs	Matrix metalloproteinases
MNPs	Magnetic nanoparticles
MOFs	Metal-organic frameworks
MPI	Magnetic particles imaging
MPS	Mononuclear phagocyte
MRI	Magnetic resonance imaging
Ms	Saturation magnetization
MSN	Mesoporous silica nanoparticles
MTO	Mitoxantrone
MTP-PE	Muramyl tripeptide phosphatidylethanolamine
MTV-MOF	Multivariate metal-organic framework
MTX	Methotrexate
NCs	Nanocomposites
Ni-IRMOF 74	Ni-based isorecticular metal-organic frameworks
NIR	Near-infrared
NU	Northwestern University
PBS	Phosphate-buffered saline
PAA	Polyacrylic acid
PAMAM	Platinum prodrug conjugated with polyamidoamine
PC-3	Human prostate cancer cells
PCN	Porous coordination network
PCSCs	Pancreatic cancer stem cells
PDAC	Pancreatic ductal adenocarcinoma
PDI	Polydispersity index

PDT	Photodynamic therapy
PEG	Polyethylene glycol
PEGPH20	PEGylated human recombinant hyaluronidase PH20
PFH	Perfluorohexane
PLA	Polylactic acid
PMA	Poly-[isobutylene-alt-maleic anhydride]-graft-dodecyl
PRL	Phospholipase-responsive liposomal formulation
PSMA	Prostate-specific membrane antigen
RES	Reticuloendothelial system
RF	Resonant radio frequency
RFA	Radiofrequency ablation
RIC	Redox-irresponsive cerasomes
RMF	Rotating magnetic field
ROS	Reactive oxygen species
RPN	ROS-responsive polyprodrug nanoparticles
RRC	Redox-responsive cerasomes
RSA	Rat serum albumin
RT	Room temperature
SA	N-stearylamine
SAR	Specific absorption rate
SBU	Secondary building unit
SEM	Scanning electron microscopy
SHH	Sonic hedgehog
SPIONs	Superparamagnetic iron oxide nanoparticles
sPLA2	Phospholipase A2
ssDNA	Single-stranded DNA
STEM	Scanning transmission electron microscopy
Suc	Hemisuccinate
TCPP	Tetracarboxyphyrin
TEM	Transmission electron microscopy
TGA	Thermogravimetric analysis
TGF- $\beta$	Transforming growth factor- $\beta$
T <sub>m</sub>	Transition temperature
UCNPs	Upconversion nanoparticles

Uio	University of Oslo
US	Ultrasound
UV	Ultraviolet
VSM	Vibrating sample magnetometer
WP6	Carboxylatopillar[6]arene
XRD	X-ray diffraction
ZFC/FC	Zero field cooled/field cooled
ZFNCs	Zn-ferrite nanocubes
ZIF-8	Zeolite imidazole frameworks-8

# Introduction

Nanomedicine formulations revolutionized the field of chemotherapeutic drug delivery thanks to their ability to enhance the physicochemical properties as well as the pharmacokinetic behavior of their drug load. There are dozens of marketed nanomedicine products and hundreds others in clinical trials; almost half of them are for cancer treatment, indicating their promise to fight against cancer. Metal-organic frameworks (MOFs) are a new class of nano-drug delivery systems that have porous hybrid (inorganic-organic) structures. They are composed through coordination bonds between inorganic metal ions or metal ions clusters and organic ligands. They have the advantages of exceptionally high porosity as well as functional and structural flexibility. The tunable MOF properties, offered through the rational choice of the metal ion and the organic linker, could enable the synthesis of MOFs with suitable optimal properties for the intended applications. For instance, biocompatible and biodegradable MOFs with optimal size, high drug loading capacity and easy functionalization could be synthesized. Due to these interesting properties, MOFs are attracting more attention in antitumor drug delivery applications. However, they usually suffer from off-target uncontrolled drug release and accumulation.

This thesis project, as a part of the [HeatNMof](#) European Innovative Training Network, was concerned with addressing these MOF delivery systems challenges. The HeatNMof project subject is **“Heating triggered drug release from nanometric inorganic – metal-organic framework composites,”** and it aims to develop smart responsive multifunctional nanocarriers based on MOFs for cancer treatment. The HeatNMof project aimed to endow the responsive properties to the MOF nanocarriers through heating either by light or magnetic fields (MF) stimuli, after incorporating gold or magnetic nanoparticles, respectively, inside the MOFs. The project involved the collaborative specialized expertise of 10 EU laboratories and two industrial partners for the preparation, physicochemical, magnetic, light and biological characterization of the heat-responsive MOF-based nanocarriers.

MOFs as porous materials were used for applications such as gas storage, water purification and catalysis. Their application in drug delivery was first reported in 2006 by Dr. Patricia Horcajada, the HeatNMof coordinator. Due to their recent employment as drug delivery systems compared to traditional ones as liposomes, the MOF full potential for therapeutic purposes, especially through the stimuli-responsive properties, has not been fully explored yet. Moreover, most studies in this field investigated MOF responsiveness to endogenous stimuli such as pH, redox or ions, and only a few investigated light- or MF-responsiveness.

This thesis project is concerned with utilizing the MF-responsive properties to enable controlled drug delivery from MOF-based magnetic nanocomposites. The nanocomposites used in this study consisted of magnetic nanoparticles (MNPs) core and MOF shells. The MNP embedded into the MOF drug delivery platform could allow controlled on-demand drug release in response to MF. Thanks to the MF versatility, this induced release could be triggered in a thermal or non-thermal mechanical way, depending on the type of applied MF. The high-frequency alternating MF (AMF) induces the MNP heating while the low-frequency rotating MF (RMF) induces MNP movement; both could trigger MF-responsive release from the nanocomposites. In addition, the MNP responsiveness could enable the targeting of the nanocomposites toward tumor tissues using the magnetic attracting forces generated by static MFs.

The magnetic nanocomposites used in this study were synthesized and physicochemical characterized by the project partners in *Bionanotools lab, the University of Santiago de Compostela, Spain*, thanks to their expertise in the synthesis of the MOF-based plasmonic nanocomposites.

Then, the nanocomposite magnetic characterizations were performed in the *Nanomagnetism group, laboratory of physics and chemistry of nano-objects, INSA-Toulouse*, thanks to their experience in the MNP characterization for various medical and non-medical applications. The group also developed setups that can fit under the confocal microscope and generate MF on cells, allowing real-time observation of MF-induced intracellular events in MNP-loaded cells. In addition, the magnetic nanocomposite interactions with cells were studied on model pancreatic cancer/cancer microenvironment cells in the *MICROPANC team, INSERM CRCT, Toulouse*, thanks to their expertise in pancreatic cancer biology. The team also has experience in exploiting the setups developed by the *Nanomagnetism group* for studying intracellular MF-induced events from MNP in real time under the confocal microscope.

During the project, three secondments were done, respectively in *Center for Hybrid Nanostructures (CHyN), Hamburg University, Germany*; *Nanomaterials for Biomedical Applications at Italian Institute of Technology Genoa, Italy*; and *Pharmidex Pharmaceutical Services LTD, London, United Kingdom*. The secondments allowed other studies on the nanocomposites, such as their hemocompatibility as well as synthesizing other MOF-based nanocomposites. This work will also be highlighted in the thesis.

In the thesis general introduction chapter, we develop a state-of-the-art background about four subjects. The first is about targeting nanomedicines to cancer tissues through passive or active targeting, or using stimuli-responsive nanomedicines. In the second part, we discuss the MF stimuli and their application to target MNP-based nanomedicines to the tumor tissues and to trigger cell death

and/or responsive drug release. Then, a third part is developed about using MOFs as promising drug delivery systems for anticancer applications. In addition, state-of-the-art about the research work done using MNP-based MOFs for anticancer treatment is discussed. Finally, in the fourth part, we present the pancreatic tumors as a case study where nanomedicines – especially MNP-based ones – could enable higher therapeutic outcomes in their treatment. The thesis objectives are then presented after the introduction.

The section presenting our results is divided into three parts. The first one presents a study of MF-responsive cargo release from MOF-based magnetic nanocomposites inside cancer cells as well as cancer associated fibroblasts. Herein, we used nanocomposites composed of iron oxide nanoparticles (IONPs) cores and nanometric zeolitic imidazolate framework (ZIF-8) as MOF shells. The nanocomposites were loaded with the cresyl violet (CV) fluorescent cargo and stabilized in aqueous media with an amphiphilic polymer coat. The synthesis and physicochemical characterization of the nanocomposites were done by the HeatNMof EU project partners in the Bionanotools lab at the University Of Santiago De Compostela (Spain). Afterwards, we investigated the magnetic properties of the synthesized nanocomposites as well as their cellular biocompatibility and uptake kinetics. Moreover, the MF-induced CV release from the nanocomposites inside cells was investigated in 2D cell culture and 3D multicellular spheroid models. Two types of MF stimuli were investigated; the AMF and the RMF inducing the IONP cores heating or mechanical movement, respectively. In addition, the effects of the MF-induced CV release on cell viability were investigated, thanks to the CV cytotoxic effects at higher concentrations. This first part gave us a proof-of-concept for the potential of having MF-responsive cargo release from MOF-based magnetic nanocomposites induced by MNP cores heating or movement.

Afterwards, a second part investigated the possibility of preparing anticancer drug-loaded MOF magnetic nanocomposites with different MNP cores. The magnetic properties of the MOF delivery systems could be affected by their MNP cores. Therefore, MNP of different shapes, dimensions and compositions were investigated to grow the ZIF-8 MOF shell on their surface. Afterwards, we investigated the possibility of loading two chemotherapeutic drugs, doxorubicin and 5-fluorouracil, into the developed magnetic nanocomposites. Two loading approaches were studied in order to allow drug loading either inside the pores of the ZIF-8 shell or on their surface. This part was done in the nanomaterials for biomedical application group at the Italian Institute of Technology (IIT Genova, Italy).

To further exploit the magnetic responsive properties of the magnetic nanocomposites, we considered investigating the development of a setup that could allow magnetic focusing of MNPs or

MNP composites towards targeted tissues. Hence, in a third part, we present a novel setup design that could enable the accumulation of MNP into deep-seated tumors and not only superficial ones. The latter is usually done by applying a magnet on the skin surface near the tumor, but it did not show promising results in clinics; that could be due to the rapid decay of the MF gradients going away from the magnet surface. Our proposed setup principle and its potential advantages were described. Afterwards, COMSOL Multiphysics® simulations were used to optimize the setup parameters and to have a simulation-based proof-of-concept for the setup design. In addition, the experimental work done for building the setup components is described. As the final steps of building the setup are still in progress, the experiments done are discussed up to the actual point of the progress.

Finally, the conclusions and perspectives of the thesis project are discussed.

# State of the art

## Part I. Targeted nanomedicines for cancer treatment

### I.1. Cancer

Cancer is a worldwide leading cause of death and a major health concern as it is an important cause of morbidity and mortality [1]. The GLOBOCAN 2020 statistics estimated  $\approx 19.3$  new cancer cases and  $\approx 10$  million cancer deaths in 2020 [1, 2]. The cancer burden is expected to increase in 2040 to  $\approx 28.4$  million cases ( $\approx 47\%$  increase from 2020). The main reason is the world population aging and growth, increased pollution and increasingly unhealthy lifestyle such as obesity and lack of exercise [1-3]. In Europe, cancer was estimated to be the second leading cause of deaths in 2020 (26%), after the circulatory diseases (34%) [4]. There was an estimate of 4.0 million new cancer cases and 1.9 million cancer deaths in Europe in 2020. Though representing almost 10% only of the global population, Europe has  $\approx 22\%$  of the cancer new cases and  $\approx 19\%$  of cancer deaths [5].

Cancer is the name given to a collection of related diseases with a common characteristic of uncontrolled cell growth and proliferation [6]. At cellular level, cancer development is a multistep process involving mutation and selection of cells with a progressive increase in their proliferation capacity, survival, invasion and metastasis. It can be divided into two major steps: tumor initiation followed by tumor progression. Due to cellular stress, carcinogen or abnormal hormonal level, genetic alteration could happen to the exposed cells leading to its abnormal proliferation and tumor initiation. Afterwards, this tumor cells proliferation leads to an overgrowth of a clonally derived tumor cell population. Additional mutations occur within the tumor population cells participating in the tumor progression. Some mutations endow selective advantage to the tumor cells conferring tumorigenic properties such as more rapid growth rate, better survival, invasion and metastasis [7].

Cancer is a very complicated and heterogeneous disease that holds different characteristics between different patients and at different stages of its development. Even a cancer emanating from the same cell in the body could have different characteristics depending on the underlying mutation and cellular microenvironment factors [8].

There are many studied known or suspected cancer risk factors including aging, hereditary reasons, alcohol, smoking, obesity, physical inactivity, carcinogenic substances exposure, infection with oncogenic microorganisms, etc. Some of these factors could be avoided, for example through lifestyle changes; others, such as aging and hereditary reasons, could not. So, developing effective therapies against cancer treatment is as important as preventing it [9].

## 1.2. Traditional treatments

The traditional tumor treatment strategies are surgical resection, Radiotherapy and chemotherapy [10]. The surgical resection is only effective in the first stages of cancer therapy before its metastasis, which is a common challenge in cancer treatment. For instance, studies indicated that 80-85 % of pancreatic ductal adenocarcinoma patients are not eligible for surgery because of the disease insidious onset, late diagnosis and metastasis [11]. Radiation therapy has wide and prominent applications in cancer treatment. However, it has intrinsic limitations of tumor radioresistance and severe side effects due to damaging healthy cells, tissues and organs [12]. Although chemotherapy reduced tumor morbidity and mortality, it suffers from non-specificity problems, i.e., killing healthy cells, especially rapidly growing ones. Other chemotherapy limitations include the development of drug resistance as well as poor physicochemical and pharmacokinetic properties such as low solubility and rapid metabolism [10].

## 1.3. Cells, targeted and ablation therapies

More recently, other cancer treatment approaches, such as cells, targeted and ablation therapies, have evolved.

Cell therapies for cancer treatment can be categorized into chimeric antigen receptor (CAR) T cells and stem cell therapies [13]. CAR T cells are clinical-grade immune cells, usually harvested from the same patient, activated, genetically transduced with CAR constructs, expanded, and then reinfused to the patient [14]. However, controlling their quality and quantities is still challenging, and they usually have limited anti-tumor activity due to their rapid differentiation into short-lived effector cells [15, 16].

On the other hand, stem cells can be exploited as antitumor therapies using different strategies due to their capacity for proliferation, migration and differentiation [13]. For example, induced pluripotent stem cells (iPSCs) were used to produce effector immune cells, which are then CAR-constructed for adoptive cell transfer technology. Using iPSCs for CAR anticancer application could be more advantageous than using the CAR T cells approach as iPSCs can be used for a larger number of patients, not only the same patient. Also, the iPSCs take more time to differentiate than the CAR T cells [16]. Another approach is using iPSCs as potential sources for the production of anticancer vaccines [13]. Also, the mesenchymal or neural stem cells' tumor tropism properties can be utilized to deliver genes, nanoparticles and oncolytic viruses to the targeted tumors [13]. Moreover, hematopoietic stem

cells could be used to treat multiple myeloma, leukemia, and lymphomas for reconstituting blood-forming cells and leukocytes after high doses of chemotherapy or radiotherapy [17].

However, there are still potential risks and side effects of the cell therapies, most importantly tumorigenesis, increased immune responses, and autoimmunity [13]. Despite several success stories due to their good benefits vs. risk ratio [18], efforts are still being made to further enhance their efficacy and safety, especially regarding their therapeutic dose control, low cell targeting, and retention in tumor sites [10].

The development of targeted therapies (such as small molecule inhibitors, monoclonal antibodies, immunomodulators, immune checkpoint inhibitors, antibody-drug conjugates and hormones) has revolutionized cancer treatment [19]. They target specific oncogenic (such as kinases and steroid hormones) or non-oncogenic (such as proteasomes) targets in the tumor tissues. Despite their initial efficacy and the improvement achieved in the overall survival of patients, drug resistance remains a major challenge. This resistance could be intrinsic due to pre-existing mutations or acquired ones during the treatment course. The pre-existing or acquired mutations are usually limited to a tumor sub-population. However, the targeted therapies could offer selective growth, proliferation and survival for this resistant clone. Efforts are being devoted to developing combinatorial-targeted therapies to overcome the resistance challenge [19-22].

Cancer ablation therapies (e.g., thermal, cryo or radiofrequency ablation) rely on destroying the tumor without surgical removal [10]. This destruction is induced by extreme heat (for thermal and radiofrequency ablations) or extreme cold (for cryoablation) [23-25]. For instance, NanoTherm<sup>®</sup>, aminosilane-coated superparamagnetic iron oxide nanoparticles (SPIONs), is used for focal ablation of cancer lesions to treat glioblastoma and prostate cancer [26, 27]. After the SPION intra-tumoral injection, alternating magnetic field (AMF) is applied to induce local hyperthermia for killing tumor cells. Combined with radiotherapy, NanoTherm<sup>®</sup> showed better overall survival compared to conventional treatment options against glioblastoma multiform with few side effects [28]. Ablation therapy is limited to small-localized tumor lesions when the surgical option is contraindicated. It usually leads to destruction of nearby healthy tissues, so it is not indicated for tumors near sensitive tissues such as major blood vessels [10].

Consequently, developing novel treatment options for more effective and safe cancer treatment is imperative.

## I.4. Nanomedicine

### I.4.1 Introduction and nanomedicine definition

Nanomedicine has emerged as an application of nanotechnology for treating diseases, including cancer. Since Richard Feynman's talk in 1959 entitled "There's Plenty of Room at the Bottom", ideas and concepts of nanotechnology started to emerge [29]. Afterwards, Norio Taniguchi coined the term "Nanotechnology" in 1974 [30].

The European medical agency (EMA) defines nanomedicines as "purposely-designed systems for clinical applications that have at least one component at nano-scale size, resulting in definable specific properties and characteristics, related to the specific nanotechnology application and characteristics for the intended use (route of admin, dose) and associated with the expected clinical advantages of the nano-engineering (e.g. preferential organ/tissue distribution). Also, it needs to meet the definition of a medicinal product" [31]. The European commission (EC) recommendation [32] refers to nanomaterial as "a natural, incidental, or manufactured material comprising particles, either in an unbound state or as an aggregate wherein one or more external dimensions are in size range of 1–100 nm for  $\geq 50\%$  of the particles, according to the number size distribution". It also acknowledged that an upper limit of 100 nm is not scientifically justified across the whole range of nanomaterials [32].

The Food and Drug Administration (FDA) has not established regulatory definitions of "nanotechnology," "nanomaterial," "nanoscale," or other related terms. Instead, it refers to these terms as they are commonly used in engineering (i.e., deliberate manipulation, manufacture or selection) of materials that have at least one dimension in the size range of approximately 1 to 100 nm [33].

Both EMA and FDA refer to small nano-sized range particles. The ability to manipulate particles on the nanometer scale caused great progress in disease treatment. The importance of being small is getting more objects, more particles, for the same volume or weight. They thus display more surface area at which all the activities can occur, such as dissolution, solubilization, absorption, bioavailability, heat dissipation, interaction with biological membranes, cell internalization and attaching targeting ligands [34].

Nevertheless, the great win at nano-sizes is that the materials do not only get smaller but also they could get different. There is unique behavior of nanoparticles *in vitro* and *in vivo* resulting from their unusual chemical, physical and biological features compared to their bulk materials [35]. This unique behavior can be exploited in novel applications to make nanoscale devices and to produce materials with new properties [34]. In most cases, this nanoscale unique behavior is due to transformative changes. There may be a change in materials' optical, magnetic, mechanical, electrical,

catalytic and/or sorptive properties. Because of the size-dependent properties of nanoparticles, they offer a vast impetus for developing new therapeutic products [34].

In the context of cancer treatment, nanomedicines were exploited for therapy and diagnosis. Nanoparticles can act as a carrier for the active pharmaceutical ingredients as drugs, genes or contrast agents to enhance their pharmacokinetic properties and enable preferential accumulation and/or controlled release in the targeted tumor tissue. In other cases, the nanoparticles, as such, can be an active entity, *e.g.*, using nanocrystals of a chemotherapeutic drug or using magnetic nanoparticles for imaging and/or hyperthermia. Other nanomedicine platforms can combine both functionalities: they are composed of active nanoparticle entities and carry active pharmaceutical ingredients to be delivered to the targeted tissues. As of June 2021, 53 % of the nanomedicine formulations, either marketed or in clinical trials, were used for cancer treatment indicating their promise to fight against cancer [36].

As delivery carriers, nanomedicine formulations could solve challenges related to physicochemical properties (such as poor solubility or instability) and pharmacokinetic behavior (poor distribution or rapid elimination and metabolism) of their cargo. The majority, and hitherto an increasing percentage, of drug molecule candidates, have either solubility only or both solubility and permeability problems [37], making it difficult to have sufficient bioavailability at the targeted tissues. Consequently, developing an appropriate formulation for their delivery to the targeted tissues is needed towards their clinical translation. Nanomedicine formulations can enhance the solubility, bioavailability and stability of their cargo [38]. In addition, nanomedicines can help to overcome the multidrug resistance that is a major obstacle in cancer chemotherapy [39, 40]. It could occur due to the higher availability of efflux transporters in cancer cells, such as P-glycoprotein. Nanocarriers can also be tailored to bypass efflux transporters. Being loaded on nanosized carriers, the anticancer drug could be internalized into the targeted cancer cells by endocytosis, making it less susceptible to the action of efflux transporters [41]. Nevertheless, the ability of the drug-loaded nanocarrier or the drug alone to escape the endosomes, to reach their cellular targeting sites, should be taken into consideration [42, 43].

Nanomedicine formulations also have advantages for genetic material (RNAs and DNAs) delivery for cancer treatment applications. Genetic materials can suppress the expression of target oncogenes, upregulate the expression of tumor suppressor genes, or induce the production of immunomodulatory proteins in the targeted cells [44, 45]. Though minimally toxic, genetic materials are rapidly degraded in the blood and tissues due to the abundance of nucleases. Consequently, genetic material complexation with or loading into nanocarriers would enhance their chemical stability

and improve their pharmacokinetic properties. A proper design of nanocarriers should allow efficient intracellular uptake and help achieve endosomal escape of genetic material for optimal efficacy and enhanced therapeutic outcomes [44].

In addition to drug and gene delivery, nanocarriers can be used in other applications for cancer treatment, such as magnetic hyperthermia and photothermal, photodynamic, chemodynamic, sonodynamic, radio and starvation therapies [46].

Moreover, nanoparticles can be used for imaging either if they have inherent imaging detectability, such as magnetic nanoparticles (MNPs), or to deliver imaging contrast agents to the targeted tumor tissues [47].

Finally, theranostic applications of nanomedicines have emerged for the simultaneous use of nanomedicine formulations for both therapy and diagnosis [47].

The benefits above fostered a revolution in nanomedicine for cancer treatment, resulting in the development of a myriad of nanomedicine formulations that can be divided according to their nature into inorganic, organic or hybrid nanomedicines [48].

#### *Inorganic nanomedicines*

Gold, silver, MNPs, carbon nanotubes, porous silica and quantum dots are examples of inorganic nanomedicines. For example, gold nanoparticles (GNPs) are well-studied nanomedicines that are used as photothermal agents for tumor ablation in animal models and have even entered clinical trials [49, 50]. Upon laser irradiation of GNP accumulated in the cancer tissue, it would absorb the applied laser light and convert it into heat [51]. The produced heat could result in intracellular events such as protein denaturation and DNA damage [52]. Also, it can increase the permeability of tumor blood vessels as well as cancer cell membranes, resulting in higher tumor and cellular uptake of more nanoparticles and/or chemotherapeutic drugs [52]. The major advantages of the GNPs are their chemical inertness, simple gold-thiol bioconjugation chemistry as well as plasmon resonance tunability. Consequently, GNPs can be easily modified with surface coaters such as polyethylene glycol (PEG) to increase their systemic circulation time and biocompatibility. In addition, they can be functionalized with targeting or therapeutic agents to enhance their accumulation in the targeted tissues or their treatment outcomes. Moreover, GNPs shape and dimensions can be easily modified to have large near infrared absorption in the bio-transparent window (750-950 nm) with large photothermal conversion efficiency [49, 50].

### Organic nanomedicines

Examples of organic nanomedicines are liposomes, solid lipid nanoparticles, nanostructured lipid carriers, micelles, polymeric nanoparticles, exosomes, cyclodextrins, dendrimers, nanocrystals, polymerosomes, hydrogels, upconversion nanoparticles, lipoplexes, polyplexes, viral-like nanoparticles and protein or polysaccharides based nanoparticles. For instance, liposomes are lipid carriers that consist of single or multiple concentric bilayers of amphiphilic phospholipids surrounding aqueous core (for single unilamellar liposomes) or with additional aqueous spaces between lipid bilayers (for multilamellar liposomes) [53]. They can be loaded with both hydrophilic and hydrophobic drugs either in their aqueous core or in lipid membrane, respectively [53, 54]. Liposomes exhibit outstanding characteristics as nano-drug delivery systems such as protecting the loaded cargo from physiological degradation, extending their half-life, controlling the release of loaded cargo and biocompatibility upon being formulated from biocompatible lipid components [53]. Liposomes are the first class of lipid-based nanomedicine formulation translated to clinical applications [55]. Currently, more than a dozen marketed liposomal formulations are approved by EMA and the FDA; around half of these products are used for cancer treatment applications [55].

### Hybrid nanomedicines

Some nanomedicines have hybrid (inorganic-organic) nature such as metal-organic frameworks, or a composite of organic and inorganic nanomedicines, such as MNPs and liposomes nanocomposites.

To exert their antitumor effect or be a contrast agent for imaging, the nanomedicine formulation should accumulate at the targeted tumor tissues. It could be achieved through passive or active targeting or using stimuli-responsive nanomedicines (Figure 1).

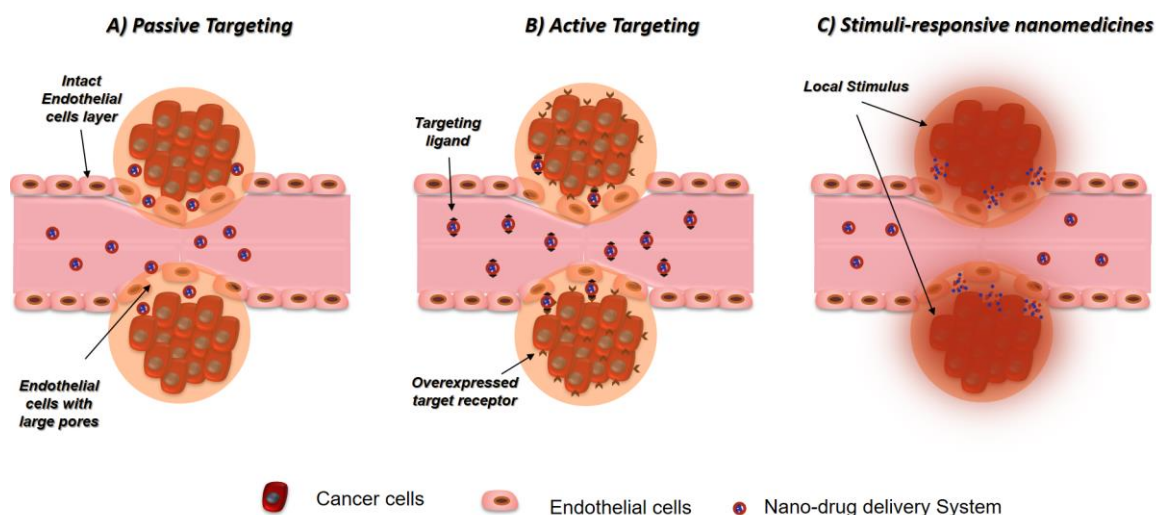


Figure 1: Schematic illustration of tumor targeting through passive and active targeting or using stimuli-responsive nanomedicines.

#### 1.4.2. Passive and active targeting

##### Passive targeting

In passive targeting, the accumulation in the targeted tissue depends on the tumor site's and the nanoparticles' properties.

In all cancer types, some cells in the body start to multiply in a non-controlled way. The rapidly growing cells could form a new tissue that suffers from hypoxia due to insufficient oxygen and nutrient supply [56]. The hypoxia could induce angiogenesis, a rapid uncontrolled and defective process, that results in the formation of highly permeable and leaky blood vessels in tumors. Besides, solid tumors tend to have inefficient lymphatic drainage. These tumor-specific anatomical characteristics, when happen, could result in preferential accumulation of nanocarriers in cancer tissues upon systemic administration (intravenous (i.v.) administration). This phenomenon is known as the enhanced permeability and retention (EPR) effect [57, 58]. Such effect is characterized by both higher permeation of the nanocarriers to the targeted cancer tissue due to wider fenestration in their blood vessels (100-780 nm [59-61] vs. an average of 107 nm in the normal liver “widest normal blood vessels fenestrations”[62]). In addition, there could be longer retention time in the cancer tissues due to inefficient lymphatic drainage [56]. Hence, higher nanomedicine levels at the targeted tissue and longer intervals for cellular uptake, cargo release and accumulation at the diseased tissue could be expected. Consequently, it could result in better therapeutic outcomes [56].

On the other hand, the nanoparticles should have sufficient blood circulation time for enough permeation through the leaky tumor vasculature. Once injected into the blood, nanoparticles are prone to interactions and coating by plasma proteins, opsonization and uptake by the mononuclear phagocyte system (MPS) available in the blood, bone marrow, spleen, liver and lung. Coating the nanoparticles with hydrophilic moieties can decrease their interaction with plasma proteins and lead to less MPS uptake [63]. This stealth property could be endowed using polymers such as PEG and poly(2-oxazoline) [63]. Factors such as the coating moiety molecular weight, surface chain densities, and surface conformation should be considered for successful camouflaging [63]. Also, biologically inspired cell membranes or CD47- ligand coating have been developed [63]. Tang *et al.* coated the nanoparticles (liposomes) with CD47-derived “don’t-eat-me” ligand to inhibit phagocytic uptake and accumulation in the MPS. The nanoparticles had prolonged circulation time and better accumulation in the targeted brain tumors [64]. Currently, the recruiting phase I clinical trial (NCT03608631) is undergoing using exosomes (derived from mesenchymal stromal cells, loaded with KrasG12D siRNA and functionalized with CD47 ligand) for treatment of pancreatic ductal adenocarcinoma. CD47-mediated protection was employed to protect them from phagocytosis by macrophages and monocytes [65].

Other factors such as size, surface charge and shape could affect their blood circulation time. For instance, nanoparticles having a hydrodynamic diameter of 5 nm or less were found to be rapidly cleared by the kidney [66]. In addition, positively charged nanoparticles were more uptaken by the MPS compared to the negatively charged ones [67]. Moreover, the shape of the nanoparticles affects their surface area, consequently affecting the amount of adsorbed plasma proteins [68].

All the marketed targeted nanomedicine formulations for cancer treatment rely on passive targeting [69, 70]. They are lipid (liposomal) or protein nanoparticle-based formulations.

Doxil® is an example of the lipid-based formulations, and it is pegylated stealth liposomal formulation of doxorubicin (DOX) used to treat Kaposi sarcoma, ovarian cancers and multiple myeloma. The nanoliposomal formulation of DOX enhanced its blood circulation time, increased the tumor accumulation and decreased its cardiotoxicity side effects, resulting in better therapeutic outcomes compared to the free DOX [71]. Abraxane® is an example of the protein-based formulations, and it is paclitaxel albumin-bound nanoparticles for treatment of breast, non-small lung and pancreatic cancers. This protein-based formulation of paclitaxel enabled its better solubility, increased circulation time, enhanced tumor uptake, and less toxicity. This resulted in better response rates and survival in metastatic breast cancer patients compared to Taxol® (single-agent paclitaxel)[72].

Although passive targeting and exploiting the EPR effect caused an increase in the efficacy of passive drug delivery into tumor cells, there are still limitations related to the passive targeting strategy [73]. The EPR effect is very heterogeneous and affected by patient biology, tumor type, and the difference in cancer circulation and blood supply even within the same tumor tissue [74, 75]. For example, a small area in the tumor blood vessels can allow particles of size 200 nm to pass; however, other areas of the same tissue could possess blood vessels that do not permit small molecules of size 3-4 nm to pass. Besides, although the clinical trials of passively targeted nanomedicines in rats showed promising results, it is not always the case in humans. This was due to the relation between the tumor growth rate and the leakiness of cancer tissue supplying blood vessels. It usually takes about 2-4 weeks to induce tumor in rats; however, it may take years in humans to develop [76]. Hence, induced tumors in rats would have more leaky blood vessels due to faster growth rate and consequently higher passive targeting to tumor tissues by EPR effect [73].

Passive targeting alone could be inefficient in achieving high level of chemotherapeutic agents in the targeted cancer tissue, and most of the nanocarriers still accumulate in the MPS, which may result in less optimal therapeutic outcomes of chemotherapy [77, 78]. Approximately 0.6 % (median) of the intravenously administered passively targeted nanomedicine dose accumulated in their targeted tumors [79].

However, it is worth mentioning that passive targeting can be very valuable for cancer treatment in cases of targeting the MPS itself; herein, the nanocarrier formulation could have a major role in decreasing the toxicity of the anticancer agent as well as increasing its accumulation in the targeted MPS. For example, Mepact<sup>®</sup>, nanoliposomal formulation of mifamurtide was developed against osteosarcoma [80, 81]. The formulation is composed of lipid membrane-enclosed muramyl tripeptide phosphatidylethanolamine (MTP-PE), a synthetic analog of a component of bacterial cell walls, in 100 nm multilamellar vesicles [82]. MTP-PE has an immunomodulatory effect, and mifamurtide has a stimulatory effect on macrophages and monocytes [82]. Therefore, Mepact<sup>®</sup> formulation did not only enhance the uptake, extended retention time and minimized side effects of mifamurtide in the lung, liver, and spleen, but it also boosted the tumor-killing ability of macrophages/monocytes, achieving better survival in osteosarcoma treated patients [80, 81, 83].

Other biologically inspired passive targeting approaches were developed either using the protein corona or extracellular vehicles (such as exosomes). For instance, coating nanoparticles with poloxamer 188 or polysorbate 80 lead to surface adsorption of apolipoproteins (ApoE). The adsorbed ApoE facilitated receptor-mediated transcytosis of the nanoparticles to cross the blood-brain barrier, leading to enhanced brain accumulation for efficient glioblastoma treatment [84, 85]. Extracellular

vesicles have the advantages of tropism to their parenteral cells and the ability to practically carry any cargo. So that, they were used as Trojan horse approach for developing nanomedicines-targeted therapeutics [86, 87].

### Active targeting

Active targeting was exploited as an alternative approach for developing targeted nanomedicine formulations instead of the passive one. Active targeting depends on using targeting moiety or ligand such as antibody or peptide, which can specifically bind to a certain receptor, presented or overexpressed at the cancer cells, or to a specific overexpressed protein in the tumor microenvironment. The targeting moiety could be adsorbed or covalently linked to the surface of the nanoparticles, and it should have sufficient strong affinity to the targeted receptor [88]. Although active targeting could result in increased nanocarrier tumor cell uptake and accumulation, it depends in the first place on the passive one [89]. It is required for the nanoparticles first to reach and be in contact with the cancer cells to be able for subsequent binding to cancer cell receptors and internalization into cells. Even if the nanoparticles passed through the pores between the leaky vascular endothelial layer of blood vessels supplying the tumor, anatomical barriers could impede their access to the cancer cell receptors. Examples of those barriers are the layers of pericyte, smooth muscle and fibroblast-based cells present between the endothelial and tumor cells. In addition, there are the challenges of high cellular densities and high interstitial pressure in solid tumors. Another challenge is the interaction tendency between the plasma proteins and the nanoparticles surface that could lead to the protein corona formation. The formed corona could shield the ligands on the nanoparticles surface, hindering their interaction with the targeted receptors [90].

Approximately 0.9 % (median) of the intravenously administered actively targeted nanomedicine dose accumulated in their targeted tumors, with no significant difference to the 0.6 (median) of passively targeted ones [79]. Though there are some anticancer actively targeted nanomedicines in clinical trials, there is not, yet, any marketed one [73, 89, 91].

Active targeting to tumor endothelium was also developed to avoid the need for the tumor tissue penetration to access the targeted receptors. In active targeting to tumor endothelium, the nanoparticles would specifically adhere to tumor endothelium and release the anticancer drug in the tumor blood vessels achieving high drug concentration at the tumor. Consequently, there are neither anatomical barriers for the nanoparticles nor the high cellular densities and interstitial pressure challenges. Moreover, similarity between endothelial cells' phenotypes of different tumors is advantageous. Therefore, the same vascular targeting can often be used to target various tumors [92]. However, this approach would be limited to delivering either small molecular drugs, that would have

the ability to penetrate the vascular endothelium once being released at tumor circulation and subsequently reach the cancer cells, or the vascular disrupting agents, that destroy the vascular endothelium itself and consequently disrupting the blood supply to the tumor tissue [73, 92].

BIND-014 was developed as the first actively targeted tumor nanomedicine formulation for cancer treatment to enter into clinical trials. It is composed of polymeric nanoparticles loaded with docetaxel and functionalized with a small molecule ligand targeting tumor prostate-specific membrane antigen (PSMA). PSMA is overexpressed on prostate cancer cells and tumor-associated neovasculature of non-prostate solid tumors. In phase I clinical trials on patients with advanced solid tumors, the formulation was well tolerated with improved pharmacokinetic behavior compared to conventional docetaxel and noticed antitumor activity [93, 94]. However, on April 2016, the company halted the clinical trial of BIND-014 due to the poor objective response rate and not meeting the endpoints [95]. Herein, the tumor heterogeneity could have been a major challenge. The targeted tumor receptors density could differ between tumor types, stages and volumes. Patient stratification and only enrolling the right targeted patients (with clinically significant PSMA-overexpressing tumors) could have improved the therapeutic outcomes of BIND-014 clinical trials [96]. The same actively targeted nanocarrier formulation loaded with a diagnostic agent, instead of the antitumor drug, can be used for patient screening before administering the nanomedicine chemotherapy-loaded one [96].

#### *1.4.3. Stimuli-responsive nanomedicines*

Stimuli-responsive targeting relies on enhancing nanoparticles accumulation, their activation or cargo release upon exposure to internal or external stimuli specifically located at the targeted tissues [97]. This could happen following physical or chemical modification in the nanoparticle, such as protonation, degradation, or a molecular or supramolecular conformational change, in response to change or stimuli in their microenvironment. There are several types of stimuli that can be divided into internal such as pH, redox, reactive oxygen species (ROS), hypoxia and enzyme, and external such as ultrasound, light, magnetic fields (MF) and heat (thermal stimulus) (Figure 2) [97].

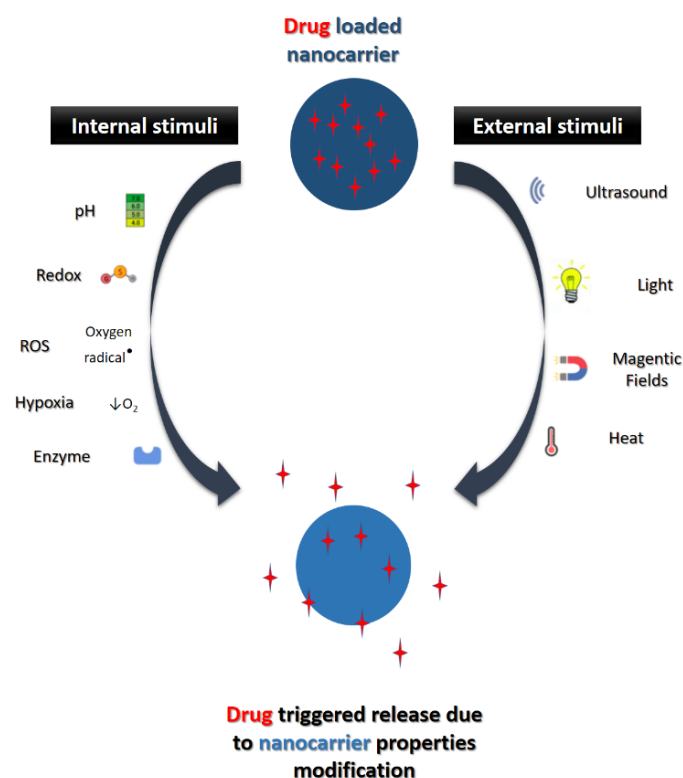


Figure 2: Schematic illustration of internal and external stimuli used to trigger drug release from nanocarriers.

#### 1.4.3.1. Internal stimuli-responsive nanomedicines

Internal stimuli, such as low pH, redox potential, ROS, hypoxia and enzymes, are triggers that could intrinsically exist in tumor microenvironment or cancer cells.

##### 1.4.3.1.1. pH-responsive nanomedicines

pH-responsive nanomedicines utilize the different lower pH in the tumor microenvironment (around 6.5 to 6.8) or in subcellular compartments, as endosomes or lysosomes inside the cancer cells (around 4 to 6), compared to the pH of blood, normal tissues and cytoplasm (around 7 to 7.4) [98]. Transfer to a more acidic microenvironment could induce changes in the nanomedicine formulations such as protonation, dissolution, dissociation and/or coating detachment [99]. This could allow specific nanomedicine formulation activation or cargo release in the targeted location, resulting in fewer side effects in other non-targeted locations and achieving better therapeutic outcomes. Several pH-responsive nanomedicine formulations were developed, such as calcium carbonate ( $\text{CaCO}_3$ ) nanoparticles, calcium phosphate (CaP) nanoparticles, nanocrystals, inorganic nanoparticles, micelles, liposomes, polymerosomes, dendrimers and metal organic frameworks [97, 100].

For instance, Mi *et al.* developed pH-responsive copolymer hybrid CaP nanoparticles, loaded with Gadolinium (Gd) chelate, for magnetic resonance imaging (MRI)-guided Gd neutron capture therapy (GdNCT) of tumors [101]. After 72 h at lower pH (6.7) in DMEM/10%FBS (Dulbecco's Modified Eagle Medium containing 10% fetal bovine serum), the CaP was dissolved, allowing enhanced pH-responsive release of the gadolinium chelate contrast agent, a release percent of 47% compared to 5% only at pH = 7.4. This property offered preferential release and accumulation of the Gd chelate cargo at the tumor tissue enabling both precise tumor location due to the selective MRI local contrast enhancement, as well as selective killing of cancer cells by thermal neutron irradiation. The developed pH-responsive Gd-chelate loaded CaP nanoparticles showed effective suppression of tumor growth in subcutaneous C26 tumor-bearing mice following MRI-guided GdNCT therapy [101].

#### 1.4.3.1.2. Redox responsive nanomedicines

The significant glutathione (GSH) higher levels inside cancer cells (1-10 mM) compared to normal ones (2-10  $\mu$ M) resulted in different redox potentials between them and made it possible to develop redox-responsive nanomedicine formulations [102]. Other studies reported that tumor tissues had at least 4-fold higher intracellular GSH concentrations than normal ones [103, 104]. Disulfide (S-S), diselenide (Se-Se) and carbon-selenide (C-Se) are examples of bonds used for GSH-induced bond cleavage in redox-responsive nanomedicines [105]. This redox-responsive strategy can be exploited to:

- A) Cleave redox-responsive bond between the nanocarrier building blocks, the drug and the nanocarrier, or seal surface molecules of the nanoparticles,
- B) Reduce the  $\text{Fe}^{3+}$  to  $\text{Fe}^{2+}$ , resulting in disruption of the drug-loaded cationic vesicles formed by chelating  $\text{Fe}^{3+}$  and pillararenes [106].

For instance, Zhou *et al.* developed DOX-loaded redox-responsive cerasomes (RRC/DOX) nanocarrier formulation [107]. Cerasome consists of a bilayer membrane of lipids that contains two fatty acid chains, but with a silicate head group instead of phosphate. It has a higher morphological stability than conventional liposomes. The RRC included a redox-cleavable disulfide bond between the silicate head group and the hydrophobic tail chains. *In vitro*, after 48 hours at 10 mM GSH concentration and pH of 7.4, the RRC/DOX showed better cumulative DOX release ( $\approx$  60%) than the DOX-loaded redox-irresponsive cerasomes (RIC/DOX) ( $\approx$ 30%). Both RRC/DOX and RIC/DOX were nontoxic to non-cancer human embryonic kidney 293 cells up to cerasome concentration of 0.5 mg/ml and 48 hours of incubation. Moreover, RRC/DOX showed a lower  $\text{IC}_{50}$  than RIC/DOX on human hepatoma cells (0.58  $\mu$ M for RRC/DOX and 2.24  $\mu$ M for RIC/DOX) and breast cancer cells (1.70  $\mu$ M for RRC/DOX and 3.84  $\mu$ M for RIC/DOX) [107].

#### I.4.3.1.3. Reactive oxygen species-responsive nanomedicines

ROS, such as superoxide anion ( $O_2^{\bullet-}$ ), singlet oxygen ( $^1O_2$ ), hydroxyl radical ( $^{\bullet}OH$ ) and hydrogen peroxide ( $H_2O_2$ ), are a class of chemical compounds that have a common feature of incomplete reduction of oxygen [108, 109]. At normal concentrations, ROS play a crucial role as signaling molecules in many biological processes, such as transcription, protein translation, and metabolic pathways [110-112]. Excessive aerobic glycolysis, followed by mitochondrial pyruvate oxidation (the Warburg effect), could generate abnormally high ROS, resulting in enhanced oncogene activity and activated oxidizing enzymes that induce genetic instability [113]. Hence, higher levels of ROS, exceeding the antioxidant ROS scavenging defense, lead to oxidative stress in tissues. This stress could be implicated in many pathological conditions, such as proliferation of tumor cells and tumor progression [112]. Consequently, oxidative stress, when exists, looks appealing to be exploited for the design and development of ROS-responsive nanomedicines. Most ROS-responsive nanomedicines are based on redox-responsive functional segments that could undergo oxidative cleavage of specific covalent bonds in the presence of ROS, enabling responsive nanomedicines activation and/or cargo release [114].

For instance, Xu *et al.* developed ROS-responsive polyprodrug nanoparticles (RPN) for cancer therapy. The RPN were prepared by self-assembly of lipid PEG as an outer shell with a ROS-responsive copolymer core (composed of mitoxantrone (MTO) and ROS-susceptible thioketal-containing linker) [115]. They were further functionalized with internalizing arginyl-glycyl-aspartic acid (iRGD) peptide to target  $\alpha v$  integrins receptors on tumor endothelial cells (Figure 3A). On LNCaP (lymph node carcinoma of the prostate) cells, the RPN had  $IC_{50} = 4.35 \text{ mg L}^{-1}$  compared to 80% survival at concentrations as high as  $20 \text{ mg L}^{-1}$  of the control nanoparticles without the thioketal-responsive functional group. The i.v. injection of targeted RPN showed efficient tumor targeting and tumor parenchyma penetration with enhanced ROS-responsive intracellular MTO release in the subcutaneously induced LNCaP xenograft tumor-bearing mice. This resulted in better tumor growth inhibition (less than 2-fold tumor volume increase) compared to the control groups of free MTO drug (3.3-fold tumor volume increase), non-targeted formulation (2.5-fold tumor volume increase) (Figure 3B) with no hematologically or histologically detected acute side effects [115].

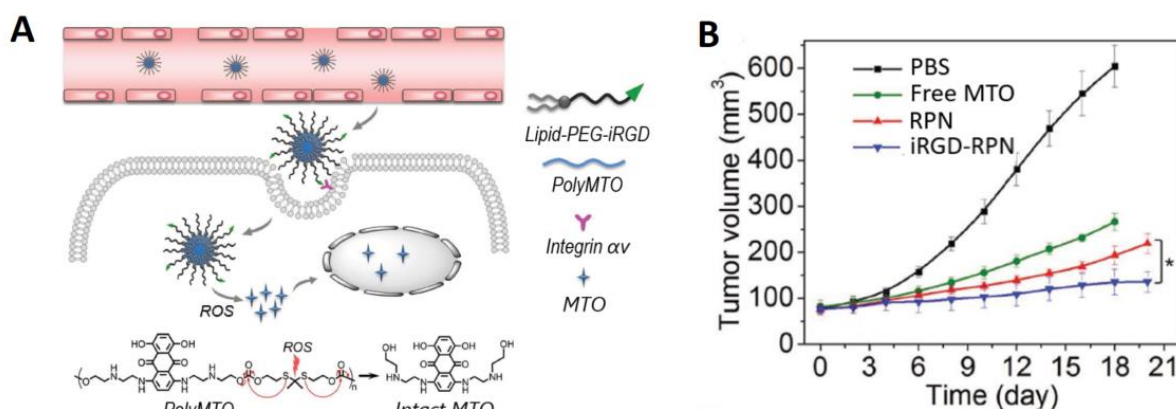


Figure 3: Schematic illustration of the targeted ROS responsive RPN platform composition, cellular targeting and uptake as well as the prodrug responsiveness to ROS through breaking the thioketal linker to release the free MTO B) Tumor growth curves after i.v. injection of PBS, free MTO, non-targeted RPN formulation or the targeted RPN formulation in LNCaP xenograft tumor-bearing mice. Adapted from [115].

#### 1.4.3.1.4. Hypoxia-responsive nanomedicines

Tumor hypoxic conditions result from poor tumor vasculature, which participates in tumor growth and progression through angiogenesis, invasion and metastasis. Moreover, hypoxic tumors generally have a bad prognosis due to their resistance to standard therapy (such as chemotherapy or radiotherapy). Though posing a challenge for tumor treatment, hypoxia conditions can be utilized for controlled targeted stimuli-responsive nanomedicine formulations [116]. Hypoxia-responsive nanocarriers are designed through introducing hypoxia-responsive groups or linker that can undergo bioreduction, such as hydrophobic nitroimidazole conversion into hydrophilic aminoimidazole, or cleavage of an AZO linker or nitrobenzyl alcohol derivative [116].

Hypoxia-responsive polyerosomes were prepared by aqueous self-assembly of a diblock copolymer (composed of hydrophilic PEG conjugated with hydrophobic polylactic acid through an azobenzene linker). In iso-osmolar HEPES buffer (pH 7.4), the prepared polyerosomes showed 90% release of its encapsulated dye cargo under hypoxia conditions (achieved by bubbling nitrogen gas) after 50 min compared to zero release under normoxic conditions. On 3D hypoxic spheroids of pancreatic cancer cells (BxPC-3), the drug (gemcitabine and erlotinib) loaded polyerosomes showed a significant decrease in cell viability ( $24 \pm 4\%$ ) compared to the nonloaded polyerosomes ( $48 \pm 2\%$ ) [117].

#### I.4.3.1.5. Enzyme-responsive nanomedicine

Upregulated levels of certain enzymes at tumor sites were employed to locally release the anticancer drug from enzyme-responsive nanomedicines. Hydrolases, such as phospholipase A2 (sPLA2) and matrix metalloproteinases (MMPs), transferases (e.g., creatine kinase) and oxidoreductases (e.g., peroxidases) are examples of main enzymes that could be upregulated in tumor microenvironment and cancer cells [97]. Having enzyme-responsive components, nanocarriers could specifically respond to release their cargo through degradation, dissociation or physical disruption. For successful rational design of the enzyme-responsive nanomedicine, the following points should be considered: 1) the accessibility of the enzyme to the enzymatic responsive group or substrate in the nanomedicine platform, 2) the presence of sufficient substrate concentration threshold at the targeted tissues to ensure the enzyme triggered reaction, and 3) the suitability of the physicochemical properties and physiological conditions to the enzymatic activity [97].

For instance, the level of sPLA2 is increased in inflammatory as well as breast, pancreatic and prostate cancer tissues. It has the ability to hydrolyze the phospholipids in the liposomal lipid bilayers into lysolipid and free fatty acid, resulting in less stable and leaky liposomal membrane and increased drug release selectively in the cancer tissues [118]. This hydrolysis occurred through cleavage of phospholipase responsive sn-2 ester bond, the ester bond of the middle hydroxyl group in the glycerol backbone of the phospholipid. Cummings *et al.* prepared phospholipase-responsive liposomal formulation (PRL) (composed of 1,2-Distearoyl-sn-glycero-3-phosphocholine, 1,2-Distearoyl-sn-glycero-3-phosphoethanolamine and distearoylphosphatidylethanolamine) loaded with 6-carboxyfluorescein dye or DOX. The fluorescent dye-loaded PRL showed increased cargo release ( $\approx 12\%$ ) upon exposure to phospholipases (after 108 h in F-12K medium containing 10% FBS at 37 °C), and the release was diminished in presence of phospholipase inhibitor ( $\approx 3\%$ ). The DOX loaded PRL resulted in decreased tumor growth ( $\approx 3$ -fold tumor volume increase) in mouse xenograft model of human prostate cancer (subcutaneously implanted) compared to non-enzyme responsive liposomal formulation ( $\approx 7$ -fold tumor volume increase), after 4 weeks of initiating the weekly tail vein injection dosage regimen [119].

#### I.4.3.1.6. Conclusion on internal stimuli-responsive nanomedicines

Relying on the internal, already existing, triggers for targeted nanomedicines looks appealing, as there is no need for extra technical and regulatory complications of using an external setup to produce external stimuli. However, several challenges could emerge during their clinical translation. First, cancer is a very complex and heterogeneous disease. For instance, increased GSH levels in tumors

for applying redox-responsive nanomedicines does not happen in all tumors. It depends on tumor type [120], cancer-associated fibroblasts involvement and infiltrating immune cells activation [121]. Also, regarding the pH-responsive nanomedicines, it was reported that tumor cells do not only acidify but also it could alkalize [122, 123].

In addition, being internal “built-in” stimuli, it is difficult to manipulate their intensity to be strong enough for rapid and effective triggered activation of (or cargo release from) the nanomedicine formulations. For instance, it was found that thiolated polymers take several hours for reduction under physiological conditions [124, 125]. In addition, pH responsiveness was found to have a slow response speed [125]. Considering also the tumor heterogeneity, it sounds complicated to have similar responses in the patient cohort due to different internal stimuli intensities in their tumors. Even the patient response could differ during the course of treatment due to changes in the tumor size and its microenvironment. Herein, a theranostic platform could be valuable for monitoring patient responsiveness and for subsequent dosage adjustment in individual patients or during the course of treatment.

Multi-stimuli responsive nanomedicine formulations have been developed for safer and efficiently targeted anticancer therapies trying to overcome the heterogeneity and the lack of stimulus threshold adjustment challenges. For instance, Duan *et al.* developed PEGylated DOX-loaded multi-stimuli-responsive dendritic copolymer nanoparticles. The dendritic copolymer had enzyme (cathepsin B) responsive properties as it was composed of poly[N-(2-hydroxypropyl)methacrylamide] segments with enzyme-responsive GFLG (Gly-Phe-Leu-Gly tetrapeptide) linkers. The DOX was loaded to the dendrimer through a pH-responsive hydrazone bond, and PEG coating was done through GSH-responsive disulfide linker. This multi-stimuli responsive nanoparticles platform showed pH, redox and enzyme-responsive drug release. It also achieved superior antitumor efficacy and great biosafety in the tumor mice model of the subcutaneously injected 4T1 breast cancer cells. After 21 days and from an initial tumor volume of 100 mm<sup>3</sup>, the measured tumor volume in nanoparticles injected mice group (at 4 mg DOX/kg) was 450.32 ± 132.16 mm<sup>3</sup> versus 830.06 ± 148.70 mm<sup>3</sup> for the free DOX injected mice group at the same dose and 1212.21 ± 218.49 for the saline control injected group; all were intravenously injected [126].

Mylotrag<sup>®</sup>, a dual pH and redox-responsive antibody-drug conjugate containing disulfide and N-acyl hydrazine linkage, was approved by FDA for the treatment of relapsed or refractory acute myeloid leukemia (AML) [127]. This could indicate the promise of the multi-responsive strategies for targeting tumor tissues and decreasing side effects on healthy tissues. However, it should be stated that the clinical translation process is very complex. Even Mylotrag<sup>®</sup> was retracted from the market in

2010 due to a higher rate of fatal toxicities compared to standard chemotherapy, before its re-approval in 2017 after modifying the dosing regimen [127].

A final challenge for the development of internal-stimuli sensitive nanomedicines is the technical need for developing suitable *in vitro* and *in vivo* models simulating the internal stimuli conditions in patients with the same intensities. Most *in vitro* cellular experiments are done at normal pH and oxygen levels, making their *in vivo* correlation and the nanomedicines clinical translation less straightforward.

#### 1.4.3.2. External stimuli-responsive nanomedicines

External stimuli are induced or signaled triggered applied from outside the body locally into the tumors to enable localized stimuli responsiveness. These triggers include ultrasound, light, MF and heat (thermal stimulus).

##### 1.4.3.2.1. Ultrasound (US)-responsive nanomedicines

Ultrasound is a noninvasive external stimulus that is safe, inexpensive, generally available in clinics and can penetrate deeply with high spatial resolution. It can be divided into two types. The first is the low-frequency ultrasound (LF-US) (< 20 kHz), which has a non-thermal mechanical cavitation effect and is also used for imaging. The second is the high-frequency ultrasound (HF-US) (> 20 kHz) that has a thermal heating effect. This part will discuss the targeted nanomedicines relying on the LF-US non-thermal stimulus. The triggered response of the HF-US stimulus is more due to the hyperthermia rather than the ultrasound waves themselves, so that it will be addressed with the thermal-responsive nanomedicines. LF-US responsive nanocarriers generally incorporate gas (such as air, nitrogen or perfluorocarbons) or a substance generating gas in biological environment (as CaCO<sub>3</sub>) [128, 129]. Due to its cavitation mechanical effect, US could widen the fenestration in tumor vasculature allowing better nanomedicine accumulation in the targeted tissues. It also could enhance nanomedicines uptake by tumor cells [130-132]. As the US-responsive component in nanomedicine formulation could commonly act as US contrast agents, this strategy is widely applied for theranostic use [133-135].

For instance, Meng *et al.* developed DOX-loaded US and pH-responsive nanodroplet for theranostic application against prostate tumors [136]. The nanodroplet was composed of O-carboxymethyl chitosan (pH-responsive component) and perfluorohexane (PFH) (US-responsive and contrast agent component). It was also loaded with DOX as chemotherapeutic agent. *In vitro*, the nanodroplets showed improved DOX release upon exposure to US (up to 82.3% DOX release after 10

min compared to 0% without US exposure) or upon exposure to acidic medium (54.5% DOX release at pH = 6.3 after 72 h compared to 16.7% at pH=7.4). The rapid efficacy and response of the external US stimulus compared to the internal pH one was evident in this study. The nanodroplets had a good US contrast ability *in vivo* after tail injection in PC-3 tumor-bearing mice (in which human prostate cancer (PC-3) cells were subcutaneously injected into their left or right forelimb). It also showed enhanced tumor growth inhibition compared to the control PC-3 tumor-bearing mice groups of free DOX, free DOX+US, nanodroplets- (without)US, and nanodroplets without PFH (non US-responsive)+US [136].

#### 1.4.3.2.2. Light-responsive nanomedicines

Several light-responsive nanomedicines have been investigated for cancer treatment. It is an attractive stimulus as it is possible to adjust its power, irradiation wavelength, and area of application [137, 138]. In cancer phototherapy, the commonly applied light sources are ultraviolet (UV) light (100-400 nm), visible light (400-760 nm) and near-infrared (NIR) light (760-1350 nm) [137]. Traditional phototherapy using UV and visible light are limited to superficial tumors due to their biological absorbance and limited tissues penetration abilities (3 cm max for visible light and even less for UV light) [139]. Utilizing NIR light, instead of UV and visible ones, could enable achieving better light penetration of up to 10 cm [140] thanks to its minimal skin and tissue absorbance. However, there is an emerged challenge of the low sensitivity of most light-responsive elements at higher wavelengths that could require the use of higher laser power affecting the healthy tissues [141]. Thus, it is important to carefully design the light-responsive nanomedicine treatment approach by selecting the light-responsive component and the irradiation characteristics suitable for the disease site and its depth. The designed light-responsive nanomedicines should incorporate a light-responsive component such as plasmatic nanoparticles (as GNPs), photosensitizers, organic molecules, or light-responsive chemical bonds [137]. The applied light stimulus could induce [97]:

- A) Conformational changes in some molecules, such as azobenzene,
- B) Cleavage of light-responsive chemical bonds leading to drug release from the nanoparticles due to its dissociation or from the prodrug precursor,
- C) Thermally-triggered release of the cargo from the nanocarrier,
- D) Local temperature increase for photothermal therapy,
- E) ROS production for photodynamic therapy,
- F) Light-assisted imaging (photoacoustic imaging) for theranostic applications.

For instance, Yuan *et al.* developed light-responsive nanoplatforms composed of upconversion nanoparticles (UCNPs) dispersed in a PEG-conjugated polyelectrolyte (CPE)–DOX polymeric matrix. The nanoplatform consisted of three light-responsive components, UCNPs and CPE (photosensitizer) and UV-cleavable ortho-nitrobenzyl linker (between the DOX and the PEG-CPE copolymer). Upon laser irradiation at 980 nm, the UCNPs emitted both UV and visible light. The up-converted UV light-induced photo-cleavage of the ortho-nitrobenzyl linker leading to light-responsive DOX release. While, the up-converted visible light-activated the CPE photosensitizer to generate ROS for photodynamic therapy (Figure 4). This combination therapy nanoplatform efficiently inhibited the U87-MG cell viability ( $36.4 \pm 7.1\%$ ) after laser irradiation (45 min,  $1.5 \text{ W cm}^{-2}$ , with 2 min break for each 5 min exposure) compared to the sole treatments ( $60.7 \pm 5.2\%$  cell viability for the drug free nanoparticles+ laser irradiation and more than 90 % cell viability for the laser irradiation alone) [142].

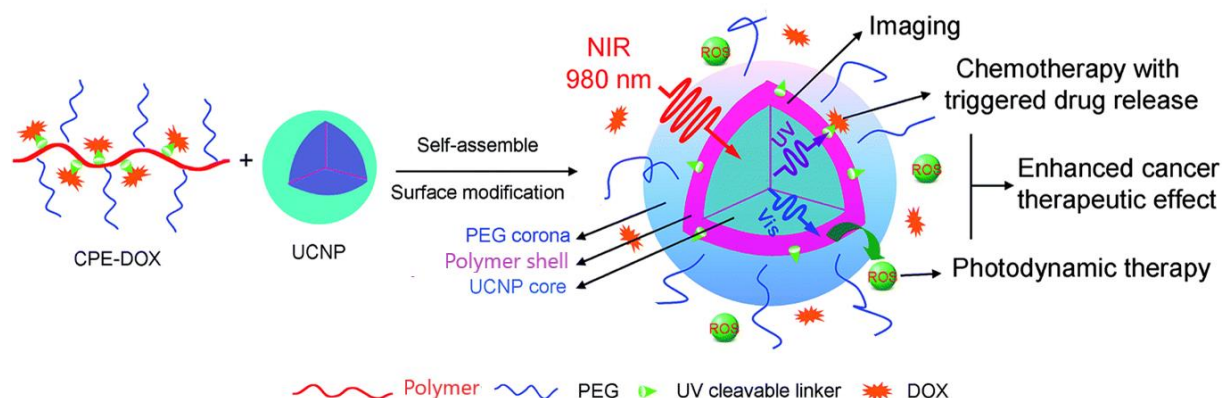


Figure 4: Schematic illustration of the light-responsive nanoplatforms composed of UCNPs dispersed in a PEG-conjugated CPE–DOX polymeric matrix where upon laser irradiation at 980 nm, the UCNPs emitted both UV and visible light. The up-converted UV light-induced photo-cleavage of the ortho-nitrobenzyl linker leading to light-responsive DOX release. While, the up-converted visible light-activated the CPE photosensitizer to generate ROS for photodynamic therapy. Adapted from [142].

#### 1.4.3.2.3. Magnetic fields (MF)-responsive nanomedicines

Magnetic nanomaterials properties were harnessed for developing targeted nanomedicines for cancer treatment. Not having penetration depth limitation, the magnetic stimulus could be more advantageous than light. Under static MF, MNPs can be directed to preferentially accumulate in tumors [143]. In addition, under AMF, MNPs could release heat, which can be used for heat-triggered cargo release or thermal ablation. Moreover, the low-frequency rotating MF (RMF) was used to induce magneto-mechanical actuation of MNPs [144]. These actuations could achieve MF-responsive cargo release, magnetically enhanced nanomedicine penetration, cellular uptake and killing of tumor cells [145-148]. The low-frequency MF stimulus offers fewer side effects such as eddy currents induced tissues heating, compared to the high-frequency one [149]. Though it is difficult to strictly apply the low or high-frequency MF to the targeted tissues, beforehand MNP focusing or targeting to the tumor

tissues using static MF could mitigate this issue [150]. In addition, magnetic nanomedicines can be used as contrast agents for MRI and magnetic particle imaging (MPI), opening an avenue for their theranostic applications [151]. MF-responsive nanomedicines applications are detailed in part II.

Cheng *et al.* investigated the efficiency of the magneto-mechanical destruction effect of disc-shaped MNPs against glioblastoma under RMF (20 Hz, 1 T). Inside tumor cells, the MNPs were aligned within the RMF plane, which enabled them to create a strong mechanical force to damage the tumor cell. *In vivo* on mice bearing brain glioblastoma xenografts (previously incubated with MNPs), 1 h MF exposure per day for 1 week reduced the size of brain tumors and enhanced the mice's survival rate without adverse side effects [152].

#### I.4.3.2.4. Heat (thermal)-responsive nanomedicines

Thermo-responsive nanomedicines are designed to be activated or release their cargo only at a temperature above 37 °C at the hyper-thermic locally heated tumor tissue (~39–42 °C) due to changes in the properties of the nanoparticles components [153]. Thermal responsiveness could be achieved in nanomedicine formulation through [97]:

- A) Phase transition or melting of lipid components in the nanoparticle,
- B) Polymer shrinkage at temperatures higher than its lower critical solution temperature, followed by nanoparticles opening or dissociation,
- C) Gas production from a thermo-responsive component resulting in the nanoparticle collapse,
- D) Cleavage of thermo-responsive chemical bonds leading to cargo release, or
- E) Thermally-triggered diffusion of the cargo from the nanoparticle.

Due to its additional benefits, hyperthermia is the most widely used and clinically advanced trigger for developing targeted nanomedicine anticancer applications. First, it could increase the delivery of the nanocarriers to the heated tissue due to the increased blood supply and perfusion, especially in case of an inefficiently vascularized tumor core [154, 155]. It also could increase the internalization of nanocarriers into the targeted cells as it enhances the cell membranes permeability [155]. Moreover, hyperthermia itself is beneficial for cancer treatment in several ways, including the increase in the responsiveness of the cancer cells towards chemotherapy [156, 157]. Cancerous cells, by themselves, are not naturally more responsive to hyperthermia than normal cells. Still, the tumor surrounding microenvironment has many stresses, such as poor blood and oxygen supply vessels within tumor tissue. This acidic and nutrient-deficient environment decreases the cancerous cells ability to withstand the added stress of heat [156, 158]. In general, the cytotoxicity of many

chemotherapeutic drugs was enhanced upon tumor heating to 40–43°C [159]. Hyperthermia could also initiate subcellular events mediated through heat shock proteins that could increase the cell's susceptibility to damage, such as apoptosis and cell death [160, 161]. Additionally, hyperthermia could interfere with temperature-dependent vital cellular processes such as DNA repair, macromolecular synthesis and cell cycle leading to cell death [162]. It also could enhance humoral and cellular immunity [163].

Thermodox<sup>®</sup>, a thermo-responsive lysoliposome containing DOX, reached phase III clinical trials for treating hepatocellular carcinoma (HCC) in combination with radiofrequency ablation [164]. Thanks to its lysolipids contents ( $\approx 10\%$ ), thermodox<sup>®</sup> liposomes showed more rapid and complete intravascular drug release upon heating, compared to the lysolipid-free conventional thermoresponsive liposomes that rely only on the lipid membrane phase transition [165, 166]. Lysolipids have only one hydrocarbon tail (compared to two hydrocarbon tails of phospholipids), so it has a relatively larger hydrophilic head-to-lipophilic tail ratio and tends to form micelles because of their intrinsic positive curvature. Near the melting-phase transition temperature ( $T_m$ ), the grain boundaries in the liposome membrane start to melt, resulting in increased lipid mobility. Due to its intrinsic positive curvature, the lysolipids accumulate on the curved walls of solid/liquid interfaces, leading to nanopores formation within the lipid bilayers and subsequent facilitated drug escape (Figure 5) [165].

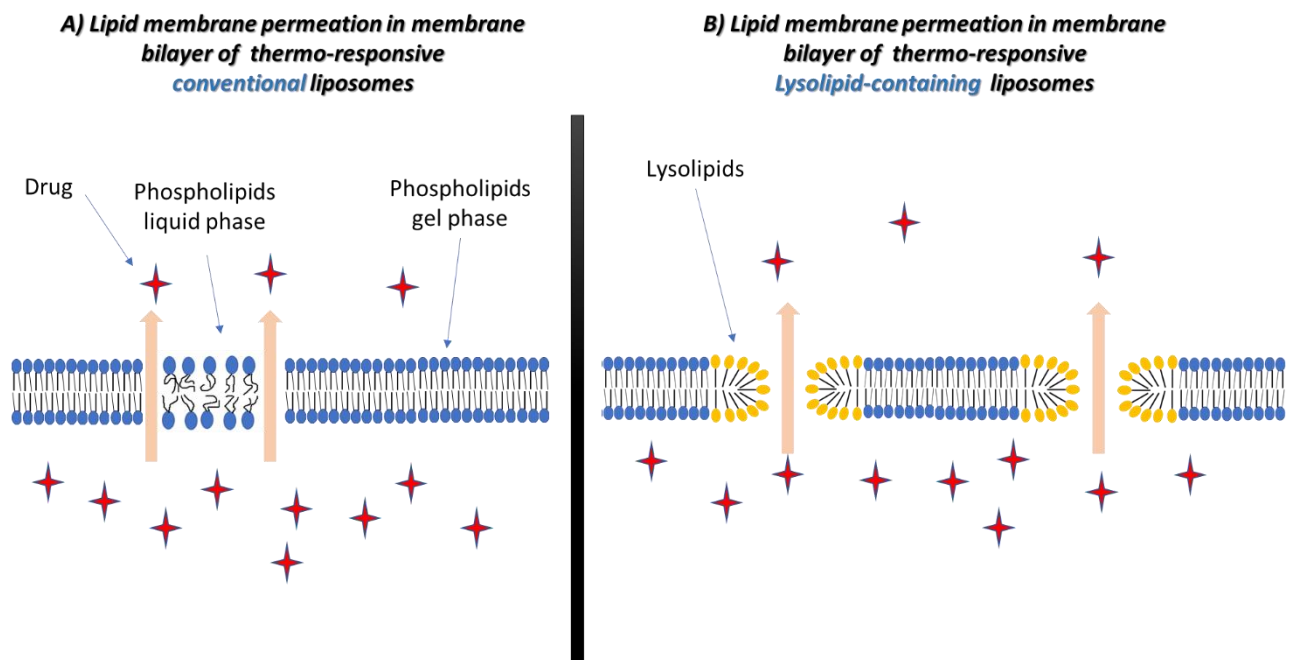


Figure 5: Lipid membrane permeation in membrane bilayer of thermo-responsive conventional (A) and lysolipid-containing (B) liposomes.

In early “HEAT” phase I clinical trials included 24 patients, ThermoDox® combination with radiofrequency ablation (RFA) showed promising results for treatment of inoperable HCC, which lead to direct accelerated route to phase III clinical trials. In the phase I study, the combination treatment achieved a significant dose-response relationship regarding the time to treatment failure and a good safety profile. Longer median time to treatment failure of 374 days was demonstrated for patients received ThermoDox® dose of at least 50 mg/m<sup>2</sup> compared to 80 days upon receiving a dose of < 50 mg/m<sup>2</sup> (p = 0.038) [167]. However, the “HEAT” phase III clinical trials included ThermoDox® with RFA had failed [164]. In this trial, ThermoDox® was employed to kill the remaining cancer cells outside the radiofrequency ablation zone. Several limitations might had contributed to the trials’ failure [168]. Most importantly is the non-uniform heat distribution, during the RFA in the tumor tissues, which looks not to be resolved even after standardization of the heating protocol in another phase III trial named “OPTIMA” [164]. This non-uniform heat distribution might not only had contributed to non-optimal tumor ablation but also it could have impeded achieving effective and homogenous thermoresponsive triggered DOX release from ThermoDox®. Studies suggested that significantly improved release rates from the thermoresponsive liposomes occur only around the T<sub>m</sub>, when grain boundaries and nanopores could form [169]. So that, during the development of external stimuli-responsive targeted nanomedicines, it is equally important to focus on the stimulus application technique beside the formulation development. RFA might not have been the ideal approach to be used for thermo-responsive targeted nanomedicines.

Instead of the poorly spatially controlled and invasive strategies to apply local deep tissues hyperthermia (as laser fibers, microwaves antennas, and radiofrequency electrodes), high intensity focused ultrasound (HIFU) has emerged as an alternative noninvasive better spatially controlled technique. Despite being noninvasive, it was still necessary to couple it with invasive optical probes or thermocouples to measure local temperatures. Recently, magnetic resonance-guided coupling to the HIFU made it a fully noninvasive technique. It also provided better spatiotemporal control of the applied hyperthermia due to the real-time noninvasive temperature feedback thanks to the MRI. Recent two phase I clinical trials were launched investigating ThermoDox® combination with HIFU. One study is for the treatment of pancreatic cancer (NCT04852367), and the other one that adds cyclophosphamide for treating primary breast tumors in metastatic breast cancer patients (NCT03749850) [164].

Alternatively, nanomaterials, such as GNPs, SPIONs and carbon nanotubes, can be employed to achieve an “inside-out” hyperthermia through its activation by a suitable external energy source, such as laser light or AMF [170]. The chemotherapeutic agents could be:

- A) Covalently attached to the heat-generating nanomaterial surface through thermo-responsive linker[171]
- B) Physically adsorbed on a thermo-responsive polymer shell around the nanoparticle [172].
- C) Loaded into thermo-responsive nanocarrier that either simultaneously administered with or injected after the heat-responsive nanomaterial [173].
- D) Co-loaded with the heat-generating nanomaterials into another thermo-responsive nanocarrier, such as liposomes [174].

Heating through nanoparticles allows inside-out hyperthermia, resulting in a more localized heating effect with minimal or no hyperthermia side effects on the surrounding healthy tissues.

Mai *et al.* developed theranostic thermo-responsive nanoplatform composed of iron oxide nanocubes coated with thermo-responsive polymer that physically adsorbed DOX. The thermo-responsive polymer undergoes shrinkage at temperatures higher than its LCST (lower critical solution temperature)  $\approx 40^\circ\text{C}$ , at the mild hyperthermia range ( $\approx 39^\circ\text{C}$  - $42^\circ\text{C}$ ) and above the body temperature  $37^\circ\text{C}$ . Upon MF (11 kA/m, 110 kHz) exposure, the heat produced by the magnetic nanocube core triggered DOX release 70% after 4h vs. 25% after 7 days at  $25^\circ\text{C}$ . *In vivo* on xenograft tumor mouse model, efficient tumor suppression without any remaining tumor mass was observed up to 3 months after intratumoral injection of the nanoparticles and magnetic hyperthermia treatment (11 kA/m, 110 kHz, 30 min over 3 subsequent days), compared to the control conditions (Figure 6). The nanoplatform was also beneficial for MRI imaging and monitoring of the response to treatment [172].

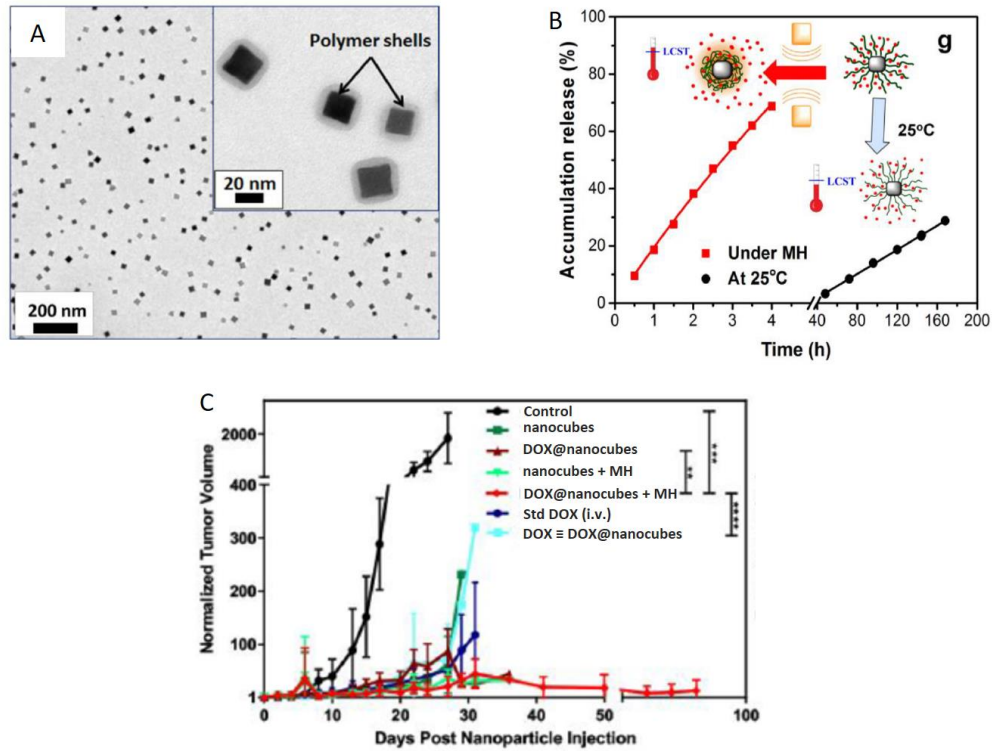


Figure 6: A) TEM images of iron oxide nanocubes coated with the thermo-responsive polymer shells, B) DOX release profile under magnetic hyperthermia (MH) (in red) compared to at room temperature (in black), C) Tumor growth curves in mice without treatment (control) and in response to different treatments (plain nanocubes, DOX-loaded nanocubes (DOX@nanocubes), nanocubes+MH, DOX@nanocubes+MH, standard DOX dose in clinics and DOX dose equivalent to the amount in the injected DOX@nanocubes, respectively from the second item on the top to the bottom). Adapted from [172].

#### 1.4.3.1.5. Conclusion on external stimuli-responsive nanomedicines

Externally triggered stimuli for targeted nanomedicines need an extra setup to generate the external trigger; however, they have many other advantages, making them very promising approaches for targeted therapies. The external application of the stimulus can be added or removed depending on the treatment requirement, enabling continuous or pulsatile therapy. There is also a possibility to manipulate the level of the trigger to have the same stimulus intensity between patients, thus mitigating the heterogeneity challenge. In addition, they show a rapid response of the nanomedicines compared to the internal triggers. To boost their clinical translation to patients, readily available moderately expensive setups of some strategies need to be developed. In addition, more optimization is needed regarding the coupling between the external triggers and the nanomedicines, especially the nanomedicine administration moment, time of applying the trigger, dosing and stimulus exposure duration.

#### I.4.3.3. Conclusion on stimuli-responsive nanomedicines

Stimuli-responsive nanomedicines are promising targeted nanomedicine formulations for cancer treatment due to the ability to switch (ON/OFF) the nanomedicine activation or cargo release upon exposure to the applied stimulus. This could enable a more potent anticancer effect at the targeted site where it is needed with minimum side effects at other healthy tissues. Nanomedicine formulations responding to pH, magnetic, thermal and phospholipase A2 (sPLA2) stimuli have entered clinical trials [97].

For clinical translation to the patient side, there could be a need to optimize the nanomedicine formulation to achieve the following:

- A) Stability in blood and keeping the responsive properties
- B) Scaled-up manufacturing ability of such commonly complex systems
- C) During formulation development and preclinical trials, it is essential to include all control conditions to have solid conclusions and get a successful clinical translation.
- D) Clarification of factors could affect the *in vivo* stimuli-responsive properties.

## Part II. The magnetic stimulus for targeting the nanomedicines to the tumor tissue and triggering cell death and/or cargo release

In the past decade, a plethora of research work has been dedicated to exploiting magnetic stimulus and MNPs-based nanomedicines for anticancer applications. The appeal of MNPs is their inherent responsiveness to the external MF. Depending on the applied MF, the MNPs can be directed to preferentially accumulate in targeted tissues, generate heat energy or rotate and exert torques. They can also serve as contrast agents for MRI and MPI, making them suitable for theranostic applications [175, 176].

### II.1. Magnetic nanoparticle properties (physicochemical properties and biological interactions)

#### II.1.1. Magnetic nanoparticle physical properties

There are different magnetic responses of materials to the applied external MF (Figure 7) depending on their chemical composition, their constituent elements' electronic configuration and temperature. They can be classified according to their magnetic responses into diamagnetic, paramagnetic, ferromagnetic, antiferromagnetic, ferromagnetic and superparamagnetic materials [176, 177].

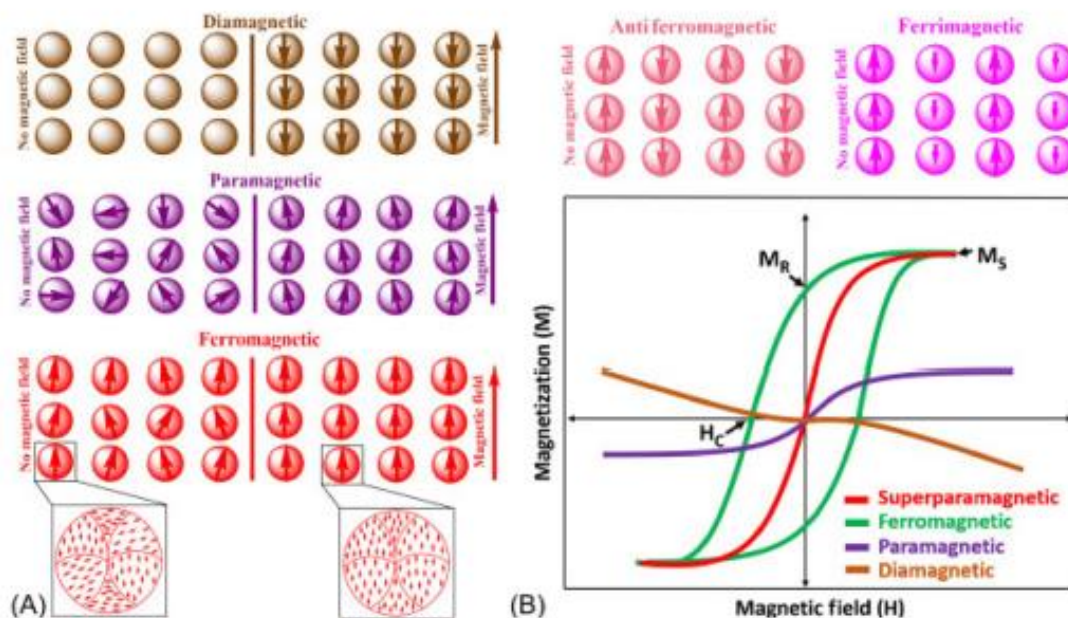


Figure 7: Responses of different materials to applied magnetic fields (A) and their representative magnetization curves (B), where diamagnets align in an opposite direction to the MF, para and ferro and ferri magnets align in the same direction to MF (less susceptibility for the paramagnets), anti-ferromagnets do not respond to moderate MF. Adapted from [178].

### Diamagnetic materials:

Diamagnetic materials are characterized by the absence of unpaired electron spins and by having a null magnetic moment in the absence of external MF. The magnetic response of a diamagnetic material acts to oppose the applied MF, so it displays a very small negative magnetic susceptibility. Organic compounds, most nonmetallic materials and inert gases are examples of diamagnetic materials [176].

### Paramagnetic materials:

Paramagnetic materials are characterized by having randomly oriented magnetic moments. An externally applied MF results in aligning these magnetic moments in its direction so that paramagnets display a small positive magnetic susceptibility. Nevertheless, they do not retain their magnetization after removal of the external field due to the randomization of their magnetic moment by thermal fluctuations. The degree of magnetic moment alignment originating from the external MF depends on its strength and inversely depends on temperature. Magnesium, aluminum, lithium and oxygen are examples of paramagnetic materials [176, 177].

### Ferro-, antiferro-, and ferri-, magnetic materials:

Individual atoms in ferromagnetic, antiferromagnetic and ferrimagnetic materials also carry magnetic moments. The particularity of these materials is that these moments interact with each other so that neighboring moments tend to be either parallelly (in ferromagnets) or anti-parallelly (in antiferromagnets and ferrimagnets) aligned (Figure 7). In the case of anti-ferromagnets, neighboring moments compensate so that the ideal materials carry a null global magnetic moment. However, antiferromagnets might have a net magnetization due to lattice defects or spin canting, but much lower than ferromagnets [177, 179]. On the other hand, ferro- and ferri-magnetic materials are formed of several magnetic domains carrying global magnetic moments. To maintain the lowest energy state, domain walls are formed between the different magnetic domains. When external MF is applied to a ferro- or ferri-magnet, the domains in the direction of the field grow in size, and so does the total magnetic moment of the materials. The magnetic response to AMF is a hysteresis loop with a typical shape schematized in Figure 7. Iron, cobalt, nickel and manganese are examples of ferromagnetic materials [179]. The most used magnetic materials in biomedical applications, magnetite ( $\text{Fe}_3\text{O}_4$ ) and maghemite ( $\text{Fe}_2\text{O}_3$ ), are ferrimagnets (see below). Typical antiferromagnets are NiO, CoO and FeMn.

### Superparamagnetic materials:

Superparamagnetism occurs in small ferro- and ferri-magnets where domain walls are energetically unfavorable, resulting in single-domain MNPs. The threshold size below which superparamagnetism occurs depends on the system thermal energy and the magneto-crystalline anisotropy energy [178, 180]. For iron oxide MNPs, the threshold size for superparamagnetic nanoparticles is 25 nm at room temperature [181].

The magnetic response of superparamagnetic nanoparticles strongly depends on temperature. At temperatures lower than their blocking temperature, there is not enough thermal energy to allow the spontaneous switching of magnetization; MNPs behave as ferromagnets. At temperatures higher than their blocking temperature, the thermal energy is enough to allow the thermal fluctuation-driven switching of magnetic moments; MNPs behave as paramagnets with a giant magnetic moment and susceptibility (where comes the name *superparamagnetism*) [177, 180]. The typical hysteresis loop of superparamagnets is given by the Langevin function [182]: the magnetic response saturates as the applied MF gets stronger; upon removal of this external MF, the superparamagnetic nanoparticles lose their magnetization without hysteresis. Superparamagnetic nanoparticles have thus both advantages of a) having a strong and rapid response to the external applied MF with large magnetic moment, and 2) losing the magnetization following MF removal, which helps towards their colloidal stability [178].

In response to AMF, MNPs (single or multidomain) respond through two main mechanisms for heat generation [183]:

- i- Brownian relaxation, where physical rotation of the particles occurs. It is thought to happen due to the locking of the particles' dipoles in a given crystal structure. So that an external AMF would exert a torque on the particles magnetic dipole resulting in their rotation and friction with surrounding solvent molecules.
- ii- Néel relaxation, where the particles are fixed, but their magnetic moment responds to the external AMF by rotating or switching. This friction between the magnetization and the atomic lattice leads to loss of electromagnetic energy in the form of thermal energy.

Both Brownian and Néel relaxation happen simultaneously; however, one of them, the faster, would predominate [176]. In any case, whatever the microscopic mechanisms, the amount of energy released in the environment equals the hysteresis area [184].

### II.1.2. Magnetic nanoparticle chemical composition for biomedical applications

Most MNPs used for biomedical applications are ferrite-based ( $M_xFe_{3-x}O_4$ ), where M could be Fe, Co, Mn or Zn. Due to the concerns related to the used MNP biocompatibility, toxicity and long-term *in vivo* fate and clearance, iron-based MNPs are the most commonly used ones [185]. The healthy human body has an average iron pool of 4 g and much lower levels of the other mentioned metals [186, 187]. The body also has mechanisms for handling, use and storage of iron. The body's two most important iron-containing proteins are ferritin and hemoglobin [188]. Ferritin is an intracellular protein that captures and stores iron in a soluble nontoxic form to avoid the free iron catalysis of cytotoxic ROS production via Fenton reactions [188, 189]. Hemoglobin is an important blood oxygen transporter with other roles as an antioxidant and regulator of iron [190, 191].

Magnetite ( $Fe_3O_4$ ) and maghemite ( $\gamma-Fe_2O_3$ ) are naturally occurring iron minerals and the most common interesting phases of iron for biomedical applications [176]. Both are ferrimagnetic materials that also exhibit superparamagnetic properties at the nanoscale. They also have similar cubic face-centered inverse spinel crystal geometry with very similar unit cell dimensions ( $a = 0.8396$  nm for magnetite and  $a = 0.8374$  nm for maghemite) [176]. Therefore, it is difficult to differentiate between them using conventional crystal phase characterization techniques such as X-ray diffraction, high-resolution transmission electron microscopy or Raman spectroscopy. A major difference between them is their iron content, where magnetite has both ferrous and ferric ions, while maghemite has only ferric ions. In an oxygen-rich environment, magnetite can be easily oxidized to maghemite. Hence, it is not easy to get pure magnetite nanoparticles and there are always concerns about the nanoparticle properties changes over time [176]. Magnetite could be intentionally fully oxidized into maghemite before use [192]. However, the mass saturation magnetization ( $M_s$ ) of magnetite ( $92 \text{ Am}^2/\text{kg}$  at 293 K) is higher than that of maghemite ( $76 \text{ Am}^2/\text{kg}$  at 293 K), which makes magnetite slightly more desirable for biomedical applications [193].

Other undesirable weak antiferromagnetic iron phases (such as hematite, wustite and goethite) could form as side products of magnetite or maghemite synthesis process; synthesis conditions should be controlled to avoid or minimize them [176, 194].

Substituted ferrite MNPs were also developed for biomedical applications. In them, one divalent iron atom is substituted by another divalent metal such as Co, Mn or Zn. This substitution introduces tunable changes in the physicochemical properties of the substituted ferrites, such as chemical stability,  $M_s$ , magnetic anisotropy ( $K_{\text{eff}}$ ) and heating power [185, 195]. Nevertheless, the inherent toxicity and ease of synthesis should also be considered when developing these systems for biomedical applications [196].

### II.1.3. Biological interaction of magnetic nanoparticles

Similar to all nanomedicines, introducing MNPs into the blood exposes them to plasma proteins, opsonization and MPS uptake unless they are coated with suitable materials to minimize these interactions. In addition, they can be designed to rely on passive or active targeting or stimulus-responsiveness to preferentially accumulate at the tumor tissues. However, as inorganic metallic nanoparticles, there could be concerns related to the MNP long-term *in vivo* fate, especially their biodegradability and excretion [197-199].

Ferumoxytol<sup>®</sup> (SPIONs) are already approved by the FDA for the treatment of iron deficiency anemia. Ferumoxytol<sup>®</sup> i.v. injection dose as high as 510 mg was tolerated in patients and increased their hemoglobin levels without serious side effects [200].

Acute iron overload could result in free radical formation and cellular damage at high doses, as observed for ingested iron doses of more than 60 mg/kg [201]. However, an optimized biocompatible coating of the iron oxide nanoparticles (IONPs) could mitigate this issue. For instance, it was reported that uncoated IONPs have LD 50 (median lethal dose) of 300-600 mg<sub>Fe</sub>kg<sup>-1</sup> body weight in rodents compared to an LD 50 of 2000-6000 mg<sub>Fe</sub>kg<sup>-1</sup> for the dextran-coated ones [202, 203]. Many studies showed intracellular lysosomal biodegradation of IONPs [204-207]. The resulting iron could be handled and stored by the ferritin protein, then transferred to other organs through the transferrin protein or incorporated into other proteins such as hemoglobin. The size and crystallinity of the nanoparticle, type of coating (organic as polymer, or inorganic as metal shell), and the availability and access of chelating agents to the metallic nanoparticle surface were among the factors that affected the IONP degradation kinetics [204, 206].

For instance, Gu *et al.* investigated the *in vivo* degradation rate of different IONPs, namely monodisperse PEG-phospholipids IO nanocrystals (IO core sized of 5, 15, 30 nm) and the dextran-coated Feridex<sup>®</sup> IONPs (IO core size of 2-4 nm). Using the dynamic light scattering, the measured nanoparticles hydrodynamic diameters were 13.3 ± 1.8, 28.7 ± 3.2, 52.1 ± 2.5, and 153.0 ± 11.9 nm for 5, 15, and 30 nm IO nanocrystals and Feridex respectively. One month after i.v. injection (5 mg<sub>Fe</sub>/kg) into wild-type BALB/c mice, the Feridex nanoparticles showed the fastest degradation rate and clearance from the liver and spleen. The remaining detected nanoparticles percent after one month, relative to the initially detected amount on day 1, were ≈20 % in the liver and ≈40 % in the spleen. In addition, relatively faster degradation kinetics was observed for the 5 nm IO nanocrystals compared to the 15 and 30 nm ones [208]. It was reported that IONPs can be retained in the tumor and stromal cells after their intratumoral delivery for 2-12 weeks, depending on their core size [209, 210].

It should be noted that the total body iron level is controlled only by absorption; however, a basal level of iron excretion is present in the body through hair or skin cell shedding, enterocyte turnover and excretion, loss in sweat and menstruation [211]. Hence, intermittent IONP treatment is rarely considered a risk for chronic iron overload. The ability to degrade the IONPs, with subsequent iron sequestration, storage, incorporation to the body or removal, makes their clinical use for biomedical application a promising avenue.

Substituted ferrites MNP containing Co, Mn or Zn have inherent toxicity challenges, and they aren't yet approved for clinical human use [196].

## II.2. Magnetic nanoparticle biomedical applications

MNPs have been an interesting option for biomedical applications. They are approved for clinical use as iron supplements to treat iron deficiency anemia [212]. They were also investigated as targeted carriers to accumulate in tumor tissues under magnetic guidance [143], as magnetic contrast agents for imaging [213] or as antitumor nanomedicines [175]. For antitumor applications, MNPs can be utilized to induce magnetic hyperthermia, magneto-destruction effect or for photothermal applications [152, 214, 215]. In addition, the MNPs can be used for chemotherapy drug delivery applications [216].

### II.2.1. Magnetic nanoparticle focusing/targeting to tumor tissues under magnetic field gradient guidance

#### The principles

Among all nanomedicine formulations, MNPs offer the possibility to be directed toward their targeted tissues in response to MF that can be applied remotely from outside of the body. There were many developed magnet setups for focusing the MNPs, which could be based on permanent magnets or electromagnets [143].

In the blood, MNPs could be subjected to many forces, such as blood flow, viscosity, buoyancy, van de Waals, thermodynamics, magnetic dipole-dipole interactions, etc. For directing the MNPs to the targeted tissues under MF gradients, a maximal magnetic force should be applied to them in order to be the predominant one governing their movement [143]. The magnetic force applied to MNPs can be expressed using the following formula [217],

$$F_m = -V \frac{\chi}{\mu_0} B \nabla B$$

where

$F_m$  is the magnetic force,

$V$  is the magnetic particle volume,

$\chi$  is the particle magnetic susceptibility,

$\mu_0$  is the magnetic permeability of the vacuum, and

$B$  and  $\nabla B$  are the applied MF and the MF gradient, respectively.

To get a large magnetic force, MNPs with a large size and a high magnetic susceptibility are preferred. Also, a magnetic focusing setup generating a strong MF with a high gradient should be used. It was reported that the MF gradient inside the human body is technically limited 1–10 T/m. Under this gradient, if all other factors (such as particles shape and colloidal stability) are optimized, it is required to have particles of sizes 100 nm to 1  $\mu\text{m}$  to get a displacement speed of 1 mm/s [218].

#### Magnetic guidance with permanent magnets

The simplest way is to apply an external magnet on the surface of the skin to focus the MNPs towards a superficial targeted site. The applied magnet enhances the accumulation of the nanoparticles to the targeted tissues; however, this technique did not show promising results in clinical trials [219]. It could be because of the limited focusing efficacy of this technique, as the MF strength and MF gradient generated from the magnet decay rapidly in proportion to the distance away from the magnet's surface. It is also worth noting that this technique could be applied only to superficial tumors, not deep-seated ones.

Alternatively, assemblies of permanent magnets were utilized to allow 3D MNP targeting that can be applied to deep-seated tumor targets [220]. For instance, Liu *et al.* investigated the use of two oppositely polarized external magnets for enhanced tumor penetration and accumulation of MNPs polymer assemblies of  $\sim 100$  nm (10 nm SPIONs embedded in polyethylene glycol-polycaprolactone diblock copolymer micelles). This magnets configuration allows the generation of a sharp zero MF point at the center surrounded by a strong and constant field gradient along the gap between the two magnets, which solved the challenge of sharp MF gradient drop going away from the single magnet surface [221]. This magnets configuration was compared to two control conditions (single magnet or no magnets used) after retro-orbital injection of the magnetic assemblies in female Balb/c mice bearing orthotopic 4T1 mammary gland tumors. The animals were positioned so that the center

between the two magnets corresponds to the tumor center or the single magnet is 10 mm away from the tumor. There was a noticed >3x increase in the tumor accumulation and >2x MRI signal for the magnetic assemblies using the two opposite magnets configuration compared to the controls. In addition, the accumulated magnetic assemblies traveled >5x more distance compared to the control conditions, indicating better tumor penetration [220]. However, the principle of driving out the MNPs out of the tumor center could have some limitations. Primarily, the MNPs could continue diffusing out until going outside the tumor tissues themselves to the nearby healthy ones. Also, it is needed to attract the MNPs to the blood vessels of the tumor tissues in the first place, before affecting their distribution within the tumors.

Another configuration named Halbach arrays are one of the best ways to strengthen the MF generated from assemblies of magnets (Figure 8). Thanks to their spatially rotating magnetization patterns, Halbach arrays squeeze the MF, resulting in its increase in one direction and decrease in the other one.

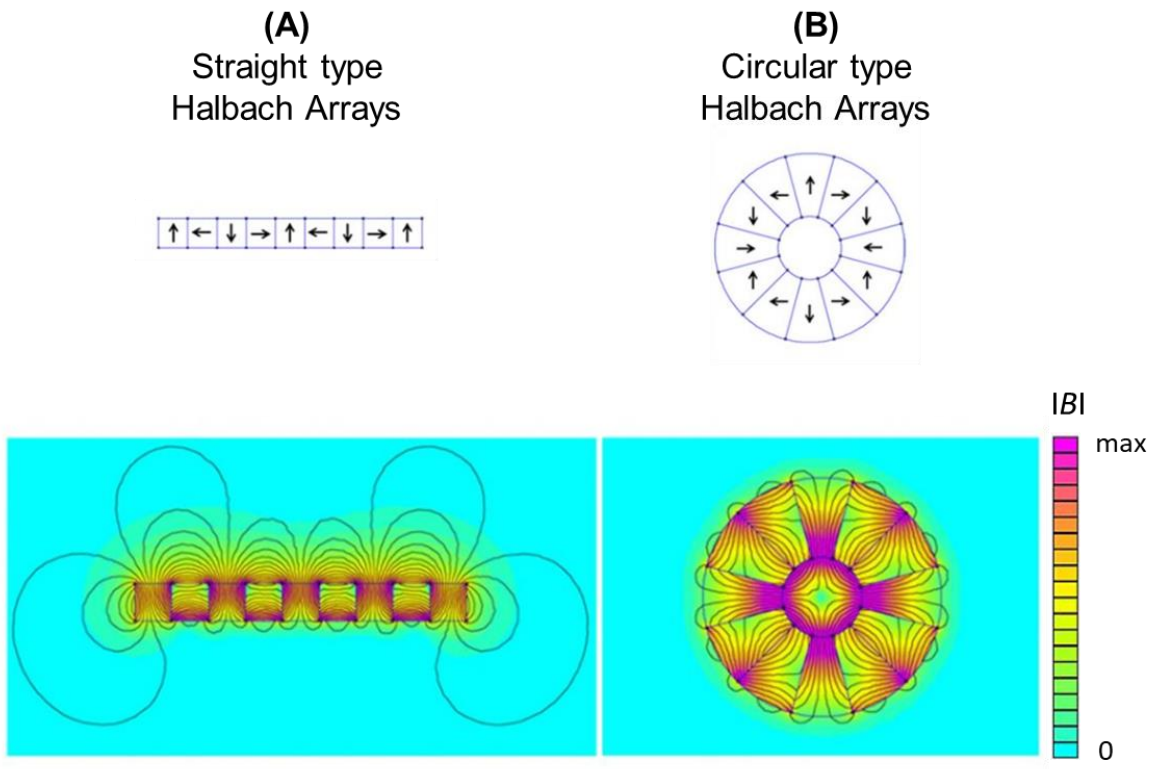


Figure 8: Halbach arrays magnets main types: a) Straight and b) Circular. The arrows represent the direction of magnetization of its magnetic block.

Many studies simulated the magnetic targeting effect of different Halbach arrays configurations and predicted a larger efficiency compared to single permanent magnets [218, 222]. Using finite elements simulations, Riegler *et al.* reported that an optimized circular Halbach array could exert magnetic forces on magnetically labeled cells in three major human arteries up to 3.5x more than magnetic rod, equilateral magnetic rod or straight Halbach arrays [222]. It is worth noting that both homogenous or high gradient MF could be obtained using the circular Halbach arrays depending on the number of poles. The dipole configuration achieves homogenous MF in the core *versus* the quadrupole one that has high gradient MF in the core (Figure 9). Consequently, if the application aim is to retain the MNPs in the tissues located in the gap of the Halbach array, the dipole configuration could be more suitable. On the other hand, if the aim was also to achieve a preferential accumulation in periphery of the area inside the gap of the Halbach cylinder, the quadrupole configuration could be the more suitable option.

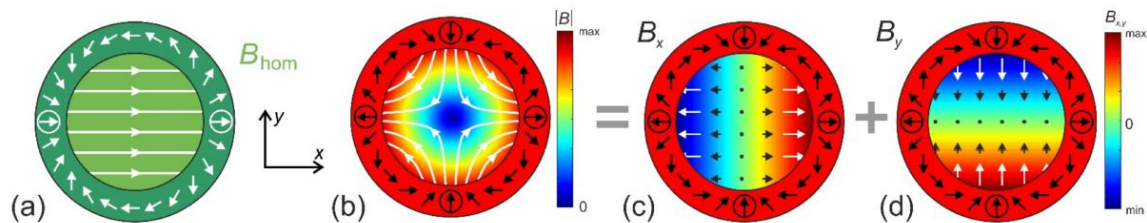


Figure 9: Circular Halbach array in a) dipole (homogenous MF) vs. b) quadrupole (gradient MF) configurations. The hollow cylinders consist of permanent magnet material with continuously changing magnetization direction (arrows). The poles are encircled. In (a,b), the magnetic field is represented by field lines, while in (c,d), the arrows are field vectors (the differences in their colors are only for better contrast). Adapted from [218].

Assembling such strong magnets is still challenging due to the magneto-mechanical forces between the magnets. These forces impose difficulties on the magnet safe assembly, handling and operation. However, starting with smaller model systems could allow developing experiences in dealing with them [218]. Finally, it should be noted that, in permanent magnet-based setups the MF cannot be switched on and off [143].

#### Alternative magnetic focusing set-ups

Setups relying on electromagnets were also developed for MNP targeting to tumor tissues. Compared to permanent magnets, the advantage of electromagnets is the possibility of varying the generated MF strength and gradient in a simple way by manipulating the passing current [223]. Electromagnets traditional coils, such as ordinary, Helmholtz, Maxwell coils or a combination of them, are the most commonly applied ones for MNP targeting due to their ability to generate relatively high MF gradients. However, they generally heat and are highly energy-consuming, which poses a challenge for generating sufficiently high MF strengths. Consequently, their generated MF strength could not be

sufficient to saturate the MNPs to subsequently follow the MF gradients and accumulate in the targeted tissues [223, 224].

Therefore, there is still a need for a rational development of magnetic targeting setups that could have a compromise between the permanent as well as the electromagnets. The ideal 3D magnetic focusing setup should have a simple design, strong generated MF with high gradient, precise targeting ability, large gap, reasonable cost, and feasible manipulation and upgrading.

#### *II.2.2. Magnetic imaging using magnetic resonance imaging (MRI) and magnetic particle imaging (MPI)*

MNPs can be used as contrast agents for magnetic field-based imaging techniques such as MRI and MPI. Both imaging techniques are noninvasive, but each one has its specific characteristics and applications [213].

MRI is commonly used to get a tomographic anatomical 3D imaging of the tissues to be examined [213]. It relies on the magnetic relaxation of proton dipoles, most commonly water ones, which are randomly orientated in the imaged tissues. First, a strong and uniform static MF is applied to align all the magnetic moments of the protons in the tissues. Afterward, a resonant radio frequency (RF) pulse is applied perpendicularly to the previously applied MF, resulting in the rotation of the proton magnetic moments out of their alignment direction. Finally, after removing the RF pulse, the proton's magnetic moment tends to return to their alignment positions, resulting in the proton's relaxation and emission of RF waves (Figure 10). The waves emitted from each location are recorded and transformed into a greyscale image according to their intensity levels. Each body tissue has a different water percent so that different relaxation rates and emitted energy intensity. Hence, MRI has the ability for anatomical distinguishment of different tissues [225, 226].

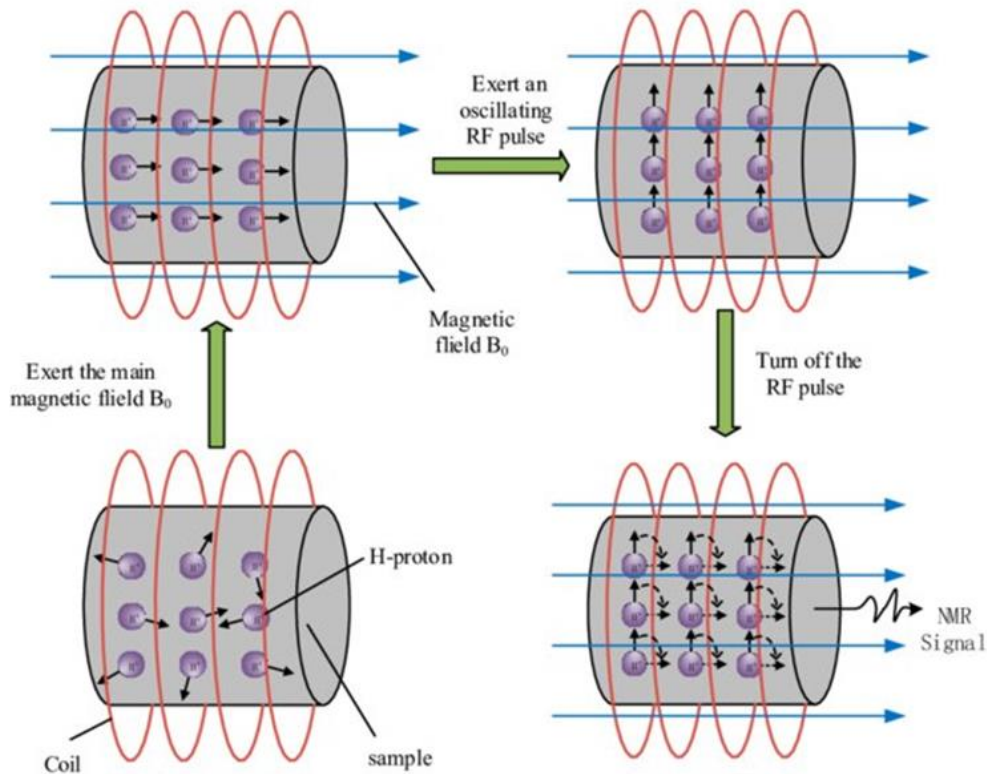


Figure 10: Schematic illustration of the signal source in MRI. Adapted from [227].

The proton relaxation times are denoted as T1 (spin-lattice) due to returning the magnetic vector to its resting state or T2 (spin-spin) due to axial spin return to its resting state. The proton relaxation is progressive, and the difference between both times is small, which could make it difficult to distinguish between some tissues without contrast agents [228].

Two types of contrast agents were used with the MRI, T1 (positive) or T2 (negative) contrast agents. T1 contrast agents are based on paramagnetic metal (gadolinium ( $Gd^{3+}$ ), iron ( $Fe^{3+}$ ) or manganese ( $Mn^{2+}$ )) complexes. As they consist of high spin paramagnetic ions, they can enable producing hyperintense signal from the water protons present in their close proximities. Hence, lighter (more emitted signal) images of their accumulation zone would be obtained. This concept of enhancing the signal is advantageous, and several Gd chelates complexes have been approved as T1 contrast agents. However, Gd chelates still cannot be used in patients with renal diseases due to their toxicity. In addition, T1 contrast agents suffer from decreased efficiency at high MF intensities [228].

On the other hand, SPIONs were used as T2 contrast agents thanks to their ability to decrease the magnetic resonance signal from their surrounding areas. SPIONs have a high magnetic moment that perturbs and delays the relaxation of the water protons in their surroundings [228]. Hence, their accumulation areas appear darker (less emitted signal) than the other tissues. SPIONs have the advantage of their *in vivo* degradation and incorporation into the iron pool of the body. Two SPIONs

products were approved as MRI contrast agents, Resovist® in Europe and Japan and Feridex® in Europe, Japan and the United States. However, Feridex® was withdrawn later from all markets, and Resovist® is currently approved only in Japan. Their first limitation is the need for selective SPIONs accumulation in the targeted lesion and for a reduced uptake by the mononuclear phagocytic system. Their coating with PEG or other hydrophilic moieties can decrease their uptake by MPS; however, it simultaneously results in decreased interactions with their surrounding water protons. Moreover, relying on generating darker spots (being T2 contrast agents) makes it difficult to distinguish them from other dark anatomical features or image artifacts [176, 228, 229].

Recently, the MPI technique was developed, and it attracted a lot of attention due to its ability to generate high-contrast images with high sensitivity. MPI imaging equipment relies on three main parts; selection static field, drive alternating field and receiving coil. A selection strong static MF is applied with a Maxwell configuration, which enables having a region of zero net magnetization (field free region (FFR)). When a small alternating drive excitation MF is applied, MNPs in the FFR are free to respond. However, other MNPs outside the FFR will not be able to respond as they are already saturated with the strong selection field. The response of the MNPs tracers at the FFR are recorded with the receiving coil, and the signal is transformed after to MPI images (Figure 11). The location of the FFR can be moved either mechanically or electronically [230].

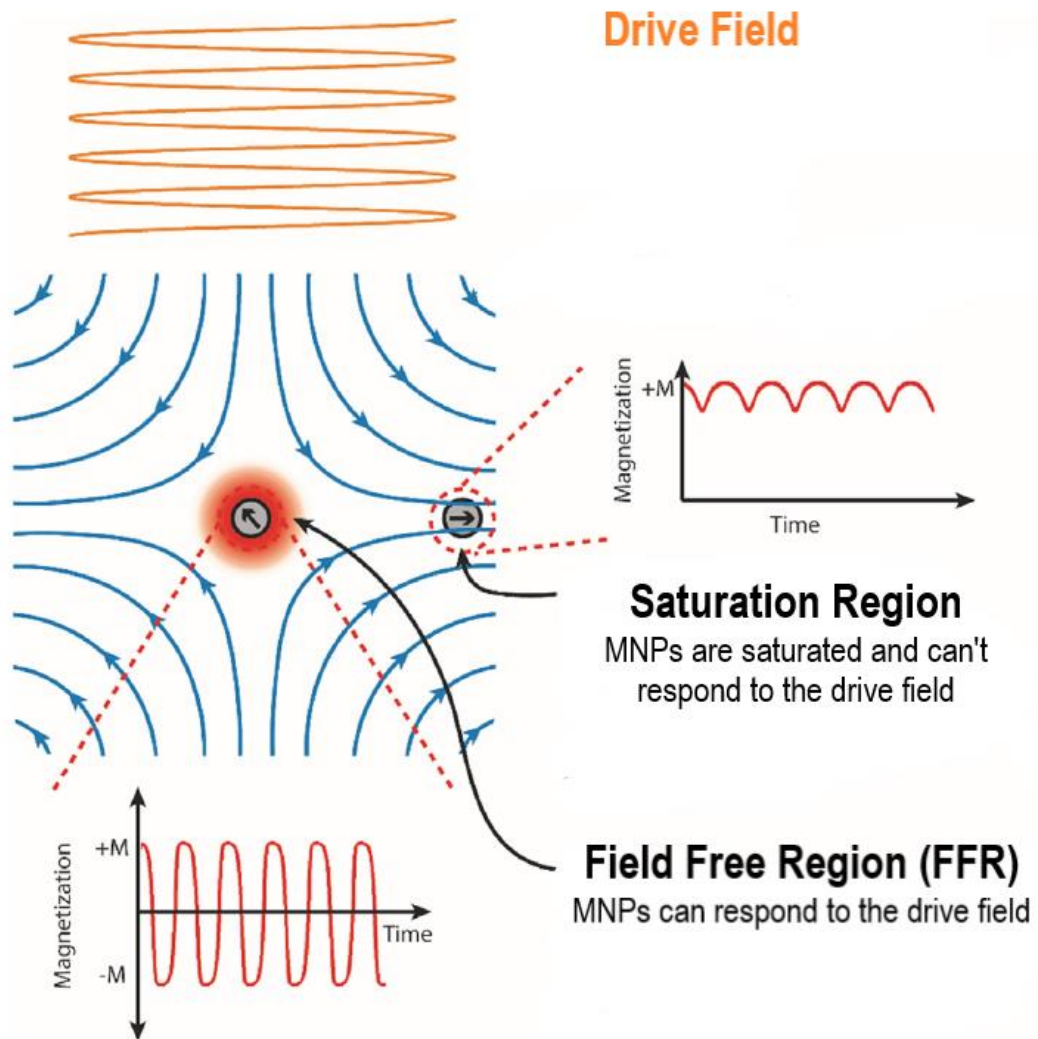


Figure 11: Schematic illustration of the signal source in MPI. MNPs in the field free region can respond to the drive field (orange) and their magnetization response can be recorded using a receiving coil. However, MNPs in the surrounding saturation area can't respond to the drive field due to their saturation with the strong selection field (blue). Adapted from [176].

Thanks to their Langevin nonlinear magnetization behavior, SPIONs are considered the most suitable MNP tracers for MPI. Indeed, in the FFR, SPIONs are at thermal equilibrium with a net zero magnetization and no recorded signal in the receiving coil. Once a drive MF is applied, SPIONs show a rapid strong “superparamagnetic” response to the applied field that can be recorded with the receiving coil [182]. If ferrimagnetic or ferromagnetic nanoparticles are used, the signal is the difference between their magnetization before and after applying the drive MF [213, 230]. Higher MNP concentration in the FFR results in a linearly higher MPI signal, allowing quantitative estimation of the MPI tracer [176]. Until now, MPI has been applied in preclinical trials; however, multiple groups are working on developing human clinical systems that could have high performance and cost-effective properties.

MRI and MPI rely on MF imaging, a noninvasive imaging technique with fewer safety concerns *vis-à-vis* some other techniques, such as X-ray imaging. However, there is a major difference between MRI and MPI: the signal source (Figure 12) [231]. MRI is an anatomical imaging technique where the signal source is the tissues themselves. On the other hand, MPI is a molecular imaging technique where the signal source is the MNP tracers. This leaves less background noise in the MPI technique, allowing higher sensitivity than MRI. However, it leads to a need for coupling an anatomical imaging technique, such as computed tomography (CT) or MRI, with the MPI in order to locate the MNP tracers in the body [231].

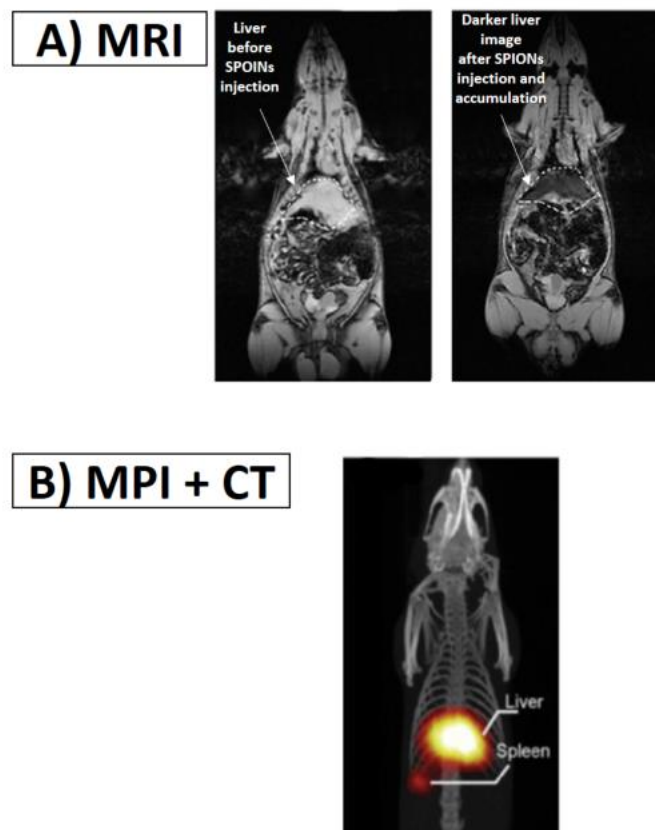


Figure 12: Sample images showing the differences between MRI and MPI. A) MRI where an anatomical image is obtained and the tissues themselves are the signal source which could be affected upon accumulation of the contrast agents as SPIOs. B) MPI where the MNP tracers emit the signal which needs an anatomical imaging technique as CT in order to locate their accumulation sites (e.g., liver and spleen as shown in the image). Adapted from [232, 233].

MNPs are used as MPI tracers for many biomedical applications, such as quantifying the MNPs accumulation in tumors and their intra-tumoral distribution and penetration, which can help in tumor diagnosis or monitoring the response to treatment [234]. It can also be coupled with magnetic hyperthermia for localizing the MNPs and guiding the hyperthermia treatment [233]. Also, MPI can be used for sentinel lymph node mapping and stem cell tracking [235, 236]. It was also used for blood pool imaging to detect traumatic injuries or bleeding and record treatment responses [237].

### *II.2.3. Magnetic nanoparticles as antitumor nanomedicines*

MNPs were utilized as antitumor nanomedicines in order to kill the targeted tumor cells in various ways, such as hyperthermia, magneto-mechanical destruction or photothermal therapy.

#### *II.2.3.1. Hyperthermia*

High-frequency MF (>100 kHz) with moderate amplitude can result in heating the MNPs through Néel or Brownian relaxation or both of them. The resulting heat can be used for antitumor applications through global or nanoscale intracellular hyperthermia.

##### *Global hyperthermia*

The MNP heating was exploited for magnetic fluid hyperthermia and tumor ablation by heating the targeted tissues at temperatures in the range of 40-47° C [238]. Nanotherm<sup>®</sup>, aminosilane-coated SPIONs, is the only nanomedicine formulation with EMA approval for the treatment of brain tumors based on hyperthermia. Nanotherm<sup>®</sup> was evaluated in clinical trials through intracranial injection in tumors of patients with recurrent glioblastoma, followed by AMF application using a human-scale applicator to induce tumor hyperthermia to 50° C. Patients treated with Nanotherm<sup>®</sup> plus radiation therapy showed an enhanced overall survival of 23.2 months compared to only 14.6 months obtained with conventional therapy (temozolomide and radiotherapy) [28, 239]. Nanotherm<sup>®</sup> also received the FDA, investigational device exemption, approval to be used in clinical trials for the treatment of intermediate-risk pancreatic cancers [240, 241].

Hyperthermia-based tumor therapy can be valuable to avoid surgical options, especially with tumors in sensitive tissues such as the brain [241]. It is worth noting that many studies reported an increase in intracellular ROS production due to magnetic hyperthermia [242, 243]. The enhanced ROS production could be due to hyperthermia-induced mitochondrial dysfunction [243]. The generated extra ROS are potent damaging agents to biological molecules such as DNA, and to lipid membranes resulting in induced cell death through ferroptosis or oxytosis [244, 245]. However, the global hyperthermia approach requires significantly high local concentrations of the MNPs in the targeted tissues, which is very challenging to be achieved after systemic administration, resulting in the use of the more invasive intratumoral injection [246]. In addition, the generated global heating could affect the nearby healthy tissues, leading to their destruction.

### Nanoscale intracellular hyperthermia

In this strategy, the AMF exposure on the lysosomally accumulated MNPs results in a local temperature increase in the MNP vicinity, enhancing ROS production. The resulting oxidative stress could induce cell death through lipid peroxidation, lysosomal membrane permeabilization and leakage of lysosomal contents into the cytosol. Using active targeting could enhance the accumulation of the MNPs inside the lysosomes of the targeted tumor cells and reduce the side effects on the other non-targeted healthy ones [247-249].

For instance, Clerc *et al.* obtained lysosomal accumulation of gastrin peptide-functionalized MNPs (magnetic core size  $8.7 \pm 1.6$  nm) after their incubation on INR1G9 cells expressing cholecystokinin-2 (CCK2) as a targeted receptor [247]. AMF exposure (275 kHz, 40 mT, 2h) of the cells internalized the nanoparticles resulted in  $19.9 \pm 1.5\%$  or  $32.3 \pm 2.7\%$  inhibition of cell survival 4h or 24 h, respectively (Figure 13). There was also an observed  $5.7 \pm 1.5$ -fold increase in the intracellular ROS level upon AMF exposure in the cells that had internalized the MNPs compared to  $\sim 2.5$ -fold increase upon AMF exposure without MNPs. After AMF exposure by  $\sim 7$  min, there was  $\sim 14.1 \pm 1.4$  °C temperature increase in the intra-lysosomal MNPs vicinity detected using a molecular thermometer fluorescent probe linked to the MNP surface via 7 nm PEG moiety. This temperature increase was not noticed at the lysosomal membrane using another molecular thermometer fluorescent probe that bound to the lysosomal membrane. AMF exposure also resulted in enhanced lipid peroxidation in the cells treated with MNPs. It was detected through an increased relative fluorescence of  $74.4 \pm 2.7\%$  for lipid peroxidation reagent compared to only  $41.5 \pm 5.6\%$  fluorescence increase upon MNP treatment without AMF exposure. Finally, there was an observed decrease in the Cathepsin-B lysosomal contents by  $25.4 \pm 4.7\%$  and  $43.9 \pm 6.3\%$  after 30 and 60-min of magnetic intra-lysosomal hyperthermia experiment [247]. These results highlight the potential of using intracellular hyperthermia for cancer treatment as an alternative technique to the global hyperthermia.

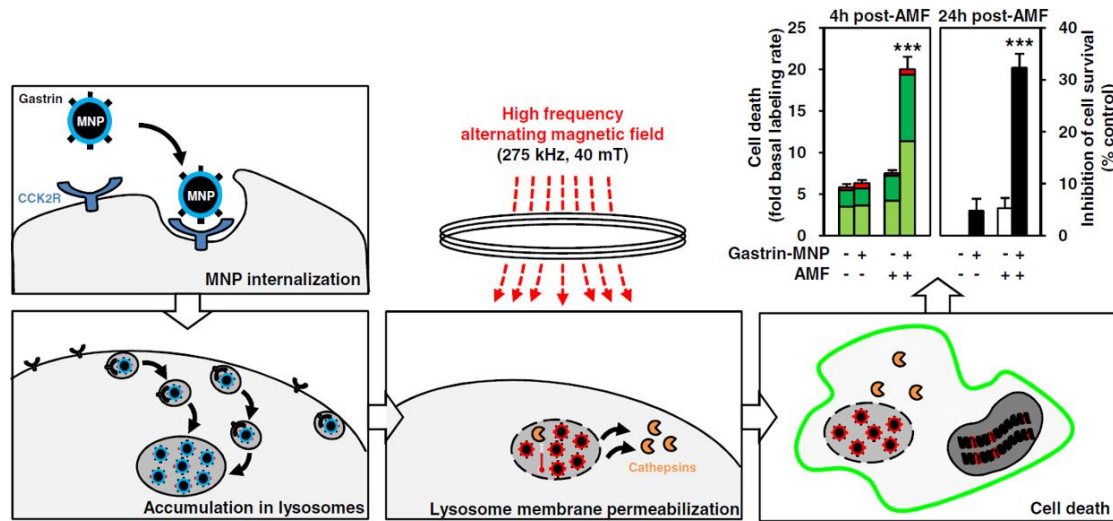


Figure 13: Schematic illustration for using the nanoscale intracellular magnetic hyperthermia for inducing targeted cell death. In this strategy, actively targeted nanoparticles could accumulate in the lysosomes of the tumor cells. Afterwards, they can locally heat upon exposure to AMF, leading to lysosomal membrane permeabilization and induced cell death. Adapted from [247].

For a highly effective hyperthermia treatment, nanoparticles with a large heating power are preferred. The MNP heating efficiency could be quantified as specific absorption rate (SAR) [183, 250, 251];

$$\text{Specific Absorption Rate (SAR)} = \frac{C \frac{dT(t)}{dt}}{m_{NP}}$$

where

$C$  is the specific heat capacity of the MNPs,

$\frac{dT(t)}{dt}$  is the heating rate (temperature increase per unit time), and

$m_{NP}$  is the mass of the MNPs used.

The used frequency ( $f$ ) and MF amplitude ( $H$ ) affect SAR values. There is a maximum clinically allowed threshold for the used  $f$  and  $H$  ( $H \times f_{\max} = 5 \times 10^6 \text{ kAm}^{-1} \text{ s}^{-1}$ ) to avoid patients side effects such as eddy currents induced tissue heating [149, 252]. So, nanoparticles with high SAR could be preferred to have significant hyperthermia under the maximum allowed threshold without the need of having very high amount of MNPs accumulated or injected in the targeted tissues.

Hence, plenty of research has been done in order to enhance the SAR of the MNPs by manipulating their magnetic material composition, size, shape and coating [214]. These parameters affect the MNP heating by affecting their  $M_s$ ,  $K_{eff}$ , magnetic susceptibility and relaxation time [253, 254].

Decreasing MNP size could result in less  $K_{eff}$  and spin disordering, leading to reduced magnetic susceptibility/ $M_s$  and modified SAR values. It has been reported that SAR values could be directly proportional to the particle size until a maximum size value and are inversely proportional to the particle size distribution [214, 255, 256]. The optimum MNP volume for magnetic hyperthermia is dependent on the material and experimental parameters [184]. Moreover, composition and shape anisotropy can enhance the  $K_{eff}$  resulting in MNPs, which thus modifies SAR values. The optimum anisotropy is dependent on the used MF parameters during the hyperthermia experiment as well as the MNP magnetization [184].

Changing the anisotropy could be obtained either through 1) doping the MNP crystalline structure with divalent transition metal cation (as  $Fe^{2+}$ ,  $Co^{2+}$ ,  $Zn^{2+}$ ,  $Mn^{2+}$  or  $Ni^{2+}$ ) or 2) exchange coupling between a magnetically hard core and a magnetically soft shell [214, 257, 258]. For instance, Lee *et al.* utilized the exchange coupling property to get SAR values of  $3,886 \text{ W g}^{-1}$  for  $CoFe_2O_4@Zn_{0.4}Fe_{2.6}O$  core-shell NPs compared to 100 to  $450 \text{ W g}^{-1}$  of the single component MNPs [258]. However, having other metals as  $Co^{2+}$ ,  $Zn^{2+}$ ,  $Mn^{2+}$ , or  $Ni^{2+}$  could change the MNP toxicity, raising safety concerns. Shape anisotropy is obtained using MNPs in disc, ring, flower shapes, or chain arrangements [183]. For instance, Gavilán *et al.* observed higher SAR values for the more anisotropic star-shaped iron oxide MNPs than cubic-shaped ones [214]. It is worth noting that getting nanoparticles with high  $K_{eff}$ /remanence/coercivity (non-superparamagnetic properties) could lead to less stable MNP formulation due to agglomeration. Hence, optimum coating of such MNP formulations is needed to mitigate their agglomeration potential.

MNP coating can also dramatically affect their heating properties. For example, Liu *et al.* observed 2.5-fold increase in the SAR of the magnetite NPs upon using poly(ethylene glycol)methyl ether 2000 (mPEG2000) coating agent instead of mPEG5000. The coating agent could affect the Brownian relaxation of the MNPs, their magnetic interaction and could also hinder the heat transfer into the surrounding medium [259].

Hence, several factors should be controlled in the design of the MNPs to get an optimally heating MNP platform with biocompatible and stable properties.

### II.2.3.2. Magneto-mechanical destruction

Low-frequency MF (<20 kHz) were used to induce magneto-mechanical destruction of cellular membranes or organelles in the targeted tumor cells [260, 261]. The low-frequency MF stimulus offers fewer side effects, such as eddy currents induced tissues heating, compared to the high-frequency one [149]. MNPs that can form high-order structures such as chains would be well suited for efficient magneto-mechanical destruction applications of tumor cells [262].

Cheng *et al.* investigated the efficiency of the magneto-mechanical destruction effect of disc-shaped MNPs against glioblastoma under RMF (20 Hz, 1 T). Inside tumor cells, the MNPs were aligned to the plane of the RMF, which enabled them to create a strong mechanical force to damage the tumor cells through damaging their cellular membrane integrity. *In vivo* experiments were performed on mice bearing brain glioblastoma xenografts previously incubated with MNPs. AMF exposure 1h per day for 1 week reduced the size of brain tumors and enhanced the mice's survival rate without adverse side effects [152].

In addition, the magneto-mechanical effect of MNPs was also exploited to affect tumor microenvironment cells such as the cancer-associated fibroblasts (CAF). These microenvironment cells could have a significant role in tumor progression and therapeutic resistance so that their targeting along with the cancer cells could help in enhancing the treatment platform efficacy [263]. In an application of this strategy, Lopez *et al.* used 6 nm core MNPs functionalized with gastrin to induce targeted magneto-mechanical destruction in the CCK2 receptor expressing cancer-associated fibroblasts [147]. Higher MNP intracellular concentration was observed on CAF cells expressing CCK2 compared to CAF not expressing the targeted receptor at MNP concentration in the range from 2-32  $\mu\text{g ml}^{-1}$  after 72 h of incubation. RMF (1 Hz, 40 mT, 2h) exposure resulted in enhanced cell death up to  $33.8 \pm 2.8\%$  in CAF-CCK2 cells after their treatment with MNPs ( $16 \mu\text{g ml}^{-1}$ ) that represented  $3.0 \pm 0.9$  and  $5.6 \pm 1.7$ -fold increase in cell death compared to cells exposed only to RMF or treated only with the MNPs, respectively [147]. This enhanced cell death was related to the MNP mechanical effect on disrupting the lysosomes' integrity and causing leakage of their contents. It was also associated with increased MNP pressure on the lysosomes attached to microtubules filaments, causing their disruption and cell shrinkage [264]. Further studies could investigate if this induced CAF cell death could be associated with favorable stroma modulatory effects and/or immune system activation for enhanced antitumor activity.

### II.2.3.3. Photothermal applications

As metallic plasmonic nanoparticles, MNPs have local plasmon surface resonance (LPSR) that can be exploited for photothermal treatment applications [265, 266]. MNPs could be considered as an alternative to the most commonly used photothermal agents, GNPs. Unlike GNPs, MNPs could be biodegradable (as iron oxide MNPs), can be magnetically directed to the tumor tissues and can act as contrast agents for magnetic-based imaging techniques [267]. However, MNPs have a low absorption coefficient in the near infra-red region where there is minimal body and tissue absorbance [267]. Using self-assembled nanoclusters of MNPs can mitigate this low absorption coefficient challenge, enabling the use of biologically safe laser powers [215, 268]. For instance, Chen *et al.* observed a ca. 3.6-fold increase in the 808 nm laser absorption for magnetite nanoclusters compared to the individual magnetite nanoparticles. Laser irradiation (808 nm, 5 W/cm<sup>2</sup>, 180 s) induced *in vitro* an increase of the magnetite nanocluster solution temperature from room temperature to 51.4 ± 1.2 °C compared to 42.0 ± 1.5 °C for the individual nanoparticles. The same laser irradiation dose on A459 cells induced 72.8% cell death due to the magnetite nanoclusters vs. only 14.5% cell death upon using the individual nanoparticles. Also, the magnetite nanoclusters showed superior reduction of the tumor volume in A549 tumor xenograft-bearing mice upon laser irradiation (808 nm, 5 W/cm<sup>2</sup>, 180 s) compared to the individual nanoparticles or the PBS control, without affecting the mice body weight [215].

The applications of MNP for hyperthermia, magneto-mechanical destruction and photothermal tumor therapy, indicate their versatility as anticancer tumor nanomedicines.

### II.2.4. Magnetic nanoparticles based nanomedicines for drug delivery

MNP response to an external MF was also used to induce drug release from nanocarriers. The cargo release could be initiated in response to hyperthermia or mechanical effect.

#### *i. Drug release in response to hyperthermia*

High-frequency MF were used to enable magnetic hyperthermia-induced cargo release. Herein, the cargo release depends on thermally induced events such as A) thermo-responsive bond cleavage, B) thermo-responsive polymer or lipid structural rearrangement or transition, C) opening of porous nanomedicines having thermo-sensitive pore gates, D) thermo-responsive matrix degradation or deformation, or E) thermodiffusion induced by local temperature gradients [216, 269].

#### A) Thermo-responsive bond cleavage

Nanomedicine formulations loaded with drugs through non-covalent or covalent bonds can be magnetically activated by hyperthermia to release their cargo.

Drug loading through non-covalent interactions, such as hydrogen bonds or  $\pi$ - $\pi$  interactions, have the advantage of not modifying the drug chemical structure and keeping its integrity and efficiency [270, 271]. For instance, Griffete *et al.* developed maghemite MNPs coated with a surface-grown molecularly imprinted polymer using DOX as a template ( $\text{Fe}_2\text{O}_3$ @DOX-MIP). Under AMF (335 kHz, 9 mT, five pulses of 2 minutes separated by 30s), enhanced DOX release of 60% after 8h was observed without global temperature rise (37°C), compared to only 15% release after 8h of incubation in water at 37°C. MNP hyperthermia-induced the DOX release due to a local temperature increase, leading to hydrogen bond cleavage between the drug and the polymer [272]. PC-3 cells internalization of  $\text{Fe}_2\text{O}_3$ @DOX-MIP after incubation for 2 hours at  $[\text{Fe}] = 2$  mM did not affect the cells viability, indicating the inactivity of DOX as it is still kept inside the nanoparticles platform. After AMF exposure (at 700 kHz, 25 mT, 1.5h), the cell viability was reduced to 60% without detected global hyperthermia (the temperature of cells medium was kept at 37°C). PC-3 tumor cells incubation for 2h with DOX at concentrations of 0.5–2  $\mu\text{M}$  (that could correspond to the released DOX from  $\text{Fe}_2\text{O}_3$ @DOX-MIP) reduced cell viability also to ~70-60% [272].

Thermo-responsive covalent bonds, such as Diel-Alder reversible thermo-reversible cycloaddition and thermo-labile azo-linkers, were utilized to allow magnetic hyperthermia-responsive controlled drug release from nanomedicine formulations. Riedinger *et al.* developed iron oxide magnetic nanoparticles (IONPs) coated with PEG-azo linker covalently bound to DOX. In this study, two PEG spacers of different molecular weights were used, a shorter one of 500 Da and a longer one of 8000 Da. Under AMF (334.5 kHz, 17 kA/m), 36% DOX load was released after one hour in the case of the shorter 500 Da PEG compared to only 15% for the longer 8000 Da PEG spacer. The major reason was the rapid decay of the local temperature increase with increasing distance from the nanoparticles' surface. Moreover, there was an observed 3-fold higher cytotoxicity on KB tumor cells after AMF exposure (1h, 334.5 kHz, 17 kA/m) upon using the IONPs of the shorter spacer compared to the ones with longer spacer [273].

Covalent bonds offer more stable linkage for better drug retention than non-covalent ones that could suffer from premature drug release risk. In addition, using spacers of different types and lengths could allow independent controlled release of different drugs from the same nanomedicine platform. However, smart design of such systems is needed to enable the release of the native drug

entity or at least an active drug conformation without significant encumbrance of the chemical modification on its antitumor efficacy [216].

#### B) Thermo-responsive polymer or lipid structural rearrangement or transition

Polymer and lipid-based nanomedicines are widely used for anticancer applications and can be adapted for thermo-responsive triggered magnetic hyperthermia cargo release. Thermosensitive polymers with LCST slightly above body temperature are well suited for magnetic hyperthermia-induced cargo release [274]. Above their LCST, the thermosensitive polymers undergo conformational changes that could increase their hydrophobicity, resulting in polymer shrinkage and cargo release. Polyn-isopropylacrylamide (PNIPAM), poly(methylmethacrylate) (PMMA) and Pluronic® F-127 (F127) are among the most commonly used thermosensitive polymers [274]. MNPs-polymer hybrid nanomedicines can be designed in two ways: either each single MNP is coated with a polymeric layer, or several MNPs are collectively embedded in the polymer matrix.

In their study, Ding *et al.* developed 30 nm magnetic nanocubes coated with folic acid decorated amphiphilic F127 polymer. The polymer coating enhanced the magnetic nanocubes biocompatibility and allowed paclitaxel cargo loading through hydrophobic interactions. The reversible sol-gel thermo-sensitivity of F127 allowed on/off pulsatile cargo release from the nanomedicine platform. Upon AMF (200 kHz) exposure for 10 min, rapid paclitaxel release is observed, which is paused after switching off the field due to gelation of the F127. The paclitaxel release was resumed after re-applying the AMF due to the phase transition of the F127 from solid gel to solution state. *In vitro* on Hela cells, the AMF (50 min, 200 kHz) exposure induced 90% cell death upon using the paclitaxel-loaded nanocubes compared to 70% cell death for the nonloaded ones [275].

Liposomes were also used with MNPs for magnetic hyperthermia-controlled cargo release. Liposomes were composed of one or more phospholipid bilayers surrounding an aqueous core, and were the first type of nanomedicine formulations to be approved for patient use [276, 277]. Liposomes are commonly composed of biocompatible lipid components that can ultimately be metabolized or excreted by the body [277]. In addition, it is currently feasible to be produced on a large scale using microfluidics technology [278]. Also, hydrophilic or hydrophobic cargos can be loaded inside the liposomes either in their aqueous core or lipid membrane bilayer, respectively. The MNPs-liposomes hybrids (Magneto-liposomes) were first described by Cuyper *et al.* in 1988 when they developed a lipid bilayer encapsulating 14 nm SPIONs [279]. The major advantage of the magneto-liposome is that both liposomes and MNPs could be synthesized from biocompatible components, making it appealing to harness the benefits of both. MNP heating, thanks to the AMF application, can induce the phase transition of the liposomal lipid bilayer membrane, creating defects/pores that can lead to cargo

release. The MNPs can be loaded inside the liposomes aqueous core, embedded in the lipid bilayer or attached to the surface [216].

MNPs with a hydrophilic coating and a particle size less than the liposome core size can be utilized to develop MNP core-loaded magneto-liposomes. This design needs a high amount of MNPs inside the liposomes, MNPs with a strong heating power, or both, for an efficient heat transfer from the MNP surface to the lipid membrane bilayer. This heat transfer process is usually hampered by fast heat dissipation inside the liposomes' aqueous core [280].

Small MNPs (< 6.5 nm) with hydrophobic coating can be embedded in the liposomal lipid bilayer membrane [281, 282]. Also, MNP surface-decorated liposomes can be developed using hydrophilic MNPs of particle size not exceeding 20 nm, mainly *via* electrostatic interactions. Larger-size MNPs can disrupt the lipid membrane bilayer and form lipid bilayer-coated MNPs [283, 284]. Magneto-liposomes with embedded MNPs or surface-decorated ones have the advantage of a direct heat transfer to the lipid bilayer, allowing an efficient phase transition and induced cargo release [216, 285, 286].

Amstad *et al.* observed an enhanced (1.8x) MF-induced calcein fluorescent cargo release from liposome embedded palmityl-nitro-DOPA coated IONPs compared to using core-loaded hydrophilic PEG(1.5 kDa)-nitroDOPA NPs. Local heat generation for inducing the cargo release without macroscopic heating have the advantage of avoiding hyperthermia side effects on nearby healthy tissues. Also, it should not be essential to use high nanoparticles concentrations [285].

In their work, Guo *et al.* developed multifunctional thermosensitive magneto-liposomes for anticancer theranostic applications. It consisted of oleic acid-coated MNPs embedded in a liposomal membrane bilayer. The liposomal membrane was composed of dipalmitoylphosphatidylcholine (DPPC), cholesterol (Chol), N-stearylamine (SA), 1,2-diacyl-SN-glycero-3-phosphoethanolamine-N-[methoxy(poly(ethyleneglycol))-2000] (DSPE-MPEG2000) and DSPE-PEG2000 functionalized with methotrexate (DSPE-PEG200-MTX). At their appropriate ratio (DPPC:Chol:SA:DSPE-MPEG:DSPE-PEG2000-MTX = 67:17:13:1:2), the liposomal membrane had a melting temperature around 45°C, well above the body temperature. MTX was not only utilized as an anticancer drug, but also as folate receptors targeting moiety due to its structure similar to folate. The liposomes were also loaded with the lipophilic fluorescent dye Cy5.5 in their membrane (as a fluorescence imaging agent) and DOX in their aqueous lumen (as an anticancer drug). The delivery system combined the possibility of multifunctionalities of dual-chemotherapy (MTX and DOX), dual-imaging modes (fluorescence and magnetic), dual targeting (active and magnetic) and dual cargo release modes (magnetic and laser) (Figure 14) [287].

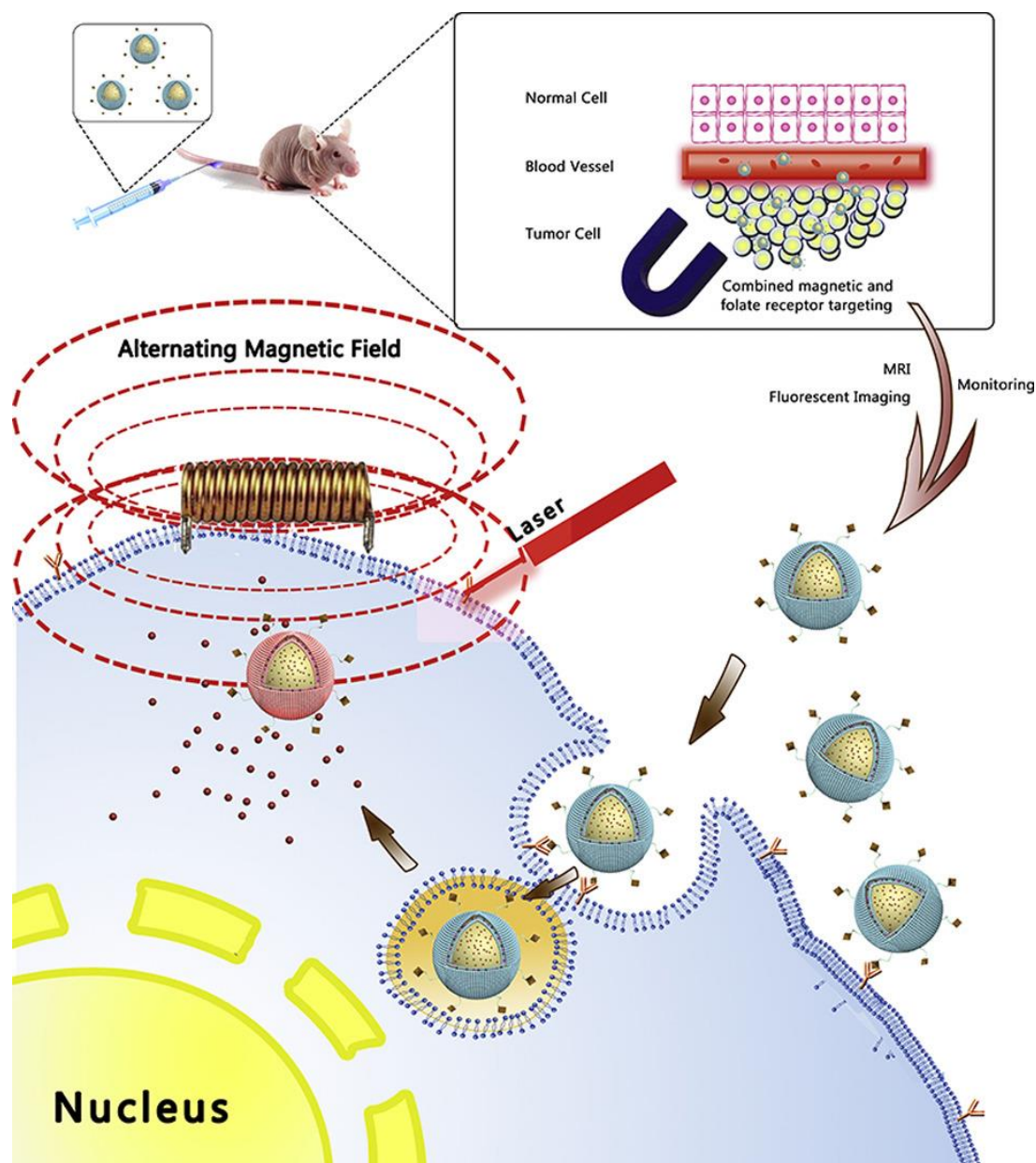


Figure 14: Schematic illustration showing the multifunctional potential of the developed MTX-functionalized magneto-thermosensitive-liposomes (MTX-MagTSLs), where it could enable dual-chemotherapy (MTX and DOX), dual-imaging modes (fluorescence and magnetic), dual targeting (active and magnetic) and dual cargo release modes (magnetic and laser). Adapted from [287].

The developed MTX-functionalized magneto-thermosensitive-liposomes (MTX-MagTSLs) showed an enhanced DOX release of 83% at 45°C compared to only 44% at 37°C, after 24h in PBS (pH=7.4) (Figure 15A). They also had higher cellular uptake in the folate receptor-positive HeLa cells compared to the folate receptor-negative A549 cells. Also, there was an observed enhanced HeLa cell uptake of the MTX-MagTSLs compared to the non-functionalized one. A static MF (using a circular magnet applied on the skin surface of the tumor) resulted in better tumor accumulation of MTX-MagTSLs in HeLa cell xenograft tumor-bearing nude mice that were characterized through both fluorescence and MR imaging. Using both AMF (500 kHz, 20 kA·m<sup>-1</sup>) and NIR laser irradiation (808 nm,

0.8 W/cm<sup>2</sup>), the MTX-MagTSLs heating properties enabled reaching the membrane melting temperature (~45°C) in 5 min, and it was higher than using AMF alone. This synergistic effect resulted in higher MTX-MagTSLs cytotoxicity on HeLa cells upon exposure to both AMF and laser irradiation compared to AMF only, laser irradiation only or no stimulus. Better *in vivo* antitumor inhibition effect with better survival was obtained on HeLa cell xenograft tumor-bearing nude mice using MTX-MagTSLs/constant static MF-targeting (CMF)/Dual AMF and laser irradiation, compared to PBS, Free-DOX, MagTSLs, MTX-MagTSLs, MTX-MagTSLs/CMF-targeting and MTX-MagTSLs/CMF-targeting/AMF (Figures 15B and C) [287].

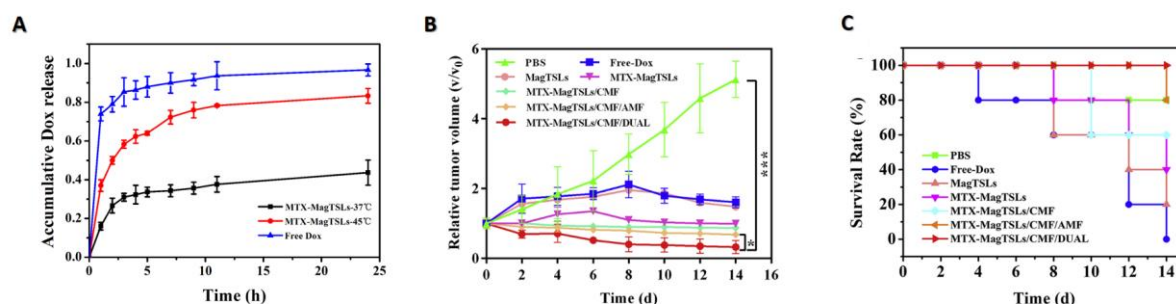


Figure 15: A) Graph showing comparison between the Dox released profiles from MTX-MagTSLs at 37 °C and 45 °C in PBS (pH 7.4), compared to the burst release of the free DOX control, B) Graph showing tumor growth curves and C) survival in HeLa cell xenograft tumor-bearing nude mice in response to MTX-MagTSLs/CMF/DUAL AMF and laser irradiation, compared to PBS, Free-DOX, MagTSLs, MTX-MagTSLs, MTX-MagTSLs/CMF-targeting and MTX-MagTSLs/CMF-targeting/AMF. Adapted from [287].

Despite the work achieved for the development of the polymer or lipid-MNP composites, the developed polymers or lipid bilayers usually have a broad melting or phase transition peak, which makes drug escape without MF exposure a common issue [275, 287]. Hence, there is still a need for developing polymers or lipid bilayer components with a sharp melting temperature to help towards their clinical translation. In such nanocomposite formulations, relying on the mechanical destruction effect for cargo release could be more promising for developing stable formulations with a more controlled cargo release.

### C) Opening of porous nanomedicines having thermos-sensitive pore gates

Porous nanomedicines can be designed to have thermo-sensitive switchable pores. Consequently, the drug delivery reservoir could have gates that can open to release their cargo locally in the targeted tumor tissues in response to magnetic hyperthermia. The gatekeeper component can be a thermo-sensitive polymer such as N-isopropylacrylamide (NIPAM) or a polymer covalently to the pore linked through thermo-sensitive bonds such as azo-linkers and Diel-Alder cycloaddition-based linkers [216]. Mesoporous materials such as silica or IONPs are the most commonly used nanomedicines for this application. For instance, MF-induced cargo release was obtained from core-

shell Fe<sub>3</sub>O<sub>4</sub>@SiO<sub>2</sub> mesoporous silica nanoparticles that were loaded with rhodamine 6G fluorescent dye inside their porosity. The pores were closed through PEG polymer functionalization using the thermo-labile azo-linker. AMF exposure (375 kHz, 20 kA m<sup>-1</sup>) resulted in azo-linker degradation, pores opening and rhodamine 6G dye release in the *in vitro* test tube. It was interesting that there was no observed macroscopic temperature elevation. The nanoparticles also did not induce cytotoxicity after AMF exposure on fibroblast cells, indicating that the cargo release without hyperthermia effect possibly prevents damage to nearby healthy tissues [288].

#### D) Thermo-responsive matrix degradation or deformation

Hyperthermia could induce the degradation or deformation of the matrix surrounding the MNPs upon MF application. In their proof of concept study, Fan *et al.* observed Nile red (fluorescent cargo) release from MNPs embedded poly(ethyl glyoxylate)-polyethyleneoxide (PEtG-PEO)-PEG copolymer assemblies upon MF exposure (10.2 kA m<sup>-1</sup> and 755 kHz) for 3h. The hyperthermia produced resulted in cleavage of a thermo-sensitive end-cap based on a Diels-Alder reaction of (PEtG-DA) and subsequent furan elimination. However, there was a long AMF exposure period of 3h that was even initiated at a global temperature of 72 °C, making a clinical application challenging for this system [289].

#### E) Thermodiffusion induced by local temperature gradients

Finally, magnetic hyperthermia could generate local temperature gradients that result in the loaded drug thermodiffusion out of the drug delivery systems based on the Soret effect. This effect describes the diffusion of molecules from hot regions to colder ones due to temperature gradients [290]. For instance, Xue *et al.* developed DOX-loaded MNPs alginate-chitosan microspheres (DM-ACMSs) for breast cancer treatment. The AMF exposure (40 kA/m, 265 kHz, 10 min) induced 22.5% cumulative DOX release from DM-ACMSs in the buffer solution (pH =6.8) compared to only 0.2% without AMF. Interestingly, 2-fold increase in the DOX release was noticed with the AMF treatment compared to the water bath heating approximately at the same temperature. The release kinetics of DOX in response to the AMF exposure fitted a developed Soret effect-derived model, suggesting a combined heat and mass transfer-based release mechanisms. In addition to the DOX release driven by the concentration gradient between inside and outside the DM-ACMSs (Fickian diffusion), the AMF-induced MNP heating could increase the DOX diffusion coefficient inside DM-ACMSs compared to the outer medium, leading to an additional release trigger (thermodiffusion) (Figures 16A-C). The confocal microscopy images of microspheres loaded with fluorescently labeled MNPs showed preservation of their integrity after the AMF exposures, further supporting the thermodiffusion-induced release mechanism. An enhanced *in vitro* MCF-7 cell death of 95.5% was observed upon incubation (24h) with DM-ACMSs (0.18 g/L) and AMF exposure (40 kA/m; 265 kHz; 10 min), compared to 63.4% and 85.5%

with AMF exposure+MNP amounts equivalent to the microspheres or DM-ACMSs incubation only. In addition, the intratumoral DM-ACMSs treatment combined with the AMF exposure (40 kA/m; 265 kHz; 10 min) in orthotropic (subcutaneous MCF-7 cells) tumor-bearing mice models resulted in tumor eradication without recurrence till 40 days after treatment compared to a recurrence within 27 days with the single treatments (AMF+equivalent MNP amounts to microspheres or DM-ACMSs only) (Figure 16D) [269].

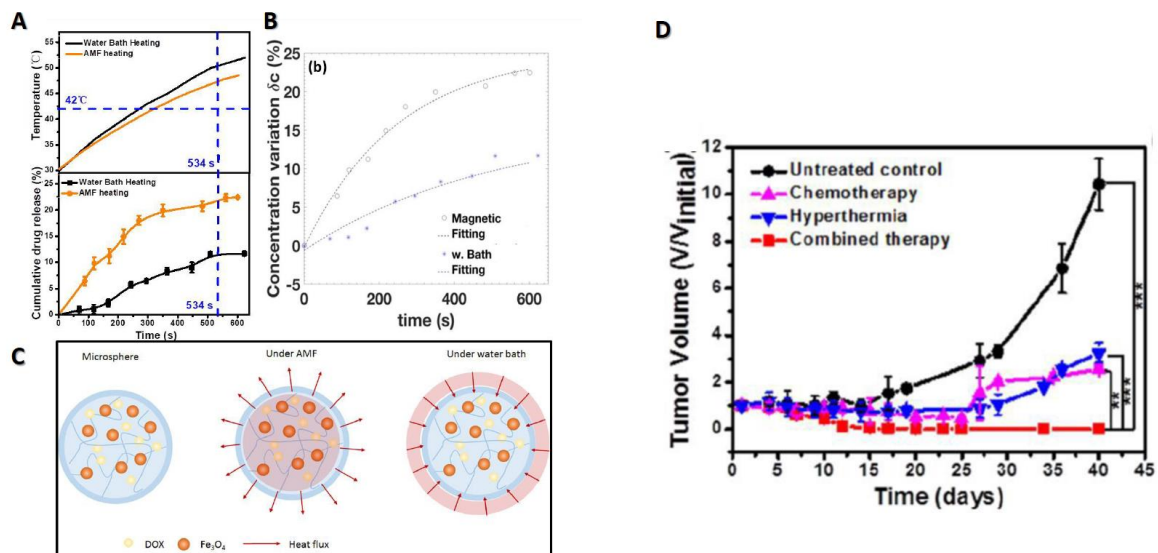


Figure 16: A) Temperature (up) and cumulative DOX release (down) evolution for DM-ACMSs under an AMF (40 kA/m; 265 kHz) or by water bath heating, B) Cumulative DOX release evolution fitted from theoretical models with bath heating (Fickian diffusion) compared to magnetic hyperthermia (combined Fickian and thermodiffusion), C) Schematic illustration of the difference in heat transfer process between bath heating and magnetic hyperthermia AMF, D) The time evolution of the tumor volume from orthotropic (subcutaneous MCF-7 cells) tumor-bearing mice upon no treatment (control), treatment with DM-ACMSs only (chemotherapy), treatment with AMF+equivalent MNP amount to the DM-ACMSs (hyperthermia) or AMF+DM-ACMSs (combined hyperthermia and chemotherapy). Adapted from [269].

i. Drug release in response to mechanical forces

Low-frequency MF can activate the MNPs to induce deformations in the nanomedicine platform scaffold with subsequent cargo release [291]. For instance, Peiris *et al.* developed 100 nm long nanochain platform composed of three MNPs linked to one DOX-loaded liposome. 10 kHz MF induced mechanical vibrations of the three MNPs in the nanochain resulting in disruption of the liposomal membrane and DOX release proportionally to the amplitude of the applied MF (Figure 17). Two MF application 24 h after the nano-chains injections inhibited tumor growth and enhanced the survival rate of triple-negative breast cancer-bearing mice compared to control treatments [292].

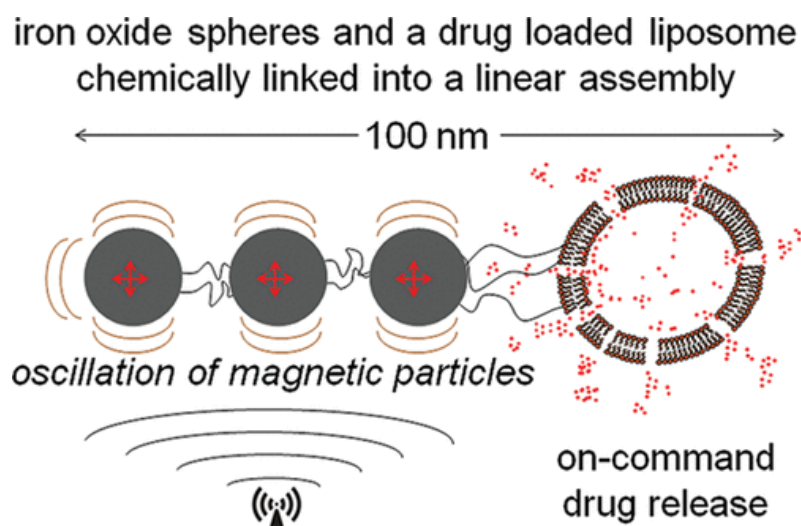


Figure 17: Illustration of the defects on the liposome caused by magnetic field induced mechanical vibrations. Adapted from [292].

In their work, Pudaro *et al.* developed magneto-liposomes with core-loaded MNPs that were able to release their cargo due to mechanical stress without significant temperature increase. Under pulsed RMF (214.8 Hz, 2393 kA/m), the MNP motion generated ultrasounds resulting in disrupting the liposomal membrane bilayer and cargo release [293].

The major advantage of the hyperthermia-free magneto-mechanical induced cargo release is that it relies on low-frequency MF with fewer side effects than the high-frequency ones. In addition, this technique can be suitable for the MF-induced release of thermo-sensitive cargo [238]. However, technologies for developing RMF setups are still being developed and are not mature to reach clinical application stages.

#### II.2.5. Conclusion on magnetic nanoparticles biomedical applications

Nanomedicines based on MNPs are promising tools that could have a remarkable impact on enhancing the anticancer efficacy of chemotherapeutic agents as they combine several advantages [294]. First, they can be magnetically directed to the tumor tissues using permanent magnets to enhance the nanomedicine accumulation in the targeted tissues and reduce the side effects on healthy tissues [143]. Besides, they are based on an externally controllable stimulus, the MF, as a trigger to enhance the anticancer cargo release. Moreover, the magnetic stimulus does not have penetration depth limitation, making it feasible to target deep-seated tumors non-invasively [238]. In addition, the magnetic stimulus could trigger not only hyperthermia using high-frequency AMF but also mechanical forces using the safer low-frequency RMF to induce cargo release [145]. Both triggers are generated

in an “inside-out” way offering localized hyperthermia or mechanical forces within the nanocarrier platform, thus avoiding side effects on the nearby healthy tissues. These localized triggers do not need high MNP concentrations inside the tumor tissues as there is no need for global microenvironment effects, in contrast to using the MNPs for tumor ablation/hyperthermia, magneto-mechanical destruction or photothermal therapies. The added MNPs component into the nanomedicine platform, through embedding or surface attachment, can also serve as a contrast agent for magnetic based imaging technique such as MPI and MRI for theranostic applications of the whole nanomedicine delivery system [295]. Despite the added benefits of having biocompatible MNPs inside the nanomedicine platform, challenges may appear regarding their scale up production compared to conventional single component nanomedicines products. In addition, their stability in biological environment should be an important consideration. For instance, the harsh intracellular lysosomal environment could degrade non-stable delivery systems leaving no opportunity for controlled MF-induced cargo release. So that, the stability of the MF-responsive delivery systems could be important attributes to enable their therapeutic efficacy. In conclusion, meticulous design of the MNP-based nanomedicine formulation based on their critical quality attributes is needed in order to develop responsive, efficient and safe platform that could be clinically translated. Future research may also be directed towards developing clinical setups to enable 3D MNPs focusing as well as rotating MF generation.

## Part III. Metal-organic frameworks (MOFs) as drug delivery systems

Metal-organic frameworks (MOFs) are a class of porous hybrid (inorganic-organic) materials attracting increasing attention for drug delivery applications [296]. They are composed through coordination bonds between inorganic metal ions or metal ions clusters and organic ligands. They have the advantages of high porosity and functional and structural flexibility [297, 298]. The tunable MOFs properties offered through the rational choice of the metal ion and the organic linker could enable the synthesis of MOFs with suitable optimal properties for the intended applications [297, 299-301]. Hence, MOFs with high biocompatibility and biodegradability, optimal size, high drug loading capacity and easy functionalization could be synthesized.

### III.1. MOF structure, synthesis and characterization

The inorganic metal ion and the organic ligand are the two basic MOF components [296, 302]. Divalent metal ions (especially those belonging to the first transition series as  $\text{Fe}^{2+}$ ,  $\text{Zn}^{2+}$ ,  $\text{Cu}^{2+}$  or  $\text{Co}^{2+}$ ) are the most commonly used for developing MOFs for drug delivery applications [303]. According to the hard and soft acid and base theory, these divalent ions have intermediate hardness/softness making their coordination interaction with the electron donor atoms in the organic ligands moderately reversible [304]. This coordination flexibility could not only help towards the MOF biodegradability, but also could enable the development of MOFs with stimuli-responsive properties. For instance, the reversible coordination bonds could break in response to a change in the pH or other triggers, resulting in controlled on-demand cargo release [302].

Monovalent ions (as  $\text{Ag}^+$  or  $\text{K}^+$ ) have also been used to synthesize MOFs; however, their corresponding MOFs usually have stability issues with sensitivity to light, heat or water [302, 305]. Moreover, tri (as  $\text{Fe}^{3+}$  and  $\text{Al}^{3+}$ ) and tetravalent (as  $\text{Zr}^{4+}$ ) ions often need severe reaction conditions for the MOFs synthesis, and they usually result in the formation of MOFs with high chemical and structural stability that could raise concerns regarding their biodegradability [302, 306, 307].

Carboxylates, pyridines and polyazole molecules are the most commonly used organic linkers for MOF synthesis [308]. Carboxylates have a net negative charge for neutralizing and coordinating with the metal ions [301]. However, they have many coordination modes that make it challenging to predict and control the resulting MOFs [301]. On the other side, pyridine has simple coordination chemistry but is a neutral moiety with weak coordination ability [302]. Pyrazole molecules (as imidazole or pyrazole) have the advantage of the possibility to remove a proton to form an anionic multi-terminal ligand with a controlled and predictable coordination mode. Also, their strong alkalinity enables the formation of MOF structures with sufficient stability, which makes them widely used [302].

The structure of the MOFs can be demonstrated at four different levels (Figure 18) [309]. The first level describes their chemical components: the metal ion cluster (node) and the organic ligand (linker) [309]. The second level is the secondary building unit (SBU), formed by coordinating multiple linkers to the metal ion node. This SBU is the repeating unit cell that builds up the MOF structure [310]. The third level is the linkage of multiple SBUs through bridging their ligands, leading to the formation of pores and cages [310]. The fourth level is the final outer morphology of the MOFs, described by their size, shape, orientation, etc [309]. The first three levels can be predetermined by the chosen metal ion and organic linker; however, the fourth level mainly depends on the MOFs synthesis and growth conditions. It is worth noting that the outer surface of the MOFs includes coordinatively unsaturated sites (CUSs) that would be active for interaction with other moieties. Therefore, these CUSs could help in MOF coating, functionalization or surface loading of drugs [309].

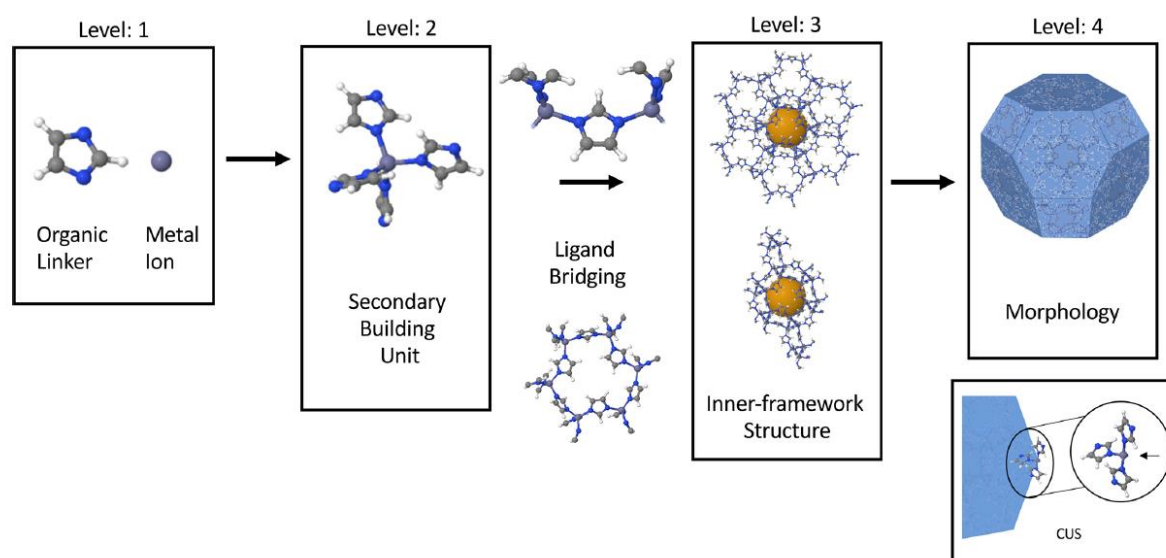


Figure 18: Structural and compositional levels of MOFs: level 1, node and linker; level 2, secondary building unit (SBU) and coordinatively unsaturated site (CUS); level 3, inner-framework structure; and level 4, morphology. Adapted from [309].

Due to the extensive possibilities of choosing the metal ion and the organic linker, applying structure-guided synthesis (reticular chemistry) could enable the design of MOFs with suitable properties for the intended application without exhaustive empirical studies [310]. Reticular chemistry provides a molecular-scale design tool to control the structure and chemistry of MOFs. Consequently, tuning the MOF properties, such as their porosity and structural attributes, could offer control over drug cargo loading, storage and release [311, 312]. In addition, the MOF macroscopic morphology, such as size and shape, can be tuned by controlling the synthesis reaction conditions (as the reaction

kinetics, solvent ratios, temperature or modular agents) [313-316]. Figure 19 shows examples of different pore topologies that could be obtained for different MOFs.

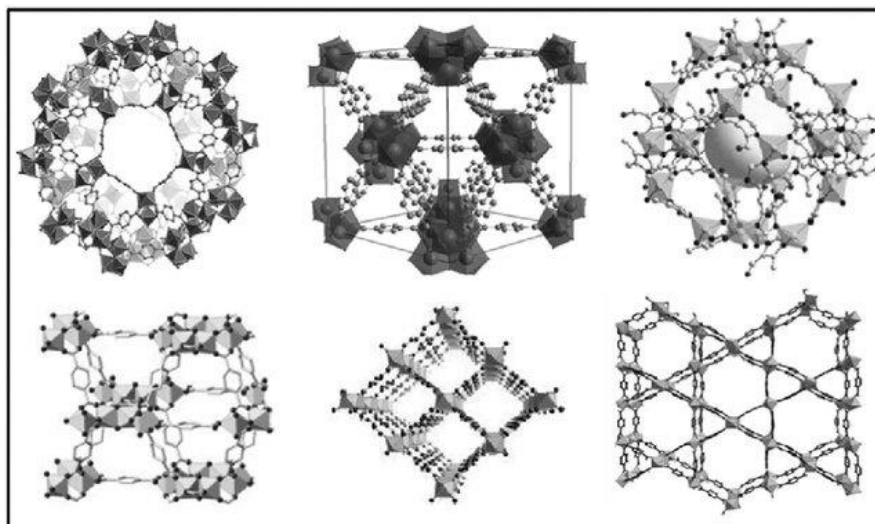


Figure 19: Scheme of pore topologies for the different MOFs. Upper line, from left to right, MIL-125, UiO-66, SIM-1. Bottom line, from left to right, MIL-125, MIL-53, MIL-68. Adapted from [317].

MOFs are most commonly synthesized by solvothermal or non-solvothermal methods by mixing the metal ion and the organic linker precursors with other reaction-controlling agents [309]. High pressure or temperatures above the solvent boiling point are usually used in solvothermal methods to dissolve the reaction components and promote the synthesis. On the other hand, the non-solvothermal synthesis relies on the reaction conditions (as pH) that favor MOF nucleation, and is usually carried out at temperatures below the solvent boiling point [309]. Other methods such as microwaves, sonication and mechanical grinding have also been used for MOF synthesis [318-320]. Most commonly, organic solvents are used in MOF synthesis in order to efficiently dissolve the reaction components. Alternatively, MOFs synthesized in aqueous conditions or using light alcohol solvents could be more suitable for biomedical applications such as drug delivery [311, 313, 321, 322].

Several characterization techniques are essentially needed for MOF development (Figure 20). Microscopy techniques such as transmission electron microscopy (TEM) and scanning electron microscopy (SEM) are most commonly used to determine MOF size and shape [323, 324]. Dynamic light scattering (DLS) could also measure MOF hydrodynamic diameter and surface  $\zeta$ -potential (effective electric charge on the nanoparticle's surface) [325]. Brunauer–Emmett–Teller (BET) is needed to characterize the surface area and pore volume [326]. X-ray diffraction (XRD) is used to confirm MOF structure crystallinity, and the thermogravimetric analysis (TGA) is used to characterize

their thermal stability, inorganic coating and drug loading [324]. Fourier transform infra-red (FTIR) could also be used to investigate the MOF bonding and drug loading [324]. Other techniques, such as UV-VIS spectrophotometry, fluorescence spectroscopy or high-performance liquid chromatography (HPLC), could be applied to characterize the drug loading and encapsulation efficiency [327].

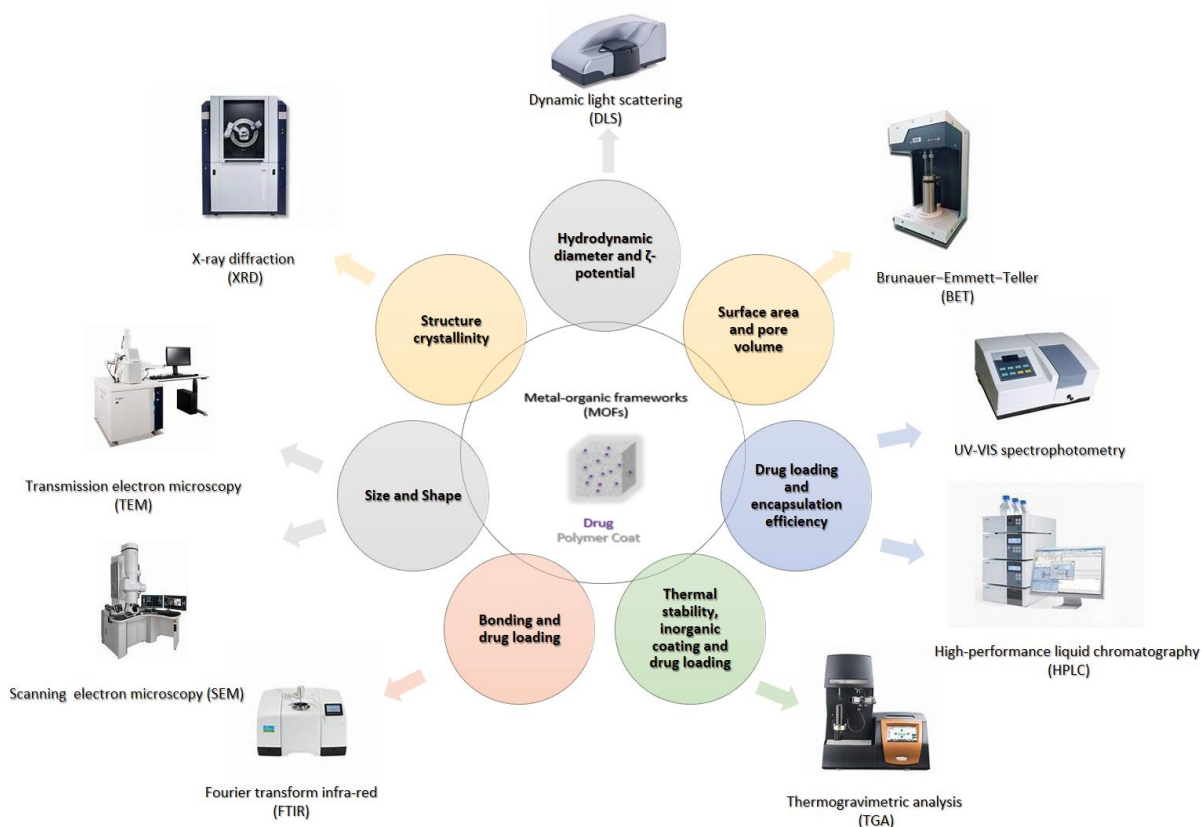


Figure 20: Schematic diagram summarizing the techniques used for MOF physicochemical characterization.

### III.2. Naming and classification of MOF families

MOF structures were first described by Richard Robson and his coworkers in 1989 when they synthesized porous solid infinite polymeric frameworks composed of 3D linked rod-like segments [328]. Later in 1995, Yaghi *et al.* reported the synthesis of microporous 2D channel structures through coordinate linking between  $\text{Co}^{2+}$  metal ion and trimesic acid (1,3,5-benzenetricarboxylate (BTC)) organic linker and named them MOFs [329]. Afterward, various types of MOF families (also known as MOF series) have been synthesized for different applications such as materials and gas storage, purification, separation, catalysis, drug delivery, etc [330].

Until now, there is no standard rule for MOF naming, but they could be named based on the first synthesizing laboratory/institution, material composition, functional groups or structure. For instance, MIL-n “Materials of Institute Lavoisier”, Uio-n “University of Oslo” and HKUST-n “Hong Kong

University of Science and Technology” were named after their first reporting institutes [331-333]. In most cases, the number “n” indicates the serial number of the MOF preparation; however, it is sometimes arbitrary [330]. MOF-n “Metal-organic frameworks” and CD-MOF-n “cyclodextrin-based metal-organic frameworks” are examples of MOFs named after their material composition [334, 335]. Multivariate metal-organic framework “MTV-MOF-n” family name was given as it is formed by introducing two or more organic functional groups such as  $-\text{NH}_2$ ,  $-\text{NO}_2$ ,  $-\text{CH}_3$  or  $-\text{Cl}$  into MOF-5 [336]. ZIF-n “zeolitic imidazolate framework” and PCN-n “porous coordination network” are examples of MOFs named after their structure [337, 338]. A standardized MOF naming protocol is still needed to properly identify and differentiate the different MOFs.

### III.3. Drug loading and encapsulation into MOFs

MOF application in drug delivery was first reported by Horcajada *et al.* in 2006 upon using the MIL-n family for drug delivery of ibuprofen. In their study, an unprecedented loading of  $\approx 58$  wt% was obtained, where the ibuprofen weight was larger than the carrier's original weight (1.4 grams of ibuprofen per 1 gram of MIL-101) [339]. Most of the other traditional drug delivery carriers achieve less than 5 wt% loadings, indicating superior loading properties that could be obtained using MOFs [311].

MOF high tunable porosity makes them an attractive option for drug delivery. For instance, MOFs could have BET surface area as high as  $7140 \text{ m}^2/\text{g}$  and pore volume up to  $4.4 \text{ cm}^3/\text{g}$ , as for Northwestern University MOFs (NU-110) [340]. Therefore, MOFs could have 6x higher surface area and 2.2x higher pore volume than mesoporous silica nanoparticles (MSN) (that could have BET surface area up to  $1200 \text{ m}^2/\text{g}$  and pore volume up to  $2 \text{ cm}^3/\text{g}$ ) [340-342]. This higher surface area and pore volume could enable exceptionally high drug loading capacity. For example, it was reported that insulin could be loaded up to 39.7 wt % into NU-1000 MOFs compared to 26.1 wt % into MSN [309, 343, 344].

The MOF pore dimensions should also be considered, especially upon loading large biomolecules. MOF pore size could be finely tuned through isoreticular chemistry by using organic linkers of increasing lengths to get larger pore size without changing the underlying MOF topology [345]. For instance, Peng *et al.* designed a series of Ni-based isoreticular metal-organic frameworks (Ni-IRMOF-74) with progressive finely tuned pore sizes from 1.5 to 4.2 nm. This progressive extension was achieved through extending the length of the 2,5-dioxidoterephthalate organic linker with phenylene units. In their study, the Ni-IRMOF-74-II having a pore size of 2.2 nm was the optimum one for achieving loading, protection of the single-stranded DNA (ssDNA) cargo as well as its efficient triggered release upon presence of complementary DNA (cDNA) in the environment. The ssDNA

triggered release from Ni-IRMOF-74 of larger pore sizes was reduced as they offered stronger binding interactions for the encapsulated ssDNA, and the cDNA molecule could also bind to and fit in its larger MOF pores [345]. This study highlighted the significance of tuning the MOFs pore sizes for controlling the loading and release of their cargo.

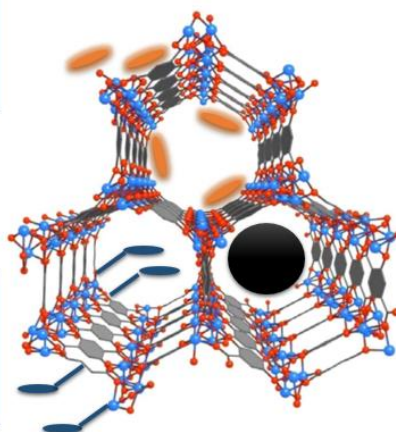
MOFs could be designed to have pore size and aperture up to 5 nm and 2 nm, respectively, which is lower than the 50 nm and 20 nm pore size and aperture that could be obtained by MSNs. Moreover, to get the highest pore dimensions for MOFs, it is required to use extended organic linkers, which raises both synthesis and biocompatibility challenges due to their poor solubility and limited biodegradability. Alternatively, biomimetic mineralization technique could be used to encapsulate large biomolecules into MOFs. In this technique, biomolecules act as nucleation sites to induce the MOF formation under physiological conditions. The MOF nucleation is triggered by bonds/interactions between biomolecule moieties and MOF building units, leading to concentrating them around the biomolecule and facilitating their crystallization [346-348]. During the biomimetic mineralization, the biomolecule could offer a control over the morphology, size and crystallinity of the synthesized MOFs [346]. This loading strategy (often called pore confinement) protects the biomolecules from chemical and enzymatic stress environments [349]. However, the biomolecule release could be delayed until the degradation of the MOF structure [350, 351].

Drug entities could also be loaded either on the MOF surface, inside their pores, or both through different covalent or non-covalent interactions with the MOF organic ligands or metal ions. Covalent binding could be achieved through several functional groups that could be available in the MOF structure, such as amino, carboxyl, hydroxyl, amide or azide. It could be achieved using organic linkers that are pre-conjugated to the drugs or done after the MOFs synthesis. On the other hand, the non-covalent binding could be achieved due to electrostatic adsorption, hydrogen bonding,  $\pi$ - $\pi$  stacking or van der Waals interactions, and it is usually done after the MOF synthesis [349].

The pore loading of drugs can be achieved through the one-pot synthesis approach or the impregnation technique (post-synthesis diffusion of the loaded cargo inside the MOF porosity). It is worth noting that upon using impregnation for pore loading, the size of the drug should allow their diffusion inside the MOF. In addition, solvents that were used during the plain MOF synthesis should be first removed from the MOF pores, to allow subsequent drug entry. This solvent removal process is called "the activation process" [352]. Surface loading is done after MOF synthesis and is generally governed by interactions with the CUSs. Figure 21 shows a schematic illustration of common strategies of drug loading in MOFs.

**Non covalent** loading of drug on the MOFs surface or in its pores through interactions such as: Electrostatic adsorption, hydrogen bonding,  $\pi$ - $\pi$  stacking or van der Waals interactions

**Covalent** loading of drug on the MOFs surface or in its pores through bonds such as: such as amino, carboxyl, hydroxyl, amide or azide



Pore confinement used for loading biomolecules larger than the MOFs pores

Figure 21: Schematic illustration of common strategies of drug loading in MOFs.

Due to interactions between the guest molecules and MOF subunits, MOF pores could exhibit some flexibility, such as breathing. Breathing phenomena in MOFs describes a reversible transition process where the MOF unit cell expansion could occur upon desorption of the loaded guest molecule without structure bond breakage and *vice versa*. It was reported that this transition could affect the cell volume of the MOF structure by 50-230 %, depending on the linker length and structure [353-355]. Hence, the breathing properties could enable the loading of a large amount of drugs in the MOF pores after activation “solvent removal” [356, 357]. It also could offer restricted diffusion of the guest molecules, i.e., controlled release, after their adsorption inside the MOFs unit cells due to its contraction. This breathing effect could occur when the MOF unit cell constituting bonds/linkers are flexible so that its dimensions could be affected by the adsorption/desorption of the guest molecules (especially strongly interacting ones) [358, 359].

For instance, Horcajada *et al.* obtained up to 20 wt% loading of ibuprofen in MIL-53(Fe) after its activation and removal of the solvent molecules from the pores. Also, due to the restricted guest molecules mobility, they observed zero order release kinetics of the loaded ibuprofen, without MOF structural degradation, for up to 3 weeks *in vitro* under simulated physiological conditions [360]. This release time was much longer than the 7-day release time from other zeolites that have pore sizes similar to MIL-53(Fe) and can have similar loading capacities (15-20 wt %) [361]. Other MOF flexibility transitions could be present such as linker rotation and subnetwork displacement, but they are more applied in gas storage applications of MOFs [362, 363].

Alternatively, drug entities in the form of active metal nodes, organic linkers or both could be used to prepare functional “intrinsically active” MOFs [349, 364, 365]. This will be discussed later in more detail in Part III.7.1.

#### III.4. Drug release from MOFs

Generally, the pattern of drug release from MOFs depends on several factors, including the loaded cargo location (inside the pores, on the surface or as a structural component), its interaction with the MOFs (covalent or non-covalent), its size relative to the MOF pores dimensions and MOF stability/response to the release site environment [309, 349].

Covalently-linked drug loads mostly rely on the covalent bond or MOF matrix degradation for being released [309, 366]. For instance, Cabrera-García *et al.* designed amine functionalized MIL-101(Fe) that is covalently loaded with camptothecin (CPT) derivatives (hemisuccinate (Suc) or hexanoate (HA)) through an acid-sensitive ester linkage. The delivery system was stable under physiological conditions with a strong drug release response under acidic conditions. After 48 h at pH 7.4, there was minimal observed CPT release from MIL-101(Fe) loaded with CPT-Suc and CPT-HA derivatives (8% and 12%, respectively). However, after 48 h at pH 5 (similar to the lysosomal acidic pH), there was an observed enhanced CPT release from MIL-101(Fe) loaded with CPT-Suc and CPT-HA derivatives (35% and 23%, respectively). This enhanced release under acidic conditions could not be only related to the ester bond cleavage but also to the MIL-101(Fe) degradation. A small quantity of free CPT was detected after release, and most of the released CPT was in the conformation of CPT-linker-ligand as detected by HPLC-MS/MS. The carboxylate organic linker (4-carboxyphenylbenzene) of the MIL-101(Fe) could get protonated under acidic conditions resulting in MOF degradation and structure collapse [367]. Although the covalent loading approach can limit the uncontrolled cargo release, achieving a complete release of the loaded cargo in their active conformation is usually a limiting factor that could affect the efficacy of the formulation [367-369]. The CPT derivatives loaded MIL-101(Fe) showed higher  $IC_{50}$  values of  $0.078 \pm 0.016$   $\mu\text{g}/\text{mL}$  (for CPT-Suc cargo) and  $0.063 \pm 0.015$   $\mu\text{g}/\text{mL}$  (for CPT-HA cargo) against HeLa cells compared to  $0.003 \pm 0.001$   $\mu\text{g}/\text{mL}$  of CPT [367]. Further studies could conclude the significance of this reduced efficacy within the *in vivo* antitumor clinical applications context. In other words, considering the additional benefits of controlled release behavior of the covalently loaded cargo inside MOFs, whether the reduced efficacy could still be enough regarding the overall benefits vs. risk ratio.

On the other hand, non-covalently linked cargos, especially when loaded on MOF surface, often show rapid release depending on their diffusion out of, or dissociation (unbounding) from, the MOF delivery system [309]. However, they may suffer from burst release upon dilution and first

contact with body fluids. Hence, MOF coating with polymers, lipids or inorganic shells is often used to mitigate the drug burst release and offer a better-controlled release pattern [370-373].

For instance, Chen *et al.* reported decreased DOX burst release from the loaded PCN-128 in PBS (pH 7.4) upon coating with phosphate-functionalized methoxy polyethylene glycol (mPEG-PO<sub>3</sub>) compared to the bare DOX@PCN-128. The PEG coating decreased the DOX burst release from DOX@PCN-128@mPEG-PO<sub>3</sub> to ≈22% after 6 h, compared to ≈ 53% from the bare DOX@PCN-128, with controlled DOX release up to 250 h. In addition, the PEG coating resulted in enhanced colloidal stability of the synthesized PCN-128 MOFs in PBS (pH = 7.4), where the coated MOFs were stable up to 7 days compared to the aggregation of the bare MOFs in 1 day [370]. Other techniques, such as partial or complete amorphization, were also used to decrease the burst release effect from MOFs and enable extended controlled release patterns [374, 375].

Stimuli-responsive MOFs were also developed for controlled on-demand cargo release in response to various endogenous (as pH, redox, ions, and enzyme) and exogenous (as light, MF, temperature, and pressure) stimuli [330]. This will be discussed in more detail later in Part III.7.3.

### III.5. MOF biocompatibility

Biocompatibility is an important aspect towards the clinical translation of drug delivery systems. Developing biocompatible MOFs with minimal cytotoxicity and immunogenicity mainly depends on the biocompatibility of the whole MOF structure and each MOF structural component (metal ion and organic linker) [376, 377]. Moreover, other factors should also be considered, such as the route of administration, dosage regime and frequency, the exposed cell types, and the kinetics of MOFs absorption, degradation, distribution, accumulation and excretion [377-379].

Based on their oral lethal dose (LD<sub>50</sub>) in rats, it was found that Ca, Mg, Zn, Fe, Ti, and Zr ions are the most suitable for synthesizing biocompatible MOFs [380]. It was also observed that Fe-based MOFs exhibit high biocompatibility and less cytotoxicity than Zn or Zr-based ones [377]. Although Fe and Zn are both endogenous elements, the human body is more able to deal with Fe contents through endogenous proteins such as ferritin [188]. The toxicity of the Zn-based MOFs is due to the local excess concentrations of the released Zn ions following MOF degradation. Excess Zn ions could induce cellular damage due to their competition with Fe and Ca for ion channels, affecting their metabolism and/or due to inducing DNA damage [381, 382]. It was reported that the Zn-based zeolite imidazole frameworks-8 (ZIF-8) MOFs, the most widely used MOFs in biological applications, can be tolerated up to 100 µg/ml in cellular studies [377]. However, the intended biological applications as well as the broader *in vivo* conditions should also be considered.

For instance, Zn ions release following the lysosomal degradation of pH-sensitive ZIF-8 in targeted cancer cells could be advantageous for antitumor applications. The released Zn ions could also help towards endosomal escape of the cargo, helping them to reach their cellular targets [302, 383-385]. Moreover, going to the broader context of the *in vivo* conditions, many MOFs showed good biocompatibility despite their cellular cytotoxicity, which could be due to the protein corona formation that could reduce the MOF degradation rate [386, 387]. For instance, ZIF-8 MOFs were able to achieve their drug delivery, controlled release and cargo protection goals, as well as their therapeutic outcomes *in vivo* without showing significant toxicity or pathology [351, 386].

The endogenous organic linkers, such as aspartate, gallate or fumarate, are generally better tolerated with fewer adverse effects than the exogenous ones, as polycarboxylates, imidazolate, sulfonates or phosphonates. It is due to the body ability to reuse, metabolize and excrete the endogenous linkers [380, 388]. However, they are not widely used for biological applications due to challenges of stability and porosity of their corresponding MOFs [380]. The exogenous linkers offer tailored functionalities that can be adapted for obtaining optimized MOF properties suitable for the intended applications. The organic linkers toxicity would depend on their polarity (hydrophobic–hydrophilic balance ( $\log P$ )) and ease of metabolism or elimination [380].

For instance, Tamames-Tabar *et al.* observed a linear tendency between the constituting organic linker's partition coefficients (experimentally estimated  $\log P$ ) and its related MOF cytotoxicity. In their study, the hydrophilic trimesic ligands based MIL-100 MOFs showed higher  $IC_{50}$  on HeLa (cervical cancer) and J774 (reticulum sarcoma) cells ( $1.10 \pm 0.15$  and  $0.70 \pm 0.02$  mg/ml, respectively) compared to the hydrophobic tetramethyl terephthalic linker based MIL-88B\_4CH<sub>3</sub> MOFs ( $0.69 \pm 0.02$  and  $0.08 \pm 0.01$  mg/ml, respectively) [377]. *In vivo*, after one day of i.v. infusion (10% glucose solution containing a dose of  $220 \text{ mg Kg}^{-1}$  MIL-100 or  $110 \text{ mg Kg}^{-1}$  of MIL-88B\_4CH<sub>3</sub>) in Wistar female rats, higher reticuloendothelial system (RES) (liver and spleen) accumulation of MIL-88B\_4CH<sub>3</sub> (49% of the iron injected dose (w/w)) was observed compared to MIL-100 (32% of the iron injected dose (w/w)). Lower concentration of MIL-88B\_4CH<sub>3</sub> was probably used due to their aggregation and colloidal instability at higher concentrations, which could be due to their hydrophobicity. Pathohistological examination showed normal liver color and morphology in rats injected with MIL-100. However, normal morphology but with lighter color was observed in the liver of rats injected with MIL-88B\_4CH<sub>3</sub>, where a progressive return to normal color started after 7 days and normal coloration was reached after 30 days. Moreover, a more rapid urinary excretion of the hydrophilic trimesic ligands of MIL-100 was detected (90 wt% in one day) compared to the hydrophobic tetramethyl terephthalic ligands of MIL-88B\_4CH<sub>3</sub> (21 wt% after one day and cumulative 31 wt% after one week) due to its association with

the lipid droplets in the macrophages. These results indicated the effects of the constituting organic ligands on MOF cytotoxicity, biodistribution and elimination [389].

### III.6. MOF cellular uptake and interactions

MOFs cellular interactions and uptake are mainly affected by MOF physicochemical properties (as particle size, shape and surface properties) as well as cell type [309, 377, 390-392]. It was reported that the endocytosis of MOFs is an energy-dependent process [390, 391, 393]. In their study, Park *et al.* synthesized a series of Zr-based PCN-224 MOFs of different TEM particle sizes ranging from 30 nm to 190 nm. There was an observed size-dependent uptake efficiency by Hela cells where the 90 nm PCN-224 showed the highest cellular uptake efficiency (using different concentrations and up to 18 h incubation times), with the following order: 90 nm > 60 nm > 30 nm > 140 nm > 190 nm (Figure 22). The nanoparticles intracellular uptake was characterized by measuring the concentration of the Zr<sup>4+</sup> metal ions of the PCN-224 inside the Hela cells [394].

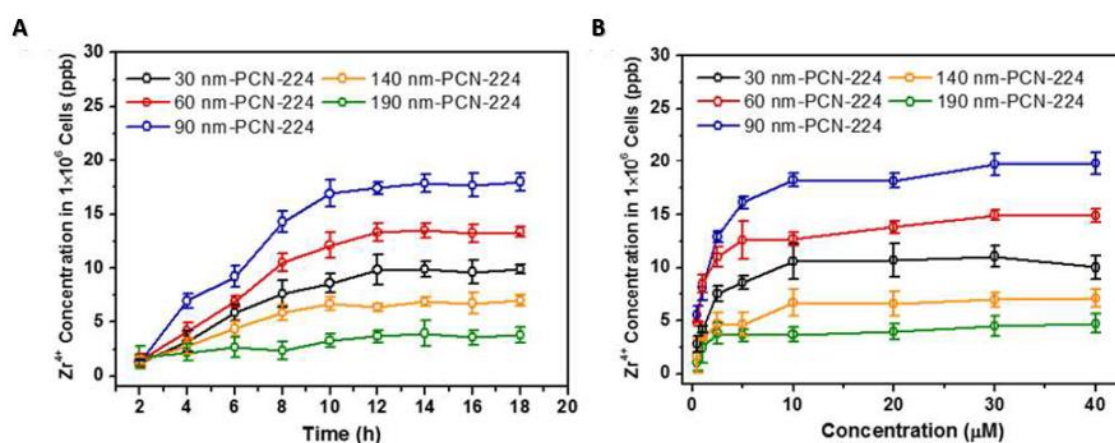


Figure 22: The cellular uptake of different-sized PCN-224 in Hela cells. A) At different incubation times up to 18h, B) At different concentrations with 24h incubation time. Adapted from [394].

Wang *et al.* also had a similar observation, where 90 nm mesoporous UiO-66 MOFs showed higher cellular uptake in 4T1 cells (6h and 12h incubation times) than 120 nm and 200 nm [323]. In other work, Duan *et al.* reported prolonged circulation time and higher tumor uptake of the DOX-loaded amorphous ZIF-8 MOFs of 60 nm compared to 130 nm ones in 4T1 tumor-bearing mice at 2, 6, 12, and 24 h after i.v. injection [395].

Though the above results could suggest that smaller particle sizes (< 100 nm) could be more promising for better cellular uptake, other factors such as cellular uptake kinetic and intracellular fate should also be considered [392]. In their cellular trafficking study, Orellana-Tavra *et al.* observed better lysosomal escape in Hela cells (2 h incubation time) for the 260 nm calcein-loaded UiO-66 (cal@<sub>260</sub>UiO-66) than the smaller 150 nm ones (cal@<sub>150</sub>UiO-66). The colocalization between cal@<sub>260</sub>UiO-66 and lysotracker was ≈37% lower compared to that for cal@<sub>150</sub>UiO-66, detected through Manders' overlapping coefficient. A combination of clathrin and caveolae-mediated endocytosis was observed for the bigger cal@<sub>260</sub>UiO-66 MOFs compared to the almost exclusive clathrin-mediated endocytosis of the smaller cal@<sub>150</sub>UiO-66 [393]. These results indicate not only the essential needs but also the advantages of tuning the MOF properties with regard to the intended biological applications.

Other MOF properties as the shape and surface characteristics, such as coating, polarity and charge, could affect their stability, cellular uptake, and biodistribution behavior [389, 391, 396]. For instance, PEG coating of the Zr-based UiO-66 was able to enhance its degradation stability in PBS at pH 7.4 and affect its cellular uptake mechanism. The calcein cargo release from the bare UiO-66 was almost complete after two days in PBS at pH 7.4, compared to only 30% release after 5 days for the PEG-coated ones either using PEG550 or PEG 2000. Moreover, The PEG2000 coating enhanced the caveolae-mediated endocytosis pathway that could allow a partial escape of the lysosomes to avoid lysosomal cargo degradation and provide better accessibility to other cellular targets. This change in the cellular uptake pathway was not observed with the bare UiO-66 nor the PEG550 coated ones, and it could be attributed to the change in the particle shape. The longer PEG2000 coat made the UiO-66 particles more rounded with less defined edges, as their surface characteristics were more determined by the bulk of the coating polymer rather than their underlying UiO-66 MOF crystal structure [391].

In another study, it was observed that the hydrophobic ligand-based MIL-88B\_4CH<sub>3</sub> MOFs did not only show higher RES accumulation than the hydrophobic ligand-based MIL-100, but they were also able to cross the blood-brain barrier and accumulate in the brains of the injected rats [389].

### III.7. MOF antitumor applications

Due to the MOF advantages of high porosity, exceptional drug loading capacities and tunable structural and functional properties, they are attracting more attention in antitumor drug delivery applications [349]. MOF antitumor applications could be achieved either by using them as traditional delivery carriers or stimuli-responsive ones. Also, MOF properties can be tuned so that the MOFs themselves could have an intrinsic antitumor activity.

### III.7.1. Antitumor MOFs

Functional MOFs composed of active antitumor metal nodes, organic linkers or both were developed for cancer treatment. Active metal nodes can be exploited for chemodynamic therapy, radiotherapy or catalytic modulation of the tumor microenvironment. Active linkers, as photosensitizers or chemotherapeutic drug entities, could be applied for photodynamic, photothermal, or chemotherapeutic applications [349, 364, 365].

For instance, Hafnium(Hf(IV)) as a radiation absorptive ion was used to construct MOFs to enhance the radiation energy deposition in the tumor tissues and increase the efficiency of the radiation therapy [397]. Thanks to its tetravalent ionic configuration and according to the hard and soft acids and bases theory, Hf(IV) can form more stable coordinate bonds with carboxylic acid containing organic linkers than di and trivalent metal cations [398]. Hf(IV) based MOFs, UiO-66(Hf) and DUT (Dresden University of Technology)-51(Hf) were first reported in 2012 [399, 400], then in 2018, Ni *et al.* employed Hf<sub>12</sub>-DBA (2,5-di(p-benzoato)aniline) and Hf<sub>6</sub>-DBA MOFs as antitumor radio-sensitizing agents [401].

In their study, Zhou *et al.* prepared UiO-66-NH<sub>2</sub>(Hf) MOF nanoparticles (Figure 23A) as radio-sensitizers against esophageal cancer. As detected using TEM, the nanoparticles synthesized through an aqueous solvothermal method had an average particle size of 95 ± 18 nm (Figure 23B). The prepared UiO-66-NH<sub>2</sub>(Hf) did not need organic solvents, making it more environmentally friendly and could be more feasibly scaled up than the previously reported Hf<sub>12</sub>-DBA and Hf<sub>6</sub>-DBA MOFs. *In vitro*, on the esophageal squamous cell line KYSE 150, a biocompatible concentration (50 µg/mL and 4h of incubation) of UiO-66-NH<sub>2</sub>(Hf) MOFs significantly increased the DNA damage and ROS production efficiency of 6 Gy X-ray irradiation resulting in enhanced killing (cell viability of 39.3 ± 0.5%) and clone inhibition efficiencies (Figures 23C and D). Intratumoral injection of UiO-66-NH<sub>2</sub>(Hf) (40 µL, 2.0 mg/mL) in KYSE 150 subcutaneous xenograft nude mice model enhanced the X-ray tumor site deposition noticed as an increase in the CT values at the tumor site from 96 Hu to 151 Hu. Eight days after single 8 Gy X-ray exposure combined with the single intratumoral dose of UiO-66-NH<sub>2</sub>(Hf), an almost complete tumor growth stop was observed compared to a limited delay achieved by 8 Gy X-ray and almost no effect of the UiO-66-NH<sub>2</sub>(Hf) intratumoral dose (Figures 23E and F). Also, there was no observed weight loss of the experimental mice during the study, indicating the negligible short-term toxicity of UiO-66-NH<sub>2</sub>(Hf) [402]. This study highlighted the promising high efficacy of Hf(IV)-based MOFs for anticancer radiotherapy applications. However, more investigations regarding the long-term biological fate and toxicity of these MOF formulations are still required, especially due to their reported high chemical and structural stability [306].

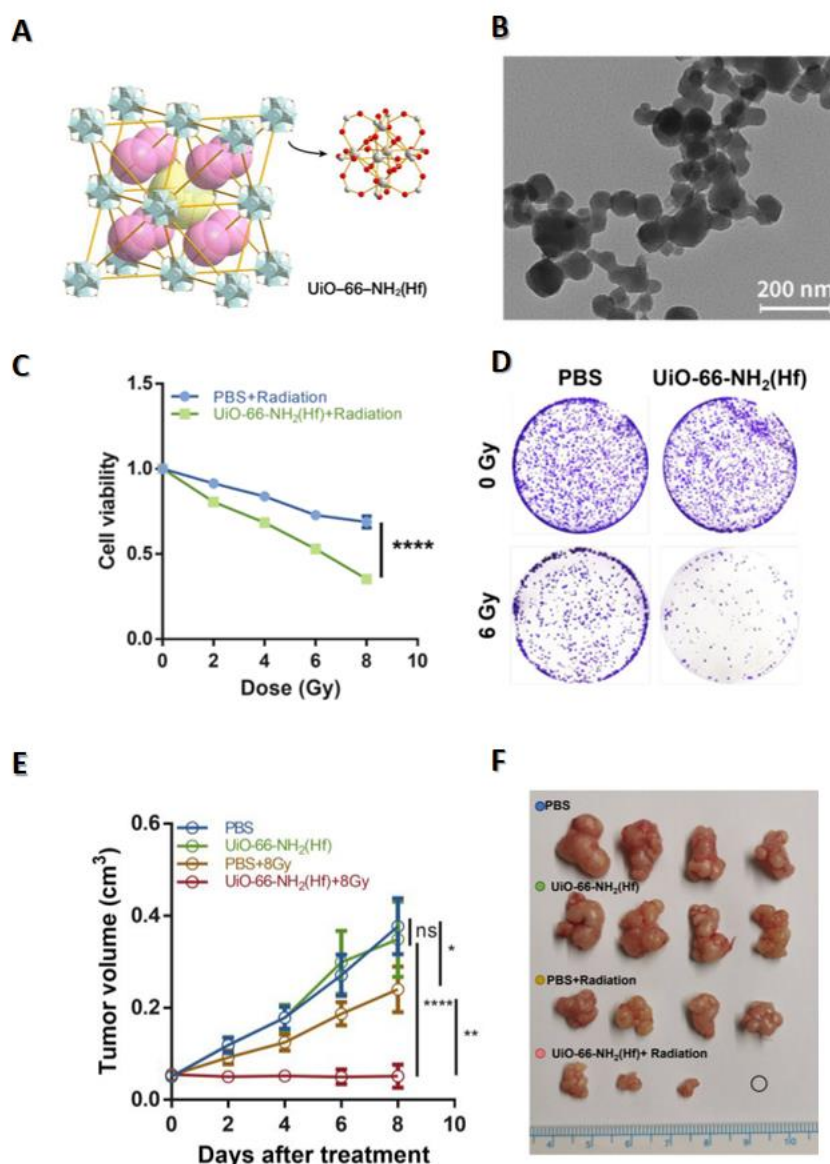


Figure 23: A) Schematic diagram of the UiO-66-NH<sub>2</sub>(Hf) MOF unit cell structure. B) TEM images of the UiO-66-NH<sub>2</sub>(Hf) MOF. C) Lower cell viability and D) enhanced clone inhibition efficiencies of UiO-66-NH<sub>2</sub>(Hf) MOFs+6 Gy X-ray irradiation compared to irradiation only, on the esophageal squamous cell line KYSE 150. E) Tumor growth curves of KYSE 150 subcutaneous xenograft tumors after treatment with UiO-66-NH<sub>2</sub>(Hf) (0 or 2.0 mg/mL) and/or irradiation (0 or 8 Gy) and F) Photographs of tumors excised on day eight after treatment. Adapted from [402].

As an example of active linkers, porphyrin-derived ligands are widely used as photosensitizers for developing antitumor, intrinsically active, MOFs for photodynamic therapy applications [403]. Porphyrins have strong UV-VIS absorption ability, high singlet oxygen quantum yield, and good photochemical stability in biomedicine, making them an interesting option for photodynamic therapy (PDT). However, their relatively low aqueous solubility and easy aggregation could lead to self-quenching and limit their singlet oxygen yield. Thanks to their interaction ability with metals, porphyrins can serve as MOF organic linkers preventing their aggregation and self-quenching and

benefiting from the MOF large surface area. Consequently, enhanced ROS production and more efficient porphyrins PDT effect could be obtained upon incorporation into the MOF structure [403].

For instance, Zhao *et al.* used tetracarboxyphyrin (TCPP) as organic linkers to synthesize Fe-based MOF nanorice particles. An illumination with a 660 nm laser for 15 min enhanced the MOF nanorice particles efficiency against KB tumor (human mouth epithelial) cells as observed in the decreased viability to 18.61% compared to 82.76% viability for the nanoparticles without laser irradiation [404]. However, PDT usually has limited penetration depth for treating deep tumors and suffers from limited oxygen supply in the hypoxic tumor tissues [404, 405]. Some studies developed porphyrin-based MOF nanocomposites containing other nanoparticles to overcome these challenges. For instance, added upconversion nanoparticles of high tissue penetration 808 nm laser absorption and subsequent UV emitting properties were used to overcome PDT's limited penetration depth ability [405]. Also, added IONPs were used to catalyze the Fenton reaction and produce hydroxyl radicals, overcoming the tumor hypoxia by generating oxygen [404]. However, these added components could further complicate the synthesis process of these treatment platforms, limiting their clinical translation.

### III.7.2. MOFs as antitumor delivery systems

MOF tunable properties, high drug loading capacities and extended cargo release abilities made them promising systems for antitumor drug delivery applications. For instance, Leng *et al.* prepared biocompatible iron-based MIL-53 MOFs loaded with up to 56.25% (w/w) of oridonin anticancer drug and a sustained release time of over 7 days in PBS solution at 37 °C under pH 7.2 or 5.5 [406]. These properties encourage the utilization of MOFs for antitumor delivery systems through passive or active targeting.

For instance, DOX-loaded UiO-68 nanoMOFs functionalized with folic acid (DOX@UiO-68-FA) were developed for hepatoma treatment. Folic acid could bind to the overexpressed folic acid receptors on the tumor cells, contributing to enhanced tumor accumulation and better therapeutic outcomes. After 14 days of tail vein injection of 5.0 mg DOX per kg of DOX@UiO-68-FA ( $140 \pm 21$  nm) in HepG2, liver cancer, cells subcutaneous xenograft-bearing mice, more efficient tumor growth suppression (0.38 relative tumor volume ratio to the original tumor size) was obtained compared to 2.06 for equivalent dose of free DOX, 1.14 for equivalent dose of DOX@UiO-68 and 2.90 for PBS [407]. Though passive and active targeting benefits MOF antitumor drug delivery applications, stimuli-responsive targeting could boost the antitumor efficacy of drug delivery systems and achieve better outcomes thanks to its ability to control the cargo release in an on-demand pattern.

### *III.7.3. MOFs as stimuli-responsive antitumor delivery systems*

Several stimuli-responsive MOFs were developed for cancer treatment applications. High drug loading capacities, high porosity and tunable properties make MOFs a particularly interesting option for stimuli-responsive drug delivery systems [330, 408]. For instance, MOF structural components that could change their chemical or physical properties upon exposure to stimuli could lead to MOF structural deformation and cargo release [409, 410]. Also, MOF high porosity could allow cargo diffusion outside the MOF carriers in response to an appropriate stimulus, such as heat-induced destruction of host(MOFs)-guest(loaded drug) interaction [411] or in response to stimuli-induced MOFs coat/gate opening [320]. In addition, MOFs could be adapted to include other types of nanoparticles, such as MNPs or GNPs that respond to MF or light [412]. The high drug-loading capacity of MOFs could also enable the development of a depot system with several cycles of on-demand cargo release, allowing less frequent dosage administration [413-415]. Controlled on-demand cargo release from MOFs was achieved in response to various endogenous (as pH, redox, ions, and enzyme) and exogenous (as light, MF, temperature, and pressure) stimuli [330, 408].

#### *pH-responsive MOFs*

The pH is one of the most investigated stimuli for developing responsive MOF drug delivery platforms. For instance, pH-responsive MOFs having acid-labile bonds were used making benefit of the lower pH of the tumor microenvironment (pH 5.7–7.8), endosome (pH 5.5–6.0) and exosome (pH 4.5–5.0) compared to blood and normal tissues [416]. ZIF-n, MIL-n, UiO-n, DUT-n MOFs families are among the most widely used MOFs for pH-responsive drug release [330, 417-419].

Thanks to its interesting intrinsic pH-sensitive properties, ZIF-8 MOFs were widely employed as pH-responsive anticancer drug delivery systems [302, 410]. ZIF-8 nanoMOFs could be prepared easily at room temperature through the solution reaction method by mixing aqueous solutions of zinc nitrate, a precursor of the  $Zn^{2+}$  metal ion, and the 2-methylimidazole organic linker, under stirring at a slightly alkaline pH=8 [420]. They showed high hydrothermal stability up to 300 °C without significant structural damage [421]. Depending on the cargo molecular size, the ZIF-8 relatively large cavity size of (11.6 Å) could allow high drug loading, while their small window size (pore opening or aperture) of ~3.4 Å could prevent premature leakage (Figure 24) [420].

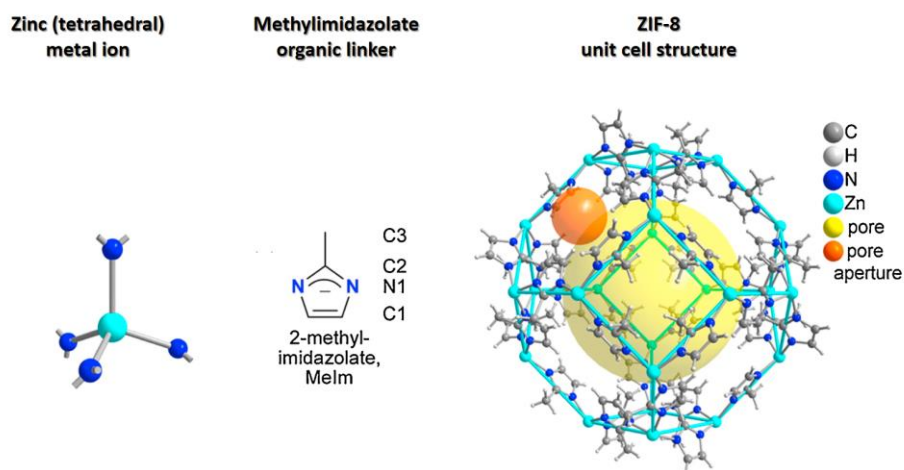


Figure 24: Schematic illustration of the building block (zinc metal ion and methyl imidazolate organic linker) and the unit cell structure of the ZIF-8 MOFs, showing their pore (in yellow) and pore aperture (in orange). Adapted from [422].

ZIF-8 nanoMOFs are stable with minimal premature cargo release under alkaline or neutral conditions; however, they collapse and release their cargo under acidic conditions, endowing pH-responsive properties [420]. This structural collapse is attributed to the protonation of the 2-methylimidazole linkers under acidic conditions (pH 5.4–6), leading to cleavage of the Zn-imidazolate coordination bonds. The acidic pH-induced structural degradation not only releases the chemotherapeutic cargo but also releases a large amount of  $\text{Zn}^{+2}$  ions, leading to a synergistic antitumor effect [423].

Chen *et al.* prepared ZIF-8 loaded nanoMOFs with high loading (19.798 wt %) of the autophagy inhibitor, 3-methyladenine (3-MA), through a one-pot synthesis process. Rapid acidic pH-induced release of the 3-MA ( $\approx 40\%$ ) was observed after 4h in PBS at 37 °C, compared to less than 15% under neutral pH 7.4 [424].

However, ZIF-8 stability could be compromised under physiological conditions due to  $\text{PO}_4^{3-}$  ions attack on the  $\text{Zn}^{2+}$  coordination bonds. This interaction leads to the formation of insoluble zinc phosphates that results in formation of ZIF-8 aggregates [425]. So, coating with polymers such as PEG could offer a shield around the ZIF-8, improving their stability under physiological conditions [426, 427]. For instance, Wang *et al.* observed improved colloidal stability of the ZIF-8 after PEG coating where they did not aggregate in DMEM/10%FBS compared to the non-coated ones. Moreover, ZIF-8 coating could enhance their versatility as stimuli-responsive drug delivery systems. For instance, ZIF-8 alginate coating was able to improve their acidic stability under simulated gastric conditions (pH = 1.5) with < 10% metformin cargo release after 8h, and achieve cargo release (> 80%) after the same period under simulated small intestine conditions (pH = 8) [298].

### Light-responsive MOFs

The light stimulus was also exploited for developing MOFs with on-demand drug release properties [428]. For instance, the release of surface-loaded 5-FU (5-fluorouracil) on GNPs@ZIF-8 nanocomposites was triggered by laser irradiation (524.5 nm and  $700\text{mWcm}^{-2}$ ) mediated through its surface desorption [428]. In another study, Carrillo-Carrion et al. reported the development of light-responsive nanocomposites composed of gold nanostars cores and ZIF-8 shells that enabled triggered cargo release inside living cells. The nanocomposites were loaded with Hoechst (HOE), as a fluorescent probe, and were also coated with an amphiphilic polymer that enhanced their stability in aqueous and biological environments. The NIR illumination (785 nm, 5 min,  $7\text{ W cm}^{-2}$ ) of the nanocomposites loaded Hela cells showed triggered HOE release concluded by cells nuclei staining that was not observed with the nanocomposites loaded non-illuminated cells (Figure 25). The HOE release could have been mediated by its thermodiffusion due to local temperature gradients created by the heated gold nanostars in the nanocomposites [429].

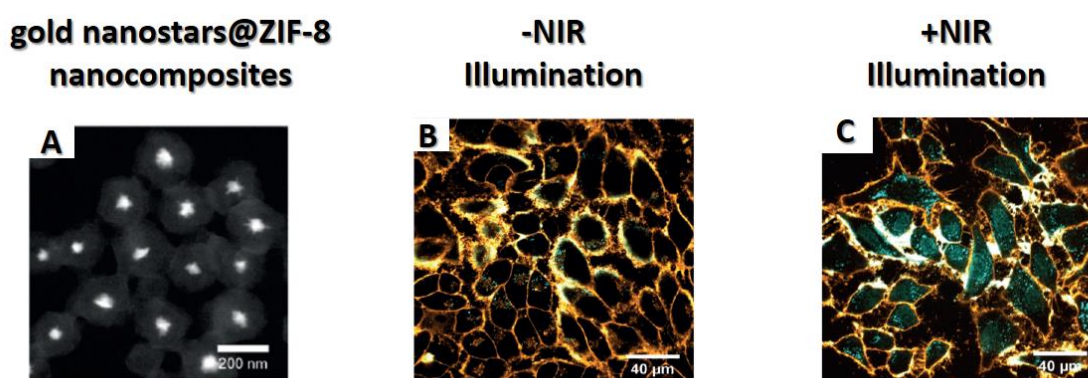


Figure 25: A) SEM of gold nanostars@ZIF-8 nanocomposites (scale bar =200 nm), B) HeLa cells that were incubated with the nanocomposites without laser illumination (scale bar =40 nm), C) HeLa cells that were incubated with the nanocomposites and exposed to NIR illumination (785 nm, 5 min,  $7\text{ W cm}^{-2}$ ) (scale bar =40 nm). The blue color represents the HOE and the orange one represents cell membrane stain (CellMask™ Deep Red). Adapted from [429].

In addition, Zeng et al. reported the development of versatile nanocomposites of gold nanorods cores and porphyrinic MOFs shells, which were loaded with camptothecin. The nanocomposites showed a synergistic photodynamic, photothermal and chemotherapeutic anticancer effect *in vitro* (on murine breast tumor 4T1 cells) and *in vivo* (on 4T1 tumor-bearing mice), due to porphyrin component response to 660 nm laser irradiation, gold nanorods heating with the 808 nm laser irradiation and camptothecin triggered photothermal release, respectively [414].

### MF-responsive MOFs

Within the external triggers employed for stimuli-responsive release from MOFs, the MF could be a very promising one, especially for cancer treatment applications. Harnessing the combined advantages of both MOFs and MNPs and achieving MF-responsive cargo release could be achieved by introducing MNPs into MOFs, forming MOF-based magnetic nanocomposites. MOFs have high functional and structural flexibility, which could enable high drug-loading capacities and biocompatibility. MNPs could allow MF-induced targeting of the nanocomposites to the tumor tissues [143] and enable contrast agent properties for MRI and MPI, opening an avenue for their theranostics applications [151]. In addition, MNPs could endow MF-induced cargo release properties. The advantages of MF-responsive cargo release for anticancer application were comprehensively discussed in parts I and II. In summary, the MF does not have penetration depth limitation allowing access to deep-seated tumors. Also, MF-induced cargo release from drug delivery systems could be achieved in thermal or non-thermal mechanical mechanisms depending on the type of the applied MF [144-147]. Examples of MNP-based MOF delivery systems are summarized in Table 1.

Table 1: Examples of MNPs based MOF delivery systems

Name of Platform	Type of MOFs	Type of MNPs	Type of cargo and Loading content in wt %, if available	Stimulus of release, if done	Cancer cell type used <i>in vitro</i> , if done	Delivery system development goal and <u>the added benefits of the magnetic component</u> ( <u>underlined</u> )	Ref.
Fe <sub>3</sub> O <sub>4</sub> @ HKUST-1	HKUST-1	Fe <sub>3</sub> O <sub>4</sub> nanorods	Nimesulide (up to 20 wt%)			Proof of concept for synthesis of MNPs-based MOFs, their drug loading and extended release	[430]
Fe <sub>3</sub> O <sub>4</sub> @ ZIF-8	ZIF-8	Fe <sub>3</sub> O <sub>4</sub>	Fluorescein (1 wt%)			Proof of concept for the MNPs based MOFs delivery system ability for <u>MF- directed targeting to tumor tissues</u>	[431]
Fe <sub>3</sub> O <sub>4</sub> @ polyacrylic acid(PAA)/gold nanoclusters/ZIF-8	ZIF-8	Fe <sub>3</sub> O <sub>4</sub> @ PAA	DOX (60.6 wt%)			Theranostic platform combining pH-responsive cargo release and trimodal <u>MRI</u> , CT and fluorescence <u>imaging</u>	[432]
Fe <sub>3</sub> O <sub>4</sub> @ZIF-90@ Rat serum albumin (RSA)	ZIF-90	Fe <sub>3</sub> O <sub>4</sub>	5-FU	Low frequency alternating magnetic field (20 Hz, 40 Hz and 70 Hz) 20 min each 1 hour for 7 hours		In vitro proof of concept of <u>MF-induced cargo release</u> from MOFs magnetic nanocomposites and <u>MRI imaging</u>	[433]
Fe <sub>3</sub> O <sub>4</sub> @IRMOF-3	IRMOF-3	Fe <sub>3</sub> O <sub>4</sub>	Paclitaxel (12.32 wt%)			Paclitaxel hydrophobic molecule drug delivery and <u>MRI contrast agent applications</u>	[434]
Fe-MIL-53-NH <sub>2</sub>	Fe-MIL-53-NH <sub>2</sub>	Metal ion cluster	5-FU (28 wt%)			<u>Magnetic</u> and optical <u>contrast agent</u>	[435]
M-NMOFs	MIL-88B	Fe <sub>3</sub> O	DOX (0.69 wt%) /methylene blue (4.3 wt%)			<u>Magnetic-aided targeting of the nanocarrier and PDT</u>	[436]
CoFe <sub>2</sub> O <sub>4</sub> @Mn-MOF	Mn-MOF	CoFe <sub>2</sub> O <sub>4</sub>	Daunorubicin		MCF-7	Enhanced antitumor effect	[437]
Fe <sub>3</sub> O <sub>4</sub> @UiO-66@ carboxylatopillar[6]arene (WP6)	UiO-66	Fe <sub>3</sub> O <sub>4</sub>	5-FU		Hela	pH, temperature and ions responsive release in addition to <u>MRI contrast properties</u>	[438]
Fe <sub>3</sub> O <sub>4</sub> @ZIF-90	ZIF-90	Fe <sub>3</sub> O <sub>4</sub>	DOX (16 wt%)	Two AMF exposures (409 kHz of frequency and 180 Gauss of field) each of 10 min separated by 8 hours	Hela	pH-triggered cargo release followed by <u>magnetic hyperthermia</u>	[439]
Fe <sub>3</sub> O <sub>4</sub> @ZIF-8	ZIF-8	Fe <sub>3</sub> O <sub>4</sub>				<u>MRI contrast properties</u>	[440]
Fe <sub>3</sub> O <sub>4</sub> @Bio-MOF-folic acid-chitosan conjugate (FC)	Bio-MOF Curcumin as organic ligand and Zn <sup>2+</sup> as metal ion	Fe <sub>3</sub> O <sub>4</sub>	5-FU (60 wt%)		MDA-MB-231	Theranostic applications, thanks to the MNPs <u>MRI contrast properties</u>	[441]

DOX@Fe@ZIF-8@gelatin methacryloyl (GelMA)	ZIF-8	Zinc ferrite and maghemite ( $\gamma$ -Fe <sub>2</sub> O <sub>3</sub> )	DOX	1-2 Hz, 12 Hz	MDA MB-231	<u>Magnetic field targeted delivery</u>	[442]
Fe@ZIF-8@GOx(glucose oxidase) nanoreactors	ZIF-8	Fe	GoX (12.15 wt%)		Hela	<u>MF-enhance cellular targeting and reactive oxygen species production for combined GoX activity</u>	[443]
Fe <sub>3</sub> O <sub>4</sub> @ALA(Amino levulinic Acid)-Zn MOF	ALA-Zn MOF	Fe <sub>3</sub> O <sub>4</sub>			C6 cancer cells	<u>MRI contrast properties</u>	[444]
PEGylated UiO-66(Zr)-(COOH) <sub>2</sub>	UiO-66(Zr)-(COOH) <sub>2</sub>	Mn <sup>+2</sup>	DOX		4T1 breast cancer cells	<u>MRI contrast properties</u>	[445]
Fe <sub>3</sub> O <sub>4</sub> @ MIL-88B-NH <sub>2</sub> MOF	MIL-88B-NH <sub>2</sub> MOF	Fe <sub>3</sub> O <sub>4</sub>	Mertansine (DM1) (33 wt%)	Two AMF exposure cycles (27.3 mT, 250 kHz), each of 10 min separated by 4 hours	U251 glioblastoma cells	<u>MF-induced cargo release</u>	[415]

In 2011, Ke *et al.* did a proof-of-concept study to fabricate MNPs-based MOF nanocomposites for drug delivery applications. In their study, they synthesized Fe<sub>3</sub>O<sub>4</sub>@HKUST-1 nanocomposites that were loaded with up to 20 wt% of nimesulide. The nanocomposites were attracted to a magnetic put near their glass bottle within 20s that could indicate their amenability to be used for targeted drug delivery applications. No MF-induced drug release experiments were done in their study; however, the nanocomposites were able to offer extended drug release up to 11 days at 37°C in physiological saline. The authors recommended the use of other more biocompatible MOF types instead of their used copper-based HKUST-1 which could pose physiological toxicity problems [430].

Afterwards in 2014, Zhuang *et al.* developed MNPs@MOFs nanocomposites based on the more biocompatible ZIF-8. The synthesized fluorescein-loaded Fe<sub>3</sub>O<sub>4</sub>@ZIF-8 nanocomposites were able to migrate to the vial side following an externally applied MF [431].

The magnetic contrast properties were also proved in the study of Bian *et al.*, who developed DOX-loaded Fe<sub>3</sub>O<sub>4</sub>@polyacrylic acid/gold nanoclusters/ZIF-8 nanocomposites (Fe<sub>3</sub>O<sub>4</sub>@PAA/AuNCs/ZIF-8 NPs) as a theranostic platform for tri-modal imaging (magnetic resonance, computed X-ray tomography and fluorescence imaging) and pH-responsive release [432].

In 2016, Fang *et al.* reported MF-induced cargo release from MNPs@MOFs nanocomposites. The nanocomposites platform had an average particle size of 64 nm (Figures 26A and B) and consisted of 12 nm superparamagnetic  $\text{Fe}_3\text{O}_4$  nanoparticles as magnetic core and ZIF-90 as MOF shell ( $\text{Fe}_3\text{O}_4$ @ZIF-90) (Figure 26C). Coating with rat serum albumin (RSA) resulted in a stable suspension of nanocomposites with a 99 nm hydrodynamic size. Small but elastic pores of the ZIF-90 and their RSA coating contributed to the slow extended 5-FU cargo diffusion and release, where 80% of the 5-FU cargo were released in 40 hours during *in vitro* in PBS solution. In contrast, exposure to extremely low frequency AMF (ELF-AMF) (20 Hz and 20 mT) for 20 min each 1 hour accelerated the *in vitro* release rate of the 5-FU release rate to 80% in only 7 hours in PBS (Figures 26D and E) [433].

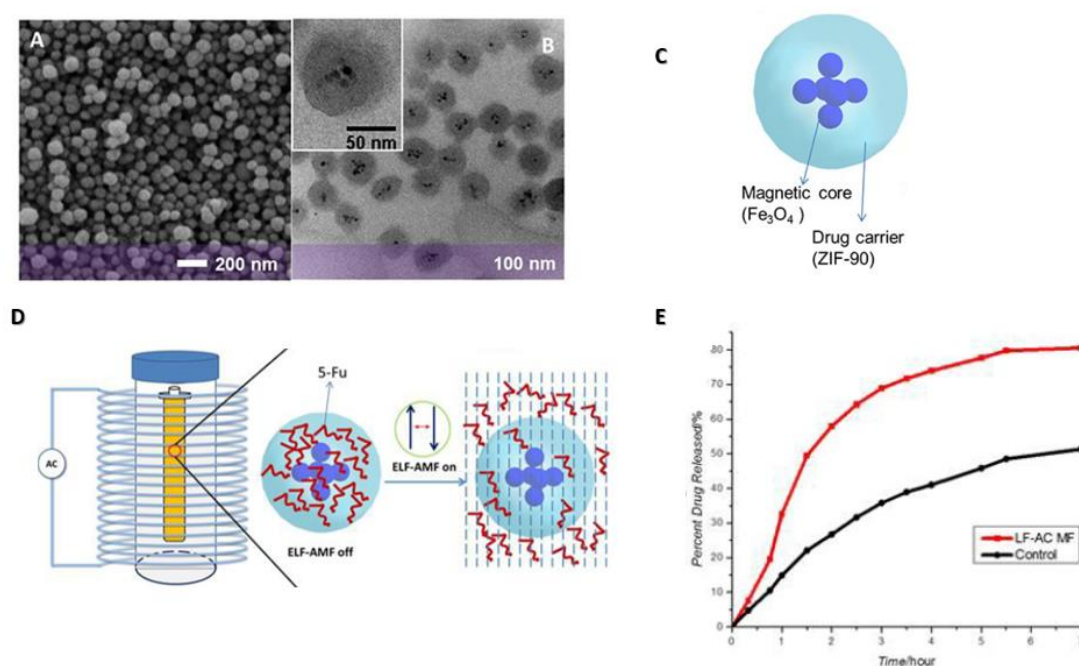


Figure 26: A) SEM and B) TEM images of  $\text{Fe}_3\text{O}_4$ @ZIF-90. C) Schematic illustration of  $\text{Fe}_3\text{O}_4$ @ZIF-90 nanocarrier composition. D) Schematic illustration of 5-FU MF-induced release from under the non-heating ELF-AMF. E) 5-FU release profile from  $\text{Fe}_3\text{O}_4$ @ZIF-90 with and without ELF-AMF. Adapted from [433].

Attia *et al.* developed magnetic MOF nanocomposites platform composed of  $\text{Fe}_3\text{O}_4$  MNPs conjugated with MIL-88B- $\text{NH}_2$  MOFs and loaded with Mertansine (DM1) against glioblastoma cancer cells. The synthesized nanocomposites had an average particle size of 117 nm and showed 33 wt% DM1 loading contents. Two AMF exposure cycles (27.3 mT, 250 kHz), each of 10 min separated by 4 hours, enhanced the cellular killing effect of the drug-loaded nanocomposites (33.9 nM equivalent DM1 concentration) on U251 glioblastoma cells demonstrated by lower  $\approx 40\%$  cell viability compared to  $\approx 65\%$  upon incubation with the same concentration of the nanocomposites but without AMF exposure. The same two AMF exposure cycles at the same concentration of drug-free nanocomposites

were biocompatible ( $\approx 100\%$  viability) on U251 glioblastoma cells. Consequently, the enhanced killing effect of the drug-loaded nanocomposites upon AMF exposure could be related to local temperature increase inside the nanocomposites that induced the anticancer drug cargo release [415]. It is worth noting that high ( $\approx 80\%$ ) cell viability was observed after AMF exposure upon using lower concentrations ( $< 33.9$  nM equivalent DM1 concentration) of drug-loaded nanocomposites. This reduced efficiency at lower nanocomposites concentrations could be due to the insufficient “non-toxic” released drug amount that could be attributed to the presence of less intracellular nanocomposites at lower concentration. On the other hand, higher concentrations ( $> 33.9$  nM equivalent DM1 concentration) of drug-loaded nanocomposites caused less than 40% of cell viability with no significant enhanced toxicity upon AMF exposure. This could be attributed to the non-controlled cargo release that was efficient to induce high cellular toxicity with no additional benefit for releasing more cargo using AMF. These results indicate the importance of achieving high enough nanocomposites intracellular concentrations for having sufficient drug cargo released amounts after the stimulus-induced release. In addition, it could highlight the importance of the nanocomposites stability and/or coating to mitigate the non-controlled cargo release.

### III.8. Conclusions

MOFs are promising systems for anticancer drug delivery applications due to their tunable properties that could enable synthesizing MOFs with high drug loading capacities and biocompatibility. Choosing appropriate coating could mitigate their colloidal instability and premature cargo release. Moreover, their controlled on-demand cargo release could be achieved through stimuli-sensitive properties. MNPs-based MOFs could provide additional advantages for anticancer applications such as MF-directed accumulation into the tumor tissues, allowing better spatiotemporal control, and enabled magnetic contrast agent properties for theranostic applications. Though some types of nano-MOFs have already been produced on a large (ton) scale by BASF SE through water-based synthesis [446], additional research efforts would be needed for the multicomponent stimuli-responsive nanoMOFs (as MNPs-based ones). Also, sufficient intratumoral/intracellular concentration of MOFs should be achieved to enable the release of enough drug cargo for inducing anticancer activity. However, such high local MOF concentrations could require high administered dose that could display toxic side effects. So that, smart design and achieving a balance between the synthesis feasibility, scaling up, high loading capacity, minimal premature/non-controlled cargo release, biocompatibility and efficient stimuli-responsive cargo release would be needed to develop a safe and efficient MOF-based stimuli-responsive delivery system. By overcoming such difficulties, the translation of MOFs from basic studies to clinical applications could be achieved in the future.

## Part IV. Pancreatic tumor treatment using magnetic stimulus-responsive drug delivery systems

Pancreatic cancers can be categorized into two groups: exocrine and endocrine tumors; among them, the exocrine pancreatic ductal adenocarcinoma (PDAC) accounts for over 90 % of pancreatic malignancies [447].

PDAC is one of the most devastating cancer malignancies, with an overall five years survival rate of 9.3% that even drops to 3% at advanced stages upon metastasizing [448, 449]. Due to its aggressive nature, its median survival rate is reported to be 5-6 months [450]. These data demonstrate the dismal prognosis of the disease, where half of the newly diagnosed patients with PDAC would not live more than six months, and most of them ( $\approx 90\%$ ) would not live more than five years. Worldwide in 2020, there were 496,000 reported cases of PDAC and almost the same number, 466,000, of deaths, and it was the seventh leading cause of cancer deaths [1]. PDAC has the highest incidence in Europe, North America and Australia/New Zealand, and it is even projected to be the third leading cause of cancer deaths in Europe by 2025 [451].

### IV.1. PDAC development and its treatment challenges

PDAC progression is characterized by multiple genetic alterations that trigger its progression from normal epithelium “mainly acinar cells” to ductal preneoplastic lesions, called PanIN, and invasive ductal adenocarcinoma [452]. The activation of the *KRAS* oncogene is one example of genetic alterations that occur in nearly 92 % of PDAC patients. The mutationally activated *KRAS* gene leads to the production of abnormal constitutively active RAS protein that results in uncontrolled activation of cellular proliferation and survival pathways [453, 454]. In addition, PDAC is also characterized by frequent inactivation of tumor suppressor genes such as *CDKN2A* (90%), *TP53* (70%) and *SMAD4* (55%) [447]. For instance, *CDKN2A* inactivation leads to loss of p16 protein, a master negative regulator of the G1-to-S cell cycle transition, resulting in uncontrolled stimulation of cellular proliferation [455]. *TP53* inactivation allows the cell to bypass important cellular checkpoints at the DNA damage level and apoptosis triggering [456]. Finally, losing *SMAD4* gene leads to aberrant signaling by the growth factor TGF- $\beta$  (transforming growth factor- $\beta$ ) [455]. An average of 63 genetic aberrations over 12 functional pathways were observed in the majority of PDAC cases [457]. This significant genomic heterogeneity makes developing tailored genetic treatment quite challenging.

The dense fibrotic desmoplastic stroma is a defining hallmark of PDAC (Figure 27), and it can occupy up to 85% of the total tumor mass [263]. This stroma formation is initiated as a defense mechanism against the malignant transformation of the ductal epithelium in a trial to limit the tumor

progression and invasion [263, 458]. However, the tumor cells produce growth factors and cytokines that interact with the stromal cells (such as fibroblasts and macrophages) to alter their biological properties and promote the tumor progression, invasion and therapeutic resistance.

So that, the PDAC stroma is composed of reactive stromal cells such as proliferated activated fibroblasts, called CAF (cancer-associated fibroblasts), along with high deposition of extracellular matrix components such as hyaluronic acid, collagen, fibronectin and laminin [263]. Due to its barrier characteristics, this dense stroma also limits the diffusion of therapeutic or imaging agents inside the tumor mass [459]. In addition, the high density of the extracellular matrix leads to compression of the blood vessels and a subsequent increase in the interstitial fluid pressure (IFP), further exacerbating the diffusion of therapeutic or imaging agents [460, 461]. Moreover, the hypo-vascularization and decreased blood perfusion lead to pathophysiological events such as hypoxia and acidic pH that change the tumor's metabolic profile and lead to activation of intrinsic cell pathways of therapeutic resistance [462-464].

Additionally, the PDAC stroma is characterized by infiltration of immune suppressive cells, such as regulatory T cells and the protumoral M2 type macrophages, along with the production of immunosuppressive cytokines and lymphokines making the PDAC immunologically "cold" tumor [263, 465]. So that PDAC is a very challenging disease to treat, and its current treatment options are broadly insufficient.

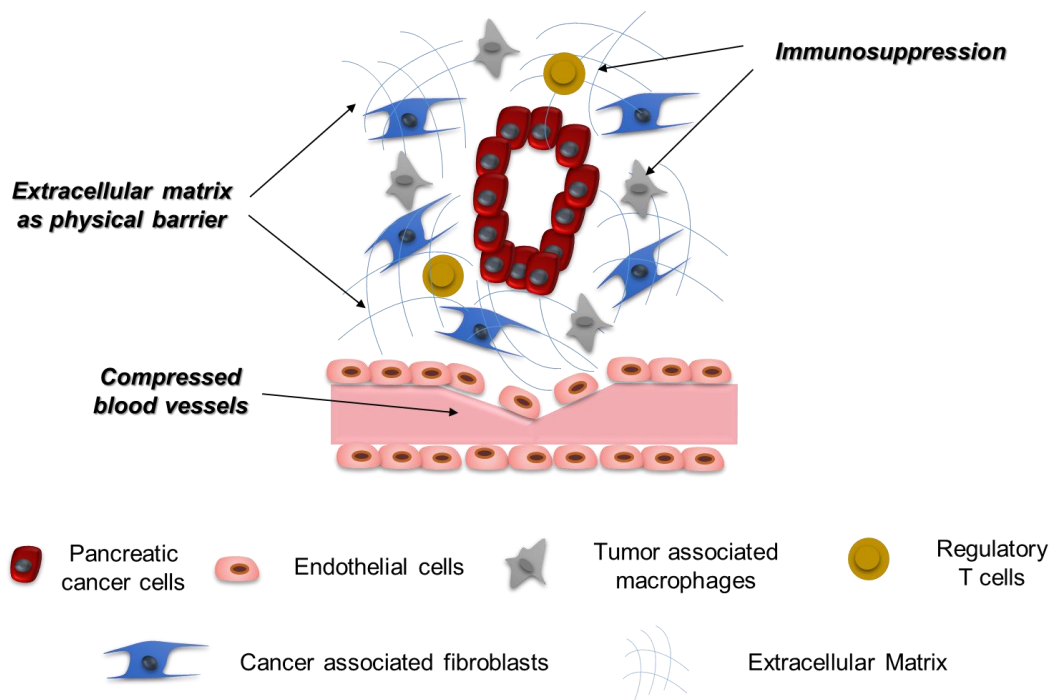


Figure 27: Key features of PDAC microenvironment as extracellular matrix deposition, compresses blood vessels and limited EPR effect as well as infiltration of immunosuppressive cells.

## IV.2. PDAC stages and their standard of care treatment options

### Resectable PDAC stage

The surgery is applied for patients with resectable tumor i.e, the tumor mass is localized inside the pancreas or extended out of the pancreas but without major contact with a major blood vessel [466]. Only ≈15-20% of PDAC patients are diagnosed at this early stage of the disease, and they usually receive adjuvant chemotherapy, such as gemcitabine, after the surgery [466]. However, almost a quarter of PDAC patients diagnosed with resectable tumors are found to have metastasis during the surgery, and 85% of the patients had tumor recurrence after the surgery [466, 467]. The five years survival rate of patients at this stage is ≈ 30%, with 26 months of median survival [466].

### Borderline PDAC stage “resectable/locally advanced unresectable tumor”

Another 20% of PDAC patients are diagnosed at a borderline stage of resectable/locally advanced unresectable tumor [468]. At this stage, the tumor mass is extended out of the pancreas with involvement of a major blood vessel that makes the tumor practically unresectable despite its localized nature [468]. The standard care for those patients starts with using FOLFIRINOX regime (5-fluorouracil with leucovorin, irinotecan, and oxaliplatin) as a neoadjuvant chemotherapy to limit the tumor mass [468]. The FOLFIRINOX treatment can convert ≈60% of these patients to the resectable stage with a higher potential for curative surgery [469]. The FOLFIRINOX multidrug regimen have the advantage of less potential for developing drug resistance compared to using single therapeutic agent. However, FOLFIRINOX is associated with severe systemic side effects and even the majority of treated patients still develop recurrent tumors after the surgery [468, 469]. At this stage, PDAC patients have five years survival rate of ≈ 13% with 22.2 months of median survival [468, 469].

### Metastatic PDAC

A larger percentage, 45-55% of PDAC patients, are diagnosed at the metastatic phase, where the tumor is spread to other normal organs [466]. There is an extremely poor prognosis at this stage, with a five-year survival of 3% [466]. Patients at this stage receive systemic chemotherapeutic treatment where the first line treatment option is FOLFIRINOX, or gemcitabine +/- Abraxane® (nab-paclitaxel), which still yield a mediocre median overall survival of 8-12 months [470, 471].

Abraxane® (nab-paclitaxel) is nanoparticles formulation of human albumin-bound paclitaxel that was approved by FDA for PDAC treatment in combination with gemcitabine [472]. The albumin-based (surfactant free) formulation of paclitaxel enhanced its delivery to the tumor tissues as well as alleviated the infusion adverse reaction compared to the previously developed chromophore(surfactant)-based formulation[473]. The enhanced tumor delivery could be attributed

to the facilitated albumin endothelial transport via the gp60 albumin receptor/caveolin-1 pathway [473, 474]. Alvarez *et al.* observed marked disorganized collagen and low CAF density in residual tumors of patients treated with nab-paclitaxel/gemcitabine combination. These observations were not noticed in patients who received conventional chemo-radiation treatment, suggesting a role of nab-paclitaxel in PDAC stroma barrier distortion[475].

Also, a nano-liposomal formulation of irinotecan (Onivyde®) has been also approved by FDA for PDAC treatment in combination with 5-FU and folinic acid [476]. This treatment is used as a second-line therapy for patients who did not respond to the gemcitabine-based therapy [476]. The PEGylated liposomal formulation of irinotecan enhanced its pharmacokinetic behavior in female Sprague-Dawley rats with better metabolic stability, slower clearance and thus longer half-life ( $\approx 10.7$  hours compared to  $\approx 0.27$  hours for the free drug) that could participate in increased accumulation to tumor site [477]. In addition, the liposomal formulation also decreased the irinotecan systemic toxicity, where it was tolerated *in vivo* in normal Swiss Webster mice up to 324 mg irinotecan/kg after i.v. administration compared to a maximum tolerated dose of 80 mg/kg for the free drug [476]. Therefore, the liposomal irinotecan formulation achieved better pharmacodynamics and therapeutic efficacy than the free drug in many mice tumor xenograft models [477, 478]. In the phase 3 NAPOLI-1 clinical trial, the nano-liposomal irinotecan, in addition to 5-FU and folinic acid, enhanced the patients' median overall survival by two months compared to the 5-FU and folinic acid treatment [476]. However, this improved median overall survival was still as low as 6.2 months [476].

These data demonstrate the huge challenge in PDAC treatment at all stages of the disease. Even the approved nanoparticle-based formulations, with their enhanced pharmacokinetics and pharmacodynamics compared to the conventional chemotherapeutic treatments, seem to have only a marginal enhancement in the therapeutic outcomes in PDAC patients [479]. The PDAC dense stroma, increased IFP, compressed blood vessels and impaired tissue perfusion made relying on the EPR effect for enhancing the nanoparticles' tumor accumulation generally insufficient [479, 480]. The nanoparticles are usually trapped in the perivascular area of the PDAC tumors with limited intratumoral diffusion and low drug levels in the tumor cells [480]. In nude mice bearing human pancreatic tumor subcutaneous xenografts (BxPC3 cells), it was reported that only the small 30 nm polymeric micelles were able to penetrate through the tumor mass and achieve therapeutic antitumor effect after their i.v. injection [480]. The larger particles of 50, 70 or 100 nm were only able to penetrate upon enhancing the tumor permeability using TGF- $\beta$  inhibitor [480]. These results could justify the limited marginal improvement in PDAC treatment upon using the nab-paclitaxel (130 nm) and nano-liposomal formulation of irinotecan (110 nm) [472, 476].

Hence, novel treatment approaches are essentially needed to tackle the PDAC treatment challenges and achieve better therapeutic outcomes.

### IV.3. New PDAC treatment strategies

Several treatment strategies have been developed, such as tumor stroma modulation, targeting the PDAC stem cells, targeting the PDAC immune cells and tailoring the nanoparticles delivery system properties.

#### IV.3.1. PDAC stroma modulation

Modulation of stromal and/or vascular barriers of PDAC tumors have been proposed to enhance the tumor accumulation and penetration of therapeutic and imaging agents.

The PEGylated human recombinant hyaluronidase PH20 (PEGPH20) and the sonic hedgehog (SHH) inhibitor (IPI-926) are two examples of stroma-affecting agents that were used against PDAC clinical trials [481, 482]. PEGPH20 depletes hyaluronic acid in the PDAC stroma, decreasing the IFP and improving the vasculature [481]. It was combined with gemcitabine and nab-paclitaxel to treat metastatic PDAC patients in phase III clinical trials [481]. IPI-926 inhibits the upregulated SHH signaling in stromal fibroblasts, preventing their activation and the subsequent increased matrix deposition [482]. It was used in combination with gemcitabine in phase II clinical trials [482]. The clinical use of PEGPH20 and IPI-926 was halted due to disappointing results related to no improvement in the median overall survival of patients [481, 482].

Diminishing the protective role of the stroma through its depletion could lead to enhanced proliferation of aggressive and metastatic tumor cells. For instance, Lee *et al.* observed that decreasing desmoplasia through genetic or pharmacological inhibition of SHH in PDAC murine models resulted in accelerated tumor progression and metastasis [483]. To this end, the use of stromal modulating agents should be realized with caution to slightly decrease the stroma stiffness, which could be dose-dependent according to the patient status, accompanied by the use of high doses of potent chemotherapies and/or radiotherapy to kill the tumor cells efficiently.

For instance, losartan was used in combination with FOLFIRINOX and radiation for treatment of the borderline resectable/locally advanced PDAC patients in phase II clinical trial [484]. Losartan as TGF- $\beta$ 1 inhibitor results in decreased stromal collagen and hyaluronic acid production associated with decreased CAF activation resulting in reduced solid stress and enhanced vascular perfusion [484, 485]. The losartan use, in addition to FOLFIRINOX and radiation, resulted in downstaging of the resectable/locally advanced PDAC patients into resectable phase with 61% of negative tumor margin

after surgical removal [484]. However, high chemotherapeutic doses and radiation could have severe side effects. For instance, FOLFIRINOX is reserved for use in patients with good performance status, limiting its wide applicability [484].

#### *IV.3.2. Targeting PDAC stem cells*

Another strategy to fight against PDAC is to target pancreatic cancer stem cells (PCSCs). Chemotherapy resistance and tumor recurrence after treatment are major challenges in PDAC treatment. It was observed that a small subpopulation (1%-5%) of tumor cells, called PCSCs, have high tumorigenic potential and are responsible for the therapeutic resistance, disease progression and tumor relapse after treatment [486, 487]. It was demonstrated that although the tumor size could diminish during treatment with conventional chemotherapy, the presence of PCSCs cells in the tumor significantly increases [488]. For instance, the gemcitabine treatment (biweekly 125 mg/kg i.p. for 3 weeks) in orthotopic L3.6pl pancreatic tumor xenograft-bearing mice resulted in a significant reduction of the tumor size compared to the vehicle ( $100.5 \pm 36.4$  vs.  $183.8 \pm 66.9$  mm<sup>3</sup>;  $p < 0.05$ ). However, the PCSCs percentage in the tumors was increased from  $\approx 1.25$  % to  $\approx 6.5$  %, highlighting the resistance properties of these cell subpopulations and the need to eradicate and/or target them [488].

Targeting PCSCs can be achieved through targeting the stem cells' associated signaling pathways, such as mTOR, Notch, Hedgehog and wingless-related integration sites. Several PCSCs targeted therapeutics have been developed and investigated in clinical trials against PDAC [489]. However, they have limited positive therapeutic outcomes, which could be due to the heterogeneous nature of the PCSCs and their ability to escape inhibition [489].

#### *IV.3.3. Targeting the PDAC immune cells*

PDAC is characterized by an immunosuppressive tumor microenvironment that participates in tumor progression and invasion. Several traditional cancer immunotherapy approaches, such as immune checkpoint inhibitors, CAR T cells or humanized antitumor antibodies, have been developed against PDAC and were investigated in clinical trials [490]. However, they failed to show promising results that could be related to the tumor ability to elaborate genetic changes to bypass the immune system [490]. These genetic adaptations could happen in several steps and ultimately maintain the immunosuppressive microenvironment in PDAC.

For instance, the first step in the cancer immunity cycle is identifying and capturing the generated tumor-specific antigens or tumor-associated antigens by the antigen-presenting cells (APCs)

[491]. Genetic modifications could happen to curb the APCs ability to detect the produced antigens, or the APCs could treat them as self-molecules. Also, the step of APCs processing for the antigens and their presentation in the form of MHC class I or II to the T cells could be interrupted. Finally, even if the T cells were activated to cytotoxic T cells (CTLs) they find themselves in a highly immunosuppressive environment that could result in their deactivation [492].

In order to address the aforementioned challenges, a multimodal therapeutic approach was proposed [490]. For instance, this novel strategy is currently being investigated in an open-label, multicenter, randomized umbrella phase Ib/II study (NCT03193190) to treat patients with metastatic PDAC [493]. The study aims to test the safety and efficacy of multiple immunotherapies combinations, and some treatment groups also have GEM/nab-paclitaxel chemotherapy in addition to the immunotherapy treatment [493]. The used immuno-therapies combinations are based on the monoclonal antibody (mAb) atezolizumab that acts as an immune checkpoint inhibitor through its anti-programmed death ligand 1 (anti-PD-L1) effect, thus preventing the cancer cells from suppressing the immune system [494]. In addition to the atezolizumab, the study investigates adding either of the following immune therapies; selicrelumab (CD40 agonist), bevacizumab (antiangiogenic mAb), AB928 (highly selective adenosine receptors (A<sub>2A</sub> and A<sub>2B</sub>) antagonist), tiragolumab (immune checkpoint inhibitor) or tocilizumab (autophagy inhibitor) [493].

The promise of this immunotherapies combination strategy is to decrease the tumor ability to escape the immune system through elaborate mutation [490]. However, the desmoplastic fibrotic stroma nature in PDAC with its high IFP and vascular dysfunction could mitigate their delivery and accumulation in the tumor tissues. To this end, the nanomedicine formulations could provide a promising alternative to overcome PDAC treatment challenges.

#### *IV.3.4. Tailoring the nanomedicine formulations properties*

Nanomedicine formulations with tailored properties for PDAC treatment have been developed. They could rely on transcytosis (using targeted peptides) or stimuli-responsive properties.

##### Transcytosis

Transcytosis is a process that includes the transfer of a molecule from one side of the cell to the other side, and it usually involves endocytosis, vesicle transfer and exocytosis. One formulation based on this concept is nanoparticles conjugated with the cyclic tumor penetrating peptide iRGD to target integrins  $\alpha_v\beta_{3/5}$  to deliver therapeutics to pancreatic cancers. These integrins are upregulated in angiogenic endothelial, tumor and stroma cells. In addition, the proteolytically activated iRGD binds to

the neuropilin-1 receptor inducing vascular transcytosis that could facilitate the targeted nanomedicines intratumoral accumulation.

For instance, Liu *et al.* developed lipid-coated mesoporous silica nanoparticles (silicasome) of  $\approx 130$  nm hydrodynamic diameter embedded with a 10 nm gold core and loaded with irinotecan [495]. Upon the silicasome i.v. co-administration with free iRGD, there was  $\approx 4$ -fold increase in their accumulation in the KPC-derived “from  $Kras^{LSL-G12D/+}Trp^{53LSL-R172H/+}Pdx1-Cre$  transgenic mouse” orthotopic PDAC tumor sites with enhanced efficacy in the primary and metastatic sites [495]. Using the TEM, the authors observed grouped vesicles in the PDAC endothelial cells carrying the GNP-labeled silicasomes from the blood vessel lumen side to the PDAC matrix side (Figure 28). It is worth noting that the authors' use of iRGD conjugated-silicasomes did not enhance the silicasomes tumor accumulation [495]. So that better understanding of the reason for this difference between the conjugated vs. co-administered iRGD in the PDAC tumor microenvironment could clarify its potential for clinical translation. It is reported that blood vessels in PDAC tumors are compressed, which could result in faster blood flow and not enough time for receptor recognition and binding.

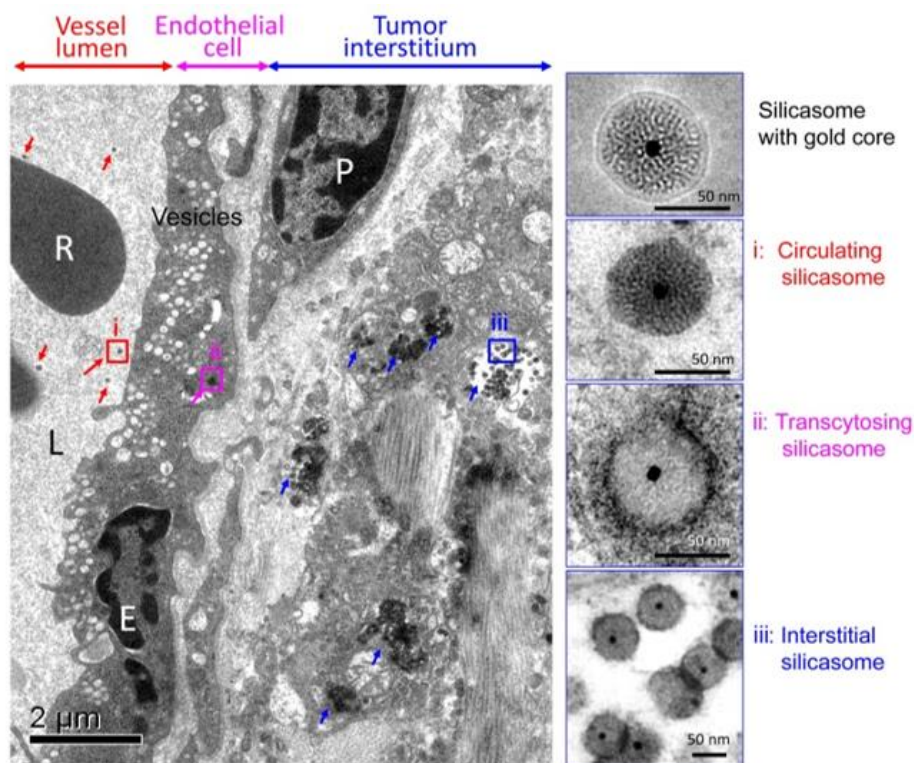


Figure 28: TEM visualization of GNP-labeled silicasomes transcytosis, upon i.v. co-administration with free iRGD, in KPC-derived orthotopic PDAC tumor-bearing mice. Adapted from [495].

### Stimuli-responsive nanomedicines

Another strategy is to exploit the stimuli-responsive nanomedicines to tackle the PDAC tumor microenvironment challenges.

For instance, Li *et al.* developed smart nanoparticles superstructure with ultrasensitive pH size switchable properties for enhanced tumor penetration and accumulation [496]. The nanoparticles were composed of an assembly of amphiphilic polymer (platinum prodrug conjugated with polyamidoamine (PAMAM) dendrimer) that has a pH-responsive tertiary amine group. The nanoparticles had an initial ~80 nm size in PBS (pH ~7.4), and upon reducing the pH to ~6.7, it underwent, within seconds, dramatic size reduction due to structure dissociation to its dendrimers building blocks of less than 10 nm. The nanoparticles' penetration ability was investigated after their labeling with cyanine5 (Cy5) and their incubation for 4h with 3D spheroids of BxPC-3 cells. Using the confocal laser scanning microscope, the Cy5 was detected at a distance of 85  $\mu\text{m}$  from the spheroid's surface upon using the culture medium of pH = 6.7. This penetration was not observed neither upon using a medium of pH = 7.4, nor for non-pH sensitive nanoparticles counterparts, where dramatic Cy5 fluorescence intensity drop happened at 25  $\mu\text{m}$  from the spheroid surface. Tail vein injection of the pH-sensitive nanoparticles (2 mg/kg equivalent dose of cisplatin, three doses at days 16, 19, 22 after tumor cell implantation) in BxPC-3 tumor xenograft-bearing nude mice resulted in 82% of tumor growth suppression after 21 days of first injection, compared to only 41% and 24% for equivalent doses of the non pH-sensitive nanoparticles counterpart and cisplatin, respectively [496]. This strategy has the advantages of having rapid responsiveness within a low pH range (~0.7) and its ability to enhance tumor penetration and tumor growth inhibition in the poorly permeable pancreatic tumor xenograft model. However, it could not be a suitable strategy for a wide range of drugs due to the complexity of the preparation of such a dendrimer-based delivery system [497].

Another strategy is to use magnetic hyperthermia and IONPs (their advantages in cancer treatment were comprehensively discussed in Parts I and II). Specifically in the context of pancreatic tumors, this technique could be particularly advantageous due to the reported hyperthermia-induced immunological cell death as well as the MNP magnetic contrast imaging properties.

For instance, Boela *et al.* reported increased expression of calreticulin (immunogenic cell death biomarker) in the plasma membrane of tumor cells, in MiaPaCa-2 subcutaneous pancreatic tumor xenograft model in nude mice, after intratumoral injection of PMAO polymer coated IONPs (11 nm core size) and exposure to AMF ( $f = 196$  kHz and  $H = 26$  kA/m) [498]. The injected IONP dose was 0.15 mg Fe/tumor, and the animals had 3 AMF exposures of 30 min each (one on the day of injection and the two others on the two following days). After euthanizing the animals 20 days after the IONP

injection, extracting the tumors and dissociating them to the tumor cells, ~80% of the tumor cells had calreticulin expression at their surface compared to only ~15% of the cells in the control animal group without IONP injection nor AMF exposure. Interestingly, it was noticed that 55% of tumor cells in the control group injected with IONPs but without AMF exposure showed surface calreticulin expression [498].

In addition, the MNPs can also be utilized as a part of a drug delivery system to enable stimuli (magnetic) responsive antitumor cargo release for enhanced efficacy against pancreatic tumors. For instance, Kim *et al.* developed a magnetic-based nanocomposites delivery system for chemohyperthermia treatment of pancreatic tumors [499]. The temperature-responsive delivery system composed of MNP cluster core ( $59 \pm 6$  nm) inside a porous silica shell ( $18 \pm 2$  nm). These nanocomposites were coated with a temperature-sensitive coat of hydroxypropyl cellulose (HPC) and loaded with gemcitabine (20 wt%). The HPC polymer has LCST at  $41^\circ\text{C}$ , so that heating a few degrees above the body temperature can induce the HPC polymer coat collapse triggering the diffusion of the gemcitabine drug load. *In vitro* in PBS solution of pH 7.2, more rapid gemcitabine release was observed at  $45^\circ\text{C}$  compared to  $37^\circ\text{C}$ , where cumulative drug release percentages of 37% and 8%, respectively, were observed after 180 min. The heating was induced by MF exposure (199 kHz, 75 Oe) for one h. The bare “non-HPC” coated nanocomposites showed a more rapid gemcitabine release but in a non-responsive way to the temperature increase. On PANC-1 cells, enhanced cell killing was observed after exposure to AMF (199 kHz, 17.5 mT) for 30 min, where 21% and 12% cell viabilities were observed upon heating to  $42^\circ\text{C}$  and  $45^\circ\text{C}$ , respectively. These achieved decreased cell viabilities were  $>30\%$  compared to hyperthermia or nanocomposites alone. Enhanced antitumor effect was also observed *in vivo* on PANC-1 subcutaneous xenograft nude mice model. The direct tumor injection of the nanocomposites followed by AMF exposure (199 kHz, 17.5 mT) for 30 min resulted in an increased tumor apoptotic area of 38% compared to only 14.7% and 17.5% for the hyperthermia-only or nanocomposites-only tumor groups ( $P > 0.05$ ) [499].

#### IV.4. Conclusions

PDAC is one of the most aggressive and challenging tumor types. The standard treatment approaches, including surgery, radiation and chemotherapy, showed limited unsatisfactory improvement in patients' prognosis. In clinical trials, immunotherapies and molecularly targeted therapies did not show effective responses yet. Consequently, novel treatment approaches are essentially needed to fight against PDAC and achieve better therapeutic outcomes. The unique multifunctionality of the MNPs-based drug delivery system makes it a very interesting tool for fighting

against PDAC. Their MF-responsive properties can be utilized to guide the delivery system under static MF gradient for preferential accumulation in the primary tumor mass. This technique could be worth investigating to assess its ability to overcome the PDAC stroma physical barrier challenge. Afterward, MF inducing MNP hyperthermia or mechanical movement could induce controlled chemotherapeutic cargo release locally in the cancer tissues. Proper choice of MF-based drug delivery system could enable having biocompatibility and high drug loading capacities. Also, using drug load/s that could not only kill the tumor cells and normalize the PDAC microenvironment but also induce protumoral response could help in fighting against metastatic tumor masses beside the primary one. Finally, the MNP contrast properties can be exploited for MRI or MPI imaging, providing a valuable theranostic tool for simultaneous imaging and monitoring during the treatment.

## V. References

1. Sung, H., et al., *Global Cancer Statistics 2020: GLOBOCAN Estimates of Incidence and Mortality Worldwide for 36 Cancers in 185 Countries*. CA: A Cancer Journal for Clinicians, 2021. **71**(3): p. 209-249.
2. (WHO), W.H.O., *Global Health Estimates 2020: Deaths by Cause, Age, Sex, by Country and by Region, 2000-2019*. WHO; 2020. Accessed December 11, 2020. [who.int/data/gho/data/themes/mortality-and-global-health-estimates/ghes-leading-causes-of-death](https://www.who.int/data/gho/data/themes/mortality-and-global-health-estimates/ghes-leading-causes-of-death).
3. HO, B.N., C.M. PFEFFER, and A.T.K. SINGH, *Update on Nanotechnology-based Drug Delivery Systems in Cancer Treatment*. Anticancer Research, 2017. **37**(11): p. 5975-5981.
4. Eurostat, *Causes of death statistics, Major causes of death in the EU in 2020*; [https://ec.europa.eu/eurostat/statistics-explained/index.php?title=Causes\\_of\\_death\\_statistics#Major\\_causes\\_of\\_death\\_in\\_the\\_EU\\_in\\_2020](https://ec.europa.eu/eurostat/statistics-explained/index.php?title=Causes_of_death_statistics#Major_causes_of_death_in_the_EU_in_2020).
5. Dyba, T., et al., *The European cancer burden in 2020: Incidence and mortality estimates for 40 countries and 25 major cancers*. Eur J Cancer, 2021. **157**: p. 308-347.
6. Cooper, G.M., *The development and causes of cancer*. The cell: A molecular approach, 2000.
7. Tysnes, B.B. and R. Bjerkvig, *Cancer initiation and progression: Involvement of stem cells and the microenvironment*. Biochimica et Biophysica Acta (BBA) - Reviews on Cancer, 2007. **1775**(2): p. 283-297.
8. McGranahan, N. and C. Swanton, *Clonal Heterogeneity and Tumor Evolution: Past, Present, and the Future*. Cell, 2017. **168**(4): p. 613-628.
9. Nahleh, Z., N.S. Bhatti, and M. Mal, *How to reduce your cancer risk: mechanisms and myths*. International Journal of General Medicine, 2011. **4**: p. 277-287.
10. Debela, D.T., et al., *New approaches and procedures for cancer treatment: Current perspectives*. SAGE Open Medicine, 2021. **9**: p. 20503121211034366.
11. Kunovsky, L., et al., *The Use of Biomarkers in Early Diagnostics of Pancreatic Cancer*. Can J Gastroenterol Hepatol, 2018. **2018**: p. 5389820.
12. Lin, J., et al., *Nanomaterials Based on Functional Polymers for Sensitizing Cancer Radiotherapy*. Macromolecular Rapid Communications, 2022. **43**(18): p. 2200194.
13. Chu, D.-T., et al., *Recent Progress of Stem Cell Therapy in Cancer Treatment: Molecular Mechanisms and Potential Applications*. Cells, 2020. **9**(3): p. 563.
14. Miliotou, N.A. and C.L. Papadopoulou, *CAR T-cell Therapy: A New Era in Cancer Immunotherapy*. Current Pharmaceutical Biotechnology, 2018. **19**(1): p. 5-18.
15. Dolnikov, A., et al., *Stem Cell Approach to Generate Chimeric Antigen Receptor Modified Immune Effector Cells to Treat Cancer*. Blood, 2014. **124**(21): p. 2437-2437.
16. Iriguchi, S. and S. Kaneko, *Toward the development of true "off-the-shelf" synthetic T-cell immunotherapy*. Cancer Sci, 2019. **110**(1): p. 16-22.
17. Copelan, E.A., *Hematopoietic Stem-Cell Transplantation*. New England Journal of Medicine, 2006. **354**(17): p. 1813-1826.
18. FDA, *list of "Approved Cellular and Gene Therapy Products."* Current as of December 2022; <https://www.fda.gov/vaccines-blood-biologics/cellular-gene-therapy-products/approved-cellular-and-gene-therapy-products>.
19. Sarmiento-Ribeiro, A.B., et al., *The emergence of drug resistance to targeted cancer therapies: Clinical evidence*. Drug Resistance Updates, 2019. **47**: p. 100646.
20. Alexa-Stratulat, T., et al., *What sustains the multidrug resistance phenotype beyond ABC efflux transporters? Looking beyond the tip of the iceberg*. Drug Resistance Updates, 2019. **46**: p. 100643.
21. Martins, F., et al., *Adverse effects of immune-checkpoint inhibitors: epidemiology, management and surveillance*. Nature Reviews Clinical Oncology, 2019. **16**(9): p. 563-580.
22. O'Donnell, J.S., M.W.L. Teng, and M.J. Smyth, *Cancer immunoediting and resistance to T cell-based immunotherapy*. Nature Reviews Clinical Oncology, 2019. **16**(3): p. 151-167.

23. Haen, S.P., et al., *More Than Just Tumor Destruction: Immunomodulation by Thermal Ablation of Cancer*. *Clinical and Developmental Immunology*, 2011. **2011**: p. 160250.
24. Gage, A.A. and J. Baust, *Mechanisms of Tissue Injury in Cryosurgery*. *Cryobiology*, 1998. **37**(3): p. 171-186.
25. Ni, Y., et al., *A review of the general aspects of radiofrequency ablation*. *Abdominal Imaging*, 2005. **30**(4): p. 381-400.
26. Grauer, O., et al., *RTHP-22. INFLAMMATORY RESPONSE AFTER MODIFIED NANOTHERM AND RADIOTHERAPY OF RECURRENT GLIOBLASTOMA*. *Neuro-Oncology*, 2016. **18**(suppl\_6): p. vi178-vi179.
27. *MagForce U S A 2022 A Pivotal, Prospective, Three-Stage, Single-Arm Study of Focal Ablation of the Prostate With NanoTherm® Therapy System for a Limited-Volume, Clinically Localized, Intermediate-Risk Prostate Cancer*. Available from NLM identifier: NCT05010759 (<https://clinicaltrials.gov/ct2/show/NCT05010759>).
28. Maier-Hauff, K., et al., *Efficacy and safety of intratumoral thermotherapy using magnetic iron-oxide nanoparticles combined with external beam radiotherapy on patients with recurrent glioblastoma multiforme*. *Journal of neuro-oncology*, 2011. **103**: p. 317-324.
29. Feynman, R.P., *There's plenty of room at the bottom: An invitation to enter a new field of physics*. *Miniaturization*, Reinhold, 1961.
30. Sandhu, A., *Who invented nano?* *Nature Nanotechnology*, 2006. **1**(2): p. 87-87.
31. Ossa, D., *Quality Aspects of Nano-Based Medicines SME Workshop: Focus on Quality for Medicines Containing Chemical Entities London*. Available online at: [http://www.ema.europa.eu/docs/en\\_GB/document\\_library/Presentation/2014/04/WC500165444.pdf](http://www.ema.europa.eu/docs/en_GB/document_library/Presentation/2014/04/WC500165444.pdf). 2014.
32. Commission., E., *Commission Recommendation of 18 October 2011 on the definition of nanomaterial, 2011/696/EU. L275, 38–40 (Official Journal of the EU, 2011)*. <https://eur-lex.europa.eu/LexUriServ/LexUriServ.do?uri=OJ:L:2011:275:0038:0040:EN:PDF>. 2011.
33. U.S. FDA Guidance for Industry Considering Whether an FDA-Regulated Product Involves the Application of Nanotechnology, *U.S. Department of Health and Human Services*: <https://www.fda.gov/media/88423/download>. 2014.
34. Soares, S., et al., *Nanomedicine: Principles, Properties, and Regulatory Issues*. *Frontiers in Chemistry*, 2018. **6**.
35. Park, K., *Facing the Truth about Nanotechnology in Drug Delivery*. *ACS Nano*, 2013. **7**(9): p. 7442-7447.
36. Shan, X., et al., *Current approaches of nanomedicines in the market and various stage of clinical translation*. *Acta Pharmaceutica Sinica B*, 2022. **12**(7): p. 3028-3048.
37. Nikolakakis, I. and I. Partheniadis, *Self-Emulsifying Granules and Pellets: Composition and Formation Mechanisms for Instant or Controlled Release*. *Pharmaceutics*, 2017. **9**(4): p. 50.
38. Athar, M. and A.J. Das, *Therapeutic nanoparticles: State-of-the-art of nanomedicine*. *Adv. Mater. Rev*, 2014. **1**(1): p. 25-37.
39. Wang, Q., et al., *Multifunctional Shell–Core Nanoparticles for Treatment of Multidrug Resistance Hepatocellular Carcinoma*. *Advanced Functional Materials*, 2018. **28**(14): p. 1706124.
40. Zhu, Y.-X., et al., *Nanomedicines for combating multidrug resistance of cancer*. *WIREs Nanomedicine and Nanobiotechnology*, 2021. **13**(5): p. e1715.
41. Xue, X. and X.-J. Liang, *Overcoming drug efflux-based multidrug resistance in cancer with nanotechnology*. *Chinese Journal of Cancer*, 2012. **31**(2): p. 100-109.
42. Selby, L.I., et al., *Nanoescapology: progress toward understanding the endosomal escape of polymeric nanoparticles*. *Wiley Interdisciplinary Reviews: Nanomedicine and Nanobiotechnology*, 2017. **9**(5): p. e1452.
43. Lucien, F., R.R. Lavoie, and C.M. Dubois, *Targeting endosomal pH for cancer chemotherapy*. *Molecular & Cellular Oncology*, 2018. **5**(3): p. e1435184.

44. Ferdows, B.E., et al., *RNA cancer nanomedicine: nanotechnology-mediated RNA therapy*. *Nanoscale*, 2022. **14**(12): p. 4448-4455.
45. Krishnamachari, Y., et al., *Nanoparticle Delivery Systems in Cancer Vaccines*. *Pharmaceutical Research*, 2011. **28**(2): p. 215-236.
46. Mohapatra, A., S. Uthaman, and I.-K. Park, *External and Internal Stimuli-Responsive Metallic Nanotherapeutics for Enhanced Anticancer Therapy*. *Frontiers in Molecular Biosciences*, 2021. **7**.
47. Dennahy, I.S., et al., *Nanotheranostics for Image-Guided Cancer Treatment*. *Pharmaceutics*, 2022. **14**(5): p. 917.
48. Patra, J.K., et al., *Nano based drug delivery systems: recent developments and future prospects*. *Journal of Nanobiotechnology*, 2018. **16**(1): p. 71.
49. Riley, R.S. and E.S. Day, *Gold nanoparticle-mediated photothermal therapy: applications and opportunities for multimodal cancer treatment*. *Wiley Interdisciplinary Reviews: Nanomedicine and Nanobiotechnology*, 2017. **9**(4): p. e1449.
50. Wang, W., J. Wang, and Y. Ding, *Gold nanoparticle-conjugated nanomedicine: design, construction, and structure–efficacy relationship studies*. *Journal of Materials Chemistry B*, 2020. **8**(22): p. 4813-4830.
51. Casu, A., et al., *Controlled Synthesis of Gold Nanostars by Using a Zwitterionic Surfactant*. *Chemistry – A European Journal*, 2012. **18**(30): p. 9381-9390.
52. Beik, J., et al., *Gold nanoparticles in combinatorial cancer therapy strategies*. *Coordination Chemistry Reviews*, 2019. **387**: p. 299-324.
53. Kim, M. and S. Williams, *Daunorubicin and Cytarabine Liposome in Newly Diagnosed Therapy-Related Acute Myeloid Leukemia (AML) or AML With Myelodysplasia-Related Changes*. *Annals of Pharmacotherapy*, 2018. **52**(8): p. 792-800.
54. Zhang, L., et al., *Co-delivery of Docetaxel and Resveratrol by liposomes synergistically boosts antitumor efficiency against prostate cancer*. *European Journal of Pharmaceutical Sciences*, 2022. **174**: p. 106199.
55. Liu, P., G. Chen, and J. Zhang, *A Review of Liposomes as a Drug Delivery System: Current Status of Approved Products, Regulatory Environments, and Future Perspectives*. *Molecules*, 2022. **27**(4): p. 1372.
56. Fang, J., H. Nakamura, and H. Maeda, *The EPR effect: Unique features of tumor blood vessels for drug delivery, factors involved, and limitations and augmentation of the effect*. *Advanced Drug Delivery Reviews*, 2011. **63**(3): p. 136-151.
57. Matsumura, Y. and H. Maeda, *A New Concept for Macromolecular Therapeutics in Cancer Chemotherapy: Mechanism of Tumor-tropic Accumulation of Proteins and the Antitumor Agent Smancs*. *Cancer Research*, 1986. **46**(12 Part 1): p. 6387-6392.
58. Maeda, H., K. Tsukigawa, and J. Fang, *A Retrospective 30 Years After Discovery of the Enhanced Permeability and Retention Effect of Solid Tumors: Next-Generation Chemotherapeutics and Photodynamic Therapy—Problems, Solutions, and Prospects*. *Microcirculation*, 2016. **23**(3): p. 173-182.
59. Kommareddy, S., S.B. Tiwari, and M.M. Amiji, *Long-Circulating Polymeric Nanovectors for Tumor-Selective Gene Delivery*. *Technology in Cancer Research & Treatment*, 2005. **4**(6): p. 615-625.
60. Yuan, F., et al., *Vascular permeability in a human tumor xenograft: molecular size dependence and cutoff size*. *Cancer research*, 1995. **55**(17): p. 3752-3756.
61. Ikeda-Imafuku, M., et al., *Strategies to improve the EPR effect: A mechanistic perspective and clinical translation*. *Journal of Controlled Release*, 2022. **345**: p. 512-536.
62. Wisse, E., et al., *The size of endothelial fenestrae in human liver sinusoids: implications for hepatocyte-directed gene transfer*. *Gene Therapy*, 2008. **15**(17): p. 1193-1199.
63. Fam, S.Y., et al., *Stealth Coating of Nanoparticles in Drug-Delivery Systems*. *Nanomaterials*, 2020. **10**(4): p. 787.

64. Tang, Y., et al., *Overcoming the Reticuloendothelial System Barrier to Drug Delivery with a “Don’t-Eat-Us” Strategy*. ACS Nano, 2019. **13**(11): p. 13015-13026.
65. Kamerkar, S., et al., *Exosomes facilitate therapeutic targeting of oncogenic KRAS in pancreatic cancer*. Nature, 2017. **546**(7659): p. 498-503.
66. Soo Choi, H., et al., *Renal clearance of quantum dots*. Nat Biotech, 2007. **25**(10): p. 1165-1170.
67. Bartneck, M., et al., *Phagocytosis Independent Extracellular Nanoparticle Clearance by Human Immune Cells*. Nano Letters, 2010. **10**(1): p. 59-63.
68. Bewersdorff, T., et al., *The influence of shape and charge on protein corona composition in common gold nanostructures*. Materials Science and Engineering: C, 2020. **117**: p. 111270.
69. Rodríguez, F., et al., *Nano-Based Approved Pharmaceuticals for Cancer Treatment: Present and Future Challenges*. Biomolecules, 2022. **12**(6): p. 784.
70. Nirmala, M.J., et al., *Cancer nanomedicine: a review of nano-therapeutics and challenges ahead*. RSC advances, 2023. **13**(13): p. 8606-8629.
71. Barenholz, Y., *Doxil® — The first FDA-approved nano-drug: Lessons learned*. Journal of Controlled Release, 2012. **160**(2): p. 117-134.
72. Gradishar, W., *Superior efficacy of albumin-bound paclitaxel, ABI-007, compared with polythylated castor oil-based pclitaxel in women with metastatic breast cancer: Results of a phase III trial*. J Clin Oncol, 2005. **23**: p. 5983-5992.
73. Lammers, T., et al., *Drug targeting to tumors: Principles, pitfalls and (pre-) clinical progress*. Journal of Controlled Release, 2012. **161**(2): p. 175-187.
74. Jain, R.K. and T. Stylianopoulos, *Delivering nanomedicine to solid tumors*. Nat Rev Clin Oncol, 2010. **7**(11): p. 653-664.
75. Bae, Y.H. and K. Park, *Targeted drug delivery to tumors: Myths, reality and possibility*. Journal of Controlled Release, 2011. **153**(3): p. 198-205.
76. Lammers, T., et al., *Effect of radiotherapy and hyperthermia on the tumor accumulation of HPMA copolymer-based drug delivery systems*. Journal of Controlled Release, 2007. **117**(3): p. 333-341.
77. Zhang, Y.-N., et al., *Nanoparticle–liver interactions: Cellular uptake and hepatobiliary elimination*. Journal of Controlled Release, 2016. **240**: p. 332-348.
78. Garcia, A.A., et al., *A phase II study of Doxil (liposomal doxorubicin): Lack of activity in poor prognosis soft tissue sarcomas*. Annals of Oncology, 1998. **9**(10): p. 1131-1133.
79. Wilhelm, S., et al., *Analysis of nanoparticle delivery to tumours*. Nature Reviews Materials, 2016. **1**: p. 16014.
80. Meyers, P.A., *Muramyl tripeptide (mifamurtide) for the treatment of osteosarcoma*. Expert Review of Anticancer Therapy, 2009. **9**(8): p. 1035-1049.
81. Nardin, A., et al., *Liposomal muramyl tripeptide phosphatidylethanolamine: Targeting and activating macrophages for adjuvant treatment of osteosarcoma*. Current cancer drug targets, 2006. **6**(2): p. 123-133.
82. Gajera, K. and A. Patel, *An Overview of FDA Approved Liposome Formulations for Cancer Therapy*. Journal of Advances in Medical and Pharmaceutical Sciences, 2022. **24**(3): p. 1-7.
83. Ando, K., et al., *Mifamurtide for the treatment of nonmetastatic osteosarcoma*. Expert Opin Pharmacother, 2011. **12**(2): p. 285-92.
84. Malinovskaya, Y., et al., *Delivery of doxorubicin-loaded PLGA nanoparticles into U87 human glioblastoma cells*. International Journal of Pharmaceutics, 2017. **524**(1): p. 77-90.
85. Dal Magro, R., et al., *Artificial apolipoprotein corona enables nanoparticle brain targeting*. Nanomedicine: Nanotechnology, Biology and Medicine, 2018. **14**(2): p. 429-438.
86. Qiao, L., et al., *Tumor cell-derived exosomes home to their cells of origin and can be used as Trojan horses to deliver cancer drugs*. Theranostics, 2020. **10**(8): p. 3474-3487.
87. Emam, S.E., et al., *Cancer cell-type tropism is one of crucial determinants for the efficient systemic delivery of cancer cell-derived exosomes to tumor tissues*. European Journal of Pharmaceutics and Biopharmaceutics, 2019. **145**: p. 27-34.

88. Vácha, R., F.J. Martinez-Veracoechea, and D. Frenkel, *Receptor-Mediated Endocytosis of Nanoparticles of Various Shapes*. Nano Letters, 2011. **11**(12): p. 5391-5395.
89. Biffi, S., et al., *Actively targeted nanocarriers for drug delivery to cancer cells*. Expert Opinion on Drug Delivery, 2019. **16**(5): p. 481-496.
90. He, H., et al., *Survey of Clinical Translation of Cancer Nanomedicines—Lessons Learned from Successes and Failures*. Accounts of Chemical Research, 2019. **52**(9): p. 2445-2461.
91. Juweid, M., et al., *Micropharmacology of monoclonal antibodies in solid tumors: direct experimental evidence for a binding site barrier*. Cancer Res, 1992. **52**(19): p. 5144-53.
92. Koren, E. and V.P. Torchilin, *Drug carriers for vascular drug delivery*. IUBMB Life, 2011. **63**(8): p. 586-595.
93. Autio, K.A., et al., *A phase 2 study of BIND-014 (PSMA-targeted docetaxel nanoparticle) administered to patients with chemotherapy-naïve metastatic castration-resistant prostate cancer (mCRPC)*. Journal of Clinical Oncology, 2016. **34**(2\_suppl): p. 233-233.
94. Von Hoff, D.D., et al., *Phase I Study of PSMA-Targeted Docetaxel-Containing Nanoparticle BIND-014 in Patients with Advanced Solid Tumors*. Clinical Cancer Research, 2016. **22**(13): p. 3157-3163.
95. BIND-Therapeutics, *BIND therapeutics axes 38% of workforce* <http://www.genengnews.com/gen-news-highlights/bind-therapeutics-axes-38-of-workforce/81252580/>. 2016.
96. Gu, W., et al., *Actively targeted nanomedicines for precision cancer therapy: Concept, construction, challenges and clinical translation*. Journal of Controlled Release, 2021. **329**: p. 676-695.
97. Mi, P., *Stimuli-responsive nanocarriers for drug delivery, tumor imaging, therapy and theranostics*. Theranostics, 2020. **10**(10): p. 4557-4588.
98. Helmlinger, G., et al., *Interstitial pH and pO<sub>2</sub> gradients in solid tumors in vivo: high-resolution measurements reveal a lack of correlation*. Nature medicine, 1997. **3**: p. 177-182.
99. Murugan, B., et al., *Smart stimuli-responsive nanocarriers for the cancer therapy—nanomedicine*. Nanotechnology Reviews, 2021. **10**(1): p. 933-953.
100. Liu, S., et al., *pH-responsive magnetic metal-organic framework nanocomposite: A smart porous adsorbent for highly specific enrichment of cis-diol containing luteolin*. Chemical Engineering Journal, 2018. **341**: p. 198-207.
101. Mi, P., et al., *Hybrid Calcium Phosphate-Polymeric Micelles Incorporating Gadolinium Chelates for Imaging-Guided Gadolinium Neutron Capture Tumor Therapy*. ACS Nano, 2015. **9**(6): p. 5913-5921.
102. Mura, S., J. Nicolas, and P. Couvreur, *Stimuli-responsive nanocarriers for drug delivery*. Nat Mater, 2013. **12**(11): p. 991-1003.
103. Meng, F., W.E. Hennink, and Z. Zhong, *Reduction-sensitive polymers and bioconjugates for biomedical applications*. Biomaterials, 2009. **30**(12): p. 2180-2198.
104. Li, R. and Y. Xie, *Nanodrug delivery systems for targeting the endogenous tumor microenvironment and simultaneously overcoming multidrug resistance properties*. Journal of Controlled Release, 2017. **251**: p. 49-67.
105. Guo, X., et al., *Advances in redox-responsive drug delivery systems of tumor microenvironment*. J Nanobiotechnology, 2018. **16**(1): p. 74.
106. Chang, Y., et al., *Cationic Vesicles Based on Amphiphilic Pillar[5]arene Capped with Ferrocenium: A Redox-Responsive System for Drug/siRNA Co-Delivery*. Angewandte Chemie International Edition, 2014. **53**(48): p. 13126-13130.
107. Zhou, G., et al., *Redox responsive liposomal nanohybrid cerasomes for intracellular drug delivery*. Colloids and Surfaces B: Biointerfaces, 2016. **148**(Supplement C): p. 518-525.
108. Li, Y.R., Z. Jia, and M.A. Trush, *Defining ROS in Biology and Medicine*. Reactive Oxygen Species, 2016. **1**(1): p. 9–21.

109. Hancock, J.T., *Oxygen Is Instrumental for Biological Signaling: An Overview*. Oxygen, 2021. **1**(1): p. 3-15.
110. Nathan, C. and A. Cunningham-Bussel, *Beyond oxidative stress: an immunologist's guide to reactive oxygen species*. Nature Reviews Immunology, 2013. **13**(5): p. 349-361.
111. Xie, A., et al., *Stimuli-responsive prodrug-based cancer nanomedicine*. EBioMedicine, 2020. **56**: p. 102821.
112. Quader, S. and J.F.R. Van Guyse, *Bioresponsive Polymers for Nanomedicine—Expectations and Reality!* Polymers, 2022. **14**(17): p. 3659.
113. Peng, X. and V. Gandhi, *ROS-activated anticancer prodrugs: a new strategy for tumor-specific damage*. Therapeutic Delivery, 2012. **3**(7): p. 823-833.
114. Yang, B., Y. Chen, and J. Shi, *Reactive Oxygen Species (ROS)-Based Nanomedicine*. Chemical Reviews, 2019. **119**(8): p. 4881-4985.
115. Xu, X., et al., *ROS-Responsive Polyprodrug Nanoparticles for Triggered Drug Delivery and Effective Cancer Therapy*. Advanced Materials, 2017. **29**(33): p. 1700141.
116. Sahu, A., W.I. Choi, and G. Tae, *Recent Progress in the Design of Hypoxia-Specific Nano Drug Delivery Systems for Cancer Therapy*. Advanced Therapeutics, 2018. **1**(4): p. 1800026.
117. Kulkarni, P., et al., *Hypoxia-Responsive Polymersomes for Drug Delivery to Hypoxic Pancreatic Cancer Cells*. Biomacromolecules, 2016. **17**(8): p. 2507-13.
118. Fouladi, F., K.J. Steffen, and S. Mallik, *Enzyme-Responsive Liposomes for the Delivery of Anticancer Drugs*. Bioconjugate Chemistry, 2017. **28**(4): p. 857-868.
119. Mock, J.N., et al., *Evidence for distinct mechanisms of uptake and antitumor activity of secretory phospholipase A2 responsive liposome in prostate cancer*. Integrative Biology, 2013. **5**(1): p. 172-182.
120. Gamcsik, M.P., et al., *Glutathione levels in human tumors*. Biomarkers, 2012. **17**(8): p. 671-691.
121. Cook, J.A., et al., *Oxidative stress, redox, and the tumor microenvironment*. Seminars in Radiation Oncology, 2004. **14**(3): p. 259-266.
122. Asgharzadeh, M.R., et al., *Molecular machineries of pH dysregulation in tumor microenvironment: potential targets for cancer therapy*. Bioimpacts. **7**(2): p. 115-133.
123. Barar, J. and Y. Omidi, *Dysregulated pH in Tumor Microenvironment Checkmates Cancer Therapy*. Bioimpacts, 2013. **3**(4): p. 149-62.
124. Schmitz, T., et al., *Development and in vitro evaluation of a thiomers-based nanoparticulate gene delivery system*. Biomaterials, 2007. **28**(3): p. 524-531.
125. Bernkop-Schnürch, A., *Strategies to overcome the polycation dilemma in drug delivery*. Advanced Drug Delivery Reviews, 2018. **136-137**: p. 62-72.
126. Duan, Z., et al., *PEGylated Multistimuli-Responsive Dendritic Prodrug-Based Nanoscale System for Enhanced Anticancer Activity*. ACS Applied Materials & Interfaces, 2018. **10**(42): p. 35770-35783.
127. Wang, Q., et al., *Disulfide based prodrugs for cancer therapy*. RSC Advances, 2020. **10**(41): p. 24397-24409.
128. Picheth, G., et al., *Echogenicity enhancement by end-fluorinated polylactide perfluorohexane nanocapsules: Towards ultrasound-activable nanosystems*. Acta Biomaterialia, 2017. **64**: p. 313-322.
129. Entzian, K. and A. Aigner, *Drug Delivery by Ultrasound-Responsive Nanocarriers for Cancer Treatment*. Pharmaceutics, 2021. **13**(8).
130. Sirsi, S.R. and M.A. Borden, *Advances in ultrasound mediated gene therapy using microbubble contrast agents*. Theranostics, 2012. **2**(12): p. 1208-22.
131. Paris, J.L., et al., *Mesoporous silica nanoparticles engineered for ultrasound-induced uptake by cancer cells*. Nanoscale, 2018. **10**(14): p. 6402-6408.
132. Florinas, S., H.Y. Nam, and S.W. Kim, *Enhanced siRNA Delivery Using a Combination of an Arginine-Grafted Bioreducible Polymer, Ultrasound, and Microbubbles in Cancer Cells*. Molecular Pharmaceutics, 2013. **10**(5): p. 2021-2030.

133. Zhou, L.-Q., et al., *Ultrasound nanotheranostics in fighting cancer: Advances and prospects*. Cancer Letters, 2020. **470**: p. 204-219.
134. Cui, X., et al., *Intrinsic chemistry and design principle of ultrasound-responsive nanomedicine*. Nano Today, 2019. **28**: p. 100773.
135. Houvenagel, S., et al., *Comb-Like Fluorophilic-Lipophilic-Hydrophilic Polymers for Nanocapsules as Ultrasound Contrast Agents*. Biomacromolecules, 2018. **19**(8): p. 3244-3256.
136. Meng, D., et al., *Dual-sensitive and highly biocompatible O-carboxymethyl chitosan nanodroplets for prostate tumor ultrasonic imaging and treatment*. Cancer Nanotechnology, 2023. **14**(1): p. 19.
137. Zhang, X., et al., *Light-Responsive Nanomaterials for Cancer Therapy*. Engineering, 2022. **13**: p. 18-30.
138. Yan, L. and X. Li, *Biodegradable Stimuli-Responsive Polymeric Micelles for Treatment of Malignancy*. Current pharmaceutical biotechnology, 2016. **17**(3): p. 227-236.
139. Lee, G.-H., et al., *Multifunctional materials for implantable and wearable photonic healthcare devices*. Nature Reviews Materials, 2020. **5**(2): p. 149-165.
140. Liu, G., W. Liu, and C.-M. Dong, *UV- and NIR-responsive polymeric nanomedicines for on-demand drug delivery*. Polymer Chemistry, 2013. **4**(12): p. 3431-3443.
141. Zhao, W., et al., *Remote Light-Responsive Nanocarriers for Controlled Drug Delivery: Advances and Perspectives*. Small, 2019. **15**(45): p. 1903060.
142. Yuan, Y., et al., *NIR photoregulated chemo- and photodynamic cancer therapy based on conjugated polyelectrolyte–drug conjugate encapsulated upconversion nanoparticles*. Nanoscale, 2014. **6**(19): p. 11259-11272.
143. Liu, Y.-L., et al., *A review of magnet systems for targeted drug delivery*. Journal of Controlled Release, 2019. **302**: p. 90-104.
144. Naud, C., et al., *Cancer treatment by magneto-mechanical effect of particles, a review*. Nanoscale Advances, 2020. **2**(9): p. 3632-3655.
145. Master, A.M., et al., *Remote Actuation of Magnetic Nanoparticles For Cancer Cell Selective Treatment Through Cytoskeletal Disruption*. Scientific Reports, 2016. **6**(1): p. 33560.
146. Golovin, Y., et al., *Modeling drug release from functionalized magnetic nanoparticles actuated by non-heating low frequency magnetic field*. Journal of Nanoparticle Research, 2017. **19**(2): p. 64.
147. Lopez, S., et al., *Magneto-mechanical destruction of cancer-associated fibroblasts using ultra-small iron oxide nanoparticles and low frequency rotating magnetic fields*. Nanoscale Advances, 2022. **4**(2): p. 421-436.
148. Ponomareva, S., et al., *Magnetic particles for triggering insulin release in INS-1E cells subjected to a rotating magnetic field*. Nanoscale, 2022. **14**(36): p. 13274-13283.
149. Dutz, S. and R. Hergt, *Magnetic nanoparticle heating and heat transfer on a microscale: Basic principles, realities and physical limitations of hyperthermia for tumour therapy*. International Journal of Hyperthermia, 2013. **29**(8): p. 790-800.
150. Liu, J.F., et al., *Use of magnetic fields and nanoparticles to trigger drug release and improve tumor targeting*. Wiley interdisciplinary reviews. Nanomedicine and nanobiotechnology, 2019. **11**(6): p. e1571-e1571.
151. Mukhatov, A., et al., *A comprehensive review on magnetic imaging techniques for biomedical applications*. Nano Select, 2023. **4**(3): p. 213-230.
152. Cheng, Y., et al., *Rotating magnetic field induced oscillation of magnetic particles for in vivo mechanical destruction of malignant glioma*. Journal of Controlled Release, 2016. **223**: p. 75-84.
153. Meyer, D.E., et al., *Drug targeting using thermally responsive polymers and local hyperthermia*. Journal of Controlled Release, 2001. **74**(1–3): p. 213-224.
154. Li, L., et al., *Improved intratumoral nanoparticle extravasation and penetration by mild hyperthermia*. Journal of Controlled Release, 2013. **167**(2): p. 130-137.

155. Chatterjee, D.K., P. Diagaradjane, and S. Krishnan, *Nanoparticle-mediated hyperthermia in cancer therapy*. *Therapeutic Delivery*, 2011. **2**(8): p. 1001-1014.
156. Ganta, S., et al., *A review of stimuli-responsive nanocarriers for drug and gene delivery*. *Journal of Controlled Release*, 2008. **126**(3): p. 187-204.
157. van Rhoon, G.C., M. Franckena, and T.L.M. ten Hagen, *A moderate thermal dose is sufficient for effective free and TSL based thermochemotherapy*. *Advanced Drug Delivery Reviews*, 2020. **163-164**: p. 145-156.
158. Bass, H., J.L. Moore, and W.T. Coakley, *Lethality in Mammalian Cells Due to Hyperthermia under Oxidic and Hypoxic Conditions*. *International Journal of Radiation Biology and Related Studies in Physics, Chemistry and Medicine*, 1978. **33**(1): p. 57-67.
159. Urano, M., *Invited Review: For the clinical application of thermochemotherapy given at mild temperatures*. *International Journal of Hyperthermia*, 1999. **15**(2): p. 79-107.
160. Fuller, K.J., et al., *Cancer and the heat shock response*. *European Journal of Cancer*, 1994. **30**(12): p. 1884-1891.
161. Harmon, B.V., et al., *The Role of Apoptosis in the Response of Cells and Tumours to Mild Hyperthermia*. *International Journal of Radiation Biology*, 1991. **59**(2): p. 489-501.
162. Wust, P., et al., *Hyperthermia in combined treatment of cancer*. *The Lancet Oncology*, 2002. **3**(8): p. 487-497.
163. Frey, B., et al., *Old and new facts about hyperthermia-induced modulations of the immune system*. *International Journal of Hyperthermia*, 2012. **28**(6): p. 528-542.
164. Regenold, M., et al., *Turning down the heat: The case for mild hyperthermia and thermosensitive liposomes*. *Nanomedicine: Nanotechnology, Biology and Medicine*, 2022. **40**: p. 102484.
165. Needham, D., et al., *Materials characterization of the low temperature sensitive liposome (LTSL): effects of the lipid composition (lysolipid and DSPE-PEG2000) on the thermal transition and release of doxorubicin*. *Faraday Discussions*, 2013. **161**(0): p. 515-534.
166. Derieppe, M., et al., *Assessment of Intratumoral Doxorubicin Penetration after Mild Hyperthermia-Mediated Release from Thermosensitive Liposomes*. *Contrast Media & Molecular Imaging*, 2019. **2019**: p. 2645928.
167. Lencioni, R. and D. Cioni, *RFA plus lyso-thermosensitive liposomal doxorubicin: in search of the optimal approach to cure intermediate-size hepatocellular carcinoma*. *Hepatic Oncology*, 2016(0).
168. Dou, Y., K. Hynynen, and C. Allen, *To heat or not to heat: Challenges with clinical translation of thermosensitive liposomes*. *Journal of Controlled Release*, 2017. **249**: p. 63-73.
169. Seynhaeve, A.L.B., et al., *Hyperthermia and smart drug delivery systems for solid tumor therapy*. *Advanced Drug Delivery Reviews*, 2020. **163-164**: p. 125-144.
170. Ribeiro, T.P., et al., *Nanomaterials in cancer: Reviewing the combination of hyperthermia and triggered chemotherapy*. *Journal of Controlled Release*, 2022. **347**: p. 89-103.
171. Mai, B.T., et al., *Clickable Polymer Ligand-Functionalized Iron Oxide Nanocubes: A Promising Nanoplatform for 'Local Hot Spots' Magnetically Triggered Drug Release*. *ACS Applied Materials & Interfaces*, 2022. **14**(43): p. 48476-48488.
172. Mai, B.T., et al., *Thermoresponsive Iron Oxide Nanocubes for an Effective Clinical Translation of Magnetic Hyperthermia and Heat-Mediated Chemotherapy*. *ACS Applied Materials & Interfaces*, 2019. **11**(6): p. 5727-5739.
173. Agarwal, A., et al., *Remote Triggered Release of Doxorubicin in Tumors by Synergistic Application of Thermosensitive Liposomes and Gold Nanorods*. *ACS Nano*, 2011. **5**(6): p. 4919-4926.
174. Theodosiou, M., et al., *Iron oxide nanoflowers encapsulated in thermosensitive fluorescent liposomes for hyperthermia treatment of lung adenocarcinoma*. *Scientific Reports*, 2022. **12**(1): p. 8697.
175. Hepel, M., *Magnetic Nanoparticles for Nanomedicine*. *Magnetochemistry*, 2020. **6**(1): p. 3.

176. Savliwala, S., et al., *Chapter 13 - Magnetic nanoparticles*, in *Nanoparticles for Biomedical Applications*, E.J. Chung, L. Leon, and C. Rinaldi, Editors. 2020, Elsevier. p. 195-221.
177. Vallabani, N.V., S. Singh, and A.S. Karakoti, *Magnetic nanoparticles: current trends and future aspects in diagnostics and nanomedicine*. *Current drug metabolism*, 2019. **20**(6): p. 457-472.
178. Kianfar, E., *Magnetic Nanoparticles in Targeted Drug Delivery: a Review*. *Journal of Superconductivity and Novel Magnetism*, 2021. **34**(7): p. 1709-1735.
179. Issa, B., et al., *Magnetic nanoparticles: surface effects and properties related to biomedicine applications*. *Int J Mol Sci*, 2013. **14**(11): p. 21266-305.
180. Neuberger, T., et al., *Superparamagnetic nanoparticles for biomedical applications: Possibilities and limitations of a new drug delivery system*. *Journal of Magnetism and Magnetic Materials*, 2005. **293**(1): p. 483-496.
181. Ho, D., X. Sun, and S. Sun, *Monodisperse Magnetic Nanoparticles for Theranostic Applications*. *Accounts of Chemical Research*, 2011. **44**(10): p. 875-882.
182. Ota, S. and Y. Takemura, *Characterization of Néel and Brownian Relaxations Isolated from Complex Dynamics Influenced by Dipole Interactions in Magnetic Nanoparticles*. *The Journal of Physical Chemistry C*, 2019. **123**(47): p. 28859-28866.
183. Liu, X., et al., *Comprehensive understanding of magnetic hyperthermia for improving antitumor therapeutic efficacy*. *Theranostics*, 2020. **10**(8): p. 3793-3815.
184. Carrey, J., B. Mehdaoui, and M. Respaud, *Simple models for dynamic hysteresis loop calculations of magnetic single-domain nanoparticles: Application to magnetic hyperthermia optimization*. *Journal of Applied Physics*, 2011. **109**(8).
185. Sharifi, I., H. Shokrollahi, and S. Amiri, *Ferrite-based magnetic nanofluids used in hyperthermia applications*. *Journal of Magnetism and Magnetic Materials*, 2012. **324**(6): p. 903-915.
186. Gropper, S.A.S. and J.L. Smith, *Nutrition and Human Metabolism*. 2013: Cengage Learning.
187. Zoroddu, M.A., et al., *The essential metals for humans: a brief overview*. *Journal of Inorganic Biochemistry*, 2019. **195**: p. 120-129.
188. Theil, E.C., *FERRITIN: STRUCTURE, GENE REGULATION, AND CELLULAR FUNCTION IN ANIMALS, PLANTS, AND MICROORGANISMS*. *Annual Review of Biochemistry*, 1987. **56**(1): p. 289-315.
189. ORINO, K., et al., *Ferritin and the response to oxidative stress*. *Biochemical Journal*, 2001. **357**(1): p. 241-247.
190. Hsia, C.C.W., *Respiratory Function of Hemoglobin*. *New England Journal of Medicine*, 1998. **338**(4): p. 239-248.
191. Biagioli, M., et al., *Unexpected expression of  $\alpha$ - and  $\beta$ -globin in mesencephalic dopaminergic neurons and glial cells*. *Proceedings of the National Academy of Sciences*, 2009. **106**(36): p. 15454-15459.
192. Schwaminger, S.P., et al., *Oxidation of magnetite nanoparticles: impact on surface and crystal properties*. *CrystEngComm*, 2017. **19**(2): p. 246-255.
193. Cullity, B.D. and C.D. Graham, *Introduction to magnetic materials*. 2011: John Wiley & Sons.
194. Singh, P., D.M. Mott, and S. Maenosono, *Gold/Wüstite Core-shell Nanoparticles: Suppression of Iron Oxidation through the Electron-Transfer Phenomenon*. *ChemPhysChem*, 2013. **14**(14): p. 3278-3283.
195. Khot, V.M., et al., *Improved magnetic induction heating of nanoferrites for hyperthermia applications: Correlation with colloidal stability and magneto-structural properties*. *Journal of Magnetism and Magnetic Materials*, 2015. **384**: p. 335-343.
196. Angelakeris, M., et al., *Enhanced biomedical heat-triggered carriers via nanomagnetism tuning in ferrite-based nanoparticles*. *Journal of Magnetism and Magnetic Materials*, 2015. **381**: p. 179-187.
197. Bourquin, J., et al., *Biodistribution, Clearance, and Long-Term Fate of Clinically Relevant Nanomaterials*. *Advanced Materials*, 2018. **30**(19): p. 1704307.
198. Monopoli, M.P., et al., *Biomolecular coronas provide the biological identity of nanosized materials*. *Nature Nanotechnology*, 2012. **7**(12): p. 779-786.

199. Senthilkumar, N., et al., *Designing magnetic nanoparticles for in vivo applications and understanding their fate inside human body*. Coordination Chemistry Reviews, 2021. **445**: p. 214082.
200. Fishbane, S., et al., *Factors affecting response and tolerability to ferumoxytol in nondialysis chronic kidney disease patients*. Clinical nephrology, 2012. **78**(3): p. 181-188.
201. Mills, K.C. and S.C. Curry, *Acute iron poisoning*. Emergency medicine clinics of North America, 1994. **12**(2): p. 397-413.
202. Arami, H., et al., *In vivo delivery, pharmacokinetics, biodistribution and toxicity of iron oxide nanoparticles*. Chemical Society Reviews, 2015. **44**(23): p. 8576-8607.
203. Wada, S., et al., *New local hyperthermia using dextran magnetite complex (DM) for oral cavity: experimental study in normal hamster tongue*. Oral diseases, 2001. **7**(3): p. 192-195.
204. Lartigue, L., et al., *Biodegradation of Iron Oxide Nanocubes: High-Resolution In Situ Monitoring*. ACS Nano, 2013. **7**(5): p. 3939-3952.
205. Javed, Y., et al., *Biodegradation Mechanisms of Iron Oxide Monocrystalline Nanoflowers and Tunable Shield Effect of Gold Coating*. Small, 2014. **10**(16): p. 3325-3337.
206. Kolosnjaj-Tabi, J., et al., *The One Year Fate of Iron Oxide Coated Gold Nanoparticles in Mice*. ACS Nano, 2015. **9**(8): p. 7925-7939.
207. Weissleder, R., et al., *Superparamagnetic iron oxide: pharmacokinetics and toxicity*. American Journal of Roentgenology, 1989. **152**(1): p. 167-173.
208. Gu, L., et al., *In Vivo Clearance and Toxicity of Monodisperse Iron Oxide Nanocrystals*. ACS Nano, 2012. **6**(6): p. 4947-4954.
209. Daldrup-Link, H.E., *Ten Things You Might Not Know about Iron Oxide Nanoparticles*. Radiology, 2017. **284**(3): p. 616-629.
210. Xie, M., et al., *Going even smaller: Engineering sub-5 nm nanoparticles for improved delivery, biocompatibility, and functionality*. WIREs Nanomedicine and Nanobiotechnology, 2020. **12**(6): p. e1644.
211. Ems, T., K. St Lucia, and M.R. Huecker, *Biochemistry, iron absorption*, in *StatPearls [internet]*. 2022, StatPearls Publishing.
212. Tay, Z.W., et al., *Magnetic Particle Imaging-Guided Heating in Vivo Using Gradient Fields for Arbitrary Localization of Magnetic Hyperthermia Therapy*. ACS Nano, 2018. **12**(4): p. 3699-3713.
213. Mohapatra, J., et al., *Principles and applications of magnetic nanomaterials in magnetically guided bioimaging*. Materials Today Physics, 2023. **32**: p. 101003.
214. Gavilán, H., et al., *Scale-up approach for the preparation of magnetic ferrite nanocubes and other shapes with benchmark performance for magnetic hyperthermia applications*. Nature Protocols, 2023. **18**(3): p. 783-809.
215. Shen, S., et al., *Magnetic nanoparticle clusters for photothermal therapy with near-infrared irradiation*. Biomaterials, 2015. **39**: p. 67-74.
216. Moros, M., et al., *Triggering antitumoural drug release and gene expression by magnetic hyperthermia*. Advanced Drug Delivery Reviews, 2019. **138**: p. 326-343.
217. Yin, D.-C., *Protein crystallization in a magnetic field*. Progress in Crystal Growth and Characterization of Materials, 2015. **61**(1): p. 1-26.
218. Blümli, P., *Magnetic Guiding with Permanent Magnets: Concept, Realization and Applications to Nanoparticles and Cells*. Cells, 2021. **10**(10): p. 2708.
219. Lübke, A.S., et al., *Clinical experiences with magnetic drug targeting: a phase I study with 4'-epidoxorubicin in 14 patients with advanced solid tumors*. Cancer Res, 1996. **56**(20): p. 4686-93.
220. Liu, J.F., et al., *Use of Oppositely Polarized External Magnets To Improve the Accumulation and Penetration of Magnetic Nanocarriers into Solid Tumors*. ACS nano, 2020. **14**(1): p. 142-152.
221. Zhou, Z., Z. Shen, and X. Chen, *Tale of Two Magnets: An Advanced Magnetic Targeting System*. ACS Nano, 2020. **14**(1): p. 7-11.

222. Riegler, J., et al., *Magnetic cell delivery for peripheral arterial disease: A theoretical framework*. Medical Physics, 2011. **38**(7): p. 3932-3943.
223. Kummer, M.P., et al., *OctoMag: An electromagnetic system for 5-DOF wireless micromanipulation*. IEEE Transactions on Robotics, 2010. **26**(6): p. 1006-1017.
224. Diller, E., J. Giltinan, and M. Sitti, *Independent control of multiple magnetic microrobots in three dimensions*. The International Journal of Robotics Research, 2013. **32**(5): p. 614-631.
225. Mai, W., *Diagnostic MRI in dogs and cats*. 2018: CRC press.
226. Lee, N. and T. Hyeon, *Designed synthesis of uniformly sized iron oxide nanoparticles for efficient magnetic resonance imaging contrast agents*. Chemical Society Reviews, 2012. **41**(7): p. 2575-2589.
227. Liu, C., et al., *Time-Varying Characteristics of Granite Microstructures after Cyclic Dynamic Disturbance Using Nuclear Magnetic Resonance*. Crystals, 2017. **7**(10): p. 306.
228. Estelrich, J., M.J. Sánchez-Martín, and M.A. Busquets, *Nanoparticles in magnetic resonance imaging: from simple to dual contrast agents*. International journal of nanomedicine, 2015. **10**: p. 1727.
229. Wang, Y.-X.J., *Current status of superparamagnetic iron oxide contrast agents for liver magnetic resonance imaging*. World journal of gastroenterology, 2015. **21**(47): p. 13400.
230. Bauer, L.M., et al., *Magnetic Particle Imaging Tracers: State-of-the-Art and Future Directions*. The Journal of Physical Chemistry Letters, 2015. **6**(13): p. 2509-2517.
231. Vogel, P., et al., *Magnetic particle imaging meets computed tomography: First simultaneous imaging*. Scientific reports, 2019. **9**(1): p. 1-9.
232. Zhao, Y., W. Zheng, and M. Hassan, *Chapter 4 - Nanoparticles for imaging application*, in *Frontiers of Nanoscience*, W.J. Parak and N. Feliu, Editors. 2020, Elsevier. p. 67-88.
233. Chandrasekharan, P., et al., *Using magnetic particle imaging systems to localize and guide magnetic hyperthermia treatment: tracers, hardware, and future medical applications*. Theranostics, 2020. **10**(7): p. 2965-2981.
234. Kuboyabu, T., et al., *Magnetic particle imaging for magnetic hyperthermia treatment: Visualization and quantification of the intratumoral distribution and temporal change of magnetic nanoparticles in vivo*. Open Journal of Medical Imaging, 2016. **6**(1): p. 1-15.
235. Finas, D., et al. *Distribution of Superparamagnetic Nanoparticles in Lymphatic Tissue for Sentinel Lymph Node Detection in Breast Cancer by Magnetic Particle Imaging*. 2012. Berlin, Heidelberg: Springer Berlin Heidelberg.
236. Billings, C., et al., *Magnetic Particle Imaging: Current and Future Applications, Magnetic Nanoparticle Synthesis Methods and Safety Measures*. Int J Mol Sci, 2021. **22**(14).
237. Orendorff, R., et al., *First in vivo traumatic brain injury imaging via magnetic particle imaging*. Physics in Medicine & Biology, 2017. **62**(9): p. 3501.
238. Mirvakili, S.M. and R. Langer, *Wireless on-demand drug delivery*. Nature Electronics, 2021. **4**(7): p. 464-477.
239. Stupp, R., et al., *Radiotherapy plus Concomitant and Adjuvant Temozolomide for Glioblastoma*. New England Journal of Medicine, 2005. **352**(10): p. 987-996.
240. Lu, C.-H. and J.-K. Hsiao, *Diagnostic and therapeutic roles of iron oxide nanoparticles in biomedicine*. Tzu Chi Medical Journal, 2023. **35**(1): p. 11-17.
241. Vahidi, H., H. Barabadi, and M. Saravanan, *Emerging Selenium Nanoparticles to Combat Cancer: a Systematic Review*. Journal of Cluster Science, 2020. **31**(2): p. 301-309.
242. Garanina, A.S., et al., *Temperature-controlled magnetic nanoparticles hyperthermia inhibits primary tumor growth and metastases dissemination*. Nanomedicine: Nanotechnology, Biology and Medicine, 2020. **25**: p. 102171.
243. Sola-Leyva, A., et al., *Reactive oxygen species (ROS) production in HepG2 cancer cell line through the application of localized alternating magnetic field*. Journal of Materials Chemistry B, 2020. **8**(34): p. 7667-7676.
244. Dixon, S.J., et al., *Ferroptosis: an iron-dependent form of nonapoptotic cell death*. cell, 2012. **149**(5): p. 1060-1072.

245. Shirlee, T., S. David, and M. Pamela, *Oxytosis: A Novel Form of Programmed Cell Death*. Current Topics in Medicinal Chemistry, 2001. **1**(6): p. 497-506.
246. Golovin, Y.I., et al., *Towards nanomedicines of the future: Remote magneto-mechanical actuation of nanomedicines by alternating magnetic fields*. Journal of Controlled Release, 2015. **219**: p. 43-60.
247. Clerc, P., et al., *Targeted Magnetic Intra-Lysosomal Hyperthermia produces lysosomal reactive oxygen species and causes Caspase-1 dependent cell death*. Journal of Controlled Release, 2018. **270**: p. 120-134.
248. Domenech, M., et al., *Lysosomal Membrane Permeabilization by Targeted Magnetic Nanoparticles in Alternating Magnetic Fields*. ACS Nano, 2013. **7**(6): p. 5091-5101.
249. Creixell, M., et al., *EGFR-Targeted Magnetic Nanoparticle Heaters Kill Cancer Cells without a Perceptible Temperature Rise*. ACS Nano, 2011. **5**(9): p. 7124-7129.
250. Kallumadil, M., et al., *Suitability of commercial colloids for magnetic hyperthermia*. Journal of Magnetism and Magnetic Materials, 2009. **321**(10): p. 1509-1513.
251. Guibert, C., et al., *Magnetic fluid hyperthermia probed by both calorimetric and dynamic hysteresis measurements*. Journal of Magnetism and Magnetic Materials, 2017. **421**: p. 384-392.
252. Dutz, S. and R. Hergt, *Magnetic particle hyperthermia—a promising tumour therapy?* Nanotechnology, 2014. **25**(45): p. 452001.
253. Liu, X.L. and H.M. Fan, *Innovative magnetic nanoparticle platform for magnetic resonance imaging and magnetic fluid hyperthermia applications*. Current Opinion in Chemical Engineering, 2014. **4**: p. 38-46.
254. Zhang, H., et al., *Magnetic nanoparticles based cancer therapy: current status and applications*. Science China Life Sciences, 2018. **61**(4): p. 400-414.
255. Fortin, J.-P., et al., *Size-Sorted Anionic Iron Oxide Nanomagnets as Colloidal Mediators for Magnetic Hyperthermia*. Journal of the American Chemical Society, 2007. **129**(9): p. 2628-2635.
256. Rosensweig, R.E., *Heating magnetic fluid with alternating magnetic field*. Journal of Magnetism and Magnetic Materials, 2002. **252**: p. 370-374.
257. Almontasser, A. and A. Parveen, *Probing the effect of Ni, Co and Fe doping concentrations on the antibacterial behaviors of MgO nanoparticles*. Scientific Reports, 2022. **12**(1): p. 7922.
258. Lee, J.-H., et al., *Exchange-coupled magnetic nanoparticles for efficient heat induction*. Nature Nanotechnology, 2011. **6**(7): p. 418-422.
259. Liu, X.L., et al., *Optimization of surface coating on Fe<sub>3</sub>O<sub>4</sub> nanoparticles for high performance magnetic hyperthermia agents*. Journal of Materials Chemistry, 2012. **22**(17): p. 8235-8244.
260. Zhang, E., et al., *Dynamic magnetic fields remote-control apoptosis via nanoparticle rotation*. ACS Nano, 2014. **8**(4): p. 3192-201.
261. Thébault, C., et al., *Magneto-mechanical treatment of human glioblastoma cells with engineered iron oxide powder microparticles for triggering apoptosis*. Nanoscale Advances, 2021. **3**(21): p. 6213-6222.
262. Yao, J., et al., *Magnetomechanical force: an emerging paradigm for therapeutic applications*. Journal of Materials Chemistry B, 2022. **10**(37): p. 7136-7147.
263. Lafaro, K.J. and L.G. Melstrom, *The Paradoxical Web of Pancreatic Cancer Tumor Microenvironment*. The American Journal of Pathology, 2019. **189**(1): p. 44-57.
264. Hillion, A., et al., *Real-Time Observation and Analysis of Magnetomechanical Actuation of Magnetic Nanoparticles in Cells*. Nano Letters, 2022. **22**(5): p. 1986-1991.
265. Ghosh Chaudhuri, R. and S. Paria, *Core/Shell Nanoparticles: Classes, Properties, Synthesis Mechanisms, Characterization, and Applications*. Chemical Reviews, 2012. **112**(4): p. 2373-2433.
266. Das, P., et al., *Tailor made magnetic nanolights: fabrication to cancer theranostics applications*. Nanoscale Advances, 2021.

267. Estelrich, J. and M.A. Busquets, *Iron Oxide Nanoparticles in Photothermal Therapy*. Molecules (Basel, Switzerland), 2018. **23**(7): p. 1567.
268. Wu, M., et al., *Magnetite nanocluster@poly(dopamine)-PEG@ indocyanine green nanobead with magnetic field-targeting enhanced MR imaging and photothermal therapy in vivo*. Colloids and Surfaces B: Biointerfaces, 2016. **141**: p. 467-475.
269. Xue, W., et al., *AMF responsive DOX-loaded magnetic microspheres: transmembrane drug release mechanism and multimodality postsurgical treatment of breast cancer*. Journal of Materials Chemistry B, 2018. **6**(15): p. 2289-2303.
270. Li, T.-J., et al., *In vivo anti-cancer efficacy of magnetite nanocrystal - based system using locoregional hyperthermia combined with 5-fluorouracil chemotherapy*. Biomaterials, 2013. **34**(32): p. 7873-7883.
271. Lee, J.-H., et al., *On-Demand Drug Release System for In Vivo Cancer Treatment through Self-Assembled Magnetic Nanoparticles*. Angewandte Chemie International Edition, 2013. **52**(16): p. 4384-4388.
272. Griffete, N., et al., *Design of magnetic molecularly imprinted polymer nanoparticles for controlled release of doxorubicin under an alternative magnetic field in athermal conditions*. Nanoscale, 2015. **7**(45): p. 18891-18896.
273. Riedinger, A., et al., *Subnanometer Local Temperature Probing and Remotely Controlled Drug Release Based on Azo-Functionalized Iron Oxide Nanoparticles*. Nano Letters, 2013. **13**(6): p. 2399-2406.
274. Kumar, C.S.S.R. and F. Mohammad, *Magnetic nanomaterials for hyperthermia-based therapy and controlled drug delivery*. Advanced Drug Delivery Reviews, 2011. **63**(9): p. 789-808.
275. Ding, X., et al., *Sol-gel system functionalized magnetic nanocubes as remote controlled drug carriers for cooperative tumor-targeted therapy*. Materials Letters, 2016. **175**: p. 236-240.
276. Crommelin, D.J.A., P. van Hoogevest, and G. Storm, *The role of liposomes in clinical nanomedicine development. What now? Now what?* Journal of Controlled Release, 2020. **318**: p. 256-263.
277. Luiz, H., J. Oliveira Pinho, and M.M. Gaspar, *Advancing Medicine with Lipid-Based Nanosystems - The Successful Case of Liposomes*. Biomedicines, 2023. **11**(2): p. 435.
278. Zhang, G. and J. Sun, *Lipid in Chips: A Brief Review of Liposomes Formation by Microfluidics*. Int J Nanomedicine, 2021. **16**: p. 7391-7416.
279. De Cuyper, M. and M. Joniau, *Magnetoliposomes*. European Biophysics Journal, 1988. **15**(5): p. 311-319.
280. Bothun, G.D. and M.R. Preiss, *Bilayer heating in magnetite nanoparticle–liposome dispersions via fluorescence anisotropy*. Journal of Colloid and Interface Science, 2011. **357**(1): p. 70-74.
281. Ginzburg, V.V. and S. Balijepalli, *Modeling the Thermodynamics of the Interaction of Nanoparticles with Cell Membranes*. Nano Letters, 2007. **7**(12): p. 3716-3722.
282. Choi, W.I., et al., *Magnetoliposomes with size controllable insertion of magnetic nanoparticles for efficient targeting of cancer cells*. RSC advances, 2019. **9**(26): p. 15053-15060.
283. Yu, Y., et al., *Cationic Nanoparticles Stabilize Zwitterionic Liposomes Better than Anionic Ones*. The Journal of Physical Chemistry C, 2007. **111**(23): p. 8233-8236.
284. Preiss, M.R. and G.D. Bothun, *Stimuli-responsive liposome-nanoparticle assemblies*. Expert Opinion on Drug Delivery, 2011. **8**(8): p. 1025-1040.
285. Amstad, E., et al., *Triggered Release from Liposomes through Magnetic Actuation of Iron Oxide Nanoparticle Containing Membranes*. Nano Letters, 2011. **11**(4): p. 1664-1670.
286. Veloso, S.R.S., R.G.D. Andrade, and E.M.S. Castanheira, *Magnetoliposomes: recent advances in the field of controlled drug delivery*. Expert Opinion on Drug Delivery, 2021. **18**(10): p. 1323-1334.
287. Guo, Y., et al., *Light/magnetic hyperthermia triggered drug released from multi-functional thermo-sensitive magnetoliposomes for precise cancer synergetic theranostics*. Journal of Controlled Release, 2018. **272**: p. 145-158.

288. Saint-Cricq, P., et al., *Magnetic field activated drug delivery using thermodegradable azo-functionalised PEG-coated core-shell mesoporous silica nanoparticles*. *Nanoscale*, 2015. **7**(31): p. 13168-13172.
289. Fan, B., et al., *Thermo-responsive self-immolative nanoassemblies: direct and indirect triggering*. *Chemical Communications*, 2017. **53**(89): p. 12068-12071.
290. H. Vazifeshenas, F. and F. Bahadori, *Investigation of Soret effect on drug delivery in a tumor without necrotic core*. *Journal of the Taiwan Institute of Chemical Engineers*, 2019. **102**: p. 17-24.
291. Nappini, S., et al., *Magnetoliposomes for controlled drug release in the presence of low-frequency magnetic field*. *Soft Matter*, 2010. **6**(1): p. 154-162.
292. Peiris, P.M., et al., *Enhanced Delivery of Chemotherapy to Tumors Using a Multicomponent Nanochain with Radio-Frequency-Tunable Drug Release*. *ACS Nano*, 2012. **6**(5): p. 4157-4168.
293. Podaru, G., et al., *Pulsed Magnetic Field Induced Fast Drug Release from Magneto Liposomes via Ultrasound Generation*. *The Journal of Physical Chemistry B*, 2014. **118**(40): p. 11715-11722.
294. Albinali, K.E., et al., *A perspective on magnetic core-shell carriers for responsive and targeted drug delivery systems*. *International Journal of Nanomedicine*, 2019. **14**: p. 1707-1723.
295. Setia, A., et al., *Theranostic magnetic nanoparticles: Synthesis, properties, toxicity, and emerging trends for biomedical applications*. *Journal of Drug Delivery Science and Technology*, 2023. **81**: p. 104295.
296. Moharramnejad, M., et al., *MOF as nanoscale drug delivery devices: Synthesis and recent progress in biomedical applications*. *Journal of Drug Delivery Science and Technology*, 2023. **81**: p. 104285.
297. Souza, B., et al., *Drug guest molecules as modulators during one-step mechanochemical encapsulation in MIL-100 (Fe) framework*. 2020.
298. Azizi Vahed, T., M.R. Naimi-Jamal, and L. Panahi, *Alginate-coated ZIF-8 metal-organic framework as a green and bioactive platform for controlled drug release*. *Journal of Drug Delivery Science and Technology*, 2019. **49**: p. 570-576.
299. Zhang, H., et al., *Rational Design of Metal Organic Framework Nanocarrier-Based Codelivery System of Doxorubicin Hydrochloride/Verapamil Hydrochloride for Overcoming Multidrug Resistance with Efficient Targeted Cancer Therapy*. *ACS Applied Materials & Interfaces*, 2017. **9**(23): p. 19687-19697.
300. Cunha, D., et al., *Rationale of Drug Encapsulation and Release from Biocompatible Porous Metal-Organic Frameworks*. *Chemistry of Materials*, 2013. **25**(14): p. 2767-2776.
301. Chen, Z., et al., *Reticular Chemistry for Highly Porous Metal-Organic Frameworks: The Chemistry and Applications*. *Accounts of Chemical Research*, 2022. **55**(4): p. 579-591.
302. Wang, Q., et al., *Synthesis and modification of ZIF-8 and its application in drug delivery and tumor therapy*. *RSC Advances*, 2020. **10**(62): p. 37600-37620.
303. Kaushal, S., et al., *First transition series metal-organic frameworks: synthesis, properties and applications*. *Materials Advances*, 2021. **2**(22): p. 7308-7335.
304. Hamisu, A.M., A. Ariffin, and A.C. Wibowo, *Cation exchange in metal-organic frameworks (MOFs): The hard-soft acid-base (HSAB) principle appraisal*. *Inorganica Chimica Acta*, 2020. **511**: p. 119801.
305. Liu, B., et al., *Microwave-Assisted Rapid Synthesis of  $\gamma$ -Cyclodextrin Metal-Organic Frameworks for Size Control and Efficient Drug Loading*. *Crystal Growth & Design*, 2017. **17**(4): p. 1654-1660.
306. Zhu, X., et al., *Inherent anchorages in UiO-66 nanoparticles for efficient capture of alendronate and its mediated release*. *Chemical Communications*, 2014. **50**(63): p. 8779-8782.
307. Wu, Y.-n., et al., *Magnetic Metal-Organic Frameworks:  $\gamma$ -Fe<sub>2</sub>O<sub>3</sub>@MOFs via Confined In Situ Pyrolysis Method for Drug Delivery*. *Small*, 2014. **10**(14): p. 2927-2936.
308. He, S., et al., *Metal-organic frameworks for advanced drug delivery*. *Acta Pharmaceutica Sinica B*, 2021. **11**(8): p. 2362-2395.

309. Lawson, H.D., S.P. Walton, and C. Chan, *Metal–Organic Frameworks for Drug Delivery: A Design Perspective*. ACS Applied Materials & Interfaces, 2021. **13**(6): p. 7004-7020.
310. Yaghi, O.M., et al., *Reticular synthesis and the design of new materials*. Nature, 2003. **423**(6941): p. 705-714.
311. Horcajada, P., et al., *Porous metal–organic-framework nanoscale carriers as a potential platform for drug delivery and imaging*. Nature Materials, 2010. **9**(2): p. 172-178.
312. Yang, Y., et al., *A Large Capacity Cationic Metal–Organic Framework Nanocarrier for Physiological pH Responsive Drug Delivery*. Molecular Pharmaceutics, 2016. **13**(8): p. 2782-2786.
313. Rojas, S., et al., *Nanoscaled Zinc Pyrazolate Metal–Organic Frameworks as Drug-Delivery Systems*. Inorganic Chemistry, 2016. **55**(5): p. 2650-2663.
314. Zhang, P., et al., *Copper-Based Metal–Organic Framework as a Controllable Nitric Oxide-Releasing Vehicle for Enhanced Diabetic Wound Healing*. ACS Applied Materials & Interfaces, 2020. **12**(16): p. 18319-18331.
315. Feng, L., et al., *Controllable synthesis of metal-organic frameworks and their hierarchical assemblies*. Matter, 2019. **1**(4): p. 801-824.
316. Cravillon, J., et al., *Controlling Zeolitic Imidazolate Framework Nano- and Microcrystal Formation: Insight into Crystal Growth by Time-Resolved In Situ Static Light Scattering*. Chemistry of Materials, 2011. **23**(8): p. 2130-2141.
317. Canivet, J., et al., *Structure–property relationships of water adsorption in metal–organic frameworks*. New Journal of Chemistry, 2014. **38**(7): p. 3102-3111.
318. Illes, B., et al., *Exosome-Coated Metal–Organic Framework Nanoparticles: An Efficient Drug Delivery Platform*. Chemistry of Materials, 2017. **29**(19): p. 8042-8046.
319. Bennett, T.D., et al., *Facile Mechanochemistry of Amorphous Zeolitic Imidazolate Frameworks*. Journal of the American Chemical Society, 2011. **133**(37): p. 14546-14549.
320. Abazari, R., et al., *Chitosan Immobilization on Bio-MOF Nanostructures: A Biocompatible pH-Responsive Nanocarrier for Doxorubicin Release on MCF-7 Cell Lines of Human Breast Cancer*. Inorganic Chemistry, 2018. **57**(21): p. 13364-13379.
321. Kida, K., et al., *Formation of high crystalline ZIF-8 in an aqueous solution*. CrystEngComm, 2013. **15**(9): p. 1794-1801.
322. Yang, X., et al., *Nanoscale ATP-Responsive Zeolitic Imidazole Framework-90 as a General Platform for Cytosolic Protein Delivery and Genome Editing*. Journal of the American Chemical Society, 2019. **141**(9): p. 3782-3786.
323. Wang, Z., et al., *Nanoscale Zr-Based MOFs with Tailorable Size and Introduced Mesopore for Protein Delivery*. Advanced Functional Materials, 2018. **28**(16): p. 1707356.
324. Su, H., et al., *A highly porous medical metal–organic framework constructed from bioactive curcumin*. Chemical Communications, 2015. **51**(26): p. 5774-5777.
325. Liu, S., et al., *Nanoscale Zinc-Based Metal–Organic Frameworks Induce Neurotoxicity by Disturbing the Metabolism of Catecholamine Neurotransmitters*. Environmental Science & Technology, 2023. **57**(13): p. 5380-5390.
326. Sinha, P., et al., *Surface Area Determination of Porous Materials Using the Brunauer–Emmett–Teller (BET) Method: Limitations and Improvements*. The Journal of Physical Chemistry C, 2019. **123**(33): p. 20195-20209.
327. Parsaei, M. and K. Akhbari, *MOF-801 as a Nanoporous Water-Based Carrier System for In Situ Encapsulation and Sustained Release of 5-FU for Effective Cancer Therapy*. Inorganic Chemistry, 2022. **61**(15): p. 5912-5925.
328. Hoskins, B.F. and R. Robson, *Infinite polymeric frameworks consisting of three dimensionally linked rod-like segments*. Journal of the American Chemical Society, 1989. **111**(15): p. 5962-5964.
329. Yaghi, O.M., G. Li, and H. Li, *Selective binding and removal of guests in a microporous metal–organic framework*. Nature, 1995. **378**(6558): p. 703-706.

330. Wang, Y., et al., *Metal-organic frameworks for stimuli-responsive drug delivery*. *Biomaterials*, 2020. **230**: p. 119619.
331. Chui, S.S.-Y., et al., *A Chemically Functionalizable Nanoporous Material*. *Science*, 1999. **283**(5405): p. 1148-1150.
332. Férey, G., et al., *A Hybrid Solid with Giant Pores Prepared by a Combination of Targeted Chemistry, Simulation, and Powder Diffraction*. *Angewandte Chemie International Edition*, 2004. **43**(46): p. 6296-6301.
333. Cavka, J.H., et al., *A New Zirconium Inorganic Building Brick Forming Metal Organic Frameworks with Exceptional Stability*. *Journal of the American Chemical Society*, 2008. **130**(42): p. 13850-13851.
334. Li, H., et al., *Design and synthesis of an exceptionally stable and highly porous metal-organic framework*. *Nature*, 1999. **402**(6759): p. 276-279.
335. Ke, F., et al., *Synergistic antioxidant activity and anticancer effect of green tea catechin stabilized on nanoscale cyclodextrin-based metal-organic frameworks*. *Journal of Materials Science*, 2019. **54**(14): p. 10420-10429.
336. Deng, H., et al., *Multiple functional groups of varying ratios in metal-organic frameworks*. *Science*, 2010. **327**(5967): p. 846-850.
337. Park, K.S., et al., *Exceptional chemical and thermal stability of zeolitic imidazolate frameworks*. *Proceedings of the National Academy of Sciences*, 2006. **103**(27): p. 10186-10191.
338. Leng, X., et al., *Zirconium-Porphyrin PCN-222: pH-responsive Controlled Anticancer Drug Oridonin*. *Evidence-Based Complementary and Alternative Medicine*, 2018. **2018**: p. 3249023.
339. Horcajada, P., et al., *Metal-organic frameworks as efficient materials for drug delivery*. *Angewandte chemie*, 2006. **118**(36): p. 6120-6124.
340. Furukawa, H., et al., *The Chemistry and Applications of Metal-Organic Frameworks*. *Science*, 2013. **341**(6149): p. 1230444.
341. Arcos, V.-R.M.B.F., *D Mesoporous materials for drug delivery*. *Angewandte Chemie International Edition*, 2007. **46**(40): p. 7548-7558.
342. Wuttke, S., et al., *Positioning metal-organic framework nanoparticles within the context of drug delivery – A comparison with mesoporous silica nanoparticles and dendrimers*. *Biomaterials*, 2017. **123**: p. 172-183.
343. Chen, Y., et al., *Acid-Resistant Mesoporous Metal-Organic Framework toward Oral Insulin Delivery: Protein Encapsulation, Protection, and Release*. *Journal of the American Chemical Society*, 2018. **140**(17): p. 5678-5681.
344. Hou, L., et al., *Self-Regulated Carboxyphenylboronic Acid-Modified Mesoporous Silica Nanoparticles with “Touch Switch” Releasing Property for Insulin Delivery*. *ACS Applied Materials & Interfaces*, 2018. **10**(26): p. 21927-21938.
345. Peng, S., et al., *Metal-organic frameworks for precise inclusion of single-stranded DNA and transfection in immune cells*. *Nature Communications*, 2018. **9**(1): p. 1293.
346. Liang, K., et al., *Biomimetic mineralization of metal-organic frameworks as protective coatings for biomacromolecules*. *Nature Communications*, 2015. **6**(1): p. 7240.
347. Gao, P., et al., *Pt nanozyme-bridged covalent organic framework-aptamer nanoplatfor for tumor targeted self-strengthening photocatalytic therapy*. *Biomaterials*, 2023. **297**: p. 122109.
348. Röder, R., et al., *Multifunctional Nanoparticles by Coordinative Self-Assembly of His-Tagged Units with Metal-Organic Frameworks*. *Journal of the American Chemical Society*, 2017. **139**(6): p. 2359-2368.
349. Gao, P., et al., *Antitumor Agents Based on Metal-Organic Frameworks*. *Angewandte Chemie International Edition*, 2021. **60**(31): p. 16763-16776.
350. Poddar, A., et al., *Encapsulation, Visualization and Expression of Genes with Biomimetically Mineralized Zeolitic Imidazolate Framework-8 (ZIF-8)*. *Small*, 2019. **15**(36): p. 1902268.
351. Luzuriaga, M.A., et al., *Enhanced Stability and Controlled Delivery of MOF-Encapsulated Vaccines and Their Immunogenic Response In Vivo*. *ACS Applied Materials & Interfaces*, 2019. **11**(10): p. 9740-9746.

352. Mondloch, J.E., et al., *Activation of metal–organic framework materials*. CrystEngComm, 2013. **15**(45): p. 9258-9264.
353. Serre, C., et al., *Role of Solvent-Host Interactions That Lead to Very Large Swelling of Hybrid Frameworks*. Science, 2007. **315**(5820): p. 1828-1831.
354. Mellot-Draznieks, C., et al., *Very Large Swelling in Hybrid Frameworks: A Combined Computational and Powder Diffraction Study*. Journal of the American Chemical Society, 2005. **127**(46): p. 16273-16278.
355. Serre, C., et al., *Very Large Breathing Effect in the First Nanoporous Chromium(III)-Based Solids: MIL-53 or CrIII(OH)·{O2C–C6H4–CO2}·{HO2C–C6H4–CO2H}x·H2Oy*. Journal of the American Chemical Society, 2002. **124**(45): p. 13519-13526.
356. Tajahmadi, S., et al., *Adsorption Behavior of a Gd-Based Metal–Organic Framework toward the Quercetin Drug: Effect of the Activation Condition*. ACS Omega, 2022. **7**(45): p. 41177-41188.
357. Schnabel, J., R. Ettliger, and H. Bunzen, *Zn-MOF-74 as pH-Responsive Drug-Delivery System of Arsenic Trioxide*. ChemNanoMat, 2020. **6**(8): p. 1229-1236.
358. Férey, G. and C. Serre, *Large breathing effects in three-dimensional porous hybrid matter: facts, analyses, rules and consequences*. Chemical Society Reviews, 2009. **38**(5): p. 1380-1399.
359. Liu, Z., L. Zhang, and D. Sun, *Stimuli-responsive structural changes in metal–organic frameworks*. Chemical Communications, 2020. **56**(66): p. 9416-9432.
360. Horcajada, P., et al., *Flexible Porous Metal-Organic Frameworks for a Controlled Drug Delivery*. Journal of the American Chemical Society, 2008. **130**(21): p. 6774-6780.
361. Horcajada, P., et al., *Controlled release of Ibuprofen from dealuminated faujasites*. Solid State Sciences, 2006. **8**(12): p. 1459-1465.
362. Seo, J., et al., *A Pillared-Layer Coordination Polymer with a Rotatable Pillar Acting as a Molecular Gate for Guest Molecules*. Journal of the American Chemical Society, 2009. **131**(35): p. 12792-12800.
363. Kitaura, R., et al., *Porous Coordination-Polymer Crystals with Gated Channels Specific for Supercritical Gases*. Angewandte Chemie International Edition, 2003. **42**(4): p. 428-431.
364. Ji, M., et al., *Recent advances in nanoscale metal–organic frameworks for cancer chemodynamic therapy*. Nanoscale, 2023.
365. Yu, W., et al., *Porphyrin-Based Metal–Organic Framework Compounds as Promising Nanomedicines in Photodynamic Therapy*. ChemMedChem, 2020. **15**(19): p. 1766-1775.
366. Sun, Y., et al., *Metal–Organic Framework Nanocarriers for Drug Delivery in Biomedical Applications*. Nano-Micro Letters, 2020. **12**(1): p. 103.
367. Cabrera-García, A., et al., *Amino modified metal-organic frameworks as pH-responsive nanoplatforms for safe delivery of camptothecin*. Journal of Colloid and Interface Science, 2019. **541**: p. 163-174.
368. Gupta, V., et al., *PEG functionalized zirconium dicarboxylate MOFs for docetaxel drug delivery in vitro*. Journal of Drug Delivery Science and Technology, 2019. **52**: p. 846-855.
369. Min, K.H., et al., *Hydrophobically modified glycol chitosan nanoparticles-encapsulated camptothecin enhance the drug stability and tumor targeting in cancer therapy*. Journal of Controlled Release, 2008. **127**(3): p. 208-218.
370. Chen, X., et al., *Formulation of Metal–Organic Framework-Based Drug Carriers by Controlled Coordination of Methoxy PEG Phosphate: Boosting Colloidal Stability and Redispersibility*. Journal of the American Chemical Society, 2021. **143**(34): p. 13557-13572.
371. Li, X., et al., *Drug-Loaded Lipid-Coated Hybrid Organic-Inorganic “Stealth” Nanoparticles for Cancer Therapy*. Frontiers in Bioengineering and Biotechnology, 2020. **8**.
372. Trushina, D.B., et al., *Doxorubicin-Loaded Core–Shell UiO-66@SiO2 Metal–Organic Frameworks for Targeted Cellular Uptake and Cancer Treatment*. Pharmaceutics, 2022. **14**(7): p. 1325.
373. Taylor-Pashow, K.M., et al., *Postsynthetic modifications of iron-carboxylate nanoscale metal-organic frameworks for imaging and drug delivery*. J Am Chem Soc, 2009. **131**(40): p. 14261-3.

374. Teplensky, M.H., et al., *Temperature Treatment of Highly Porous Zirconium-Containing Metal–Organic Frameworks Extends Drug Delivery Release*. Journal of the American Chemical Society, 2017. **139**(22): p. 7522-7532.
375. Orellana-Tavra, C., et al., *Amorphous metal–organic frameworks for drug delivery*. Chemical Communications, 2015. **51**(73): p. 13878-13881.
376. Singh, N., S. Qutub, and N.M. Khashab, *Biocompatibility and biodegradability of metal organic frameworks for biomedical applications*. Journal of Materials Chemistry B, 2021. **9**(30): p. 5925-5934.
377. Tamames-Tabar, C., et al., *Cytotoxicity of nanoscaled metal–organic frameworks*. Journal of Materials Chemistry B, 2014. **2**(3): p. 262-271.
378. Wuttke, S., et al., *Validating Metal-Organic Framework Nanoparticles for Their Nanosafety in Diverse Biomedical Applications*. Advanced Healthcare Materials, 2017. **6**(2): p. 1600818.
379. Hao, F., Z.-Y. Yan, and X.-P. Yan, *Recent Advances in Research on the Effect of Physicochemical Properties on the Cytotoxicity of Metal–Organic Frameworks*. Small Science, 2022. **2**(9): p. 2200044.
380. Horcajada, P., et al., *Metal–Organic Frameworks in Biomedicine*. Chemical Reviews, 2012. **112**(2): p. 1232-1268.
381. Borovanský, J. and P.A. Riley, *Cytotoxicity of zinc in vitro*. Chemico-Biological Interactions, 1989. **69**(2): p. 279-291.
382. Karlsson, H.L., et al., *Copper Oxide Nanoparticles Are Highly Toxic: A Comparison between Metal Oxide Nanoparticles and Carbon Nanotubes*. Chemical Research in Toxicology, 2008. **21**(9): p. 1726-1732.
383. Zou, M.-Z., et al., *A Multifunctional Biomimetic Nanoplatform for Relieving Hypoxia to Enhance Chemotherapy and Inhibit the PD-1/PD-L1 Axis*. Small, 2018. **14**(28): p. 1801120.
384. Lin, G., et al., *Metal-organic frameworks nanoswitch: Toward photo-controllable endo/lysosomal rupture and release for enhanced cancer RNA interference*. Nano Research, 2020. **13**(1): p. 238-245.
385. Zhang, H., et al., *A Versatile Prodrug Strategy to In Situ Encapsulate Drugs in MOF Nanocarriers: A Case of Cytarabine-IR820 Prodrug Encapsulated ZIF-8 toward Chemo-Photothermal Therapy*. Advanced Functional Materials, 2018. **28**(35): p. 1802830.
386. Cheng, G., et al., *Self-Assembly of Extracellular Vesicle-like Metal–Organic Framework Nanoparticles for Protection and Intracellular Delivery of Biofunctional Proteins*. Journal of the American Chemical Society, 2018. **140**(23): p. 7282-7291.
387. Gan, N., et al., *Protein corona of metal-organic framework nanoparticles: Study on the adsorption behavior of protein and cell interaction*. International Journal of Biological Macromolecules, 2019. **140**: p. 709-718.
388. Keskin, S. and S. Kızılel, *Biomedical Applications of Metal Organic Frameworks*. Industrial & Engineering Chemistry Research, 2011. **50**(4): p. 1799-1812.
389. Baati, T., et al., *In depth analysis of the in vivo toxicity of nanoparticles of porous iron (III) metal–organic frameworks*. Chemical Science, 2013. **4**(4): p. 1597-1607.
390. Ding, Y., et al., *A Nanomedicine Fabricated from Gold Nanoparticles-Decorated Metal–Organic Framework for Cascade Chemo/Chemodynamic Cancer Therapy*. Advanced Science, 2020. **7**(17): p. 2001060.
391. Abánades Lázaro, I., et al., *Selective Surface PEGylation of UiO-66 Nanoparticles for Enhanced Stability, Cell Uptake, and pH-Responsive Drug Delivery*. Chem, 2017. **2**(4): p. 561-578.
392. Linnane, E., et al., *The uptake of metal–organic frameworks: a journey into the cell*. Chemical Society Reviews, 2022. **51**(14): p. 6065-6086.
393. Orellana-Tavra, C., S.A. Mercado, and D. Fairen-Jimenez, *Endocytosis Mechanism of Nano Metal-Organic Frameworks for Drug Delivery*. Advanced Healthcare Materials, 2016. **5**(17): p. 2261-2270.

394. Park, J., et al., *Size-Controlled Synthesis of Porphyrinic Metal–Organic Framework and Functionalization for Targeted Photodynamic Therapy*. *Journal of the American Chemical Society*, 2016. **138**(10): p. 3518-3525.
395. Duan, D., et al., *Size-Controlled Synthesis of Drug-Loaded Zeolitic Imidazolate Framework in Aqueous Solution and Size Effect on Their Cancer Theranostics in Vivo*. *ACS Applied Materials & Interfaces*, 2018. **10**(49): p. 42165-42174.
396. Haddad, S., et al., *Design of a Functionalized Metal–Organic Framework System for Enhanced Targeted Delivery to Mitochondria*. *Journal of the American Chemical Society*, 2020. **142**(14): p. 6661-6674.
397. Liu, J.-Q., et al., *Current and promising applications of Hf(IV)-based MOFs in clinical cancer therapy*. *Journal of Materials Chemistry B*, 2023.
398. Ding, S., et al., *Harnessing Hafnium-Based Nanomaterials for Cancer Diagnosis and Therapy*. *Small*. **n/a**(n/a): p. 2300341.
399. Bon, V., et al., *Zr(IV) and Hf(IV) based metal–organic frameworks with reo-topology*. *Chemical Communications*, 2012. **48**(67): p. 8407-8409.
400. Jakobsen, S., et al., *Structural determination of a highly stable metal-organic framework with possible application to interim radioactive waste scavenging: Hf-UiO-66*. *Physical Review B*, 2012. **86**(12): p. 125429.
401. Ni, K., et al., *Nanoscale metal-organic frameworks enhance radiotherapy to potentiate checkpoint blockade immunotherapy*. *Nat Commun*, 2018. **9**(1): p. 2351.
402. Zhou, W., et al., *Hafnium-Based Metal–Organic Framework Nanoparticles as a Radiosensitizer to Improve Radiotherapy Efficacy in Esophageal Cancer*. *ACS Omega*, 2022. **7**(14): p. 12021-12029.
403. Xu, D., et al., *Photodynamic therapy based on porphyrin-based metal-organic frameworks*. *Journal of Materials Chemistry B*, 2023.
404. Zhao, Y., et al., *Metal–Organic Frameworks with Enhanced Photodynamic Therapy: Synthesis, Erythrocyte Membrane Camouflage, and Aptamer-Targeted Aggregation*. *ACS Applied Materials & Interfaces*, 2020. **12**(21): p. 23697-23706.
405. Liu, C., et al., *Nd<sup>3+</sup>-Sensitized Upconversion Metal–Organic Frameworks for Mitochondria-Targeted Amplified Photodynamic Therapy*. *Angewandte Chemie International Edition*, 2020. **59**(7): p. 2634-2638.
406. Leng, X., et al., *Biocompatible Fe-Based Micropore Metal-Organic Frameworks as Sustained-Release Anticancer Drug Carriers*. *Molecules*, 2018. **23**(10): p. 2490.
407. Li, Y.-A., et al., *A drug-loaded nanoscale metal–organic framework with a tumor targeting agent for highly effective hepatoma therapy*. *Chemical Communications*, 2016. **52**(98): p. 14113-14116.
408. Zhou, Z., M. Vázquez-González, and I. Willner, *Stimuli-responsive metal–organic framework nanoparticles for controlled drug delivery and medical applications*. *Chemical Society Reviews*, 2021. **50**(7): p. 4541-4563.
409. Bunzen, H., *Chemical Stability of Metal-organic Frameworks for Applications in Drug Delivery*. *ChemNanoMat*, 2021. **7**(9): p. 998-1007.
410. Feng, S., et al., *Zeolitic imidazolate framework-8 (ZIF-8) for drug delivery: A critical review*. *Frontiers of Chemical Science and Engineering*, 2021. **15**(2): p. 221-237.
411. Jiang, K., et al., *Thermal Stimuli-Triggered Drug Release from a Biocompatible Porous Metal–Organic Framework*. *Chemistry – A European Journal*, 2017. **23**(42): p. 10215-10221.
412. Feng, J., et al., *Stimuli-responsive multifunctional metal–organic framework nanoparticles for enhanced chemo-photothermal therapy*. *Journal of Materials Chemistry B*, 2019. **7**(6): p. 994-1004.
413. Xiang, Z., et al., *MOF-derived novel porous Fe<sub>3</sub>O<sub>4</sub>@C nanocomposites as smart nanomedical platforms for combined cancer therapy: magnetic-triggered synergistic hyperthermia and chemotherapy*. *Journal of Materials Chemistry B*, 2020. **8**(37): p. 8671-8683.

414. Zeng, J.-Y., et al., *Porphyritic Metal–Organic Frameworks Coated Gold Nanorods as a Versatile Nanoplatforform for Combined Photodynamic/Photothermal/Chemotherapy of Tumor*. *Advanced Functional Materials*, 2018. **28**(8): p. 1705451.
415. Attia, M., et al., *Optimized metal-organic-framework based magnetic nanocomposites for efficient drug delivery and controlled release*. *Journal of Drug Delivery Science and Technology*, 2022. **76**: p. 103770.
416. Guan, X., et al., *A pH-Responsive Detachable PEG Shielding Strategy for Gene Delivery System in Cancer Therapy*. *Biomacromolecules*, 2017. **18**(4): p. 1342-1349.
417. Karakeçili, A., et al., *Metal-organic frameworks for on-demand pH controlled delivery of vancomycin from chitosan scaffolds*. *Materials Science and Engineering: C*, 2019. **105**: p. 110098.
418. Javanbakht, S., et al., *Carboxymethylcellulose capsulated Cu-based metal-organic framework-drug nanohybrid as a pH-sensitive nanocomposite for ibuprofen oral delivery*. *International Journal of Biological Macromolecules*, 2018. **119**: p. 588-596.
419. Yang, K., et al., *A supramolecular hybrid material constructed from pillar[6]arene-based host–guest complexation and ZIF-8 for targeted drug delivery*. *Chemical Communications*, 2018. **54**(70): p. 9817-9820.
420. Zheng, H., et al., *One-pot Synthesis of Metal–Organic Frameworks with Encapsulated Target Molecules and Their Applications for Controlled Drug Delivery*. *Journal of the American Chemical Society*, 2016. **138**(3): p. 962-968.
421. Low, J.J., et al., *Virtual High Throughput Screening Confirmed Experimentally: Porous Coordination Polymer Hydration*. *Journal of the American Chemical Society*, 2009. **131**(43): p. 15834-15842.
422. Railey, P., et al., *Metal organic frameworks with immobilized nanoparticles: Synthesis and applications in photocatalytic hydrogen generation and energy storage*. *Materials Research Bulletin*, 2017. **96**: p. 385-394.
423. Jiang, K., et al., *Indocyanine green–encapsulated nanoscale metal–organic frameworks for highly effective chemo-photothermal combination cancer therapy*. *Materials Today Nano*, 2018. **2**: p. 50-57.
424. Chen, X., et al., *MOF Nanoparticles with Encapsulated Autophagy Inhibitor in Controlled Drug Delivery System for Antitumor*. *ACS Applied Materials & Interfaces*, 2018. **10**(3): p. 2328-2337.
425. Velásquez-Hernández, M.d.J., et al., *Degradation of ZIF-8 in phosphate buffered saline media*. *CrystEngComm*, 2019. **21**(31): p. 4538-4544.
426. Yan, L., et al., *Size Controllable and Surface Tunable Zeolitic Imidazolate Framework-8–Poly(acrylic acid sodium salt) Nanocomposites for pH Responsive Drug Release and Enhanced in Vivo Cancer Treatment*. *ACS Applied Materials & Interfaces*, 2017. **9**(38): p. 32990-33000.
427. Wang, H., et al., *One-pot synthesis of poly(ethylene glycol) modified zeolitic imidazolate framework-8 nanoparticles: Size control, surface modification and drug encapsulation*. *Colloids and Surfaces A: Physicochemical and Engineering Aspects*, 2019. **568**: p. 224-230.
428. Silva, J.Y.R., et al., *A thermo-responsive adsorbent-heater-thermometer nanomaterial for controlled drug release: (ZIF-8,EuxTby)@AuNP core-shell*. *Materials Science and Engineering: C*, 2019. **102**: p. 578-588.
429. Carrillo-Carrión, C., et al., *Aqueous Stable Gold Nanostar/ZIF-8 Nanocomposites for Light-Triggered Release of Active Cargo Inside Living Cells*. *Angewandte Chemie International Edition*, 2019. **58**(21): p. 7078-7082.
430. Ke, F., et al., *Facile fabrication of magnetic metal–organic framework nanocomposites for potential targeted drug delivery*. *Journal of Materials Chemistry*, 2011. **21**(11): p. 3843-3848.
431. Zhuang, J., et al., *Optimized Metal–Organic-Framework Nanospheres for Drug Delivery: Evaluation of Small-Molecule Encapsulation*. *ACS Nano*, 2014. **8**(3): p. 2812-2819.
432. Bian, R., et al., *A combination of tri-modal cancer imaging and in vivo drug delivery by metal–organic framework based composite nanoparticles*. *Biomaterials Science*, 2015. **3**(9): p. 1270-1278.

433. Fang, J., et al., *Extremely low frequency alternating magnetic field-triggered and MRI-traced drug delivery by optimized magnetic zeolitic imidazolate framework-90 nanoparticles*. *Nanoscale*, 2016. **8**(6): p. 3259-3263.
434. Ray Chowdhuri, A., D. Bhattacharya, and S.K. Sahu, *Magnetic nanoscale metal organic frameworks for potential targeted anticancer drug delivery, imaging and as an MRI contrast agent*. *Dalton Transactions*, 2016. **45**(7): p. 2963-2973.
435. Gao, X., et al., *Controllable Synthesis of a Smart Multifunctional Nanoscale Metal–Organic Framework for Magnetic Resonance/Optical Imaging and Targeted Drug Delivery*. *ACS Applied Materials & Interfaces*, 2017. **9**(4): p. 3455-3462.
436. Sharma, S., K. Sethi, and I. Roy, *Magnetic nanoscale metal–organic frameworks for magnetically aided drug delivery and photodynamic therapy*. *New Journal of Chemistry*, 2017. **41**(20): p. 11860-11866.
437. Ebrahimi, A.K., M. Barani, and I. Sheikshoae, *Fabrication of a new superparamagnetic metal-organic framework with core-shell nanocomposite structures: Characterization, biocompatibility, and drug release study*. *Materials Science and Engineering: C*, 2018. **92**: p. 349-355.
438. Wu, M.-X., et al., *Multistimuli Responsive Core–Shell Nanoplatfom Constructed from Fe<sub>3</sub>O<sub>4</sub>@MOF Equipped with Pillar[6]arene Nanovalves*. *Small*, 2018. **14**(17): p. 1704440.
439. Chen, J., et al., *Metal-organic framework-coated magnetite nanoparticles for synergistic magnetic hyperthermia and chemotherapy with pH-triggered drug release*. *Science and Technology of Advanced Materials*, 2019. **20**(1): p. 1043-1054.
440. Lin, J., et al., *Fe<sub>3</sub>O<sub>4</sub>–ZIF-8 assemblies as pH and glutathione responsive T<sub>2</sub>–T<sub>1</sub> switching magnetic resonance imaging contrast agent for sensitive tumor imaging in vivo*. *Chemical Communications*, 2019. **55**(4): p. 478-481.
441. Nejadshafiee, V., et al., *Magnetic bio-metal–organic framework nanocomposites decorated with folic acid conjugated chitosan as a promising biocompatible targeted theranostic system for cancer treatment*. *Materials Science and Engineering: C*, 2019. **99**: p. 805-815.
442. Terzopoulou, A., et al., *Biodegradable Metal–Organic Framework-Based Microrobots (MOFBOTs)*. *Advanced Healthcare Materials*, 2020. **9**(20): p. 2001031.
443. Li, J., et al., *Construction and characterization of magnetic cascade metal-organic framework/enzyme hybrid nanoreactors with enhanced effect on killing cancer cells*. *Colloids and Surfaces A: Physicochemical and Engineering Aspects*, 2020. **601**: p. 124990.
444. Ebrahimpour, A., et al., *Magnetic Metal–Organic Framework Based on Zinc and 5-Aminolevulinic Acid: MR Imaging and Brain Tumor Therapy*. *Journal of Inorganic and Organometallic Polymers and Materials*, 2021. **31**(3): p. 1208-1216.
445. Meng, Z., et al., *Functional metal–organic framework-based nanocarriers for accurate magnetic resonance imaging and effective eradication of breast tumor and lung metastasis*. *Journal of Colloid and Interface Science*, 2021. **581**: p. 31-43.
446. Gaab, M., et al., *The progression of Al-based metal-organic frameworks – From academic research to industrial production and applications*. *Microporous and Mesoporous Materials*, 2012. **157**: p. 131-136.
447. Pelosi, E., G. Castelli, and U. Testa, *Pancreatic Cancer: Molecular Characterization, Clonal Evolution and Cancer Stem Cells*. *Biomedicines*, 2017. **5**(4).
448. Ducreux, M., et al., *Systemic treatment of pancreatic cancer revisited*. *Seminars in Oncology*, 2019. **46**(1): p. 28-38.
449. Siegel, R.L., et al., *Cancer Statistics, 2021*. *CA: A Cancer Journal for Clinicians*, 2021. **71**(1): p. 7-33.
450. Rahib, L., et al., *Projecting cancer incidence and deaths to 2030: the unexpected burden of thyroid, liver, and pancreas cancers in the United States*. *Cancer Res*, 2014. **74**(11): p. 2913-21.
451. Ferlay, J., C. Partensky, and F. Bray, *More deaths from pancreatic cancer than breast cancer in the EU by 2017*. *Acta Oncologica*, 2016. **55**(9-10): p. 1158-1160.

452. Yachida, S., et al., *Distant metastasis occurs late during the genetic evolution of pancreatic cancer*. Nature, 2010. **467**(7319): p. 1114-7.
453. Korc, M., *Driver mutations: a roadmap for getting close and personal in pancreatic cancer*. Cancer Biol Ther, 2010. **10**(6): p. 588-91.
454. Buscail, L., B. Bournet, and P. Cordelier, *Role of oncogenic KRAS in the diagnosis, prognosis and treatment of pancreatic cancer*. Nat Rev Gastroenterol Hepatol, 2020. **17**(3): p. 153-168.
455. Zhang, Q., et al., *Pancreatic Cancer Epidemiology, Detection, and Management*. Gastroenterol Res Pract, 2016. **2016**: p. 8962321.
456. Morton, J.P., et al., *Mutant p53 drives metastasis and overcomes growth arrest/senescence in pancreatic cancer*. Proceedings of the National Academy of Sciences, 2010. **107**(1): p. 246-251.
457. Jones, S., et al., *Core signaling pathways in human pancreatic cancers revealed by global genomic analyses*. science, 2008. **321**(5897): p. 1801-1806.
458. Storz, P. and H.C. Crawford, *Carcinogenesis of Pancreatic Ductal Adenocarcinoma*. Gastroenterology, 2020. **158**(8): p. 2072-2081.
459. Meng, H. and A.E. Nel, *Use of nano engineered approaches to overcome the stromal barrier in pancreatic cancer*. Advanced Drug Delivery Reviews, 2018. **130**: p. 50-57.
460. Nia, H.T., L.L. Munn, and R.K. Jain, *Mapping Physical Tumor Microenvironment and Drug Delivery*. Clin Cancer Res, 2019. **25**(7): p. 2024-2026.
461. Wang, J., et al., *Tumor Priming by SMO Inhibition Enhances Antibody Delivery and Efficacy in a Pancreatic Ductal Adenocarcinoma Model*. Mol Cancer Ther, 2019. **18**(11): p. 2074-2084.
462. Cheng, Z.X., et al., *Effects of the HIF-1 $\alpha$  and NF- $\kappa$ B loop on epithelial-mesenchymal transition and chemoresistance induced by hypoxia in pancreatic cancer cells*. Oncol Rep, 2014. **31**(4): p. 1891-8.
463. Shukla, S.K., et al., *MUC1 and HIF-1 $\alpha$  Signaling Crosstalk Induces Anabolic Glucose Metabolism to Impart Gemcitabine Resistance to Pancreatic Cancer*. Cancer Cell, 2017. **32**(1): p. 71-87.e7.
464. Zhang, Z., et al. *Hypoxia potentiates gemcitabine-induced stemness in pancreatic cancer cells through AKT/Notch1 signaling*. Journal of experimental & clinical cancer research : CR, 2018. **37**, 291 DOI: 10.1186/s13046-018-0972-3.
465. Sperb, N., M. Tsesmelis, and T. Wirth, *Crosstalk between Tumor and Stromal Cells in Pancreatic Ductal Adenocarcinoma*. International Journal of Molecular Sciences, 2020. **21**(15): p. 5486.
466. Neoptolemos, J.P., et al., *Therapeutic developments in pancreatic cancer: current and future perspectives*. Nature Reviews Gastroenterology & Hepatology, 2018. **15**(6): p. 333-348.
467. Liu, X., et al., *Predictors of distant metastasis on exploration in patients with potentially resectable pancreatic cancer*. BMC Gastroenterology, 2018. **18**(1): p. 168.
468. Hackert, T., et al., *Locally Advanced Pancreatic Cancer: Neoadjuvant Therapy With FOLFIRINOX Results in Resectability in 60% of the Patients*. Annals of Surgery, 2016. **264**(3): p. 457-463.
469. Janssen, Q.P., et al., *Neoadjuvant FOLFIRINOX in Patients With Borderline Resectable Pancreatic Cancer: A Systematic Review and Patient-Level Meta-Analysis*. JNCI: Journal of the National Cancer Institute, 2019. **111**(8): p. 782-794.
470. Von Hoff, D.D., et al., *Increased Survival in Pancreatic Cancer with nab-Paclitaxel plus Gemcitabine*. New England Journal of Medicine, 2013. **369**(18): p. 1691-1703.
471. Jiang, Y. and D.P.S. Sohal, *Pancreatic Adenocarcinoma Management*. JCO Oncology Practice, 2023. **19**(1): p. 19-32.
472. Kim, G., *nab-Paclitaxel for the treatment of pancreatic cancer*. Cancer Manag Res, 2017. **9**: p. 85-96.
473. Desai, N., et al., *Increased antitumor activity, intratumor paclitaxel concentrations, and endothelial cell transport of cremophor-free, albumin-bound paclitaxel, ABI-007, compared with cremophor-based paclitaxel*. Clin Cancer Res, 2006. **12**(4): p. 1317-24.
474. Giordano, G., et al., *Nano albumin bound-paclitaxel in pancreatic cancer: Current evidences and future directions*. World J Gastroenterol, 2017. **23**(32): p. 5875-5886.

475. Alvarez, R., et al., *Stromal disrupting effects of nab-paclitaxel in pancreatic cancer*. British journal of cancer, 2013. **109**(4): p. 926-933.
476. Ur Rehman, S.S., K. Lim, and A. Wang-Gillam, *Nanoliposomal irinotecan plus fluorouracil and folinic acid: a new treatment option in metastatic pancreatic cancer*. Expert Review of Anticancer Therapy, 2016. **16**(5): p. 485-492.
477. Drummond, D.C., et al., *Development of a highly active nanoliposomal irinotecan using a novel intraliposomal stabilization strategy*. Cancer research, 2006. **66**(6): p. 3271-3277.
478. Kang, M.H., et al., *Activity of MM-398, nanoliposomal irinotecan (nal-IRI), in Ewing's family tumor xenografts is associated with high exposure of tumor to drug and high SLFN11 expression*. Clinical Cancer Research, 2015. **21**(5): p. 1139-1150.
479. Zhu, L., H. Mao, and L. Yang, *Advanced iron oxide nanotheranostics for multimodal and precision treatment of pancreatic ductal adenocarcinoma*. WIREs Nanomedicine and Nanobiotechnology, 2022. **14**(4): p. e1793.
480. Cabral, H., et al., *Accumulation of sub-100 nm polymeric micelles in poorly permeable tumours depends on size*. Nature Nanotechnology, 2011. **6**(12): p. 815-823.
481. Cutsem, E.V., et al., *Randomized Phase III Trial of Pegvorhialuronidase Alfa With Nab-Paclitaxel Plus Gemcitabine for Patients With Hyaluronan-High Metastatic Pancreatic Adenocarcinoma*. Journal of Clinical Oncology, 2020. **38**(27): p. 3185-3194.
482. Catenacci, D.V.T., et al., *Randomized Phase Ib/II Study of Gemcitabine Plus Placebo or Vismodegib, a Hedgehog Pathway Inhibitor, in Patients With Metastatic Pancreatic Cancer*. Journal of Clinical Oncology, 2015. **33**(36): p. 4284-4292.
483. Lee, J.J., et al., *Stromal response to Hedgehog signaling restrains pancreatic cancer progression*. Proceedings of the National Academy of Sciences, 2014. **111**(30): p. E3091-E3100.
484. Murphy, J.E., et al., *Total Neoadjuvant Therapy With FOLFIRINOX in Combination With Losartan Followed by Chemoradiotherapy for Locally Advanced Pancreatic Cancer: A Phase 2 Clinical Trial*. JAMA Oncology, 2019. **5**(7): p. 1020-1027.
485. Diop-Frimpong, B., et al., *Losartan inhibits collagen I synthesis and improves the distribution and efficacy of nanotherapeutics in tumors*. Proceedings of the National Academy of Sciences, 2011. **108**(7): p. 2909-2914.
486. Hidalgo, M., *Pancreatic cancer*. N Engl J Med, 2010. **362**(17): p. 1605-17.
487. Zhan, H.-x., et al., *Pancreatic cancer stem cells: New insight into a stubborn disease*. Cancer Letters, 2015. **357**(2): p. 429-437.
488. Hermann, P.C., et al., *Distinct populations of cancer stem cells determine tumor growth and metastatic activity in human pancreatic cancer*. Cell stem cell, 2007. **1**(3): p. 313-323.
489. Lei, F., et al., *Combination Therapies and Drug Delivery Platforms in Combating Pancreatic Cancer*. The Journal of Pharmacology and Experimental Therapeutics, 2019. **370**(3): p. 682-694.
490. Bear, A.S., R.H. Vonderheide, and M.H. O'Hara, *Challenges and opportunities for pancreatic cancer immunotherapy*. Cancer cell, 2020. **38**(6): p. 788-802.
491. Vesely, M.D., et al., *Natural Innate and Adaptive Immunity to Cancer*. Annual Review of Immunology, 2011. **29**(1): p. 235-271.
492. Chen, Daniel S. and I. Mellman, *Oncology Meets Immunology: The Cancer-Immunity Cycle*. Immunity, 2013. **39**(1): p. 1-10.
493. Roche, H., *A Study of Multiple Immunotherapy-Based Treatment Combinations in Participants With Metastatic Pancreatic Ductal Adenocarcinoma (Morpheus-Pancreatic Cancer).* Accessed April 10, 2023.
494. Kim, D.K., et al., *PD-L1-directed PIGF/VEGF blockade synergizes with chemotherapy by targeting CD141+ cancer-associated fibroblasts in pancreatic cancer*. Nature Communications, 2022. **13**(1): p. 6292.
495. Liu, X., et al., *Tumor-penetrating peptide enhances transcytosis of silicasome-based chemotherapy for pancreatic cancer*. The Journal of clinical investigation, 2017. **127**(5): p. 2007-2018.

496. Li, H.-J., et al., *Smart Superstructures with Ultrahigh pH-Sensitivity for Targeting Acidic Tumor Microenvironment: Instantaneous Size Switching and Improved Tumor Penetration*. ACS Nano, 2016. **10**(7): p. 6753-6761.
497. Lu, T. and J. Prakash, *Nanomedicine strategies to enhance tumor drug penetration in pancreatic cancer*. International journal of nanomedicine, 2021. **16**: p. 6313.
498. Beola, L., et al., *Critical Parameters to Improve Pancreatic Cancer Treatment Using Magnetic Hyperthermia: Field Conditions, Immune Response, and Particle Biodistribution*. ACS Applied Materials & Interfaces, 2021. **13**(11): p. 12982-12996.
499. Kim, D.-H., et al., *Temperature-Sensitive Magnetic Drug Carriers for Concurrent Gemcitabine Chemohyperthermia*. Advanced Healthcare Materials, 2014. **3**(5): p. 714-724.

# Objectives

The overall aim of the thesis project is to participate within the HeatNMof EU project into the development of magnetic nanocomposites (NCs) based on MOFs to enable magnetic field (MF)-responsive cargo release in the targeted tumors.

To achieve this major aim, we first worked to provide a proof-of-concept for the ability to control the cargo release from the NCs by MF. In this part, NCs prepared by the project partners in the University of Santiago De Compostela were used in order to study their magnetic characterization as well as to study their biological interactions on model tumor cells. The synthesized NCs consisted of iron oxide nanoparticle cores and zeolitic imidazolate frameworks-8 MOF shells, which were loaded with cresyl violet (CV) fluorescent probe. The magnetic properties of the NCs were investigated, notably their saturation magnetization as well as their zero-field-cooled/field-cooled cycles. Afterwards, MiaPaCa2 cancer cells and cancer-associated fibroblasts (CAF) were used as model cells on which the NC cellular uptake kinetic and subcellular localization were studied. Thereafter, the MF-induced CV cargo release from the NCs uptaken by the model cells were studied in response to high-frequency alternating MF or the low-frequency rotating MF to induce MNP heating or mechanical movement, respectively. Events associated with the intracellular CV release were also characterized in the used cell in 2D as well as 3D multicellular spheroid models.

After the proof-of-concept on the NCs loaded with the model fluorescent cargo, we aimed to do a preliminary study to investigate the feasibility of synthesizing the NCs with different anticancer drug loads. Herein, two chemotherapeutic drugs (5-fluoruracil and doxorubicin) were used for preparing drug-loaded nanocomposites where the loading of each drug was investigated by two approaches, in-situ approach as well as the post-synthesis impregnation one.

In order to enhance the accumulation of the magnetic NCs in the targeted tumors, we aimed to investigate designing of a novel setup that could enable the accumulation of MNP-based carriers into deep-seated tumors. For this study, COMSOL Multiphysics® simulations were used to optimize the parameters of the setup components, especially the coils and the permanent magnet parameters. Also, we worked to provide a simulation-based proof-of-concept for the setup design to target MNP-based nanocarriers to deep tumors. Afterwards, the experimental work was done for building the setup components, notably the coils and the setup support.

Collectively, this work aimed to participate towards the development of MOF-based magnetic nanocomposites for targeted on-demand MF-cargo release inside targeted tumors. Using a MNP focusing setup, the magnetic NCs could have preferential accumulation in the targeted tissues.

Afterwards, by applying the AMF or RMF, the NCs cargo can be released in a controlled pattern inside the targeted tissues allowing high drug concentrations in the targeted tissues and less side effects on the other healthy non-targeted ones.

# Results

First part of results: Magnetic field-induced cargo release from magnetic nanoparticles@metal-organic frameworks nanocomposites through heating or mechanical actuation

Enabling magnetic field(MF)-responsive cargo release from magnetic nanoparticles@metal-organic frameworks (MOFs) nanocomposites could be a promising strategy for cancer treatment, as explained in the thesis state-of-the-art part. MOFs have a major advantage of high porosity and consequently potential high loading capacities. A sudden on-demand triggered release of high local amounts of cytotoxic cargos in the cancer cells could help to enhance their tumor-killing ability. This stimuli-responsive cargo release could be triggered by exposing the nanocomposites to high-frequency alternating MF (AMF) or low-frequency rotating MF (RMF) inducing the MNP heating or movement, respectively.

This part mainly investigated the AMF and RMF responsive release from the MNP-based MOFs. It was done using nanocomposites synthesized and physicochemical characterized by our HeatNMofs project collaborators in *Bionanotools lab at the University of Santiago de Compostela*. Then, we investigated the nanocomposite magnetic properties, cellular interactions and the intracellular MF-induced cargo release by both AMF and RMF. This part will be presented in a research paper format.

**Magnetic field-induced cargo release from magnetic nanoparticles@metal-organic  
frameworks nanocomposites through heating or mechanical actuation**

Ahmed Abdelhamid<sup># 1,2,3</sup>, Aitor Álvarez<sup># 4</sup>, Loubna Laib<sup># 1,2</sup>, Pascal Clerc<sup>1</sup>, Manuel Ceballos<sup>4</sup>, Anil Misra<sup>3</sup>,  
Mohammad S. Alavijeh<sup>3</sup>, Corinne Bousquet<sup>2</sup>, Beatriz Pelaz<sup>4</sup>, Pablo del Pino\*<sup>4</sup>, Julian Carrey\*<sup>2</sup>,  
Véronique Gigoux\*<sup>1</sup>

1. INSERM UMR 1037, Team 6 MICROPANC, Cancer Research Center of Toulouse, Toulouse, France
2. Laboratoire de Physique et Chimie des Nano-Objets, CNRS-UPS-INSA UMR5215, Toulouse, France
3. Pharmidex Pharmaceutical Services, Office 3.05, 1 King Street, London, EC2V 8AU, United Kingdom
4. Centro Singular de Investigación en Química Biológica y Materiales Moleculares (CIQUS), Santiago de Compostela, Spain

# : equal participation

\* : Corresponding authors : Véronique Gigoux, Centre de Recherches en Cancérologie de Toulouse, INSERM U1037, Team MICROPANC, 2 Avenue Hubert Curien, 31037 Toulouse, France. Email: [veronique.gigoux@inserm.fr](mailto:veronique.gigoux@inserm.fr) – Julian Carrey, LPCNO-CNRS UMR5215, 135 avenue de Rangueil, F-31077 Toulouse, France. Email: [julian.carrey@insa-toulouse.fr](mailto:julian.carrey@insa-toulouse.fr) - Pablo del Pino González de la Higuera, Centro Singular de Investigación en Química Biológica y Materiales Moleculares (CIQUS), C/ Jenaro de la Fuente s/n | Campus Vida | Universidade de Santiago de Compostela, 15782 Santiago de Compostela, Spain. Email: [pablo.delpino@usc.es](mailto:pablo.delpino@usc.es)

## ABSTRACT

Metal-organic frameworks (MOFs) hold a great promise for anticancer drug delivery applications due to their large tunable porosity and structural flexibility, allowing their design with high drug loading capacity and biocompatibility. However, it is still challenging to reduce their off-target non-controlled drug release. The aim of this study is to develop magnetic field (MF)-responsive magnetic nanocomposites based on MOFs to enable controlled site-specific drug release. The synthesized nanocomposites consisted of superparamagnetic iron oxide magnetic nanoparticle cores and a nanometric zeolitic imidazolate frameworks-8 (ZIF-8) MOF shells, which were loaded with cresyl violet (CV) fluorescent probe. They were also stabilized in aqueous media through coating with an amphiphilic polymer that prevented the ZIF-8 shell degradation. Afterwards, the CV release was studied in MiaPaCa2 cancer cells and cancer-associated fibroblasts (CAF) upon exposure to alternating high-frequency MF (AMF) or rotating low-frequency MF (RMF). Both the AMF and RMF exposures resulted in a significantly increased CV release inside the cells. Moreover, it was observed that the CV release was associated with a decrease in cell viability in MiaPaCa2 exposed to AMF or RMF, and in CAF exposed to AMF. In addition, both AMF or RMF exposures induced a CV release from the nanocomposites in MiaPaCa2/CAF spheroids and decreased their size. These results indicate that spatiotemporal control over the cargo release from the developed MOF nanocomposites could be achieved through MF-responsive properties either thermally or mechanically. Hence, the developed MOF-based magnetic nanocomposites could be promising platforms for developing MF-responsive delivery systems for cancer treatment applications.

**Keywords (5-7):** magnetic nanoparticles, magnetic hyperthermia, mechanical forces, cancer, metal-organic frameworks, drug delivery

## Introduction

The application of nanotechnology in the field of medicine fostered the development of new drug delivery systems for cancer treatment. Myriad of organic, inorganic and composites nanomedicines have been developed for anticancer drug delivery applications to improve the bioavailability and reduce the side effects of chemotherapeutic drugs, enhancing their efficacy and therapeutic outcomes [1, 2]. For example, pegylated liposomal doxorubicin, also known as Doxil/Caelyx, was the first FDA-approved nanomedicine for a variety of tumors such as ovarian cancer. It offered an extended circulation time and improved metabolic stability of doxorubicin. Consequently, it showed an enhanced accumulation in the tumor sites with high vascular permeability and reduced undesirable side effects, such as cardiac toxicity [3]. Pharmacokinetics and tissue targeting of nanomedicine are largely associated with their physicochemical properties such as hydrodynamic size, shape, charge, and other surface properties [4, 5]. Depending on these properties, intravenously administrated nanoparticles could be rapidly eliminated by the kidney or interact with blood components. The nanoparticles interaction with plasma proteins and opsonins leads to their phagocytosis by the mononuclear cells (as macrophages) with accumulation in the liver and spleen [6]. Although key breakthroughs were recently made with stealth polymer coating such as poly(ethylene glycol) (PEG) and active targeting, it is still challenging to reduce the nanocarriers off-target accumulation and drug release [7, 8].

Alternatively, stimuli-sensitive nanocarriers have recently emerged as novel systems with spatial and temporal controllability in response to various endogenous or exogenous stimuli. Such stimuli could allow site-specific responsive release of the loaded drug, reducing the potential side effects caused by its premature or off-target release [9]. Endogenous stimuli enriched in the biological microenvironment, such as pH variation, enzymes or redox gradient, could trigger drug release by activating responsive components in the nanocarriers. In addition, exogenous stimuli such as light, magnetic field, ultrasound, temperature, electric field or radiofrequency waves can achieve a responsive remote spatiotemporal control over the release of the loaded drug.

Magnetic fields (MF) are key triggers that do not suffer from tissue penetration depth limitation. Hence, they could allow noninvasive controlled responses of magnetic nanoparticles (MNPs). Therefore, MNP integration in drug delivery systems could offer a responsive probe for a remotely controlled drug release *via* MF stimuli. In addition, they can be used as contrast agents for magnetic resonance imaging (MRI) or magnetic particle imaging (MPI), opening avenues for theranostic applications [10]. Iron oxide magnetic nanoparticles (IONPs), owing to their properties, represent one of the most promising tools to elaborate stimuli-responsive drug delivery systems by releasing thermal or mechanical energy upon MF exposure [11]. Moreover, IONPs are highly biocompatible due to their degradation over weeks resulting in iron recycling [12].

In recent years, the application of metal-organic frameworks (MOFs) – especially nanoscale MOFs – in biomedicine has become a rapidly developing research topic. MOFs are porous hybrid materials composed of inorganic metal ions coordinated with organic linkers to form cavities of diverse sizes and shapes. Compared to traditional MOFs, nanoscale MOFs possess a similarly high porosity but with a larger surface area that could endow enhanced biological activity, chemical/colloidal stability, more effective surface modification, and improved pharmacokinetic properties [13, 14]. Thanks to their versatile composition and structural features, MOFs with a large tunable porosity, high drug loading capacity and biocompatibility could be synthesized [15-17]. Moreover, the hydrophilic/hydrophobic internal microenvironment of MOFs makes them conveniently adapted to host a wide variety of molecules (small molecules, macromolecules including enzymes and nucleic acids...) [16].

Although progressive drug release can be achieved from MOFs, mainly by pore diffusion, drug-matrix interaction and/or degradation, stimuli-responsive MOFs have attracted tremendous attention to achieve on-demand controlled drug release for cancer treatment applications [16]. However, most of them respond to endogenous stimuli such as pH, redox or ions, and only few light- or MF-responsive MOF-based drug delivery systems have been developed [16, 18, 19].

For example, a plasmonic core-shell Au nanoparticles / zeolitic-imidazolate-framework-8 (ZIF-8) nanocomposites were previously developed as a thermoresponsive nanocarrier, in which gold nanoparticle was a photothermal agent and ZIF-8 shell was a carrier to load doxorubicin [20, 21]. In addition, rat serum albumin coated  $\text{Fe}_3\text{O}_4$ @ZIF-90 nanocomposites were developed by Fang *et al.* to release their 5-fluorouracil drug load in response to one exposure to extremely low frequency alternating MF (20 Hz and 20 mT) [22]. Another study by Attia *et al.* reported an enhancing killing effect of mertansine loaded nanocomposites ( $\text{Fe}_3\text{O}_4$  conjugated with MIL-88B- $\text{NH}_2$  MOFs) on U251 glioblastoma cells after two alternating MF exposures (27.3 mT, 250 kHz) [23]. To date, the control of the drug release from MOFs by the MF stimuli remains largely unexplored, with no study comparing the release efficiency in response to different types of MF stimuli. For instance, MNP exposure to alternating high-frequency MF (AMF) can induce their heating, while the rotating low-frequency MF (RMF) can trigger MNP movement and mechanical actuation. The interest in comparing the AMF and RMF stimuli is to get more insights into the difference between thermal and non-thermal MF triggers in inducing drug release from MOF delivery systems.

In this study, we developed core-shell magnetic nanocomposites that consisted of superparamagnetic IONPs cores and nanometric ZIF-8 MOF shells for MF-induced anticancer drug delivery applications. The IONPs were utilized as a magnetic heating or mechanical seed, and the ZIF-8 porous shell served as a nanocarrier to load a fluorescent probe, cresyl violet (CV). Coating with an amphiphilic polymer, poly-[isobutylene-alt-maleic anhydride]-graft-dodecyl (PMA), enabled the

aqueous stability of the nanocomposites (IONP-CV@ZIF-8@PMA). The PMA polymer coat was labeled with fluorescein to allow cellular trafficking of the nanocomposites.

The physicochemical and magnetic properties of IONPs and magnetic nanocomposites were determined. We also studied the biocompatibility and subcellular localization of the IONP-CV@ZIF-8@PMA nanocomposites on pancreatic MiaPaCa2 cancer cells and cancer-associated fibroblasts (CAF). In addition, the CV release from the IONP-CV@ZIF-8@PMA nanocomposites in response to thermal or mechanical actuation of IONPs was investigated inside MiaPaCa2 and CAF cells 2D culture models, as well as on their spheroids. The impact of the nanocomposite heating or motion and CV release on cell viability and spheroid growth was finally analyzed.

## **MATERIALS AND METHODS**

Iron (III) chloride (97%, Sigma-Aldrich #157740), iron (II) chloride (98%, Sigma-Aldrich #372870), 1-Octadecene (90%, Sigma-Aldrich #O806), oleic acid (90%, Sigma-Aldrich #364525), hexadecyltrimethylammonium bromide (98%, Sigma-Aldrich #H5882), 2-methylimidazole (99%, Sigma-Aldrich #M50850) and zinc nitrate hexahydrate (98%, Sigma-Aldrich #228737) sodium oleate (99%, Strem Chemicals #11-1280) were used for NP synthesis. All reagents were used as received without purification. Poly[isobutylene-*alt*-maleic anhydride]-graft-dodecyl (PMA) polymer was synthesized as described previously [24]. All glassware was cleaned with aqua regia and rinsed with Milli-Q water, methanol and acetone. Aqua regia oxidizes and dissolves inorganic and organic impurities, which may interfere with the nanoparticle synthesis. Aqua regia solution is prepared by mixing 3 volume parts of hydrochloric acid (HCl) with 1 volume part of nitric acid (HNO<sub>3</sub>) and should be used fresh.

### **Synthesis of Fe<sub>3</sub>O<sub>4</sub> Superparamagnetic iron oxide nanoparticles (IONPs)**

Spherical Fe<sub>3</sub>O<sub>4</sub> IONPs were synthesized by thermal decomposition following a protocol adapted from that described by Polina Anikeeva et al. [25]. 1 mmol of organometallic precursor was prepared by dissolving 2 mmol of FeCl<sub>3</sub>, 1 mmol of FeCl<sub>2</sub> and 8 mmol of sodium oleate in 10 ml of ethanol, 10 ml of Milli-Q water and 20 ml of hexane. It was heated at reflux at 75 °C with magnetic stirring (400 rpm) for 4 h. The organic phase was then separated and heated for 2 h at 85 °C and another 2 h under vacuum at 110 °C. In a 3 necked round bottom flask (50 ml), the precursor (1 mmol) was dissolved in 5 ml of 1-octadecene and 175 µl of oleic acid. The solution was heated at 110 °C under vacuum for 1 hour. Next, the temperature was increased up to 200 °C under nitrogen flow, and finally, it was raised to 320 °C with a gradient of 1 °C/min and maintained for 1 h. Then, the mixture was cooled to 160 °C and left for

3 days. The mixture was transferred into a conical tube along with 40 ml of a 1:1 mixture of ethanol (EtOH): hexane. The sample was centrifuged (7000 rcf for 10 min). The precipitate was redispersed in 10 ml hexane, 5 ml EtOH and centrifuged (7000 rcf for 10 min) twice. Finally, the pellet was redispersed in 10 ml of hexane. For water transfer, 9 mg of IONPs dispersed in hexane were added to 5 ml of an aqueous solution of CTAB 0.2M. The mixture was vigorously stirred for 40 minutes. The organic phase was then evaporated by heating at 65 °C for 30 min. Then, the IONPs were centrifuged 2 times (35,000 rcf, 10 min) and redispersed in 1 ml of an aqueous solution of 0.2 mg/ml of cetyltrimethylammonium bromide (CTAB). Finally, the dispersion was centrifuged (5000 rcf, 5 min) to precipitate aggregates; the precipitate was discarded, and the supernatant was transferred to an Eppendorf.

### **Synthesis of IONP@ZIF-8 nanocomposites**

These nanocomposites were synthesized following a previously reported protocol with slight modifications [26]. The CTAB stabilized IONPs were used as seeds onto which a shell of ZIF-8 was grown. In a 5 ml glass vial under magnetic stirring and at room temperature (RT), 1 ml of aqueous solution of 2-methylimidazole 1.3 M, 1 ml of aqueous solution of zinc nitrate hexahydrate 0.025 M, and 1 ml of 2 nM IONPs dispersed in 0.2 mg/ml CTAB aqueous solution were mixed. The mixture was stirred for 5 min and allowed to stand for 3 h at RT. The appearance of white turbidity indicated the formation of ZIF-8. Finally, the particles were precipitated by centrifugation (7200 rcf, 10 min) and washed twice with methanol (MeOH). After washing, they were redispersed in 1 mL of MeOH.

To load the ZIF-8 with CV, the one-pot synthesis strategy was used where the aqueous solution of CTAB used in the synthesis included CV at 0.1 g/l. The rest of the procedure was kept the same.

For the nanocomposites polymer coating with PMA-fluorescein, the polymer was firstly synthesized as described previously [24]. Thereafter, PMA-fluorescein dissolved in  $\text{CHCl}_3$  (ratio of 600 monomers/nm<sup>2</sup> of nanocomposites surface) was added to the nanocomposites dispersed in MeOH. The solvent was then slowly evaporated on a rotary evaporator. Once dry, the PMA-fluorescein was hydrolyzed (to allow nanocomposites dispersion) by adding an aqueous solution of 0.1 M NaOH and sonicating. Finally, the nanocomposites were washed by centrifuging them twice (7200 rcf, 10 min) and redispersing in Milli-Q water.

The nanocomposite particle concentration was determined by nanoparticle tracking analysis (NTA), where the samples were analyzed in water using a NanoSight NS300 (Malvern Instrument Ktd) equipped with a 405 nm laser. All measurements were carried out at 24 °C.

### **Particle size and shape characterization**

Scanning electron microscopy (SEM) micrographs were obtained using a ZEISS FSEM ULTRA Plus operated at 3 and 20 kV. Transmission electron microscopy (TEM) measurements were carried out on a JEOL JEM-2010 microscope operated between 80 and 200 kV. Scanning TEM mode was used during the TEM characterization. Samples were prepared by adding a drop of diluted samples on a Cu grid and letting them dry. The hydrodynamic diameter ( $d_h$ ) and polydispersity index (PDI) of the nanoparticles or the nanocomposites were determined by dynamic light scattering (DLS) using a Malvern Zetasizer Nano ZSP equipped with a 10 mW He–Ne laser operating at a wavelength of 633 nm and fixed scattering angle of  $173^\circ$ .

### **Thermogravimetric analysis (TGA) and N<sub>2</sub> adsorption-desorption analysis**

TGA measurements were carried out using a TA Instruments Inc, SDT Q-600 thermobalance with a general heating profile from 25 to 800 °C with a heating rate of 5 °C/min under air using a flux of 100 mL/min. N<sub>2</sub> sorption isotherms at 77 K were measured on a Micromeritics 3Flex adsorption analyzer. The specific surface area was extrapolated within the range of relative pressure ( $P/P_0$ , where  $P_0$  is the saturation pressure) of 0.05–0.3 using the Brunauer, Emmett & Teller (BET) equation. Data were analyzed using 3Flex V5.03 software (Micromeritics Instrument Corp., Norcross, GA, USA).

### **Magnetic properties measurements**

Saturation magnetization and ZFC/FC (zero field cooled/field cooled) measurements were performed on samples containing an equal quantity of magnetic nanoparticles using a vibrating sample magnetometer (VSM) (PPMS, Quantum Design, USA). For the measurements, an aliquot of the corresponding sample was placed inside the VSM vial (plastic) and left to dry. All measurements were done using MF intensities from -5 to 5 T. The saturation magnetization measurements were done at 300 K, and the ZFC/FC measurements were performed from 5 to 300 K. Diamagnetic correction for the sample holder and non-magnetic material was done in the saturation magnetization measurements analysis by adjusting the S curve slope until getting a straight line with zero slope at values above saturation.

### **Heating power measurements**

500  $\mu$ l of the IONP sample (at 232  $\mu$ l Fe/ml) were exposed to AMF to measure their heating power. The temperature increase of the sample was monitored during 180 s while being exposed to a frequency of 93 kHz at 40.3, 53.7 and 67 kA/m MF intensities, delivered by a commercial magnetic inductor (Fives Celes, Lautenbach, France). Another tube containing 500  $\mu$ l of water was used as a control in order to remove the potential contribution of eddy current and room temperature variations

to the temperature increase. Temperature measurements were performed using a thermal probe (Reflex 4, Neoptix, Canada). The specific absorption rate (SAR) was calculated using the following equation:

$$SAR = \frac{C \frac{dT(t)}{dt}}{m_{IONPs}}$$

where *SAR* is the specific absorption rate (W/g), *C* is the total specific heat of water and glass (J/K), *dT(t)* is the temperature increase during the MF exposure, *dt* is the exposure time (s), *m<sub>IONPs</sub>* is the mass of the IONPs inside the SAR tubes (g). Correction factors were applied to compensate for performing the experiment under non-adiabatic conditions. The resulting SAR values were then divided by the applied frequency (93 kHz) to get the corresponding hysteresis area (mJ/g).

### **Cell lines and 2D cell culture**

The MiaPaCa2, an epithelial cell line derived from pancreatic tumor tissue, was cultured in Dulbecco's Modified Eagle Medium (DMEM) with Glutamax, supplemented with 10% (v/v) fetal bovine serum (FBS) and 100 IU/ml penicillin/streptomycin (Penicillin-Streptomycin P4333; Sigma-Aldrich). The immortalized human CAF line was established by retrovirus-mediated gene transfer of simian virus 40 (SV40) T antigen and human telomerase reverse transcriptase (hTERT) into human pancreatic fibroblasts isolated from the resected pancreas tissue of a patient undergoing operation for pancreatic adenocarcinoma cancer (PDAC), and obtained from Dr C. Bousquet's laboratory (INSERM U1037-CRCT, France). The CAF cell line was cultured in DMEM/F-12 medium (DMEM/F-12 GlutaMAX™, ThermoFisher Scientific) containing 10% FBS, 100 IU/ml penicillin/streptomycin. Cells were maintained at 37 °C in a 5% CO<sub>2</sub> in a humidified incubator.

### **3D Spheroid formation and treatment**

GFP-expressing MiaPaCa2 and CAF cell lines were cultured as above, and the confluent cultures were trypsinized, washed in phosphate-buffered saline (PBS), and resuspended in DMEM containing 20% FBS and 100 IU/ml penicillin/streptomycin. An automated cell counter was used to determine the cell concentration of the suspensions. 3 000 cells per spheroid were formed with the hanging drop technique starting from a cell suspension solution containing 50% of GFP-expressing MiaPaCa2 and 50% of CAF in DMEM containing 20% FBS, 100 IU/ml penicillin/streptomycin and 0.3% of methylcellulose (Acros Organics, #182311000). Drops of the cell suspension (25µl) were placed on the lids of 100 mm dishes, which were inverted over dishes containing 10 ml of PBS. Hanging drop cultures were incubated 24h, the resulting cellular aggregates were harvested and introduced into a 35 mm

dish, previously washed with Anti-Adherence Rinsing Solution (StemCell™, #07010) and filled with 1.5 ml of complete medium.

### **Cytotoxicity assays of nanocomposites**

For 2D cell culture,  $10^4$  cells per well were plated into 96-well plates (Thermo Scientific™). After overnight growth, the cells were incubated with increased concentrations (up to 4 pM) of the indicated nanocomposites for 24 h, 48h and 72h. Cell viability was determined using MTT viability assay.

For 3D spheroid, the spheroids were incubated with 1 pM of the indicated nanocomposites for 24h, 48h and 72h. The spheroids were trypsinized and their viability was assessed by counting the number of cells contained in one spheroid.

### **Hemolysis Assay**

Heparinized blood was obtained from male CD-1 mice and male Sprague-Dawley rats by cardiac puncture under anesthesia, and from male human healthy volunteers (with no major medical history and absence of medications). The collected blood was incubated with increasing concentrations of IONP-CV@ZIF-8@PMA (up to 10 pM), 1 mg/ml Triton X- 100 (positive control) or PBS (negative control) for 4h at 37°C. The samples were centrifuged at 1,000 g for 10 min. Optical density of the supernatant was measured at 540 nm with a Tecan Safire 2 plate reader. All measurements were performed in triplicates. The hemolysis percent was calculated relative to the positive control (Triton X-100), which represented 100% hemolysis.

### **Quantification of IONP-CV@ZIF-8@PMA uptake by flow cytometry**

For 2D cell culture,  $10^4$  cells per well were seeded into 24-well plates (Thermo Scientific™) and grown overnight. The cells were incubated with IONP -CV@ZIF-8@PMA (1 pM) for 2 to 72 h at 37° C. Then, cells were rinsed twice with ice-cooled PBS containing 0.5% BSA (bovine serum albumin) (Sigma-Aldrich). Cells were trypsinized, centrifuged and resuspended in 300  $\mu$ l of PBS- EDTA 2mM at 4° C in FACS tubes. Cell-associated fluorescence of fluorescein and CV were determined using a BD FACSCalibur™ flow cytometer. The cells maintained in the incubation medium without adding the nanocomposites served as negative controls and used to subtract the autofluorescence signal.

For 3D spheroid, the spheroids were incubated with 1 pM of IONP-CV@ZIF-8@PMA during 24h, 48h and 72h. After the incubation time, the spheroids were dissociated using trypsin treatment that was stopped with 200 $\mu$ l ice-cooled PBS containing 0.5% BSA. Cell-associated fluorescence of the CV was determined using a BD FACSCalibur™ flow cytometer.

### **Intracellular nanocomposites localization by transmission electron microscopy**

In 2D culture,  $10^5$  cells were seeded into 35 mm dish and incubated with IONP-CV@ZIF-8@PMA at 1 pM for 72 h. After two washes with PBS, cells were fixed with 4% glutaraldehyde in Sorensen buffer for 4 h at 4 °C. After washes, cells were postfixed in 1% osmium tetroxide (osmium 2%, saccharose 0.25 M, Sorensen 0.05 M) for 1 h at 20 °C, followed by washings with distilled water and uranyl acetate 2% for 12 h at 4 °C. After dehydration, 70 nm sections of cells embedded in EMBed 812 resin were stained with uranyl acetate and lead citrate and examined with a TEM (Hitachi HU12A, Japan) operating at 75 kV.

### **Intracellular nanocomposites localization by confocal microscopy**

In 2D culture,  $25 \times 10^3$  cells/compartiment were seeded onto 4-compartment Cellview culture dishes (Greiner Bio-One). After overnight growth, cells were incubated for 72 h with IONP-CV@ZIF-8@PMA (1 pM). For lysosome staining, cells were incubated 15 min in the presence of 10 nM LysoBrite™ Blue (excitation: 405 nm, AAT Bioquest, Inc.). The IONP-CV@ZIF-8@PMA (excitation: 405 nm for the LysoBrite™ Blue, 488 nm for fluorescein and 633 nm for CV) and the blue lysotraker co-localization were analyzed using LSM780 confocal microscope (Zeiss).

### **Cell treatment by AMF and RMF**

The exposure of cells to MF was performed as follows. The indicated number of cells per compartment were seeded into two 4-compartment Cellview dishes (Greiner Bio-One) and grown overnight. Two compartments in each dish were treated with the indicated nanocomposites (1 pM) for 72 h at 37 °C in DMEM medium containing 0.5% FBS and 100 IU/ml penicillin-streptomycin. Meanwhile, fresh DMEM medium containing 0.5% FBS and 100 IU/ml penicillin-streptomycin (without nanocomposites) was added to the other two compartments in each dish. After the 72 h incubation, the cells (in both dishes) were rinsed twice with the incubation medium, and a fresh incubation medium was added. One of the prepared 2 dishes was exposed to the MF, not the other. So that at the end of each exposure to MF there were four populations of cells as follows: cells incubated with the nanocomposites and exposed to MF, cells without nanocomposites but exposed to MF, cells incubated with the nanocomposites but without MF exposure and cells without nanocomposites incubation nor MF exposure.

For the AMF exposure (275 kHz, 40 mT), the cells were exposed to the AMF delivered by a magnetic inductor (Fives Celes, Lautenbach, France) for 2 h as previously described [27]. For RMF exposure, the cells were exposed to the RMF delivered by a homemade magnet rotated with a motor (Fives Celes, Lautenbach, France) for 2 h as previously described [28]. Different amplitudes (10, 20, 30, 40, 50, 60 and 70 mT) were assessed at 1 Hz frequency before choosing an optimum amplitude value. In all these experiments, the temperature of the Cellview dish was maintained at  $37.0 \pm 0.2$  °C during MF exposure.

### **Analysis of CV intracellular release by flow cytometry**

For 2D culture,  $25 \times 10^3$  cells/compartiment were seeded into 4-compartment Cellview dishes (Greiner Bio-One) and grown overnight. The cells were incubated with IONP-CV@ZIF-8@PMA nanocomposites (1 pM) for 72 h at 37°C. Then, the cells were rinsed twice with incubation medium and exposed one or two times to MF (AMF or RMF) for 2 h once/day. After the exposure, the supernatant was collected, and the cells were trypsinized, centrifuged and resuspended in 300  $\mu$ l of PBS- EDTA 2mM at 4°C in FACS tubes. Cell-associated fluorescence of CV was determined using a BD FACSCalibur™ flow cytometer.

For 3D spheroid, the spheroids were incubated with 1 pM of IONP-CV@ZIF-8@PMA nanocomposites for 48 hours. After the incubation time, the spheroids are washed with complete medium and then exposed one or two times to MF (AMF or RMF) for 2 h once/day. After the exposure to MF, the spheroids were dissociated using trypsin treatment that was stopped with 200  $\mu$ l ice-cooled PBS containing 0.5% BSA. Cell-associated fluorescence of the CV was determined using a BD FACSCalibur™ flow cytometer.

After subtracting the basal fluorescence of the control cells (weren't treated with the nanocomposites) for each condition (exposed to the MF or not), the fluorescence intensity of CV contained in cells treated with nanocomposites subjected to MF was related to the intensity in cells treated with nanocomposites not subjected to MF.

### **Analysis of CV release in real-time by confocal microscopy**

$10^5$  cells were plated onto 1-compartment Cellview culture dishes (Greiner Bio-One). After overnight growth, cells were incubated with IONP-CV@ZIF-8@PMA (1 pM) for 72 h. After removing the medium, cells were rinsed twice with incubation medium, incubated in fresh medium (buffered with 10 mM HEPES buffer pH 7.4) and then exposed to MF. Another dish with cells that were treated with the nanocomposites but not exposed to MF serves as a control. In order to induce thermal heating of the IONPs, we used a homemade electromagnet that fits under the microscope and generates the AMF as previously described [29]. The electromagnet was put inside a CELLview dish (Greiner Bio-One) containing the adherent cells having uptaken IONP-CV@ZIF-8@PMA. In this configuration, applying a current of 1.5 A inside the driving coil brought an AMF of amplitude 40 mT. The field had a frequency 300 kHz and was applied for 120 min. In order to induce mechanical forces onto the IONPs, we used another homemade electromagnet that fits under the microscope and generates an RMF, as previously described [30]. The application of a sinusoidal current with a 90° phase shift between two sets of coils creates a rotating MF around the symmetry plane separating them. Under the conditions used for *in vitro* experiments, simulations indicated that the MF inside the gap was 40 mT. The temperature of the cell incubation medium was monitored and maintained around 37°C during both AMF and RMF exposures using a thermal probe (Reflex 4, Neoptix, Canada) that was put inside the medium. A first image of the cells

was recorded before turning on the MF generator. Then, after turning on the MF generator, the cells were imaged each 10 minutes for 2 hours. The control cells were imaged in the same way but without exposure to the MF.

### **Analysis of cell viability**

For 2D culture,  $7.5 \times 10^3$  cells/compartiment were seeded into 4-compartment Cellview dishes (Greiner Bio-One) and grown overnight. The cells were incubated or not with IONP@ZIF-8@PMA or IONP-CV@ZIF-8@PMA (1 pM, 72 h) at 37°C. Two similar 4-compartment Cellview dishes were prepared simultaneously. After removing the incubation medium, cells were rinsed twice with fresh medium, then wells in one dish only were exposed to AMF or RMF for 2 h once/day in three consecutive days. The effects of MF treatments were investigated on cell proliferation by counting the cell number by a cell counter (Beckman cell counter z2) 24 h after MF exposure. Cells were counted once per day for the 3 days.

### **Analysis of spheroid growth**

The spheroids were incubated with 1 pM of IONP@ZIF-8@PMA or IONP-CV@ZIF-8@PMA for 48 hours. After the incubation time, the spheroids were washed with fresh medium and then exposed to AMF or RMF for 2 h once/day in three consecutive days. The spheroid growth was monitored daily under an inverted phase-contrast microscope, and the size of the spheroids was measured from collected images were analyzed using ImageJ software.

### **Statistical Analysis**

Results are expressed as the mean  $\pm$  SEM of at least three independent experiments. Statistical analysis was performed using one- or two-way ANOVA test. Differences were considered significant when  $p < 0.05$ .

## Results

### Nanocomposites synthesis

This study presents the design of MF-responsive drug delivery nanocarriers composed of IONP cores and ZIF-8 MOFs shells that were loaded with CV fluorescent probe and stabilized with the PMA polymer coat.

The spherical IONP cores were prepared, and they displayed average SEM size and hydrodynamic diameter of  $22.3 \pm 1.6$  and  $35.5 \pm 5.1$  nm, respectively (Figures 1 A, B, E). During the growth of the ZIF-8 shell on the surface of the IONPs, the CV fluorescent cargo was added to allow its loading inside the ZIF-8 pores. Afterwards, both loaded and nonloaded nanocomposites were coated with the PMA polymer. The synthesized IONP@ZIF-8@PMA and IONP-CV@ZIF-8@PMA displayed core-shell nanocomposite structures of cubic shape (Figures S1A and 1C). In addition, they showed similar average microscopic sizes ( $137.1 \pm 13.2$  and  $137.9 \pm 14.4$  nm, respectively) and similar hydrodynamic diameters in number mean ( $225.5 \pm 9.6$  and  $229.5 \pm 1.9$  nm, respectively) (Figures S1B, 1D and E). Moreover, both nanocomposites, IONP@ZIF-8@PMA and IONP-CV@ZIF-8@PMA, presented similar surface charge ( $\zeta$ -potential =  $-16.4 \pm 1.6$  and  $-16.0 \pm 0.6$  mV, respectively) (Figure 1F). The TGA analysis showed that magnetic nanocomposites without PMA coating presented a pronounced weight loss (50–60 wt %) at around  $400^\circ\text{C}$  due to the combustion of 2-methylimidazole, indicating their thermal stability up to  $400^\circ\text{C}$  (Figure S1C). In addition, PMA-coated nanocomposites experienced a small mass loss (10 wt %) at  $\sim 150$ – $250^\circ\text{C}$  attributed to the polymer glass transition and a higher loss mass ( $\approx 20$  wt %) around  $250$ – $350^\circ\text{C}$ .

The  $\text{N}_2$  sorption of the magnetic nanocomposites showed type-I isotherms, indicating the formation of microporous material (Figure S1D). The BET surface area ( $S_{\text{BET}}$ ) of IONP@ZIF-8, IONP-CV@ZIF-8, IONP@ZIF-8@PMA and IONP-CV@ZIF-8@PMA were  $1466 \pm 22$ ,  $1268 \pm 18$ ,  $962 \pm 17$  and  $683 \pm 9$   $\text{m}^2 \cdot \text{g}^{-1}$ , respectively. The important reduction of the  $S_{\text{BET}}$  between the IONP@ZIF-8@PMA and IONP-CV@ZIF-8@PMA indicates the loading of the CV in the ZIF-8 shell. The evaluation of the colloidal stability in  $\text{H}_2\text{O}$  by DLS confirmed that the PMA-coated nanocomposites (IONP-CV@ZIF-8@PMA) are stable up to 72h, while the bare non-coated ones (IONP-CV@ZIF-8) aggregated and were not detectable after 24h (Figure S1E). Additionally, the PMA-coated nanocomposites (IONP-CV@ZIF-8@PMA) were also stable in DMEM culture medium and in artificial lysosomal fluid (ALF) up to 72h.

In addition to the physicochemical characterization, the magnetic properties of the IONPs and the prepared nanocomposites were studied. After their incorporation inside the ZIF-8 shell, the IONPs kept their superparamagnetic behavior with a similar saturation magnetization compared to free IONP@PMA ( $M_s = 73.7$  and  $74.0$   $\text{Am}^2/\text{kg Fe}$ , respectively) (Figure 1G). Moreover, ZFC/FC magnetization curves showed that ZIF-8 coated IONPs presented a slightly lower blocking temperature ( $T_{\text{max}} \sim 243$  K)

compared to the IONP@PMA ferrofluid ( $T_{\max} \sim 265$  K), indicating the reduction of the dipolar interaction between IONPs inside the ZIF-8 shells compared to the ferrofluid (Figure S1F). The analysis of IONP heating properties as a function of MF amplitude showed that the heating power of IONP@PMA ferrofluid increased with the MF amplitude (Figure 1H).

All together, these results indicated that unloaded and CV-loaded magnetic nanocomposites presented similar physicochemical properties (size, surface charge). Also, it showed that the nanocomposites preserved the magnetization of the IONPs to be exploited for MF-responsive controlled release.

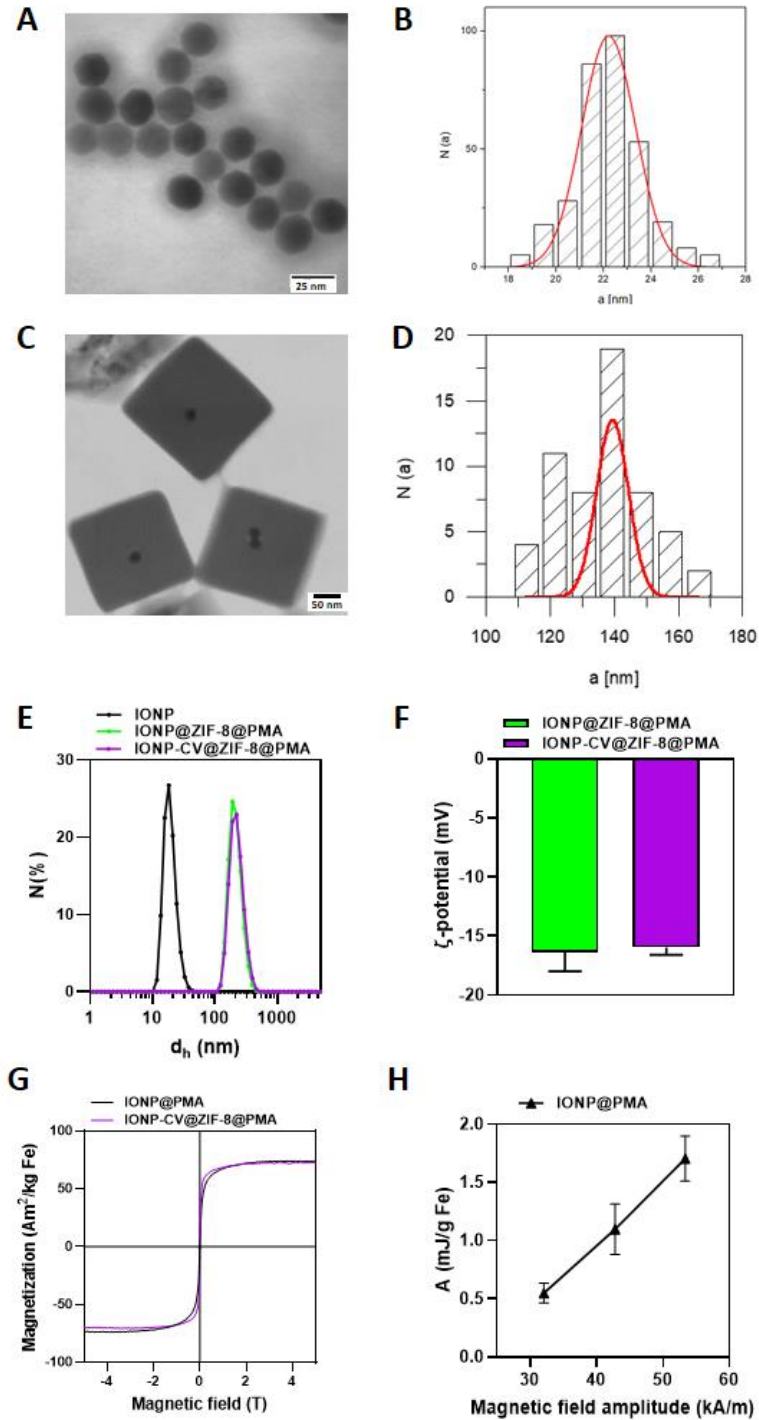


Figure 1: **A)** Representative SEM image at 20 kV of IONPs (scale bar: 25 nm). **B)** Histogram of the number distribution ( $N$ ) of the diameters of the IONPs as determined from SEM images. **C)** Representative TEM image of the IONP-CV@ZIF-8@PMA nanocomposites confirming their core-shell structure and cubic shape (scale bar: 50 nm). **D)** Histogram of the number distribution ( $N$ ) of the size of the IONP-CV@ZIF-8@PMA (vertex-to-vertex distance), as determined from TEM images. **E)** DLS intensity distributions of the hydrodynamic diameter of the IONPs, IONP@ZIF-8@PMA and IONP-CV@ZIF-8@PMA. **F)**  $\zeta$ -potential measurements of IONP@ZIF-8@PMA and IONP-CV@ZIF-8@PMA. **G)** Saturation magnetization measurements of the IONP@PMA and IONP-CV@ZIF-8@PMA. **H)** Heating power values as a function of alternating MF intensity amplitude of the IONPs at 93 kHz.

## Nanocomposites uptake and subcellular localization

The cancer progression and aggressiveness are not only dictated by the tumor cells, but also involve the tumor microenvironment notably the cancer-associated fibroblasts (CAF) that play a critical role in tumor progression and resistance acquisition to anticancer treatments, such as in pancreatic cancer [31, 32]. We analyzed the cytotoxicity, uptake and subcellular localization of IONP-CV@ZIF-8@PMA nanocomposites on pancreatic cancer cells MiaPaCa2 and CAF, chosen as models. The IONP-CV@ZIF-8@PMA nanocomposites did not present cytotoxic activity on MiaPaCa2 cancer cells and cancer-associated fibroblasts (CAF), up to 1 pM and 72 h of incubation (Figure S2). The nanocomposites hemocompatibility was also investigated, where the hemolysis ratios of the red blood cells incubated with IONP-CV@ZIF-8@PMA were negligible at concentrations up to 10 pM. These results indicate that these magnetic nanocomposites could represent a biocompatible drug delivery system for intravenous administration (Figure S3).

The kinetics of IONP-CV@ZIF-8@PMA cellular uptake were first determined by measuring the fluorescence intensity of fluorescein, present on the nanocomposites PMA polymer coat, using flow cytometry. The results indicated that the amount of IONP-CV@ZIF-8@PMA taken up by MiaPaCa2 cells increased with the time of incubation (Figure 2a). The IONP-CV@ZIF-8@PMA uptake by CAF through measuring the fluorescence intensity of fluorescein could not be determined due to the high level of CAF autofluorescence on fluorescein wavelength. We also evaluated the IONP-CV@ZIF-8@PMA uptake by measuring the fluorescence intensity of CV, encapsulated in the nanocomposites, using flow cytometry, on both MiaPaCa2 and CAF cells. The kinetics of IONP-CV@ZIF-8@PMA uptake by MiaPaCa2 cells indicated that the amount of uptaken IONP-CV@ZIF-8@PMA increased up to 6h of incubation, then slightly decreased that could be attributed to a partial leak of the loaded CV from the nanocomposites which can be expelled out of the cells (Figure 2B). The uptake of IONP-CV@ZIF-8@PMA by CAF cells increased with the incubation time up to 24h, and then it was stabilized (Figure 2B).

Furthermore, the amount of uptaken IONP-CV@ZIF-8@PMA was higher and faster in CAF than in MiaPaCa2 cells, indicating that the nanocomposites uptake depends on the cell type. We next characterized the cellular fate of IONP-CV@ZIF-8@PMA in MiaPaCa2 and CAF cells (Figures 2 C-F). The transmission electron microscopy (TEM) images of MiaPaCa2 and CAF cells indicated that IONP-CV@ZIF-8@PMA were mainly localized in lysosomes (Figures 2C and D). Also, the confocal microscopy studies confirmed that IONP-CV@ZIF-8@PMA accumulated in the lysosomes compartment of MiaPaCa2 and CAF cells (Figures 2 E and F). The analysis of IONP-CV@ZIF-8@PMA / LysoTracker colocalization showed that  $86.8 \pm 0.9$  and  $90.2 \pm 3.1$  % of the uptaken IONP-CV@ZIF-8@PMA were localized inside the lysosomes of MiaPaCa2 and CAF cells, respectively.

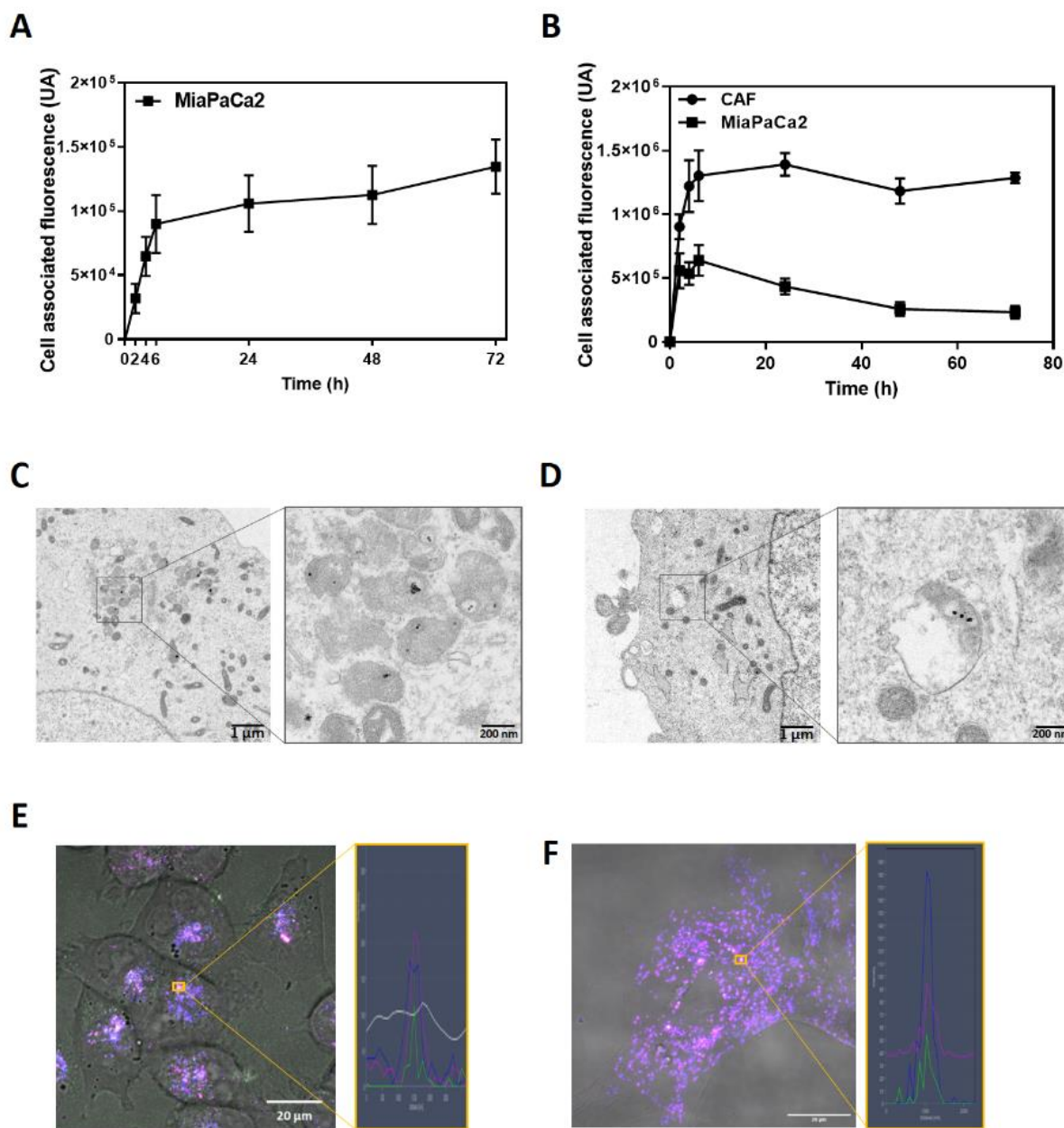


**Figure 2: Uptake and subcellular localization of SPION-CV@ZIF-8@PMA-FITC.** **A)** Kinetics of IONP-CV@ZIF-8@PMA-FITC uptake by MiaPaCa2 cells. Cells were incubated with 1 pM of IONP-CV@ZIF-8@PMA for 2 to 72 h. Fluorescence intensity associated to the fluorescein was measured by flow cytometry, and results are expressed as the mean  $\pm$  SEM of at least three separate experiments. **B)** Kinetics of IONP-CV@ZIF-8@PMA uptake by MiaPaCa2 and CAF cells. Cells were incubated with 1 pM of IONP-CV@ZIF-8@PMA for 2 to 72 h. Fluorescence intensity associated to the CV was measured by flow cytometry, and results are expressed as the mean  $\pm$  SEM of at least three separate experiments. **C and D)** Representative TEM images of IONP-CV@ZIF-8@PMA in MiaPaCa2 (C) and CAF (D) cells that were incubated with 1 pM of IONP-CV@ZIF-8@PMA for 72h. **E and F)** Subcellular colocalization of IONP-CV@ZIF-8@PMA in MiaPaCa2 (E) and CAF (F) cells that were incubated with 1 pM of IONP-CV@ZIF-8@PMA for 72 h, then with 10 nM Blue Lysotraker for 15 minutes and observed under confocal microscope (Scale bars are 20  $\mu$ m).

### **MF-induced cargo release in 2D cultured MiaPaCa2 cancer cells and CAF**

The controllable responsive cargo release behavior was then studied in response to MF application. Toward this aim, MiaPaCa2 and CAF cells were incubated with 1 pM of IONP-CV@ZIF-8@PMA for 72h, then washed to eliminate non-internalized IONP-CV@ZIF-8@PMA and exposed to AMF (40 mT, 275 kHz) or RMF (40 mT, 1 Hz) for 2h while temperature was maintained at 37°C. Control cells were incubated with the IONP-CV@ZIF-8@PMA for 72 h, but not exposed to MF. The impact of MF exposure was determined by analyzing the CV fluorescence intensity associated with cells by flow cytometry, comparatively to control cells.

We showed that AMF exposure significantly increased the CV fluorescence intensity by  $1.22 \pm 0.04$  and  $1.33 \pm 0.06$ -fold in MiaPaCa2 and CAF cells respectively, compared to control cells that were not exposed to AMF (Figure 3A), suggesting thermally induced CV release from the nanocomposites. Moreover, a second AMF exposure resulted in an enhanced CV release by  $1.60 \pm 0.09$  and  $1.72 \pm 0.34$ -fold in MiaPaCa2 and CAF cells respectively, indicating that the cargo release from the magnetic nanocomposites can be improved by repeated AMF application.

We then studied the impact of IONP movement induced by RMF application on CV release from the magnetic nanocomposites. First, we screened the efficiency of a 1 Hz RMF of different amplitudes (10-70 mT), this frequency being known to induce mechanical forces from small IONPs [28, 33]. As shown in Figure S4, RMF exposure caused the CV release from the magnetic nanocomposites at most amplitudes, in MiaPaCa2 cells. The maximal effect was observed with the 40 mT amplitude, inducing significantly the CV release from the nanocomposites by  $1.20 \pm 0.02$  in MiaPaCa2 cells, compared to control cells in absence of RMF application (Figure 3B). IONP movement induced by RMF application also significantly increased the CV release from the nanocomposites by  $1.31 \pm 0.18$ -fold in CAF cells. We also observed that a second RMF exposure did not significantly enhance the CV escape from the nanocomposites compared to a single exposure.

Noticeably, the double AMF exposure induced a higher CV release from the nanocomposites in MiaPaCa2 and CAF cells than the RMF one, suggesting that MNPs heating could be more efficient than MNPs movement to trigger drug release using spherical 22 nm IONPs (Figure 3C). Other physicochemical properties such as the size, the shape (i.e., nanorod) and the anisotropy may optimize the generation of mechanical forces by the IONPs to enhance their efficiency in inducing the cargo release from the nanocomposites. The enhancement of CV fluorescence intensity, observed in the release experiments, could be due to reduced quenching. Indeed, partial self-quenching due to a high concentration of fluorescent molecules or quenching by MNPs or the MOF shells can occur [34-39], when the CV is inside the nanocomposites. Consequently, the CV escape from the nanocomposites induced by IONP heating or movement results in the decrease of such quenching mechanisms, leading to the enhancement of its fluorescence intensity.

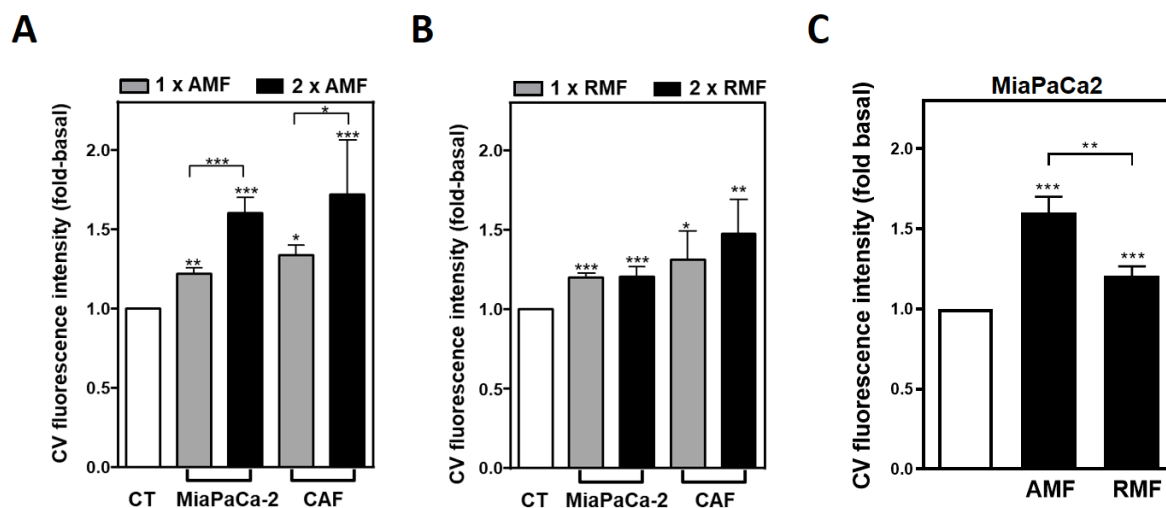


Figure 3: MF-induced CV release in 2D cultured cells. **A and B)** Analysis of CV fluorescence intensity in MiaPaCa2 and CAF cells after their incubation with IONP-CV@ZIF-8@PMA (1 pM, 72h) and exposure to AMF (A) or RMF (B) once or twice in two subsequent days, measured by flow cytometry. **C)** Analysis of CV fluorescence intensity in MiaPaCa2 cells after their incubation with IONP-CV@ZIF-8@PMA (1 pM, 72h) and two exposures to AMF or RMF. Control cells (CT) were incubated with the IONP-CV@ZIF-8@PMA for 72 h, but not exposed to MF. The results are expressed in fold-basal of CV fluorescence intensity compared to the control cells and are the mean  $\pm$  SEM of at least three independent experiments.

The CV escape from magnetic nanocomposites was also monitored in real-time on living cells by confocal microscopy, using homemade AMF or RMF miniaturized electromagnets [29, 30]. Confocal images of cells containing IONP-CV@ZIF-8@PMA with or without exposure to AMF or RMF are shown in Figure 4A. In these representative images, an increase in CV fluorescence intensity in cells is observed after 120 minutes of AMF or RMF application, in comparison to control cells before and in absence of MF exposure. The CV fluorescence intensity was then analyzed from confocal images comparatively to t0 of each condition (Figure 4B). AMF and RMF application led to significant increase in the CV fluorescence intensity ( $2.57 \pm .40$  or  $2.60 \pm 0.33$ -fold basal in response to 120 minutes AMF or RMF exposure), whereas it did not vary in cells in absence of MF exposure ( $0.74 \pm 0.1$ -fold basal). Indeed, the CV fluorescence intensity increased significantly since 50 or 60 minutes of AMF or RMF application respectively, displaying intensities of  $1.52 \pm 0.12$  and  $1.57 \pm 0.10$ -fold higher than the initial intensity values. These findings indicate that the CV release from the magnetic nanocomposites is rapidly induced by the IONP heating or movement.

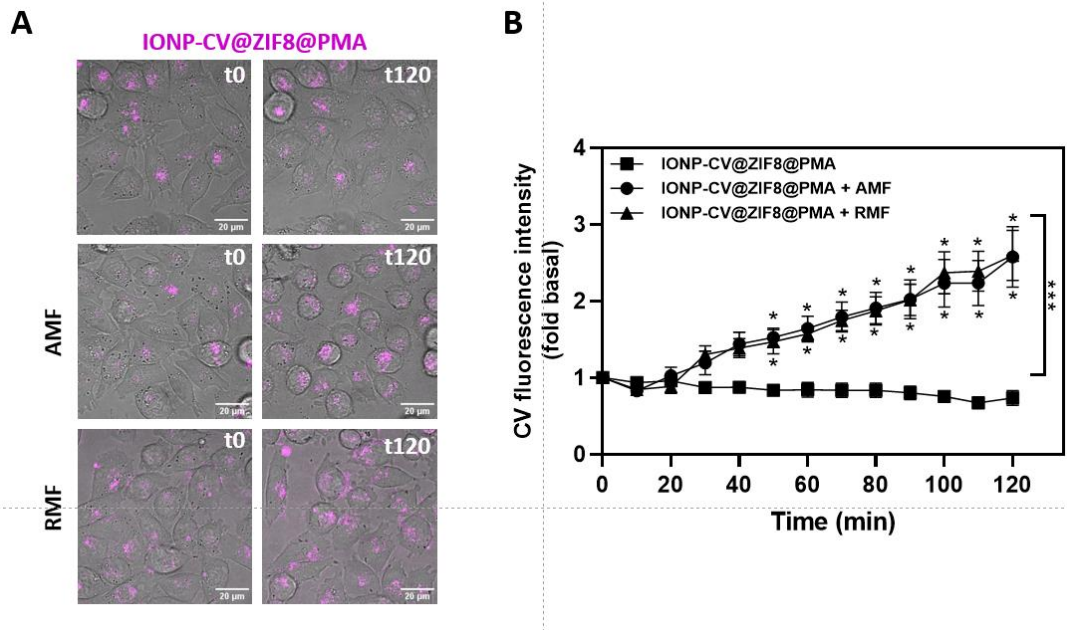


Figure 4: Real-time analysis of MF-induced CV release in 2D cultured cells, by confocal microscopy. The analysis of CV fluorescence intensity inside the MiaPaCa2 cells after their incubation with IONP-CV@ZIF-8@PMA (1 pM, 72h) was measured in real-time by confocal microscopy for 120 min without MF exposure, with AMF or RMF exposure using miniaturized home-made electromagnets. **A)** Representative confocal images of CV labeling. **B)** Quantitative analysis of CV fluorescence intensity. The results are expressed in fold-basal of CV fluorescence intensity comparatively to control cells (with IONP-CV@ZIF-8@PMA in absence of MF application) and are the mean  $\pm$  SEM of at least three independent experiments.

### MF-induced cargo release in 3D MiaPaCa2/CAF spheroids

We next investigated the magnetic nanocomposites uptake and cargo release in a 3D cell culture model integrating different cellular components and capable to mimic the heterogeneity of the pancreatic tumor. Pancreatic tumor spheroids made of MiaPaCa2 cancer cells and CAF stromal cells (1:1 ratio) were constructed by the hanging drop technique, then transferred to dishes previously treated with anti-adherence rinsing solution and incubated with IONP-CV@ZIF-8@PMA for 24, 48 and 72h. At this last time point, spheroids showed an average diameter of about 600  $\mu$ m. After spheroids dissociation, the IONP-CV@ZIF-8@PMA uptake was determined by measuring the fluorescence intensity of CV by flow cytometry (Figure 5 A and B).

The kinetics of IONP-CV@ZIF-8@PMA uptake showed that the % of MiaPaCa2 cells having internalized magnetic nanocomposites is higher than the CAF cells ( $67.4 \pm 4.8$  vs  $22.4 \pm 4.4$  %,  $57.8 \pm 1.4$  vs  $16.1 \pm 2.6$  %,  $54.4 \pm 6.5$  vs  $15.8 \pm 1.6$  % for 24, 48 and 72h of incubation respectively). Noticeably, the amount of IONP-CV@ZIF-8@PMA taken up by MiaPaCa2 cells in spheroids tends to slightly decrease at 72h of incubation, suggesting partial leak of the loaded CV from the nanocomposites that can be expelled out as observed in the 2D cell culture models (Figure 5A and 2B). Furthermore, the analysis of CV fluorescence intensity showed that the amount of IONP-CV@ZIF-8@PMA in CAF positive cells is 7.7, 6.2 and 4.7-fold higher than in MiaPaCa2 positive cells after 24, 48 and 72h of incubation, respectively. These results could suggest that CAF populations are probably heterogeneous and

present different capacities to uptake nanoparticles. These results also indicate that the efficiency of IONP-CV@ZIF-8@PMA uptake depends on cell type.

The CV release from magnetic nanocomposites was then studied in response to one or two MF applications, by analyzing the CV fluorescence intensity associated with cells in MiaPaCa2/CAF spheroids by flow cytometry, compared to control conditions. AMF exposure significantly increased the CV intensity fluorescence by  $1.73 \pm 0.37$  and  $1.76 \pm 0.52$ -fold in MiaPaCa2 and CAF cells, respectively, compared to the control cells without AMF exposure (Figure 5C). A second AMF exposure achieved more important CV release by  $3.26 \pm 1.56$  and  $1.77 \pm 0.23$ -fold in MiaPaCa2 and CAF cells, respectively, which is not significantly different than the first exposure. IONP movement induced by RMF application also significantly increased the CV release from the nanocomposites by  $1.47 \pm 0.17$  and  $1.68 \pm 0.22$ -fold after the first exposure, and by  $2.65 \pm 1.24$  and  $2.34 \pm 0.49$ -fold after second exposure in MiaPaCa2 and CAF cells respectively, compared to control cells without RMF exposure (Figure 5D). These results agree with the previous ones observed in 2D-culture model and confirm that IONP heating is more efficient than MNP movement to induce the CV release from the magnetic nanocomposites.

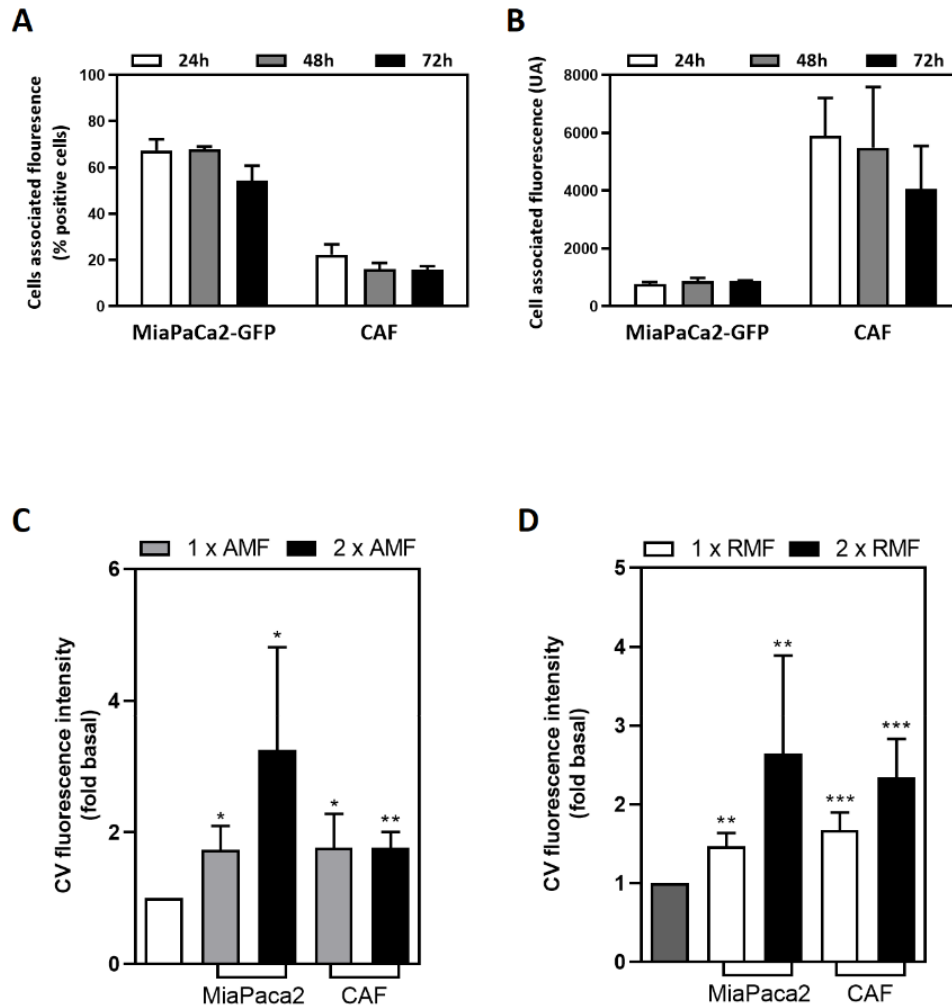


**Figure 5: Analysis of IONP-CV@ZIF-8@PMA uptake by MiaPaCa2/CAF spheroids and MF-induced CV release. A)** Percentage of MiaPaCa2-GFP and CAF cells in spheroids that had internalized IONP-CV@ZIF-8@PMA. Spheroids were incubated with 1 pM of IONP-CV@ZIF-8@PMA for 24, 48 and 72h. **B)** Fluorescence associated to the CV in MiaPaCa2-GFP and CAF in spheroids which had internalized the IONP-CV@ZIF-8@PMA. Spheroids were incubated with 1 pM of IONP-CV@ZIF-8@PMA for 24, 48 and 72 h. Fluorescence associated to the CV was measured by flow cytometry, and results are expressed as fluorescence associated with the cells and are the mean  $\pm$  SEM of at least three separate experiments. **C and D)** CV fluorescence intensity in MiaPaCa2 and CAF cells after the spheroid's incubation with IONP-CV@ZIF-8@PMA (1 pM, 72 h) and exposure to **AMF** (40 mT, 275 kHz, 2 h) (C) or **RMF** (40 mT, 1 Hz, 2 h) (D) once or twice in two subsequent days, measured by flow cytometry. Spheroids incubated with the IONP-CV@ZIF-8@PMA for 72 h, but were not exposed to MF served as control. The results are expressed in fold basal of CV fluorescence associated to IONP-CV@ZIF-8@PMA with the MF, compared to the control ones, and are the mean  $\pm$  SEM of at least three independent experiments.

### Impact on cell viability and spheroids growth

Since the CV could induce cytotoxic effects on MiaPaCa2 and CAF at high concentrations, we analyzed the effect of CV release on their viability (Figures 6 A-D, Figures S9). MiaPaCa2 and CAF were incubated or not with IONP@ZIF-8@PMA or IONP-CV@ZIF-8@PMA (loaded vs non-loaded nanocomposites) at 1 pM for 72 h. Afterwards, the cells were washed to eliminate unbound and non-internalized magnetic nanocomposites and were exposed to AMF or RMF for 2 h once per day (from day 5 to 7) while temperature was maintained at 37°C. The results showed that the AMF exposure decreased significantly the viability of IONP-CV@ZIF-8@PMA-loaded MiaPaCa2 cells compared to control ones without nanocomposites nor AMF exposure ( $3.0 \pm 0.5$ -fold), to cells with IONP@ZIF-8@PMA and IONP-CV@ZIF-8@PMA without AMF exposure ( $2.9 \pm 0.7$ -fold and  $3.0 \pm 0.6$ -fold, respectively) and to AMF-exposed cells devoid of magnetic nanocomposites ( $3.0 \pm 0.4$ -fold) (Figures 6 A). There was less viability, although not significant, for the cells loaded with IONP-CV@ZIF-8@PMA and exposed to AMF compared to cells with IONP@ZIF-8@PMA and AMF exposure.

AMF exposure also significantly decreased the viability of IONP-CV@ZIF-8@PMA-loaded CAF cells while it had no significant effect on the number of IONP@ZIF-8@PMA-loaded cells and compared to control conditions (1.5 to 1.8-fold) (Figure 6B). Interestingly, the AMF-induced CV release resulted in more inhibition of the MiaPaCa2 cells than the CAF, although the impact of AMF on CV release in both of them was close. These results confirm that CAF cells are more resistant than MiaPaCa2 cells to CV in agreement with the free CV cytotoxicity results ( $IC_{50} = 7.5 \times 10^{-7}$  M and  $1.9 \times 10^{-5}$  M in MiaPaCa2 and CAF cells at 72h of incubation) (Figure S8A and S9).

We also studied the RMF-induced CV release on MiaPaCa2 and CAF cell viability. While the RMF exposure had no significant effect on the number of IONP@ZIF-8@PMA-loaded MiaPaCa2 cells compared to control conditions, it significantly inhibited the proliferation of IONP-CV@ZIF-8@PMA-loaded MiaPaCa2 cells after RMF treatment (Figure 6C). In contrast, RMF-induced CV escape from magnetic nanocomposites did not affect the viability of CAF cells, confirming once again that CAF cells are more resistant than MiaPaCa2 cells to CV release (Figure 6D, Figure S8B). The comparison of AMF and RMF-induced CV release on cell viability showed that IONP heating is more efficient than MNP movement in inhibiting the viability of IONP-CV@ZIF-8@PMA-loaded MiaPaCa2 and CAF cells (Figure S8 C and D).

We also studied the effect of CV release on MiaPaCa2/CAF spheroids growth by measuring their size by microscopy (Figures 6 E and F). AMF and RMF exposure significantly decreased the size of IONP-CV@ZIF-8@PMA-loaded spheroids by  $13.4 \pm 1.9$  % and  $12.9 \pm 2.1$  %, respectively, compared to control cells (without nanocomposites nor MF exposure). Moreover, the AMF exposure had no significant effect on the size of IONP@ZIF-8@PMA-loaded cells and unloaded cells. IONP@ZIF-8@PMA and IONP-CV@ZIF-8@PMA incubation did not also affect the spheroids size, indicating the

biocompatibility of the nanocomposites on the spheroids. All together, these results demonstrated that CV release from magnetic nanocomposites through IONP heating and movement decreased the viability of 2D or 3D culture models.

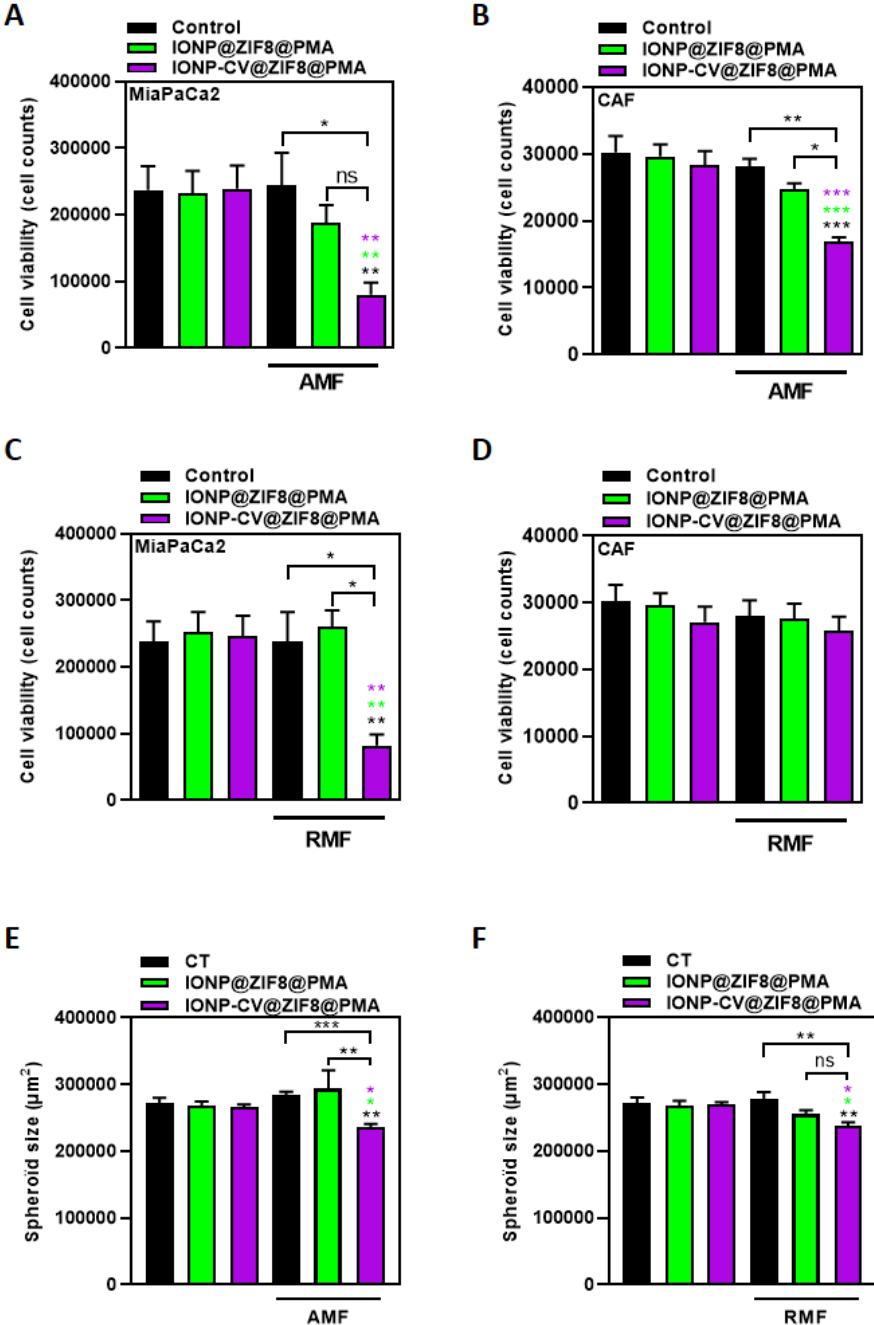


Figure 6: **Impact of CV release on 2D cultured cell viability and 3D spheroids size.** **A and B)** Analysis of *MiaPaCa2* (A) and *CAF* (B) cell viability following their incubation with IONP@ZIF-8@PMA or IONP-CV@ZIF-8@PMA for 72 h, washing, and exposure or not to AMF (40 mT, 275 kHz) for 2 h, once/day during 3 days. Cell viability was evaluated by counting cells 24 h after the last exposure. Results are expressed as mean  $\pm$  SEM of at least three separate experiments. **C and D)** Analysis of *MiaPaCa2* (C) and *CAF* (D) cell viability following their incubation with IONP@ZIF-8@PMA or IONP-CV@ZIF-8@PMA for 72 h, washing, and exposure or not to RMF (40 mT, 1 Hz) for 2 h, once/day during 3 days. Cell viability was evaluated by counting cells 24h after last exposure. Results are expressed as mean  $\pm$  SEM of at least three separate experiments. **E and F)** Spheroids size measurement after their incubation with IONP@ZIF-8@PMA or IONP-CV@ZIF-8@PMA for 72 h, washing, and exposure or not to AMF (40 mT, 275 kHz) (E) or RMF (40 mT, 1 Hz) (F) for 2 h, once/day for 3 days. Spheroid size measurement was evaluated 24 h after each AMF exposure, during 3 days. The spheroid size of the last day after 3 exposures are expressed as mean  $\pm$  SEM.

## Discussion

In this study, we developed and characterized aqueous stable magnetic nanocomposites loaded with CV fluorescent probe. We also compared the induced CV release from the magnetic nanocomposites delivery systems in response to AMF or RMF inside MiaPaCa2 cancer cells and CAF cancer microenvironment ones. The induced cargo release was investigated in 2D cell culture as well as 3D multicellular spheroids environments.

Electron microscopy images confirmed the core-shell structure of the prepared nanocomposites. The synthesized IONP cores showed superparamagnetic behavior that was also observed after their coating with the ZIF-8 shells. This superparamagnetic behavior indicates the potential of the prepared nanocomposites for being used as magnetic contrast agents for biomedical imaging applications as MRI and MPI. Interestingly, the  $M_s$  of the IONPs ( $\text{Fe}_3\text{O}_4$ ) did not change after the growth of the ZIF-8 MOF shells. A similar observation was reported by Fang *et al.* upon preparing  $\text{Fe}_3\text{O}_4$ @ZIF-90 core-shell nanocomposites [22]. However, other studies observed a decrease in  $M_s$  of the  $\text{Fe}_3\text{O}_4$  MNP cores after the MOF shell growth, namely the university of Oslo frameworks (UiO-66) and the isorecticular MOFs (IRMOF-3) [40, 41]. One can note that the growth of the UiO-66 and IRMOF-3 was done in an autoclave up to  $100^\circ\text{C}$  in organic solvents, where either dimethylformamide alone or in 1:1 mixture with ethanol were used [40, 41]. However, the ZIF-8 shells in our study, and the ZIF-90 ones in the study by Fang *et al.*, were both synthesized under ambient conditions in aqueous solutions [22]. The ZIF-8 mild aqueous preparation conditions could have helped to keep the  $M_s$  of the MNP cores inside the nanocomposites, indicating the ZIF-8 potential for developing MF-responsive MOF-based nanocomposites.

Additionally, a decrease in the magnetic dipolar interaction of the IONPs was observed after the growth of the ZIF-8 shells on their surface. These findings are in agreement with the TEM images that show discrete one or two IONPs inside the ZIF-8 shells without large agglomeration. A lower magnetic dipolar interaction of the MNPs after being inside the MOF shell was also previously reported [22].

Afterwards, the IONP @ZIF-8 nanocomposites were loaded with the CV fluorescence probe inside their pores. This loading was characterized by the lower  $S_{\text{BET}}$  of the CV-loaded nanocomposites compared to the non-loaded ones. The ZIF-8 pores were reported to have a pore size of  $11.6\text{ \AA}$  and a pore opening of  $\sim 3.4\text{ \AA}$  [42]. Using ChemDraw<sup>®</sup>, the CV molecule was found to be flat with dimensions of  $\sim 13\text{ \AA}$  long and  $\sim 7\text{ \AA}$  width, which is larger than the ZIF-8 pore size. Indeed, several studies showed the feasibility of loading the ZIF-8 with molecules larger than their pore sizes, such as the Hoechst dye ( $18.5 \times 4.1 \times 4.1\text{ \AA}$ ) [18] or doxorubicin ( $14.64 \times 10.02 \times 6.90\text{ \AA}$ ) [43]. These larger cargos were loaded following the one-pot synthesis strategy used in our study. The larger molecules loading inside the ZIF-8 pores was related either to the flexibility in the ZIF-8 pore structure [18, 44, 45] or to the formation

of mesopores inside the ZIF-8 crystal by the loaded cargo [43]. The CV loading into the ZIF-8 MOFs points out their versatility to load a wide variety of therapeutic cargos with different sizes.

For their testing on cells, the CV-loaded IONP@ZIF-8 nanocomposites were coated with PMA polymer that enhanced their colloidal stability in PBS, cell culture media and ALF conditions. Similar ZIF-8 based nanocomposites stabilization through PMA coating was reported, with the ability to allow induced diffusion-controlled flow of molecules through the polymer layer [18, 26, 46]. The IONP-CV@ZIF-8@PMA nanocomposites accumulated in the lysosomes of the MiaPaCa2 and CAF cells. Other studies also observed lysosomal accumulation of PMA-coated ZIF-8 nanocomposites of similar size on tumor cells [18, 26].

A significantly increased CV release from IONP-CV@ZIF-8@PMA nanocomposites was observed inside MiaPaCa2 and CAF cells (in 2D models and their 3D spheroids) in response to the AMF and RMF exposures. These results confirm that an intracellular on-demand cargo release from the developed ZIF-8 magnetic nanocomposites in response to MF can be achieved *via* both heating and mechanical actuation, making them promising candidates for MF-responsive anticancer drug delivery applications.

The CV-induced release in response to high-frequency AMF could be attributed to a local temperature gradient generated by the MNP cores heating that induced the CV thermodiffusion out of the nanocomposites [47]. It could also be due to changes in the pores of the ZIF-8, considering their pore structure flexibility [18, 44, 45]. Other studies have reported a high hydrothermal stability of the ZIF-8 up to 300 °C [48], and our study showed a TGA stability of ZIF-8 shells up to 400°C. Thus, we think it is unlikely that the ZIF-8 shells would be degraded in response to heating the IONPs. Hyperthermia-induced cargo release from other metal nanoparticle-based delivery systems due to thermodiffusion mechanism was previously observed both from gold nanostars@ZIF-8 in response to light and from magnetic nanoparticles@polymeric microspheres in response to AMF [18, 49].

The cargo release in experiments with RMF could be due to induced IONP movements, which could result in either diffusion-associated or deformation-assisted magneto-mechanical effects [50-52]. A recent study by Li *et al.* showed direct attachments through coordination bonding between ZIF-8 shells (namely, their imidazolate organic ligand) and the surface of the metal nanoparticle cores in similar ZIF-8 nanocomposites [53]. Also, Carrey *et al.* reported that a significant torque could be induced by RMF upon having large magnetic assemblies [33]. However, in our case, there was a small number of magnetic nanoparticles (one or two) inside each nanocomposite that could be unlikely to induce bond breakage between the magnetic nanoparticle cores and the bounded ZIF-8 shells under the RMF. Moreover, we observed mechanical vibrational and rotational movements of whole nanocomposites systems of ZIF-8 loaded with other types of MNPs, that were feasible to be followed, under RMF (data not shown). This mechanical vibrational and rotational movement could induce fluid

flow in the nanocomposites especially in the pores near the surface leading to releasing their CV load. We thus propose that the cargo release could be due to the motion of the whole nanocomposite inducing a fluid flow.

A comparative study of MF-induced release and its kinetics between surface vs. pore-loaded cargos from the same nanocomposite platform may help to get more insights about the release mechanisms induced by AMF and RMF from this type of delivery systems.

Herein, we were able to point out two studies that investigated the MF-responsive release from MOF-based magnetic nanocomposites: one was done following the low-frequency non-heating MF [22], and the other used the AMF [23]. In both studies, the magnetic nanocomposites had superparamagnetic properties similar to our case. Also, the MNP cores were similarly composed of iron oxide.

In the study used the low-frequency non-heating MF (20 Hz and 20 mT, applied for 20 min each 1h), there was an observed MF-induced release of the 5-fluorouracil cargo from the nanocomposites ( $\text{Fe}_3\text{O}_4@ZIF-90$ ) in PBS solution. The MF-induced release was  $\sim 2.28$ -fold higher after 2 h compared to the control condition without MF exposure. In our case, we obtained  $2.60 \pm 0.33$ -fold higher intracellular CV release in the real-time experiment under the confocal microscope with the low-frequency RMF (1 Hz and 40 mT, applied for 2h). However, it should be noted that there are differences in the release conditions and the applied MF and frequencies. Also, there is a difference in the MF application time, 2 h continuous exposure in our study compared to their intermittent 20 min exposure every 1 h.

In the other study, two AMF exposures (27.3 mT, 250 kHz, applied for 10 min separated by 4 h) were applied to enhance the mertansine drug release from  $\text{Fe}_3\text{O}_4@MIL-88B-NH_2$  nanocomposites after their incubation with glioblastoma cells. Although the study did not report MF-responsive release experiments, the authors observed lower cell viability on the nanocomposite-loaded cells after AMF exposure compared to the loaded cells that were not exposed to the AMF. We had a similar observation. However, their results cannot be compared quantitatively with ours as they used a chemotherapeutic cargo, which was not the case in our study.

Interestingly, differences were observed in our study between the AMF and RMF-induced CV release inside the cells. For instance, we noticed enhanced CV release from the nanocomposites in MiaPaCa2 and CAF cells after a second AMF exposure compared to the RMF. Also, there was observed higher efficiency of the MF-induced CV release in inhibiting the MiaPaCa2 and CAF cells viability with AMF compared to RMF, after repeated MF exposures. Both findings indicate the higher efficiency of the IONP cores (22 nm) heating in inducing the CV release compared to their mechanical movement.

In addition, different inhibition of cell viabilities was noticed between MiaPaCa2 and CAF in response to AMF and RMF-induced CV release. More inhibition of MiaPaCa2 cell viability compared to

CAF occurred with the repeated AMF-induced CV release. Moreover, cell viability inhibition was observed with MiaPaCa2 cells only, not CAF, with the repeated RMF-induced CV release. These observations indicate the complexity of the tumor microenvironments, especially ones with high degree of stroma involvement such as pancreatic cancers, that could exacerbate the efficacy of therapeutic agents. This complexity points out the need for the development of tailored therapeutic strategies for efficient treatment of cancer malignancies.

## **Conclusion**

This study proved the ability to design ZIF-8 based magnetic nanocomposites of superparamagnetic IONP cores to enable on-demand cargo release in response to MF. It also revealed differences in the cargo release between the AMF thermal trigger *vis-à-vis* the RMF mechanical one in intracellular conditions. In addition, it showed that different responses to therapeutic agents could occur between cancer cells and the tumor microenvironment ones. Hence, our study is a step forward in investigating the magnetic properties and the intracellular MF-induced release behavior from MOF-based magnetic nanocomposites toward their development as anticancer nanotheranostics.

**Acknowledgments:** This work is funded by the HeatNMof project that receives funding from the European Union's Horizon 2020 research and innovation program under grant agreement No 860942.

### Supplementary Figures and Tables:

**Figure S1:** **A)** Representative SEM images of IONP@ZIF-8@PMA collected with AsB detector at 20 kV (scale bar is 200 nm). **B)** Histogram of the number distribution (N) of the sizes of the IONP@ZIF-8@PMA (vertex-to-vertex distances), as determined from SEM images. **C)** TGA of the magnetic nanocomposites. **D)** N<sub>2</sub> sorption isotherms at 77 K of the magnetic nanocomposites. **E)** Colloidal stability of the magnetic nanocomposites analyzed by DLS in different aqueous media (water, DMEM culture medium, ALF). **F)** ZFC/FC magnetization curves of IONP@PMA and IONP-CV@ZIF-8@PMA.

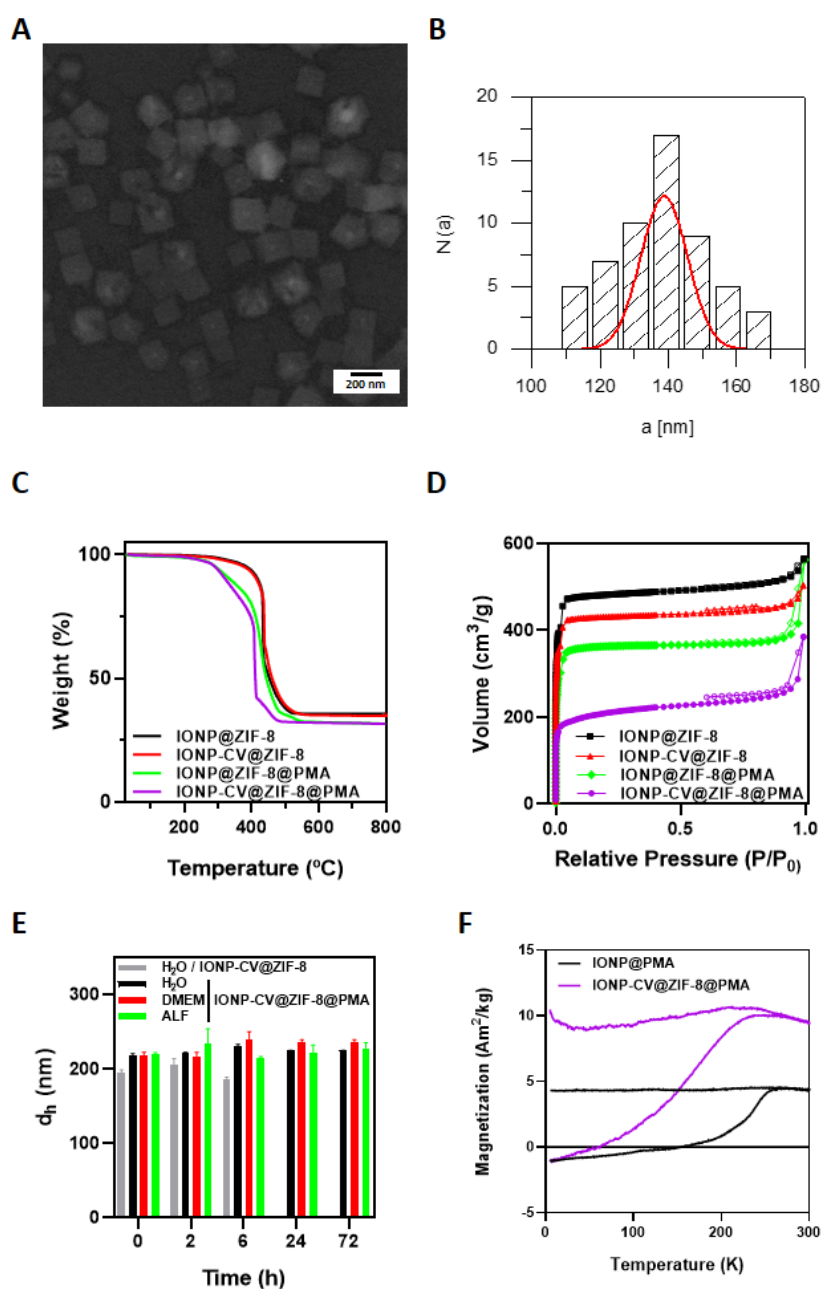


**Table S1:** Hydrodynamic diameters (number mean value  $\pm$  SD) obtained from DLS measurements of the nanocomposites in different media (water, Phosphate saline Buffer, 10% FBS supplemented cell medium (DMEM), artificial lysosomal fluid (ALF)) and nanocomposites in water. The IONP-CV@ZOF-8@PMA were stable in different media for up to 72 hours. The IONP-CV@ZOF-8 dispersed in water, aggregated at 24 h and were not detectable at 72 h.

T [h]	No PMA H <sub>2</sub> O	H <sub>2</sub> O	PBS	DMEM	ALF
0	194.7 $\pm$ 4.0	217.6 $\pm$ 3.1	203.3 $\pm$ 4.2	218.7 $\pm$ 3.8	220.3 $\pm$ 1.6
2	206 $\pm$ 7.6	220.8 $\pm$ 1.7	186.5 $\pm$ 5.2	216 $\pm$ 6.0	234.1 $\pm$ 19.6
6	185 $\pm$ 3.7	229.7 $\pm$ 3.0	206.8 $\pm$ 5.5	239.3 $\pm$ 10.8	214 $\pm$ 2.4
24	674.5 $\pm$ 474	224.5 $\pm$ 0.2	223.6 $\pm$ 6.0	235.2 $\pm$ 3.9	222.1 $\pm$ 9.7
72	0	224.5 $\pm$ 0.2	220.3 $\pm$ 8.7	235.6 $\pm$ 3.8	227.8 $\pm$ 7.2

**Figure S2: A and B)** Cytotoxicity of IONP-CV@ZIF-8@PMA in MiaPaCa2 (A) and CAF (B) cells. **C and D)** Cytotoxicity of IONP@ZIF-8@PMA in MiaPaCa2 (C) and CAF (D) cells. MiaPaCa2 or CAF cells were incubated with increased concentration of nanocomposites for 24, 48 or 72 h. The nanocomposites cytotoxicity was analyzed by MTT assay. Results are expressed as mean  $\pm$  SEM of at least three independent experiments.

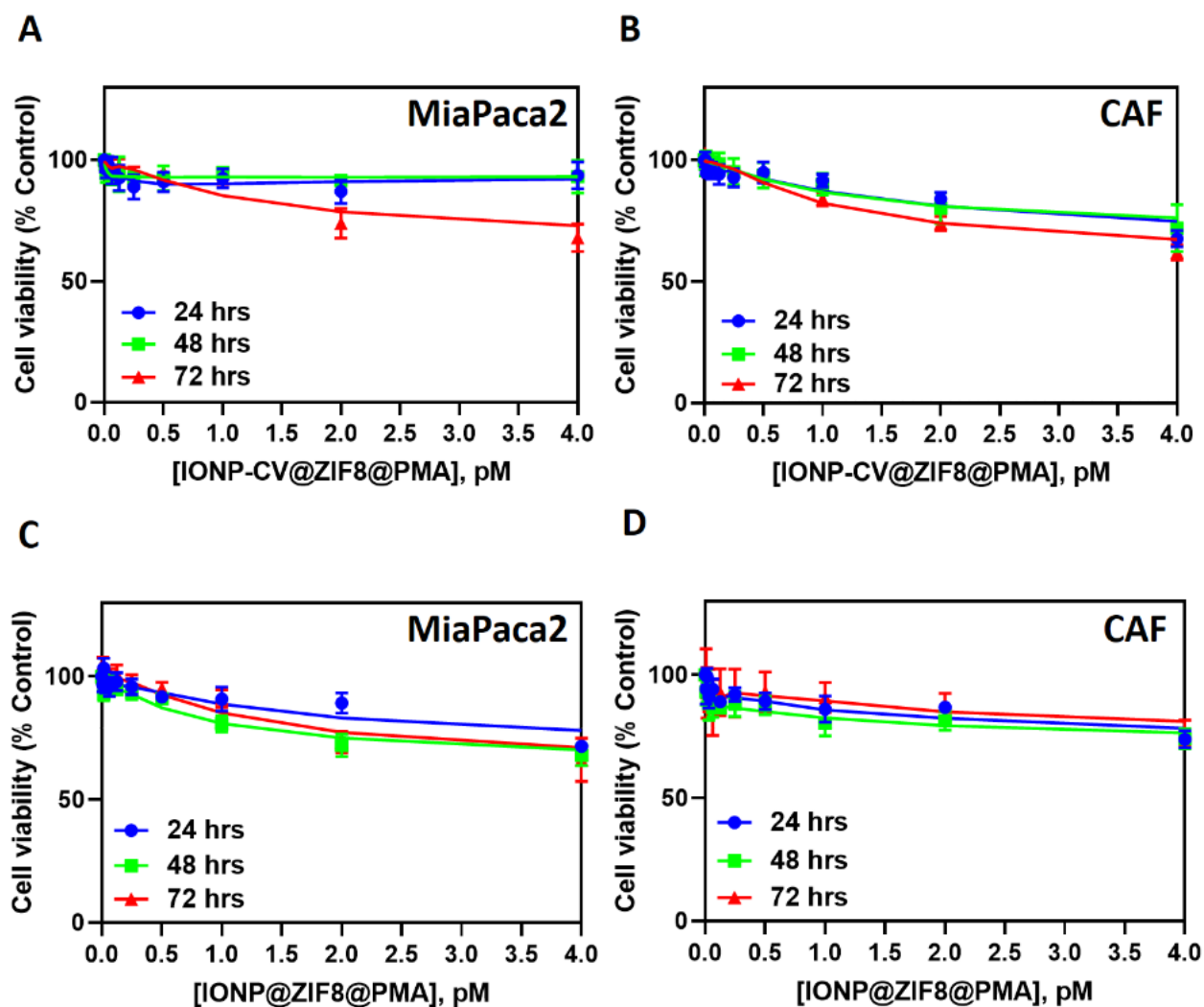


**Figure S3:** Analysis of hemocompatibility of IONP-CV@ZIF-8@PMA. Murine, rat or human blood was incubated with increasing concentrations of IONP-CV@ZIF-8@PMA, 1 mg/ml Triton X- 100 (positive control) or PBS (negative control) for 4 h at 37°C. Optical density of the supernatant was then measured at 540 nm and the hemolysis percent was calculated relative to the positive control (Triton X-100) represented 100% hemolysis. Results are expressed as mean ± sem.

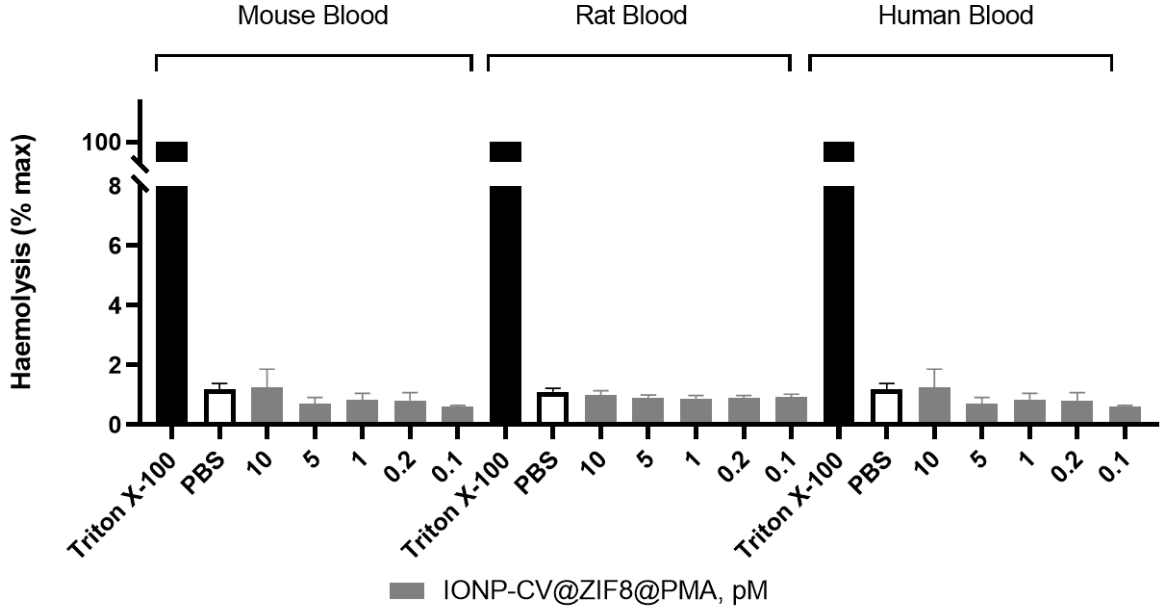


**Figure S4:** Induction of CV release upon RMF exposure. MiaPaCa2 cells were incubated with IONP-CV@ZIF-8@PMA for 72 h, washed, and exposed for 2 h to RMF (1Hz) with different amplitudes (10, 20, 30, 40, 50 60 and 70 mT). CV fluorescence intensity was analyzed by flow cytometry. Control cells were incubated with the IONP-CV@ZIF-8@PMA for 72 h, washed, but were not exposed to MF. The results are expressed as fold-basal of CV fluorescence intensity in control cells and are the mean  $\pm$  SEM of at least three independent experiments.

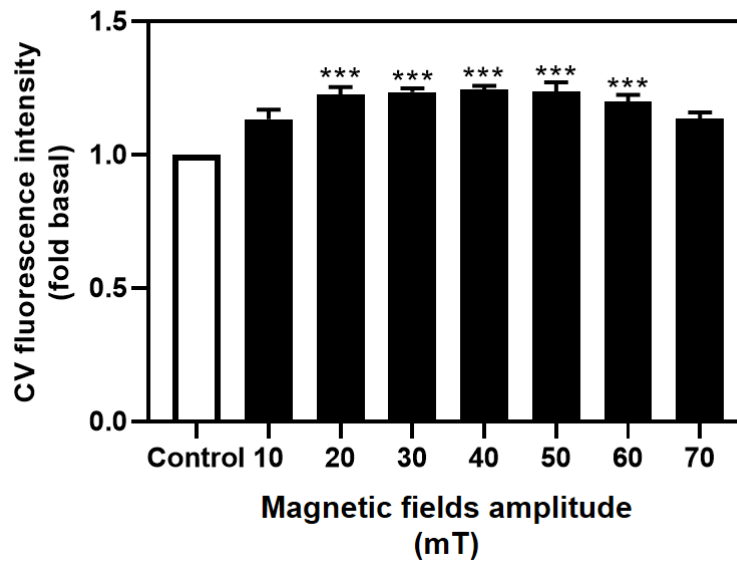


**Figure S5: A)** Induction of CV release upon AMF exposure. MiaPaCa2 cells were incubated with IONP-CV@ZIF-8@PMA for 72 h, washed, and exposed to AMF (40 mT, 275 kHz) for different times (30 min, 1h, 2 h and 2 exposures of 2h in two subsequent days). CV fluorescence intensity was analyzed by flow cytometry. Control cells were incubated with the IONP-CV@ZIF-8@PMA for 72 h, washed, but were not exposed to MF. The results are expressed as fold-basal of CV fluorescence intensity in control cells and are the mean  $\pm$  SEM of at least three independent experiments. **B)** Induction of CV release upon RMF exposure. MiaPaCa2 cells were incubated with IONP-CV@ZIF-8@PMA for 72 h, washed, and exposed to RMF (40 mT, 1 Hz) for different times (30 min, 1h, 2h and 2 exposures of 2h in two subsequent days). CV fluorescence intensity was analyzed by flow cytometry. Control cells were incubated with the IONP-CV@ZIF-8@PMA for 72 h, washed, but were not exposed to MF. The results are expressed as fold-basal of CV fluorescence intensity in control cells and are the mean  $\pm$  SEM of at least three independent experiments.

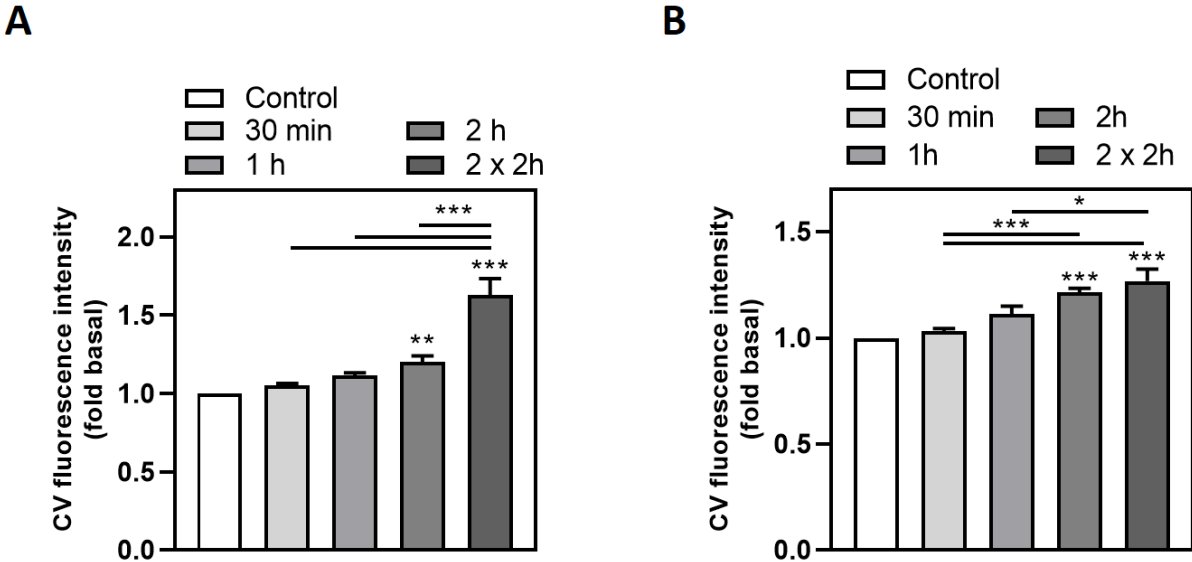


**Figure S6: A)** Number of cells per spheroid after their incubation or not with IONP-CV@ZIF-8@PMA for 24h, 48h and 72 h. **B)** Cell type proportion in spheroids during 3 days after spheroid formation (62% MiaPaCa2-GFP / 38% CAF).

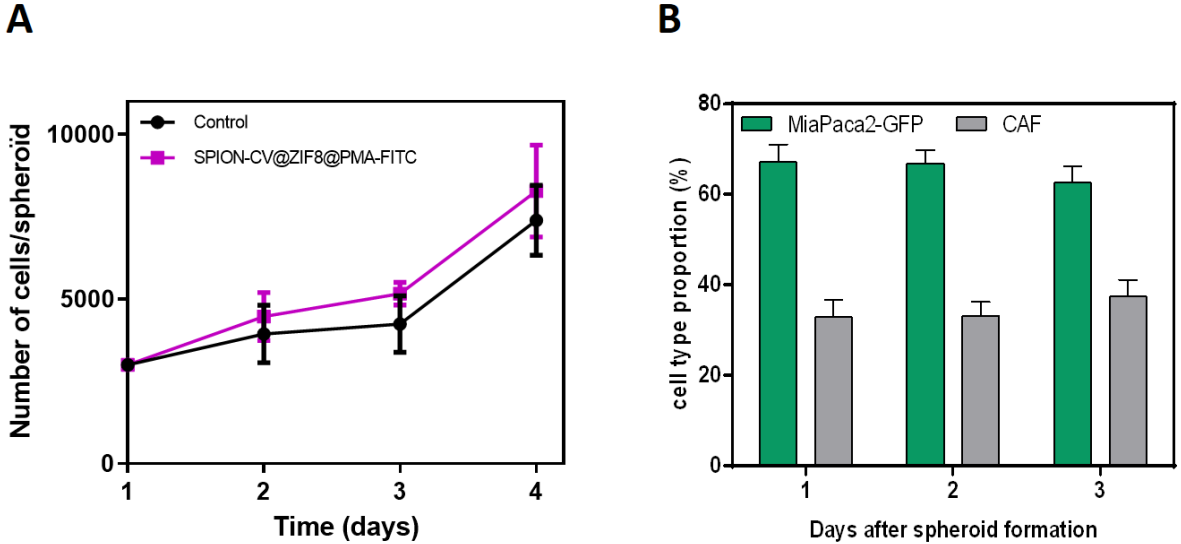


**Figure S7: A and B) MiaPaCa2 (A) and CAF (B) cellular proliferation assay following their incubation with IONP@ZIF-8@PMA or IONP-CV@ZIF-8@PMA (1 pM, 72 h), washing, and exposure or not to AMF (40 mT, 275 kHz) for 2 h, once/day during 3 days. Cell proliferation was evaluated by counting cells 24h after AMF exposure, during 3 days. Results are expressed as mean  $\pm$  SEM of at least three separate experiments. C and D) MiaPaCa2 (C) and CAF (D) cellular proliferation assay following their incubation with IONP@ZIF-8@PMA or IONP-CV@ZIF-8@PMA (1 pM, 72 h), washing, and exposure or not to RMF (40 mT, 1 Hz) for 2 h, once/day during 3 days. Cell proliferation was evaluated by counting cells 24h after RMF exposure, during 3 days. Results are expressed as mean  $\pm$  SEM of at least three separate experiments.**

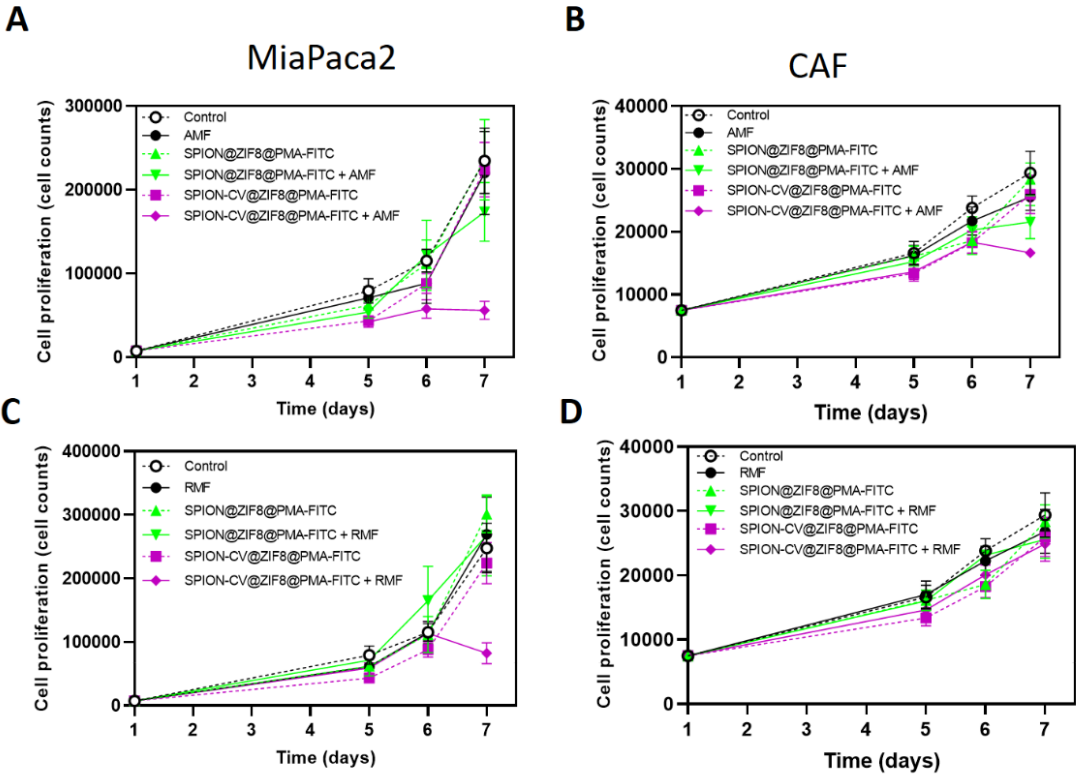


**Figure S8: Comparing the impact of CV-induced release (AMF vs. RMF) on cells viability (MiaPaCa2 vs. CAF) on 2D cultures. A and B) Analysis of MiaPaCa2 vs. CAF cell viability following their incubation with IONP-CV@ZIF-8@PMA for 72 h, washing, and exposure or not to AMF (40 mT, 275 kHz) (A) or RMF (40 mT, 1 Hz) (B) for 2 h, once/day during 3 days. Cell viability was evaluated by counting cells 24 h after last exposure. Results are expressed as mean  $\pm$  SEM of at least three separate experiments. C) Analysis of MiaPaCa2 cell viability following their incubation with IONP-CV@ZIF-8@PMA for 72 h, washing, and exposure or not to AMF (40 mT, 275 kHz) or RMF (40 mT, 1 Hz) for 2 h, once/day during 3 days. Cell viability was evaluated by counting cells 24h after last exposure. Results are expressed as mean  $\pm$  SEM of at least three separate experiments. D) Analysis of CAF cell viability following their incubation with IONP-CV@ZIF-8@PMA for 72 h, washing, and exposure or not to AMF (40 mT, 275 kHz) or RMF (40 mT, 1 Hz) for 2 h, once/day during 3 days. Cell viability was evaluated by counting cells 24h after last exposure. Results are expressed as mean  $\pm$  SEM of at least three separate experiments**

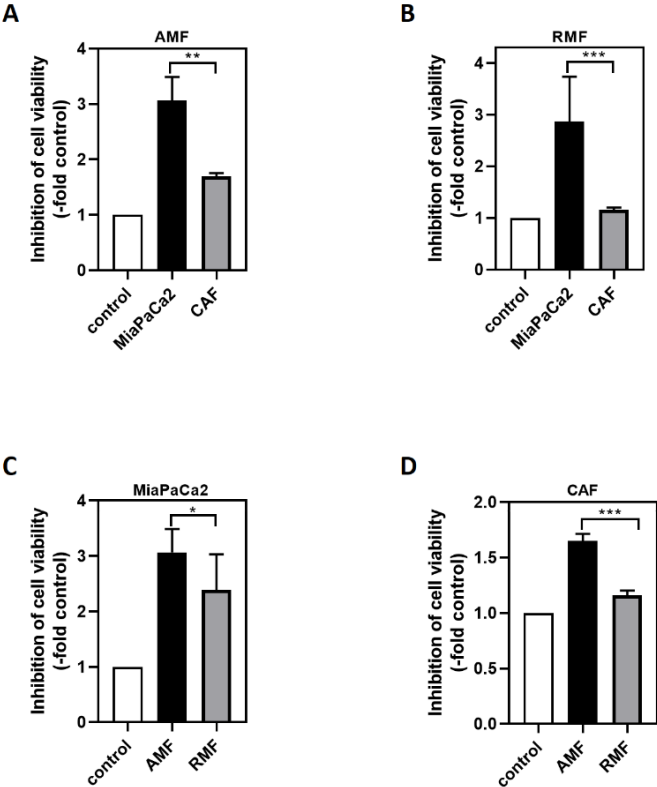


**Figure S9:** Cytotoxicity of CV on MiaPaCa2 (A) and CAF (B) cells. Cells were incubated with increased concentrations of CV for 24, 48 or 72 h. Cytotoxicity was analyzed by MTT assay. Results are expressed as mean  $\pm$  SEM of at least three independent experiments.

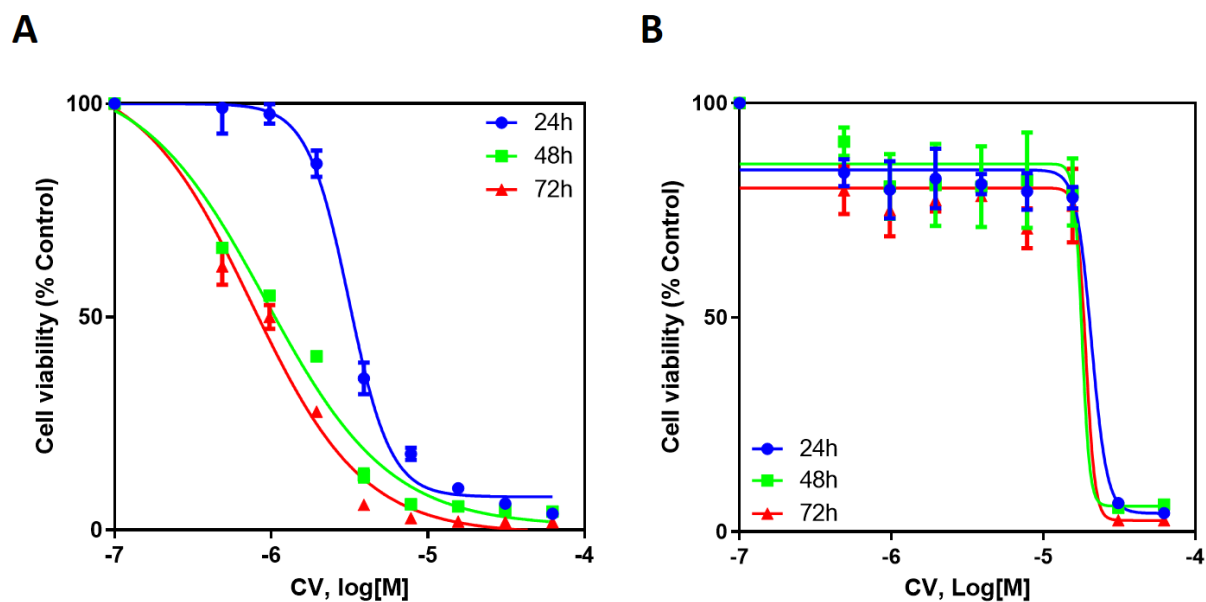


**Table S2:** IC<sub>50</sub> values of CV on MiaPaCa2 and CAF cells. Cells were incubated with increased concentrations of CV for 24, 48 or 72 h. Cytotoxicity was analyzed by MTT assay.

Cell	Incubation time (h)	IC <sub>50</sub> (μM)
MiaPaCa2	24	3.14
	48	0.92
	72	0.75
CAF	24	20.79
	48	17.99
	72	19.09

## References

1. Abbasi Kajani, A., et al., *Recent Advances in Nanomaterials Development for Nanomedicine and Cancer*. ACS Applied Bio Materials, 2021. **4**(8): p. 5908-5925.
2. Kim, K.Y., *Nanotechnology platforms and physiological challenges for cancer therapeutics*. Nanomedicine: Nanotechnology, Biology and Medicine, 2007. **3**(2): p. 103-110.
3. Gabizon, A.A., Y. Patil, and N.M. La-Beck, *New insights and evolving role of pegylated liposomal doxorubicin in cancer therapy*. Drug Resistance Updates, 2016. **29**: p. 90-106.
4. Zhao, Z., et al., *Effect of physicochemical and surface properties on in vivo fate of drug nanocarriers*. Advanced Drug Delivery Reviews, 2019. **143**: p. 3-21.
5. Duan, X. and Y. Li, *Physicochemical Characteristics of Nanoparticles Affect Circulation, Biodistribution, Cellular Internalization, and Trafficking*. Small, 2013. **9**(9-10): p. 1521-1532.
6. Panico, S., et al., *Biological Features of Nanoparticles: Protein Corona Formation and Interaction with the Immune System*. Pharmaceutics, 2022. **14**(12).
7. Fam, S.Y., et al., *Stealth Coating of Nanoparticles in Drug-Delivery Systems*. Nanomaterials, 2020. **10**(4): p. 787.
8. Wilhelm, S., et al., *Analysis of nanoparticle delivery to tumours*. Nature Reviews Materials, 2016. **1**: p. 16014.
9. Li, F., et al., *Stimuli-responsive nano-assemblies for remotely controlled drug delivery*. Journal of Controlled Release, 2020. **322**: p. 566-592.
10. Li, X., et al., *Magnetic nanoparticles for cancer theranostics: Advances and prospects*. Journal of Controlled Release, 2021. **335**: p. 437-448.
11. Golovin, Y.I., et al., *Towards nanomedicines of the future: Remote magneto-mechanical actuation of nanomedicines by alternating magnetic fields*. Journal of Controlled Release, 2015. **219**: p. 43-60.
12. Levy, M., et al., *Long term in vivo biotransformation of iron oxide nanoparticles*. Biomaterials, 2011. **32**(16): p. 3988-3999.
13. Yang, J. and Y.-W. Yang, *Metal–Organic Frameworks for Biomedical Applications*. Small, 2020. **16**(10): p. 1906846.
14. Horcajada, P., et al., *Metal–Organic Frameworks in Biomedicine*. Chemical Reviews, 2012. **112**(2): p. 1232-1268.
15. Ni, K., et al., *Nanoscale metal-organic frameworks enhance radiotherapy to potentiate checkpoint blockade immunotherapy*. Nat Commun, 2018. **9**(1): p. 2351.
16. Osterrieth, J.W.M. and D. Fairen-Jimenez, *Metal–Organic Framework Composites for Theragnostics and Drug Delivery Applications*. Biotechnology Journal, 2021. **16**(2): p. 2000005.
17. Haider, J., et al., *A review of synthesis, fabrication, and emerging biomedical applications of metal-organic frameworks*. Biomaterials Advances, 2022. **140**: p. 213049.
18. Carrillo-Carrión, C., et al., *Aqueous Stable Gold Nanostar/ZIF-8 Nanocomposites for Light-Triggered Release of Active Cargo Inside Living Cells*. Angewandte Chemie International Edition, 2019. **58**(21): p. 7078-7082.
19. Chen, J., et al., *Metal-organic framework-coated magnetite nanoparticles for synergistic magnetic hyperthermia and chemotherapy with pH-triggered drug release*. Science and Technology of Advanced Materials, 2019. **20**(1): p. 1043-1054.
20. Li, Y., et al., *Coordination-responsive drug release inside gold nanorod@metal-organic framework core–shell nanostructures for near-infrared-induced synergistic chemo-photothermal therapy*. Nano Research, 2018. **11**(6): p. 3294-3305.
21. Huang, J., et al., *Metal organic framework-coated gold nanorod as an on-demand drug delivery platform for chemo-photothermal cancer therapy*. Journal of Nanobiotechnology, 2021. **19**(1): p. 219.
22. Fang, J., et al., *Extremely low frequency alternating magnetic field–triggered and MRI–traced drug delivery by optimized magnetic zeolitic imidazolate framework-90 nanoparticles*. Nanoscale, 2016. **8**(6): p. 3259-3263.

23. Attia, M., et al., *Optimized metal-organic-framework based magnetic nanocomposites for efficient drug delivery and controlled release*. Journal of Drug Delivery Science and Technology, 2022. **76**: p. 103770.
24. Hühn, J., et al., *Selected Standard Protocols for the Synthesis, Phase Transfer, and Characterization of Inorganic Colloidal Nanoparticles*. Chemistry of Materials, 2017. **29**(1): p. 399-461.
25. Chen, R., M.G. Christiansen, and P. Anikeeva, *Maximizing Hysteretic Losses in Magnetic Ferrite Nanoparticles via Model-Driven Synthesis and Materials Optimization*. ACS Nano, 2013. **7**(10): p. 8990-9000.
26. Martínez, R., et al., *Core-Shell Palladium/MOF Platforms as Diffusion-Controlled Nanoreactors in Living Cells and Tissue Models*. Cell Reports Physical Science, 2020. **1**(6): p. 100076.
27. Sanchez, C., et al., *Targeting a G-Protein-Coupled Receptor Overexpressed in Endocrine Tumors by Magnetic Nanoparticles To Induce Cell Death*. ACS Nano, 2014. **8**(2): p. 1350-1363.
28. Lopez, S., et al., *Magneto-mechanical destruction of cancer-associated fibroblasts using ultra-small iron oxide nanoparticles and low frequency rotating magnetic fields*. Nanoscale Advances, 2022. **4**(2): p. 421-436.
29. Connord, V., et al., *Real-Time Analysis of Magnetic Hyperthermia Experiments on Living Cells under a Confocal Microscope*. Small, 2015. **11**(20): p. 2437-2445.
30. Hillion, A., et al., *Real-Time Observation and Analysis of Magnetomechanical Actuation of Magnetic Nanoparticles in Cells*. Nano Letters, 2022. **22**(5): p. 1986-1991.
31. Hwang, R.F., et al., *Cancer-Associated Stromal Fibroblasts Promote Pancreatic Tumor Progression*. Cancer Research, 2008. **68**(3): p. 918-926.
32. Duluc, C., et al., *Pharmacological targeting of the protein synthesis mTOR/4E-BP1 pathway in cancer-associated fibroblasts abrogates pancreatic tumour chemoresistance*. EMBO Mol Med, 2015. **7**(6): p. 735-53.
33. Carrey, J. and N. Hallali, *Torque undergone by assemblies of single-domain magnetic nanoparticles submitted to a rotating magnetic field*. Physical Review B, 2016. **94**(18): p. 184420.
34. Hu, S.-H., S.-Y. Chen, and X. Gao, *Multifunctional Nanocapsules for Simultaneous Encapsulation of Hydrophilic and Hydrophobic Compounds and On-Demand Release*. ACS Nano, 2012. **6**(3): p. 2558-2565.
35. Hanuš, J., et al., *Remotely Controlled Diffusion from Magnetic Liposome Microgels*. Langmuir, 2013. **29**(13): p. 4381-4387.
36. Xue, Z., et al., *An integrated targeting drug delivery system based on the hybridization of graphdiyne and MOFs for visualized cancer therapy*. Nanoscale, 2019. **11**(24): p. 11709-11718.
37. Chen, X.-X., et al., *ATP-responsive near-infrared fluorescence MOF nanoprobe for the controlled release of anticancer drug*. Microchimica Acta, 2021. **188**(9): p. 287.
38. Tiwari, A., et al., *Curcumin encapsulated zeolitic imidazolate frameworks as stimuli responsive drug delivery system and their interaction with biomimetic environment*. Scientific Reports, 2017. **7**(1): p. 12598.
39. Zhang, Z., et al., *Temperature responsive fluorescent polymer nanoparticles (TRFNPs) for cellular imaging and controlled releasing of drug to living cells*. Colloids and Surfaces B: Biointerfaces, 2017. **159**: p. 905-912.
40. Wu, M.-X., et al., *Multistimuli Responsive Core-Shell Nanoplatfrom Constructed from Fe<sub>3</sub>O<sub>4</sub>@MOF Equipped with Pillar[6]arene Nanovalves*. Small, 2018. **14**(17): p. 1704440.
41. Ray Chowdhuri, A., D. Bhattacharya, and S.K. Sahu, *Magnetic nanoscale metal organic frameworks for potential targeted anticancer drug delivery, imaging and as an MRI contrast agent*. Dalton Transactions, 2016. **45**(7): p. 2963-2973.
42. Vasconcelos, I.B., et al., *Cytotoxicity and slow release of the anti-cancer drug doxorubicin from ZIF-8*. RSC Advances, 2012. **2**(25): p. 9437-9442.

43. Zheng, H., et al., *One-pot Synthesis of Metal–Organic Frameworks with Encapsulated Target Molecules and Their Applications for Controlled Drug Delivery*. Journal of the American Chemical Society, 2016. **138**(3): p. 962-968.
44. Fairen-Jimenez, D., et al., *Opening the Gate: Framework Flexibility in ZIF-8 Explored by Experiments and Simulations*. Journal of the American Chemical Society, 2011. **133**(23): p. 8900-8902.
45. Yang, B., et al., *A flexible, strong, heat- and water-resistant zeolitic imidazolate framework-8 (ZIF-8)/ aramid nanofibers (ANFs) composite nanopaper*. Composites Communications, 2020. **17**: p. 192-196.
46. Carrillo-Carrión, C., et al., *Plasmonic-Assisted Thermocyclizations in Living Cells Using Metal–Organic Framework Based Nanoreactors*. ACS Nano, 2021. **15**(10): p. 16924-16933.
47. H. Vazifeshenas, F. and F. Bahadori, *Investigation of Soret effect on drug delivery in a tumor without necrotic core*. Journal of the Taiwan Institute of Chemical Engineers, 2019. **102**: p. 17-24.
48. Low, J.J., et al., *Virtual High Throughput Screening Confirmed Experimentally: Porous Coordination Polymer Hydration*. Journal of the American Chemical Society, 2009. **131**(43): p. 15834-15842.
49. Xue, W., et al., *AMF responsive DOX-loaded magnetic microspheres: transmembrane drug release mechanism and multimodality postsurgical treatment of breast cancer*. Journal of Materials Chemistry B, 2018. **6**(15): p. 2289-2303.
50. Peiris, P.M., et al., *Enhanced Delivery of Chemotherapy to Tumors Using a Multicomponent Nanochain with Radio-Frequency-Tunable Drug Release*. ACS Nano, 2012. **6**(5): p. 4157-4168.
51. Nikitin, A.A., et al., *Magneto-Mechanical Approach in Biomedicine: Benefits, Challenges, and Future Perspectives*. International Journal of Molecular Sciences, 2022. **23**(19): p. 11134.
52. Golovin, Y., et al., *Modeling drug release from functionalized magnetic nanoparticles actuated by non-heating low frequency magnetic field*. Journal of Nanoparticle Research, 2017. **19**(2): p. 64.
53. Li, Y., et al., *Creating an Aligned Interface between Nanoparticles and MOFs by Concurrent Replacement of Capping Agents*. Journal of the American Chemical Society, 2021. **143**(13): p. 5182-5190.

## Second part of results: Synthesis of chemotherapeutic drug loaded metal-organic frameworks magnetic nanocomposites

**The major aim of this part was to continue the work beyond the proof of concept using the fluorescent probe towards using anticancer drugs. So that, this work investigated the feasibility of preparing magnetic metal-organic frameworks nanocomposites loaded with anticancer drugs. In addition, we investigated here the possibility of having magnetic nanoparticle cores of different sizes, shapes and compositions that could affect the magnetic properties of the prepared nanocomposites.**

**This part was done during a secondment to Nanomaterials for biomedical application group in the Italian institute of technology (Genova, Italy), PI: Prof. Teresa Pellegrino. This experimental work was done by me, Ana Maria Panaite and Aleksandra Predeina (early-stage researchers from the HEATNMof project)**

## **Contents**

- I. Introduction
- II. Materials and methods
- III. Results and discussions
- IV. Conclusions and perspectives
- V. References

## I. Introduction

After the proof of concept using the cresyl violet fluorescent probe, the next step was to load the magnetic metal-organic frameworks (MOFs) nanocomposites (NCs) with anticancer drugs. In addition, it could be interesting to assess other types of magnetic nanoparticles (MNPs) of different shapes, sizes and compositions. Herein, a preliminary study was done to investigate the feasibility of synthesizing zeolitic imidazolate frameworks-8 (ZIF-8) NCs with different types of MNP cores and loading them with two different chemotherapeutic drugs.

The MNPs used in the study in order to grow the ZIF-8 shells on their surface were iron oxide nanoflowers (IONFs) of ~32 nm, Zn-ferrite nanocubes (ZFNCs) of ~23 nm and ~18 nm, and iron oxide nanocubes (IONCs) of ~16 nm. Having MNP cores of different sizes, shapes and compositions inside the NCs could result in different heating power and mechanical movement responses the applied magnetic fields (MF) [1, 2].

On the other hand, loading the NCs with chemotherapeutic drugs could allow to study more in depth their intracellular-induced effects after the magnetic MF-induced release. The chemotherapeutic drugs selected for this study were doxorubicin (DOX) and 5-fluorouracil (5-FU), figure 1 shows their chemical structure.

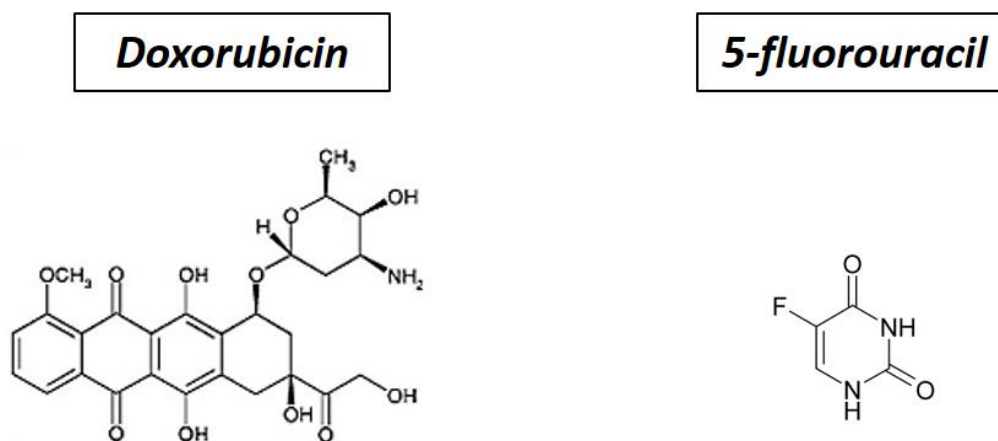


Figure 1: Chemical structures of doxorubicin and 5-fluorouracil.

DOX is a fluorescent molecule that can be followed and monitored using fluorescence-based spectroscopic and imaging techniques [3]. DOX loading into ZIF-8 surface could be mediated by its interaction with the surface Zn<sup>2+</sup> cations *via* its quinone and the phenolic oxygens chelating sites on both sides of the DOX anthracene aromatic moiety. The Zn<sup>2+</sup> cations in ZIF-8 have tetrahedral

geometry, making them bind to four imidazolate groups. While on the ZIF-8 surface,  $Zn^{2+}$  binds only to two imidazolate and water molecules replace the other two imidazolate organic linkers. So that DOX could replace the two water molecules on the ZIF-8 surface and maintain the  $Zn^{2+}$  tetrahedral geometry [4]. DOX loading through surface adsorption into ZIF-8 was reported using the impregnation post-synthesis approach, and it achieved a loading of 4.9% w/w [4].

DOX has a large molecular size of  $14.64 \times 10.02 \times 6.90 \text{ \AA}$  that is larger than the ZIF-8 pores (pore size of  $11.6 \text{ \AA}$  and pore opening of  $\sim 3.4 \text{ \AA}$ ) [3, 4]. However, Zheng *et al.* investigated its loading inside the ZIF-8 crystal using the one-pot *in-situ* synthesis approach, and interestingly, they were able to achieve loadings up to 20% w/w [3]. In their study, there were observed mesopores (5-15 nm) that contained DOX inside the ZIF-8 crystals, detected using the transmission electron microscope (TEM) [3]. The powder X-ray diffraction revealed that DOX is loaded in its molecular form, as no DOX crystals were detected inside the ZIF-8 [3].

DOX was also loaded through impregnation to the surface of gold nanorods-based ZIF-8 NCs, and its release was triggered by dual near infra-red (NIR) irradiation and pH stimuli [5, 6]. Moreover, it was possible to trigger the release of 95% of the surface-loaded DOX after 12h in PBS solution under pH = 5.5 and NIR laser irradiation ( $808 \text{ nm}$ ,  $1 \text{ W}\cdot\text{cm}^{-2}$ ), compared to 60% under pH = 5.5 without laser irradiation, 50% with laser irradiation under pH = 7.4 and 17% under pH=7.4 without laser irradiation [5]. Hence, it was reported that DOX can be loaded into the ZIF-8 MOFs either on their surface or inside their pores, and its release could be triggered by light-mediated hyperthermia.

On the other side, 5-FU is a flat molecule with a smaller size ( $5.42 \times 4.50 \text{ \AA}$ ) compared to DOX ( $14.64 \times 10.02 \times 6.90 \text{ \AA}$ ) [3, 7]. Although it could fit inside the ZIF-8 pores, it was reported using molecular dynamics simulations that 5-FU cannot diffuse under normal conditions inside them due to their smaller pore window (ca.  $3.4 \text{ \AA}$ ). So that, the impregnation approach resulted in loading the 5-FU into the surface of gold nanoparticle-based ZIF-8 NCs. Afterwards, it was successfully released in response to heating using visible light laser irradiation through surface desorption [7]. There was an observed 29.5% hyperthermia-induced 5-FU release from the gold nanoparticles@ZIF-8 NCs after 30 min of laser irradiation ( $524.5 \text{ nm}$  and  $700 \text{ mW}\cdot\text{cm}^{-2}$ ) compared to  $\sim 12\%$  without laser irradiation in water at pH=7.0 [7].

Therefore, it could be interesting to investigate the feasibility of DOX *versus* 5-FU release from ZIF-8 in response to MF stimuli (magnetic hyperthermia or mechanical stress) that have their potential advantages *vis-à-vis* the photo-thermal one, as discussed in the state-of-the-art chapter. The two drugs have different sizes and molecular weights, thus could show different diffusion coefficients. Comparing their kinetics of release from magnetic NCs after the MF exposure could be interesting. In addition, as

was noted in the first results part, having NCs loaded with drugs on their surface and others loaded with drugs inside the pores could be interesting for getting insights into the triggered release mechanisms. Hence, we will investigate the loading of each drug using two approaches: the one-pot *in-situ* loading to allow pore loading of the drugs, or the post-synthesis impregnation approach to allow the drug surface loading.

In summary, the research of this preliminary study was done in two steps. First, NC synthesis by growing ZIF-8 shells on the surface of each of the chosen MNP cores was investigated. Afterwards, loading the optimized selected NCs with DOX and 5-FU using one-pot synthesis and impregnation approaches was studied.

## II. Materials and Methods

Methyl imidazole (Melm), zinc nitrate hexahydrate ( $\text{Zn}(\text{NO}_3)_2 \cdot 6\text{H}_2\text{O}$ ), DOX hydrochloride (98.0–102.0%), 5-FU ( $\geq 99\%$ ), methanol (99.8%) and ethanol ( $\geq 99.8\%$ ) were purchased from Sigma Aldrich. Milli-Q water filtered through 0.22 mm pore size hydrophilic filters (18.2 MO-cm) was supplied by a Milli-Q integral water purification system.

### NC synthesis:

1 mL of 1.3 M Melm aqueous solution was placed in a glass vial under sonication at room temperature (RT). Then 1 mL of 0.025 M  $\text{Zn}(\text{NO}_3)_2 \cdot 6\text{H}_2\text{O}$  aqueous solution was added. Immediately after, 1 mL of  $5 \times 10^{-4}$  M cetyltrimethylammonium bromide (CTAB) aqueous solution containing 2nM MNPs (IONFs ( $\text{Fe}_3\text{O}_4$ ) of  $\sim 32$ nm, or ZFNCS ( $\text{Zn}_{0.6}\text{Fe}_{2.4}\text{O}_4$ ) of  $\sim 23$  nm or of  $\sim 18$  nm) was added. These three MNPs were tried at the beginning to grow the ZIF-8 shells on their surface and were synthesized according to the protocol previously published [8]. The mixture was sonicated at RT for 5 min. Then, it was left undisturbed for 3h at RT and observed during this time for the gradual appearance of whitish turbidity, which indicates the growth of the ZIF-8 shell. Finally, the NCs were collected by centrifugation (7000 RCF, 10 min), washed twice with methanol and finally, redispersed in 3 mL of methanol. As the NCs aren't stable in water, they were finally dispersed in methanol.

Since synthesizing the NCs using the previously used MNPs at RT yielded aggregated structures, a modified protocol for their synthesis at a higher temperature was tested. In this approach, the glass vial containing the methyl imidazole aqueous solution was placed under sonication at 60°C. Then, the zinc nitrate and CTAB-coated MNPs solutions were added. Afterwards, the mixture was sonicated for

5 min at 60°C and left in the hot water bath 60°C without sonication for another 5 minutes. The remaining steps were kept the same.

Since the NCs aggregated structure challenge was not solved at the higher temperature, smaller IONCs ( $\text{Fe}_3\text{O}_4$ ) of  $16 \pm 2$  nm were used for the NC synthesis and the reaction was done at RT as previously described. The solvent here was changed to ethanol as it was observed in separate study trials that it could yield more monodisperse nanocomposites. In addition, different ZIF-8 shell growth times were tried, ranging from 1.5 h to 3 h.

After all syntheses, the prepared NCs were characterized by TEM and dynamic light scattering (DLS)

#### **One-pot *in-situ* drugs encapsulation in NCs:**

1 ml of 1,3M MeIm was added in a glass vial placed under sonication at RT. Then, 1 ml of 0,025M of zinc nitrate containing the drug, [500  $\mu\text{g}/\text{ml}$ ] 5-FU or DOX, was added to the glass vial. Afterward, 1 ml of previously sonicated 5 nM of IONCs (16 nm) in CTAB aqueous solution (0.2 mg/ml) was added as seeds for the ZIF-8 shells growth. The final drug concentration in the growth solution of the ZIF-8 shell was 166.7  $\mu\text{g}/\text{ml}$ . The mixture was sonicated at RT for 5 min and then left undisturbed at RT for 3 hrs. After the incubation, the solution (3 ml) was transferred from the glass vial into two 2 ml microtubes (1.5 ml microtube), centrifugated at 7000 rcf for 10 min, water was removed and it was redispersed in ethanol. The contents of the two microtubes were pooled and centrifuged again at 7000 rcf for 10 min. The supernatant was removed and the NCs were finally redispersed in ethanol.

Since the DOX-loaded NCs did not form at the previously used concentration of 500  $\mu\text{g}/\text{ml}$  in the zinc nitrate solution (equivalent to 166.67  $\mu\text{g}/\text{ml}$  in the reaction mixture of the ZIF-8 shell growth solution), synthesizing the NCs using 10x, 15x and 20x lower DOX concentrations was investigated. The new used concentrations of DOX were 50, 37.5 and 25  $\mu\text{g}/\text{ml}$  in the zinc nitrate solution (equivalent to 16.67, 12.5 and 8.33  $\mu\text{g}/\text{ml}$ , respectively, in the reaction mixture of the ZIF-8 shell growth solution).

The drugs encapsulation efficiencies were assessed indirectly using the amounts of the remaining drug in the reaction supernatants and the wash with the UV-spectrophotometer. The loaded NCs were checked using the TEM.

It was observed that a larger amount of DOX was present in the ethanol wash compared to the aqueous CTAB supernatant of the reaction. Hence, the washing solution was recharged to methanol for the next loading approach.

### Drugs encapsulation in the NCs through post-synthesis impregnation:

400 µl of the NCs prepared using IONCs (16 nm) in methanol ([0.5 mg/ml] Fe and [2.34 mg/ml] Zn) and 100 µl of methanol were added in 4 ml glass vial. Then, 500 µl of the drug solution in methanol was added, [2 mg/ml] DOX or 5-FU. So that the final drugs concentration in the NCs and drugs mixture was 1000 µg/ml, at the same concentration of DOX that was used by Li *et al.* to load it into the goldnanorods@ZIF-8 NCs through the impregnation method, although the NCs concentrations could be different [5]. The mixture was left overnight under shaking at 800 rpm. After the overnight incubation, the mixture was centrifuged for 10 min at 7000 rcf and supernatant was collected, and the pellets were suspended in 1 ml of methanol. Then, it was centrifuged again for 10 min at 7000 rcf, supernatant was collected, and the pellets were suspended in 1 ml of methanol.

The encapsulation efficiencies were indirectly assessed using the amounts of the remaining drug in the reaction supernatants and the wash with the UV-VIS Spectrophotometer. The loaded NCs were checked using the TEM and DLS.

### NCs characterization

Zetasizer Nano ZS90 Malvern instrument was used to measure the hydrodynamic diameter (expressed here by mean number), polydispersity index (PDI) and ζ- potential of the synthesized NCs after their 1:10 dilution in their respective solvent. The shape and size of the NCs was assessed using JEOL JEM 1011 or JEOL JEM 1400. Finally, the UV-Vis absorption of DOX and 5-FU were measured using Cary 60, Agilent instruments, after establishing their calibration curves in the respective solvents.

The encapsulation efficiency (EE) was determined indirectly by subtracting the drug amount in the synthesis/loading reaction supernatant and washes (free drug) from the total initially added drug amount using the following equation:

$$EE (\%) = \frac{m_{initial\ drug} - m_{free\ drug}}{m_{initial\ drug}} * 100$$

### III. Results and discussion

#### NCs synthesis:

The synthesis of core-shell ZIF-8 MOFs magnetic NCs using the chosen MNPs (IONFs of ~32 nm, or ZFNCs of ~23 nm or ~18 nm) was first investigated under sonication at RT (Figures 2a, 2b and 2c). It was noticed that there were loops or aggregates of MNPs themselves, and the ZIF-8 shells either grew on the surface of these loops (upon using ZFNCs of ~23 nm or IONFs of ~32nm) (Figures 2d and 2f) or did not grow on their surface (upon using ZFNCs of ~18 nm) (Figure 2e). To decrease the interactions between the MNPs to form individual NC particles, the synthesis of the NCs was then investigated at a higher temperature (60 °C). However, the loops and aggregates of the MNPs still did not dissociate, resulting in the growth of ZIF-8 shells on their surface (Figures 2g, 2h and 2i). This growth resulted in the formation of large composites particles with loops or aggregates of MNPs [9]. It was reported that aggregates of MNPs could have a low susceptibility that reduces their heating power due to the intra-aggregates dipolar interactions [10].

The aggregation of the MNPs could be due to having remanent magnetization at RT that hindered their colloidal stability and made them form aggregates that seem not to be efficiently dissociated with sonication and at higher temperature. To overcome this challenge, smaller-sized superparamagnetic IONCs (16 nm) (Figure 3a) were tried to grow the ZIF-8 shell on their surface, and the NC synthesis was done at RT [8].

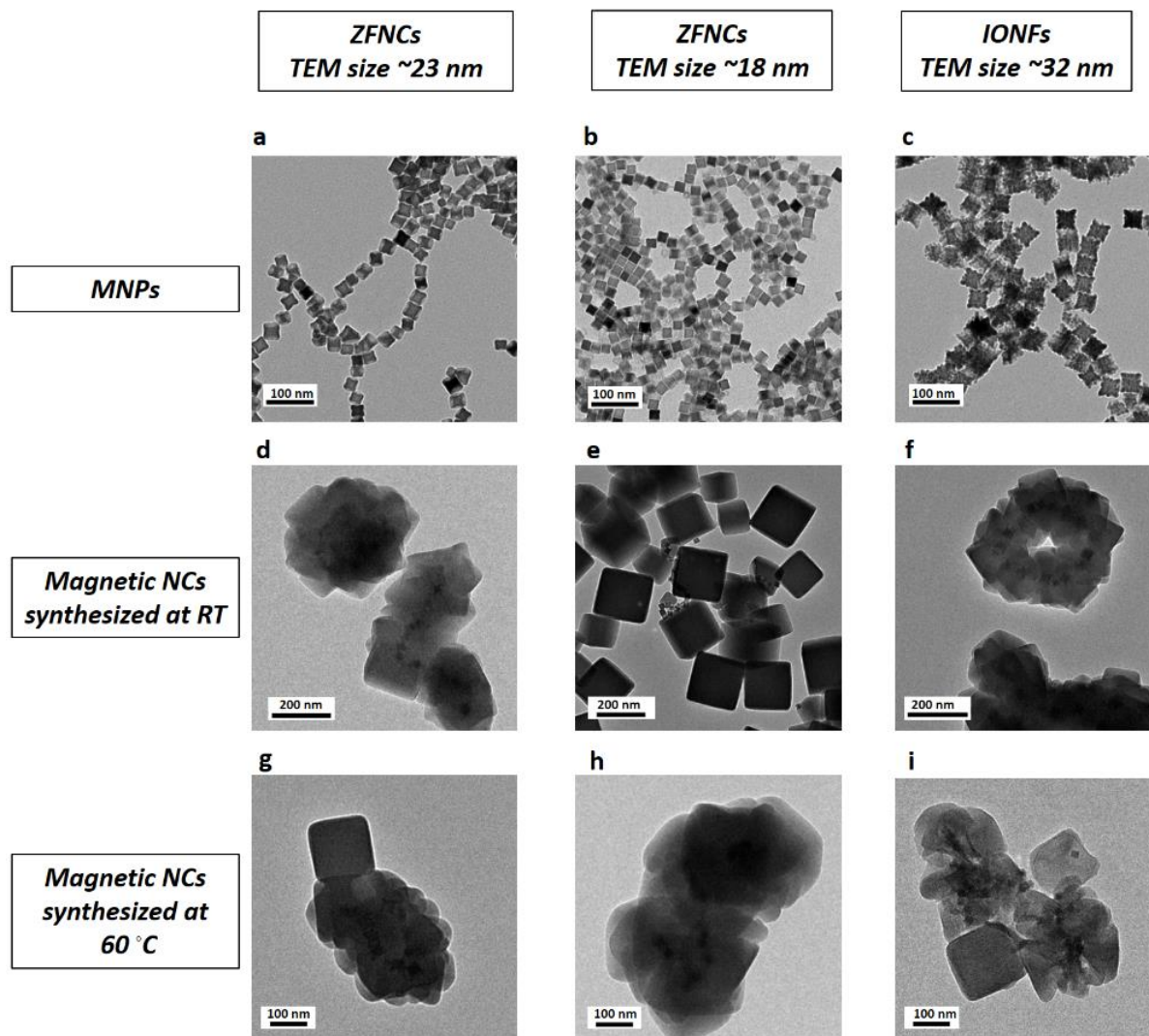


Figure 2: TEM images of the different MNPs (a-c) used in the preparation of the magnetic NCs by growing the ZIF-8 shells on their surface at room temperature (d-f) and at 60 °C (g-i).

The ZIF-8 shells were grown on the surface of the superparamagnetic IONCs (16 nm) without observed aggregates or loops (Figure 3b). It was also observed that multi-faceted nanoZIF-8 shells were grown on the IONCs (16 nm) cores, which was reported to be related to the used concentration of CTAB in the ZIF-8 growth solution on the surface of the metal nanoparticles cores [11]. The formed NCs had a TEM size of ~200 nm, a hydrodynamic diameter of  $314 \pm 102$  nm, a PDI of 0.06 and a  $\zeta$ -potential of +40.3 mV.

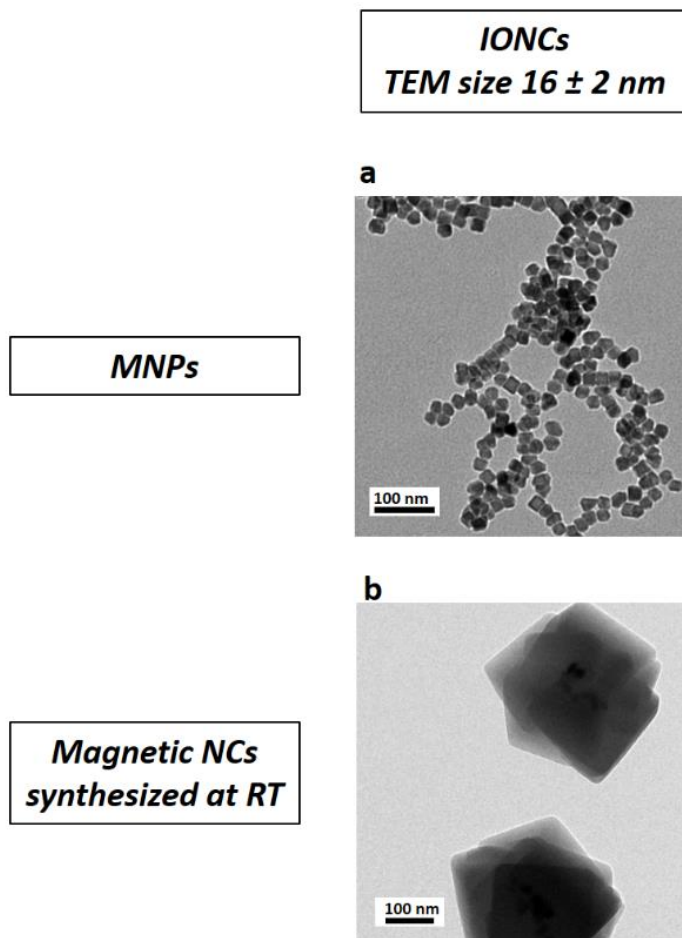


Figure 3: TEM images of the IONCs (16 nm) (a) used in the preparation of the magnetic NCs by growing the ZIF-8 shells on their surface at room temperature (b).

ZIF-8 shell growth times shorter than 3h were also investigated to assess the possibility of tuning the NC size by controlling the reaction time. The investigated times of ZIF-8 shell growth were 1.5h, 2h and 2.5h (Figure 4). The growth time of 1.5 h was not sufficient for yielding homogenous NCs with fully-grown ZIF-8 shells, as shown in their TEM images (Figure 4a). There was no significant difference in the hydrodynamic diameter between the NCs synthesized after 2h ( $285 \pm 76$  nm), 2.5h ( $371 \pm 118$  nm) and 3h ( $314 \pm 102$  nm). The formed NCs do not have a spherical shape, and the DLS determines the hydrodynamic diameter of an equivalent sphere that diffuses at the same speed [12], so the DLS here could not reveal the particle size differences of the prepared NCs. Using TEM, it was observed that reducing the ZIF-8 growth time resulted in smaller NC size: they had a size of  $\sim 200$  nm after 3h,  $\sim 190$  nm after 2.5h and  $\sim 165$  nm after 2h. Hence, it was possible to control the NC size by controlling the ZIF-8 shell growth time.

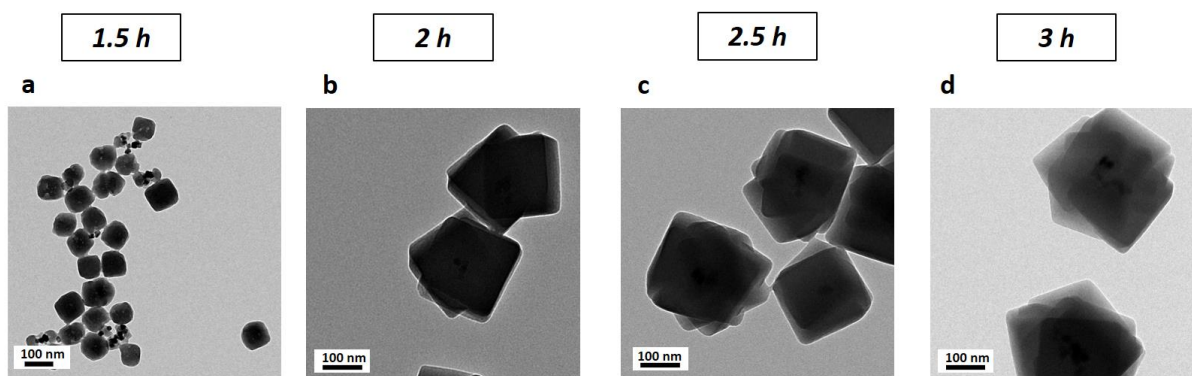


Figure 4: TEM images of NCs prepared by growing the ZIF-8 shell on the surface of the IONCs after different growth times: 1.5h (a), 2h (b), 2.5h (c) and 3h (d).

The next step was to assess the possibility of loading the synthesized NCs composed of the IONCs (16 nm) cores and ZIF-8 shells with the anticancer drugs (DOX and 5-FU) using two different approaches: the one-pot or the impregnation. For these trials, the ZIF-8 shells growth time was kept initially at 3h and could be re-optimized separately for the drug-loaded nanocomposites.

#### **One-pot *in-situ* drugs encapsulation in NCs:**

The one-pot *in situ* synthesis was investigated for preparing drug-loaded NCs. Using this approach, NCs loaded with 5-FU, upon having [166.67  $\mu\text{g/ml}$ ] 5-FU in the ZIF-8 growth solution, were successfully synthesized (Figures 5c and 5d), with an encapsulation efficiency of 69%. However, at the same concentration of DOX, the ZIF-8 crystal shells failed to grow on the surface of the IONCs (16 nm) cores (Figures 5a and 5b). The reason could be related to strong interactions between the DOX and  $\text{Zn}^{2+}$  cations that hindered the ZIF-8 crystal growth. It was reported that DOX loading into ZIF-8 is mediated by its interaction with the  $\text{Zn}^{2+}$  cations *via* chelating sites comprised of the quinone and the phenolic oxygens on both sides of its anthracycline aromatic moiety [4]. As a consequence, high DOX concentration could have hindered the  $\text{Zn}^{2+}$  cations from interacting with the imidazolate organic linkers that prevented the ZIF-8 shell crystal growth.

Alternatively, preparing DOX-loaded NCs through one-pot *in-situ* synthesis method was investigated at 10x, 15x, 20x lower DOX concentrations than the previously used concentration. The new concentrations used of DOX were 16.67, 12.5 and 8.33  $\mu\text{g/ml}$  in the ZIF-8 shell growth solution.

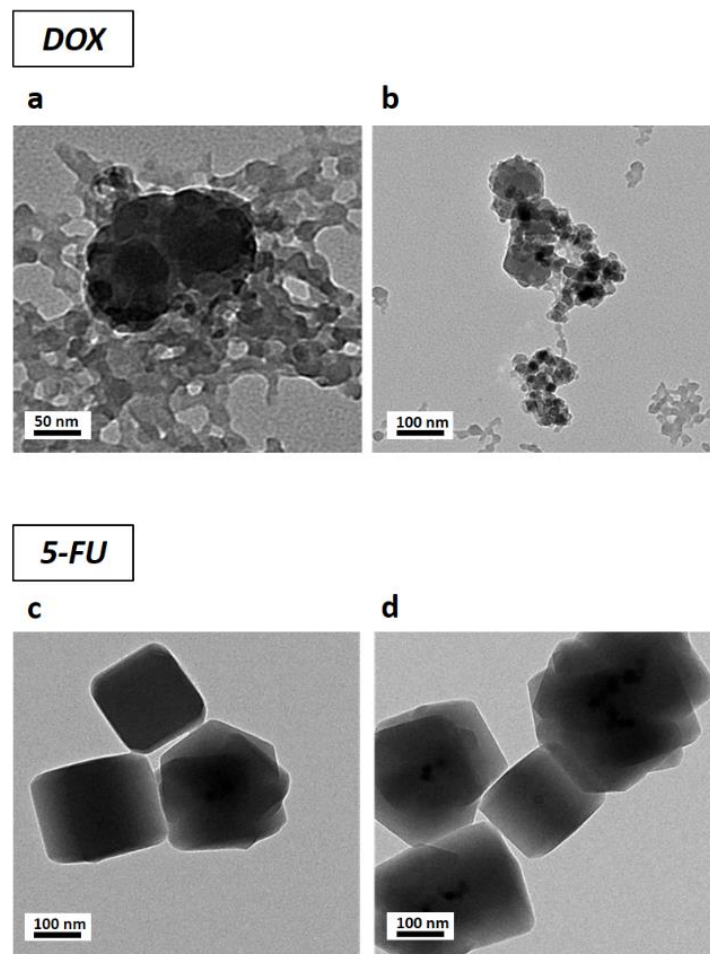


Figure 5: TEM images for using the one-pot *in-situ* synthesis approach for preparing NCs loaded with DOX (a and b) and 5-FU (c and d).

The NCs prepared using the lower DOX concentrations showed well-formed ZIF-8 shells grown on the surface of the IONCs (16 nm) cores (Figure 6). They showed 85.8%, 90.4% and 95.3 % encapsulation efficiencies upon using DOX concentrations of 16.67, 12.5 and 8.33  $\mu\text{g}/\text{ml}$ , respectively, in the ZIF-8 growth solution. This correlation between the used drug concentrations and the encapsulation efficiency could be expected. In the reactions series, the same amount of NC precursors were used, that could load the same amount of drug. Therefore, the lower initial concentration (amount) of the added drug during the synthesis would result in less non-encapsulated amount and consequently higher encapsulation efficiency.

Interestingly, when a DOX concentration of 16.67  $\mu\text{g}/\text{ml}$  was used (Figure 6a), mesopores were noticed inside the ZIF-8 shell in the TEM images (Figure 6a). These mesopores were not observed in NCs prepared using the two lower DOX concentrations (Figure 6b, 6c). Similar mesopores appearance was observed by Zheng *et al.* in DOX-loaded ZIF-8 nanoparticles prepared by one-pot *in situ* synthesis

approach. In their study, the mesopores also observed in the ZIF-8 TEM images at higher loading efficiencies of 14 % and 20 % w/w, but not at the lower one of 4 % w/w [3].

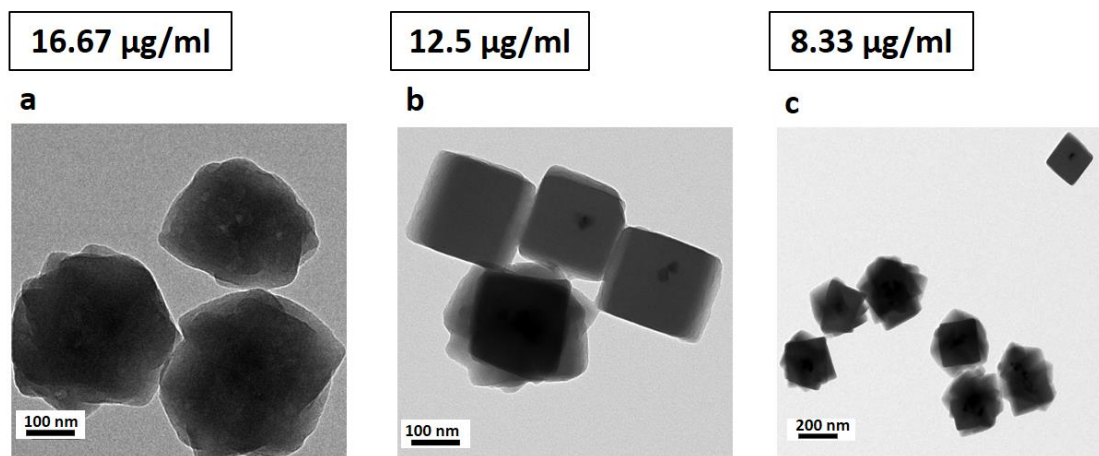


Figure 6: TEM images of DOX loaded NCs prepared through one-pot in situ synthesis approach upon using DOX concentrations of 16.67 µg/ml (a), 12.5 µg/ml (b) and 8.33 µg/ml (c).

#### Drugs encapsulation in the NCs through post-synthesis impregnation:

Through the post-synthesis impregnation approach when mixing NCs of IONCs (16 nm) cores with drugs concentration of 1000 µg/ml in the loading solution, the NCs were loaded with DOX and 5-FU with 59% and 51% encapsulation efficiencies, respectively. The drugs loading did not affect the shape of the NCs, as observed in the TEM images (Figure 7). The DOX-loaded NCs showed a hydrodynamic diameter of  $369 \pm 7$  nm, a PDI of 0.18 and a  $\zeta$ -potential of +34.7 mV. The 5-FU loaded NCs had a hydrodynamic diameter of  $382 \pm 5$  nm, a PDI of 0.17 and a  $\zeta$ -potential of +37.8 mV. The drug-loaded NCs showed similar hydrodynamic diameters, slightly higher PDI values and a slightly less positive  $\zeta$ -potential compared to the non-loaded NCs (hydrodynamic diameter of  $314 \pm 102$  nm, PDI of 0.06 and  $\zeta$ -potential of +40.3 mV). The drug-loaded NCs still showed a low PDI with no observed aggregates in DLS measurements, indicating no negative impact of the drug loading on their colloidal stability. The slight  $\zeta$ -potential decrease after both drug-loading into the NCs could be related to the adsorption of the negatively charged drug molecules at the NCs surface, decreasing their surface positive charge.

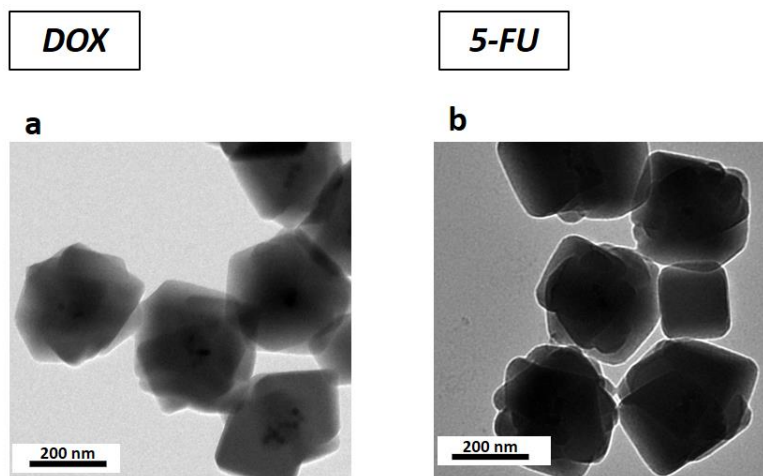


Figure 7: TEM images of NCs loaded with DOX (a) and 5-FU (b) through post-synthesis impregnation approach.

#### IV. Conclusions and perspectives

This study investigated the feasibility of synthesizing NCs of MNP cores of different sizes, shapes and dimensions, and ZIF-8 shells loaded with 5-FU and DOX. In addition, the study examined the loading of each drug into the NCs through one-pot *in-situ* or post-synthesis impregnation approaches. The initially used MNPs (IONFs of  $\sim 32$  nm, and ZFNCs of  $\sim 23$  nm and of  $\sim 18$  nm) formed loops and aggregates during the synthesis that did not disperse by sonication nor at the higher temperature of  $60$  °C. The growth of ZIF-8 on the surface of aggregated nanoparticles resulted in the formation of large NCs particles. The aggregated MNPs inside the large NC particles could result in a smaller magnetic susceptibility and less heating power due to the intra-aggregates dipolar interactions. Alternatively, using superparamagnetic smaller-sized IONCs (16 nm) as cores allowed ZIF-8 shell growth on their surface without observed aggregates or loops. Consequently, it could indicate the importance of having superparamagnetic MNP cores for synthesizing the core-shell MNP@MOF nanocomposites. Also, the results showed that it was possible to tune the nanocomposites final size by changing the ZIF-8 shell growth time on the surface of the MNP cores.

Afterwards, DOX and 5-FU loading into the NCs of IONCs (16 nm) cores was investigated using both the one-pot *in-situ* as well as the post-synthesis impregnation approaches. Both drugs were successfully loaded into the NCs using both techniques. However, it was noticed that lower concentrations of DOX should be used for the one-pot *in-situ* synthesis of the NCs to allow the ZIF-8 shells growth. So that, the compatibility between the loaded drugs and the MOF synthesis conditions should be considered when choosing the drugs to be loaded using the one-pot synthesis approach.

In addition, we observed that doxorubicin could lead to the formation of mesopores inside the ZIF-8 shells with the one-pot synthesis approach, indicating that the loaded drugs inside the ZIF-8 pores could change their structural porous architecture.

In further studies, the synthesized NCs would be stabilized with a surface polymer coating to allow their stabilization in aqueous media for their investigation in biological experiments on cancer cells and/or tumor spheroids.

Finally, having the NCs loaded with two different molecularly-sized drugs (DOX and 5-FU), each one with two different methods (one-pot *in-situ* for pore loading or post-synthesis impregnation for surface loading), could allow a comparative study of their release efficiencies and kinetics in response to MF stimuli. Furthermore, it could permit the investigation of the effects of different drug release behaviors on the anticancer efficacy of the prepared MF-responsive NCs, which could be performed on cancer/cancer microenvironment cells or their 3D spheroids, for optimal design of these drug delivery platforms.

## V. References

1. Carrey, J. and N. Hallali, *Torque undergone by assemblies of single-domain magnetic nanoparticles submitted to a rotating magnetic field*. Physical Review B, 2016. **94**(18): p. 184420.
2. Carrey, J., B. Mehdaoui, and M. Respaud, *Simple models for dynamic hysteresis loop calculations of magnetic single-domain nanoparticles: Application to magnetic hyperthermia optimization*. Journal of Applied Physics, 2011. **109**(8).
3. Zheng, H., et al., *One-pot Synthesis of Metal–Organic Frameworks with Encapsulated Target Molecules and Their Applications for Controlled Drug Delivery*. Journal of the American Chemical Society, 2016. **138**(3): p. 962-968.
4. Vasconcelos, I.B., et al., *Cytotoxicity and slow release of the anti-cancer drug doxorubicin from ZIF-8*. RSC Advances, 2012. **2**(25): p. 9437-9442.
5. Li, Y., et al., *Coordination-responsive drug release inside gold nanorod@metal-organic framework core–shell nanostructures for near-infrared-induced synergistic chemo-photothermal therapy*. Nano Research, 2018. **11**(6): p. 3294-3305.
6. Huang, J., et al., *Metal organic framework-coated gold nanorod as an on-demand drug delivery platform for chemo-photothermal cancer therapy*. Journal of Nanobiotechnology, 2021. **19**(1): p. 219.
7. Silva, J.Y.R., et al., *A thermo-responsive adsorbent-heater-thermometer nanomaterial for controlled drug release: (ZIF-8,EuxTby)@AuNP core-shell*. Materials Science and Engineering: C, 2019. **102**: p. 578-588.
8. Gavilán, H., et al., *Scale-up approach for the preparation of magnetic ferrite nanocubes and other shapes with benchmark performance for magnetic hyperthermia applications*. Nature Protocols, 2023. **18**(3): p. 783-809.
9. Xiong, R., et al., *Preparation and characterization of intravenously injectable nimodipine nanosuspension*. International Journal of Pharmaceutics, 2008. **350**(1): p. 338-343.

10. Ovejero, J.G., et al., *Effects of inter- and intra-aggregate magnetic dipolar interactions on the magnetic heating efficiency of iron oxide nanoparticles*. *Physical Chemistry Chemical Physics*, 2016. **18**(16): p. 10954-10963.
11. Li, Y., et al., *Creating an Aligned Interface between Nanoparticles and MOFs by Concurrent Replacement of Capping Agents*. *Journal of the American Chemical Society*, 2021. **143**(13): p. 5182-5190.
12. Bhattacharjee, S., *DLS and zeta potential – What they are and what they are not?* *Journal of Controlled Release*, 2016. **235**: p. 337-351.

Third part of results: Development of magnetic nanoparticles focusing setup with tunable targeting area

**This part presents a study for developing a setup that could enable the focusing of magnetic nanoparticles toward the targeted tissues with the ability to tune the position of the targeting area. First, a short directly related state-of-the-art is presented. Afterwards, the setup principle is introduced with a brief overview of flow of the work. The setup parameters optimization using simulation softwares is explained. Finally, the experiments that were done for constructing the setup with the optimized characteristics are described. The final steps of building the setup are still in progress, so the experiments done will be discussed up to the actual point of the progress.**

## **Contents**

- I. State of the art
- II. Description of the setup principle, its general parameters and brief description of the flow of work
- III. Simulations, experiments, results and discussion
  - III.1. Optimization of the permanent magnets blocks parameters
  - III.2. Optimization of coils parameters
  - III.3. Experimental development of the coils
  - III.4. Experimental development of the setup
- IV. Conclusions and perspectives
- V. References

## I. State of the art

Nanomedicine formulations have emerged as promising therapeutic and imaging agents, particularly for cancer treatment and diagnosis [1, 2]. They could offer enhanced physicochemical and pharmacokinetics properties of the loaded drug as well as its controlled release [1, 3]. As detailed in the state of the art of the thesis, the magnetic fields (MF) as external triggers could be an interesting tool to enhance the tumor accumulation of the magnetic nanoparticles (MNPs)-based nanomedicines.

Magnets applied to the body surface were utilized to attract the MNPs to surface lesions [4]. However, this strategy didn't show promising results in clinical trials; that could be due to the rapid decay of MF strength and its gradient in proportion to the distance away from the magnet's surface. Moreover, this principle could be applied, in a noninvasive way, only to surface tumors and not to deep-seated ones [4].

In order to overcome these challenges, assemblies of permanent magnets were utilized to allow 3D MNP targeting that can be applied to deep-seated tumor targets [5]. For instance, Liu *et al.* developed a device composed of two oppositely polarized external permanent magnets. This magnets configuration allowed the generation of a sharp zero MF point at the center of the gap between them. The zero MF point was surrounded by a strong and constant MF gradient along the gap from the center to the magnets surface (Figure 1) [6].

The efficacy of this magnets configuration was compared to two control conditions (single magnet or no magnets) after retro-orbital injection of the magnetic assemblies in female Balb/c mice bearing orthotopic 4T1 mammary gland tumors. The animals were positioned so that the center between the two magnets corresponded to the tumor center, or the single magnet was at 10 mm away from the tumor. There was a noticed >3x increase in the tumor accumulation and >2x magnetic resonance imaging (MRI) signal of the targeted magnetic assemblies (~85 nm core size) when using the two opposite magnet configuration compared to control conditions. In addition, the accumulated magnetic assemblies traveled >5x more distance deep inside the tumors compared to the control conditions, indicating better tumor penetration [5].

The maximum MF strength measured in the gap was around 300 mT at the edges of the gap near the magnets surface, and the generated MF gradient was 30 mT/mm on the axial plane and 15 mT/mm on the radial plane (Figure 1c). However, the principle of driving out the MNPs out of the tumor center could have some limitations. Primarily, the MNPs could continue diffusing out until going outside the tumor tissues themselves to the nearby healthy ones. Also, it is needed to attract the MNPs to the blood vessels of the tumor tissues in the first place, before affecting their distribution within the tumors.

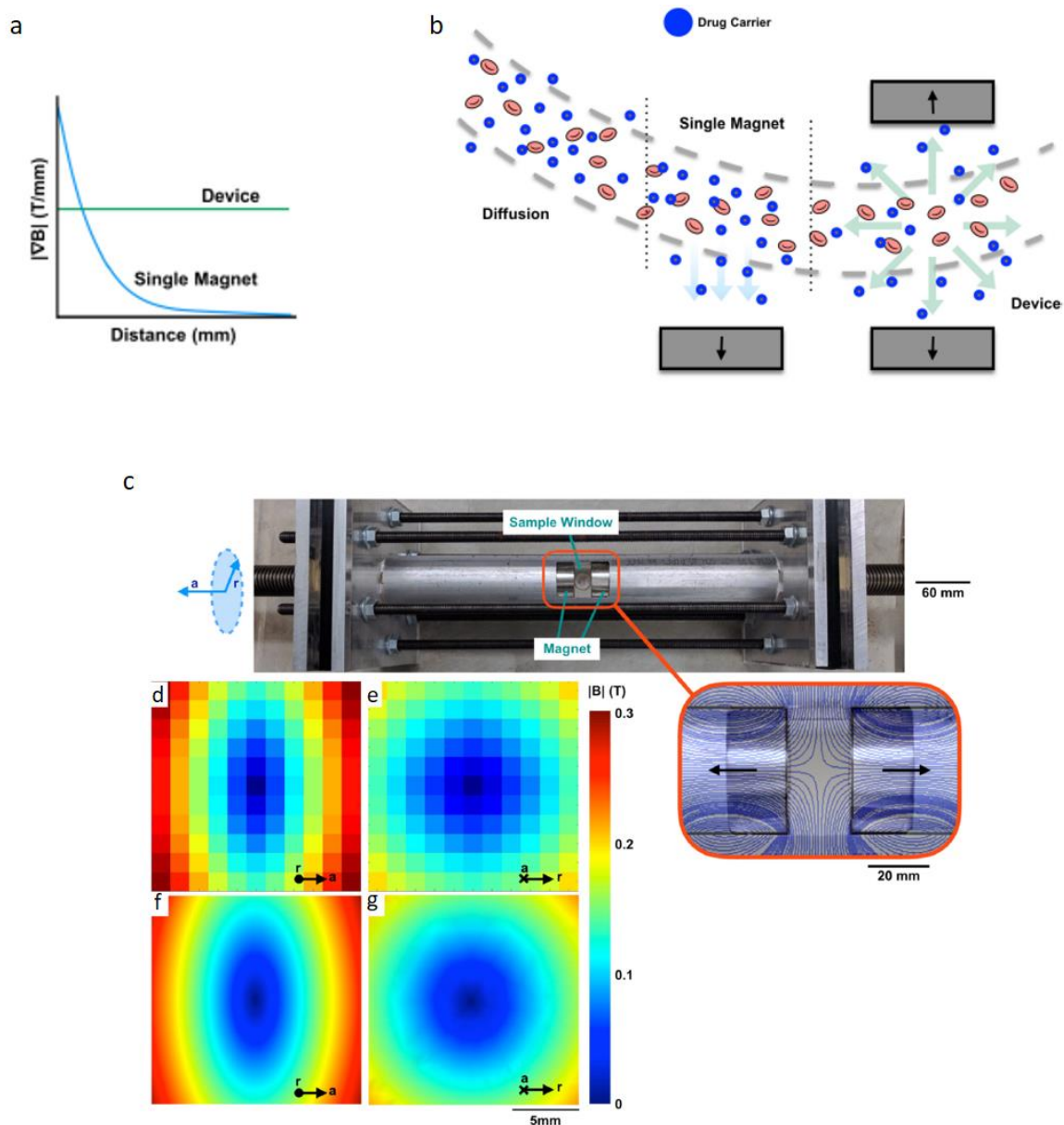


Figure 1: a) Illustration of the MF gradient produced using the device composed of two oppositely polarized permanent magnets where the gradient is constant deep into the tissues, compared to the gradients produced by single magnet where gradients drop rapidly going away from the magnet surface. b) Illustration of the MF-induced diffusion of magnetic carriers towards the magnet surface using a surface magnet vs. the two opposite magnets, the latter could allow outward radial force deep in the tissues. c) The magnetic targeting device composed of the two oppositely-polarized permanent magnets that were aligned within an aluminum tube. The distance between the magnets was controlled by a large steel threaded rods and the system was mechanically stabilized by aluminum plates and steel rods. An avoidance region (outset) is generated in the middle from which particles could diffuse out. The MF measurements showed zero point at the center between the magnets in both the radial (d) and axial (e) directions and they were consistent with COMSOL® simulations (f,g). Adapted from [6]

In another study, Krzyminiewski *et al.* developed a setup composed of two external permanent magnets that enclosed two oppositely polarized smaller permanent magnets [7]. The principle of this setup was to create a stronger and more homogenous MF distribution by the external magnets that could be inverted by the smaller internal ones, which generate oppositely oriented weaker MF but with higher gradients. Thus, it achieved a net MF distribution with the highest intensity in the center of the gap, upon rotating the magnets (figure 2).

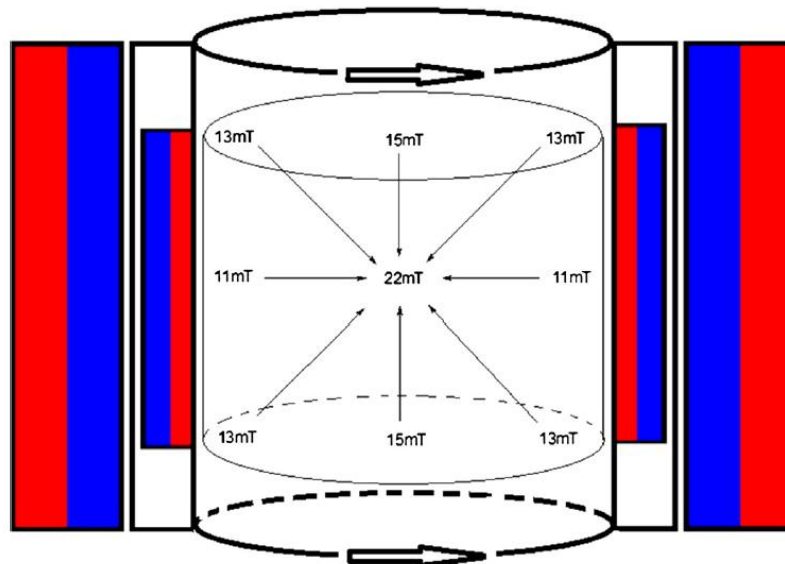


Figure 2: Illustration of the MNPs focusing setup developed by Krzyminiewski *et al.* that was composed of two external permanent magnets which enclosed two oppositely polarized smaller internal permanent magnets. The MF distribution in a beaker in the gap during the rotation of the magnets is represented. Adapted from [7]

Using this approach, magnetic silica nanoparticles ( $\text{Fe}_3\text{O}_4@\text{SiO}_2$ ), having particle size of 20-50 nm, were successfully focused to the center of a tissue like-structure (polyurethane sponge) positioned in the gap. The nanoparticles had 2.5x and 4.4x higher concentrations in the center of the polyurethane sponge *versus* at its edge after 30 and 60 min, respectively. The average generated MF gradient in the gap was 0.59 mT/mm : with such value, MNP focusing was observed after 30 min. However, the MF strength in the gap of the setup was rather low ( $\sim 22$  mT in the rotation center and  $\sim 12$  mT at the edge of the gap). For instance, it was reported that a MF intensity of 65 mT is needed to saturate 40-50% of the ferumoxytol<sup>®</sup> superparamagnetic iron oxide nanoparticles [8]. Another major limitation of this setup is that the focusing position is fixed in the center of the gap and cannot be changed. As the setup relies on permanent magnets, the generated MF could neither be regulated nor switched off. It could be advantageous to have the option of changing the focusing position, as it could be difficult to position the tumor in the center of the gap.

An alternative option to permanent magnets is using electromagnets to generate variable MF [9]. Compared to permanent magnets, the advantage of the electromagnets is the possibility of varying the generated MF strength and gradient in a simple way by manipulating the passing current [9]. These electromagnets can be based on superconducting coils as the ones used for MRI equipment, or based on traditional coils. The latter can be divided into ordinary, Helmholtz, Maxwell coils or a combination of them.

First, MRI systems based on superconducting coils were used to guide magnetic particles inside the body. The advantage of using the MRI system is its simultaneous imaging, which could enable the positioning of the magnetic particles with regard to the blood vessels and body tissues. Moreover, using the MRI system control algorithms, the motion of magnetic particles could be manipulated and adjusted in a stepwise manner by changing the MF distribution. However, the MF gradients in the MRI system are usually limited to avoid a too strong heating of its gradient coil component due to Joule effect. Such low gradients were applied to drive the movement of ferromagnetic materials of micron or millimeter sizes or magnetically labeled cells [10-13], however, they were too weak to allow targeting of MNPs, the most commonly used one for magnetic drug delivery applications [14]. On the other hand, non-superconducting coils could have the ability to generate relatively high MF gradients. However, they generally heat and are highly energy-consuming, which poses a challenge for generating sufficiently high MF strengths. Consequently, their generated MF strength could not be sufficient to saturate the MNPs to subsequently follow the MF gradients and accumulate in the targeted tissues [9, 15].

In summary, setups based on permanent magnets have the advantage of generating strong MF with a relatively low cost, but their generated MF and its gradient are fixed. In addition, there are difficulties towards the magnets assembly due to their magneto-mechanical attraction forces. On the other hand, setups based on ordinary coils are able to generate controllable MFs with high gradients. However, they consume a large energy that becomes evident upon the need to generate a strong MF [14].

## **II. Description of the setup principle, its general parameters and brief description of the flow of work**

In the present study, we present a new setup design for MNP targeting that can combine benefits from systems that can generate strong homogenous and fixed MF (as permanent magnets) as well as components that could generate controllable high gradient MF (as ordinary coils). Harnessing the strength points from both could be a good compromise to get both strong MF to saturate the MNPs and simultaneously have a high MF gradient for getting enough directional forces.

The setup design relies on generating a strong and homogenous (low gradient) MF in one direction in a gap between two permanent magnets blocks. Afterwards, ordinary coils are added in that gap to generate an oppositely-oriented, less strong (yet sufficiently intense) and with higher gradient MF to inverse the MF distribution generated by the permanent magnets. Consequently, the overall MF distribution generated in the gap between the coils would have the highest intensity in the center (see Figure 3). This highest MF intensity position could allow 3D MNPs focusing towards it, which can be exploited to enable the accumulation of the MNPs away from the MF sources in areas corresponding to deep seated tumors. This setup configuration could permit having strong MF to saturate the MNPs as the generated MF strength would be mainly originating from the permanent magnets. In addition, this proposed setup design could allow the manipulation of the highest MF intensity area (MNPs focusing area) though varying the current in the coils.

This study aimed to optimize the setup parameters through simulations, and building it to be assessed in proof-of-concept experiments.

COMSOL Multiphysics® simulations were used to optimize the permanent magnets blocks as well as the ordinary coils parameters through assessing their generated MF distribution. The optimized parameters should allow higher MF intensity in an adjustable position in the gap to provide MNPs focusing towards it.

Magnetic field study module of COMSOL Multiphysics® version 6.0 was the one used to assess the generated MF distribution generated by the various setup components.

It is worth noting that optimizing the setup parameters took into consideration the final sample that could be used to do the proof-of-concept experiments. The field of application of the setup to do focusing in certain samples would depend on the gap width where the sample would be placed. In this study, a minimal gap width of 5 cm was aimed where samples such as cell culture dishes or small animals can fit.

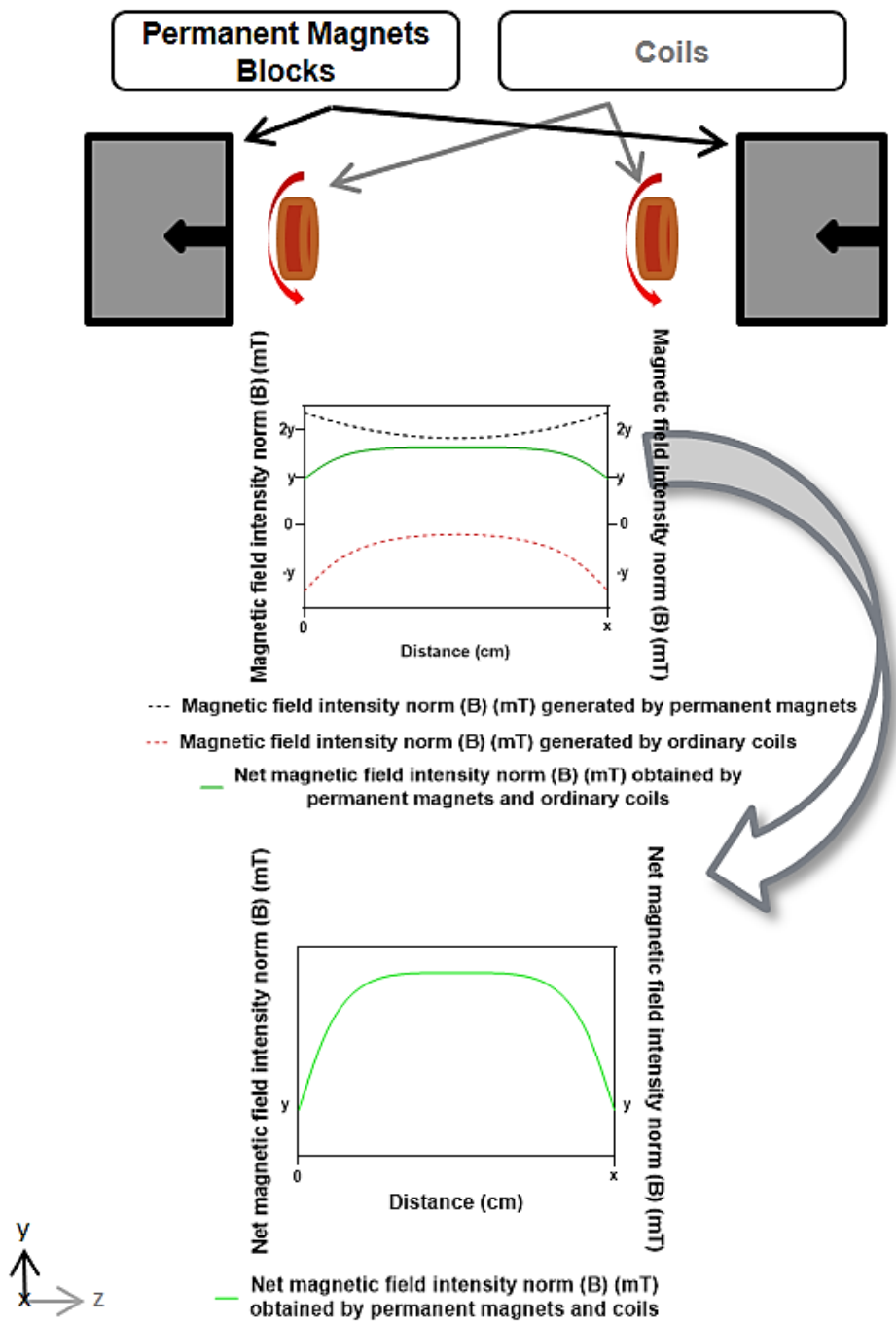


Figure 3: Illustration of the principle of the magnetic nanoparticles focusing setup. It relies on generating strong and low gradient MF using permanent magnets blocks (dotted black line). Afterwards, upon adding ordinary coils in the gap that generate less strong and higher gradient MF in an opposite direction to the one generated by the permanent magnets blocks (dotted red line), the net MF gradient generated would have the highest intensity in the center (green line).

#### The two permanent magnets blocks:

Neodymium ( $\text{Nd}_2\text{Fe}_{14}\text{B}$ ) magnets were chosen to build the two permanent magnets blocks, in order to get the most strong and homogenous MF possible. Neodymium is the strongest known

magnetic material; it was reported that only ~1 mm thick neodymium magnetic block can generate MF equivalent to a loop of 1000 A [16]. Their magnetic flux density value is 1.4 T [17].

In COMSOL® simulations, the following magnets parameters were varied to generate strong and low gradient MF: a) the used magnets shapes and dimensions to construct the blocks, b) the number of magnets in each block and c) the distance between the two blocks of magnets.

#### **Ordinary-coils:**

First, the wire material was determined to be copper. The standard Equation (1) that describes the parameters affecting the MF generated by coils was used to identify the coil parameters needed to be optimized:

$$B = \frac{\mu_0 N I}{(L^2 + D^2)^{0.5}} \quad \text{Equation (1)}$$

where

$B$  is the magnetic flux density norm (T)

$\mu_0$  is the magnetic permeability of free space

$N$  is the total number of wire turns

$I$  is the current passing through the coil (A)

$L$  is the coil length (m)

$D$  is the coil diameter (m)

The coil dimensions (length and inner and outer diameters) were firstly determined to fit in the gap between the two permanent magnets blocks and to allow their generated MF to inverse the MF distribution of the permanent magnets.

Afterwards, a previously-developed software in the lab (coded in National Instrument® CVI ; we will call it below the "CVI-software") was initially used to understand the effects of the number of turns and of the current on the MF generated by the coils, their power consumption and wire resistance. Thereafter, within a current range of the power supplies that could be available in the lab and based on the optimized coils dimensions, the wire diameter was optimized through the CVI software simulation. Finally, the effect of changing the current levels in the coils was studied in COMSOL®, with the aim to first inverse the MF distribution created by the permanent magnets blocks to get the highest MF intensity in the center of the gap, then to check the possibility of varying the highest MF intensity position within the gap.

Finally, experimental work was realized to build the optimized coils. Also, work was done towards mounting the setup.

### III. Simulations, experiments, results and discussion

#### III.1. Optimization of the permanent magnets blocks parameters

The function of the two permanent magnets blocks is to generate strong and low gradient MF in the gap between them to be inverted later using the two ordinary coils. Using COMSOL® simulations, the magnets shape and dimensions in the two blocks were firstly optimized, followed by optimizing needed number of magnets in each block and finally the distance between the two blocks.

##### A) Optimizing the permanent magnets shapes and dimensions

Two permanent magnets shapes (cube and disc), each with two different dimensions, were selected to be investigated using COMSOL® simulations (Figure 4). The exact magnets dimensions were determined by their availability at the magnet suppliers.

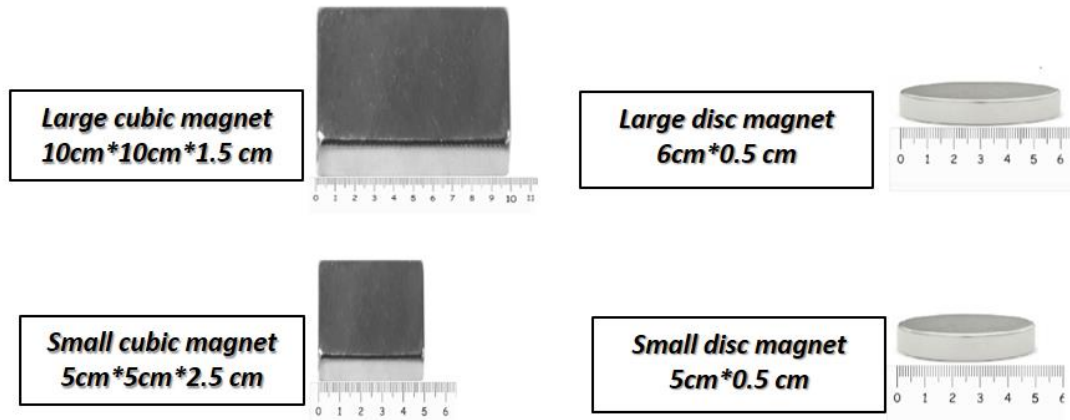


Figure 4: Shapes and dimensions of the magnets selected to be investigated as building units of the two blocks of permanent magnets.

First, the generated MF intensity from each of the selected single magnets was simulated in COMSOL® along the z-axis up to 20 cm away from the center of the magnet surface (Figure 5a). The selected cubic magnets generated stronger MF at their surface compared to the disc ones. It was also found that the small cubic magnet generated stronger MF intensity at the center of its surface, but the intensity decreased faster with distance than for the larger cubic one, and the same for the small and

large disc magnets. These behaviors are related to the difference of aspect ratio in the case of the discs: high aspect ratio magnets are expected to present a smaller MF at their surface. In the case of the cubes, it is related to both the higher aspect ratio as well as the thickness of the magnets, since thinner magnets generate smaller MF at their surface.

Moreover, it was found that it is unlikely that a single magnet of any shape among the selected ones could generate a significant MF more than 8 cm away from its surface (Figure 5b). Since our aim here is to optimize the design of two permanent magnet blocks with regard to the strength of their generated MF and gradient in the gap between them, an initial gap width of 8 cm was initially used. At this gap width, the MF generated by the first magnet in one block would extend along the gap until the first magnet in the opposite block so that there is enough room to study the interaction between the MF generated by the two magnets block. After establishing the magnets blocks parameters (shape and dimensions of the used magnets and the number of magnets in each block), an optimized gap width will be determined based on these selected blocks parameters.

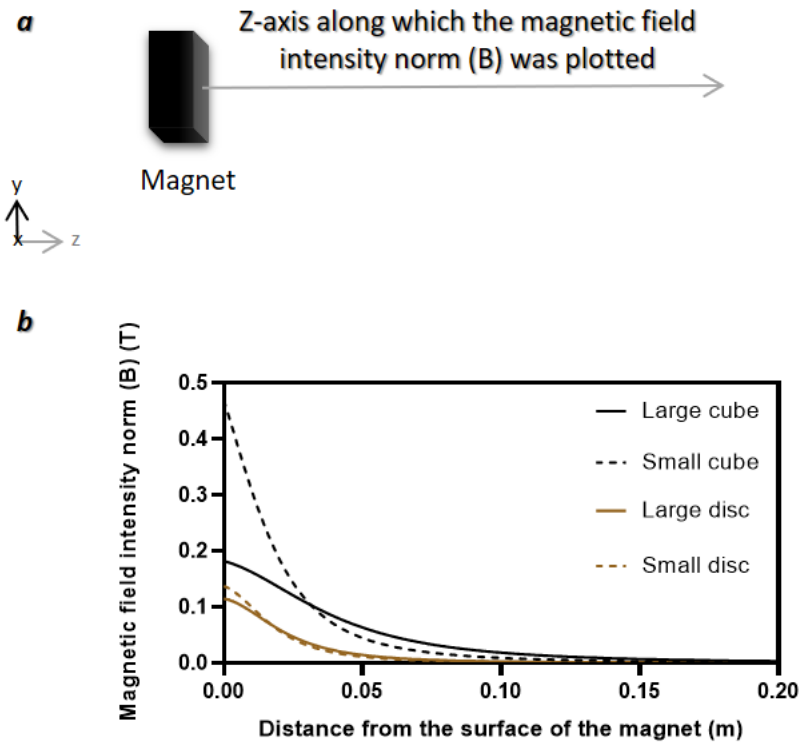


Figure 5: A) Illustration of the z-axis along which the MF intensity norm was simulated for the cubic magnets and the same was done for the disc ones. B) COMSOL® simulation results of the MF intensity norm along the z-axis up to 20 cm away from the center of the magnet surface for each of the selected magnets.

Afterwards, to decide on the most suitable magnet shape and dimensions among the chosen ones, a COMSOL® simulation was done to study the MF distribution along the z-axis in the center of the gap between two equivalent blocks of magnets that were separated by 8 cm gap. Magnets block thickness of 15 cm was chosen for this simulation as 15 cm is a common multiple of the thicknesses of the used magnets (2.5, 1.5 and 0.5 cm). Therefore, similarly thick blocks of magnets can be constructed and compared. The 15 cm magnets block length was equivalent to 6 small cubic magnets, 10 large cubic magnets, 25 large disc magnets or 30 small disc magnets.

It was found that large cubic magnets resulted in the strongest and most homogenous (least gradient) MF generated in the gap between the two blocks of the magnets (Figure 6). The order of the minimum MF strength generated at the center of the gap along the z-axis was as follows: large cubic magnets (0.522 T) > large disc magnets (0.261 T) > small cubic magnets (0.236 T) > small discs (0.199 T). In addition, the order of the MF gradient (edge to center) in the gap was as follows: large cubic magnets (5.9 mT/mm) < large discs (11.55 mT/mm) < small cubic magnets (12.09 mT/mm) < small discs (12.93 mT/mm). Hence, the cubic large magnets were chosen as the optimum ones to construct the two permanent magnets blocks as they resulted in the strongest MF in the gap (at least 2-fold) with the least gradient (~half) compared to other magnets.

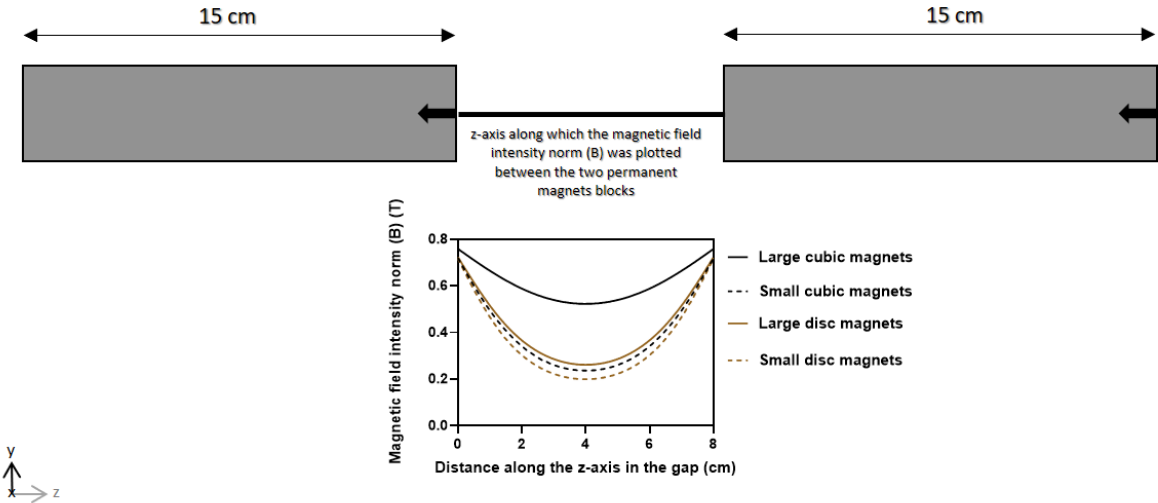


Figure 6: COMSOL® simulation results for optimizing the permanent magnets shapes and dimensions. It simulated MF distribution along the z-axis (8 cm) in the center of the gap between two equivalent lengths (15 cm) of blocks composed of permanent magnets with different shapes and dimensions. The length of 15 cm of each magnetic block was equivalent to 6 small cubic magnets, 10 large cubic magnets, 25 large disc magnets or 30 small disc magnets.

## B) Optimizing the number of large cubic magnets in each block

To optimize the number of large cubic magnets needed, COMSOL® simulations were done to investigate the effect of increasing the number of magnets in each block on the generated MF strength (maximum at the edge and minimum in the center of the gap) as well as its gradient along the z-axis in the center of the gap (8 cm).

It was noted that adding more magnets in each block up to 10 magnets results in an increased strength of the generated MF (maximum at the edge and minimum in the center) in the gap between the two blocks (Figure 7). Also it was observed that, adding more than 10 magnets in each block did not result in a significant increase in the achieved MF strength in the gap along the z-axis.

On the other hand, increasing the number of magnets in each block up to 10 magnets resulted in generating a less homogenous (higher gradient) MF. This is due to the higher increase in the maximum MF strength at the edges of the gap near the permanent magnets blocks surface upon adding extra magnets compared to the increase of the minimum MF strength in the center of the gap. In addition, increasing the number of magnets in each block more than 10 seems did not significantly affect the MF gradient in the gap. This is due to the increased distance between the added magnets and the gap (when it is more than 10 magnets). Consequently, generated MF of the added magnet did not significantly affect the MF distribution in the gap.

The aim of the two permanent magnets blocks is to generate strong and as homogenous (low gradient) MF in the gap between them. Herein, adding more than 10 magnets in each block seems not to affect the generated MF strength or its gradient, so a maximum number of 10 magnets would be the optimum. Increasing the number of magnets from one to ten resulted in an increased MF strength but with a higher gradient, so a compromise had to be made. The number of 10 magnets was considered as the best option. It resulted in a strong MF in the gap (a minimum of at least 0.522 T), and the resulted gradient was considered still low, especially within the larger context that the MF gradient generated by the 10 large cubic magnets (5.9 mT/mm) was still far less compared to previous gradients of the small cubic magnets (12.09 mT/mm), small disc magnets (12.93 mT/mm) and large disc magnets (11.55 mT/mm).

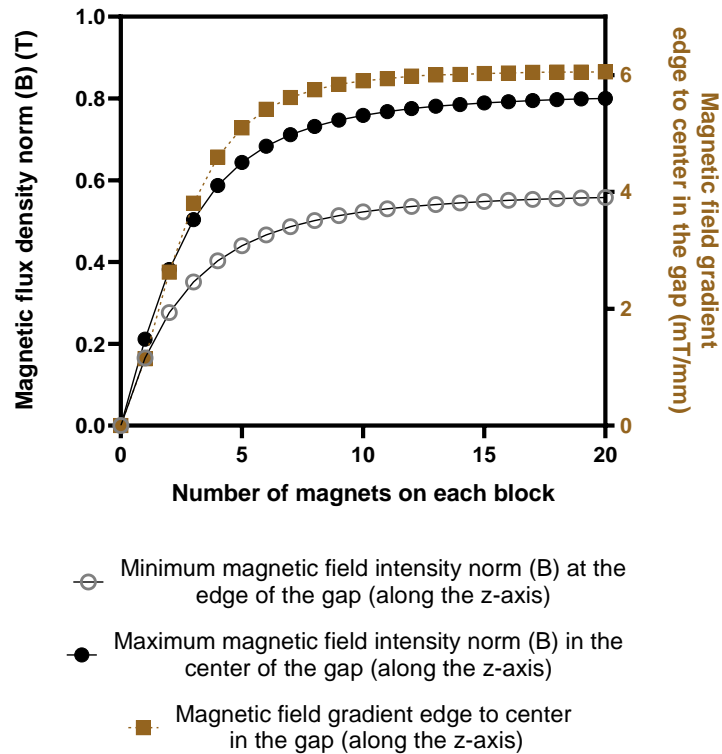


Figure 7: COMSOL® simulation results for optimizing the number of large cubic magnets in each block. It investigated the effect of increasing the number of large cubic magnets in each of the permanent magnets blocks on the maximum and minimum MF intensity and on the resulting MF gradient along the z-axis in the center on the gap (8 cm).

### C) Optimizing the gap width between the two blocks of magnets

The last magnets blocks parameter to be optimized is the gap width. COMSOL® simulations was done to investigate the generated MF strength and gradient along the z-axis in the center of the gap upon increasing gap width (5 to 45 cm) between two permanent magnets blocks, each of 10 large cubic magnets (Figure 8).

It was found that increasing the gap width resulted in a decrease in MF intensity (minimum in the center and maximum at the edge) in the gap between the two magnets blocks. The reduction in the minimum MF intensity value in the gap center was steadier than the decrease of the maximum MF at the edge. The minimum MF intensity in the center of the gap depends on the MF generated by the two magnets blocks so it is highly affected by increasing the gap width. However, the maximum MF at the edge of the gap (at the magnets blocks surface) is mainly dependent on the MF generated by the magnets in the same block not the opposite one. So when the opposite blocks move away from each other (i.e. for larger gap distances), the maximum MF intensity only slightly decreases.

Regarding the MF gradient, increasing the gap width from 5 cm to 11 cm results in an increase in the MF gradient along the z-axis in the center of the gap. It is mainly due to the larger increase in the difference between the maximum and minimum MF gradient generated in the gap compared to the small constant 2 cm gap width increase. However, a totally opposite pattern of the MF gradient change happened upon increasing the gap width more than 11 cm.

To decide on the gap width, there were three factors to be taken into consideration. The first most important one is to have enough room for adding the coils and for the sample itself. The targeted minimum space for the sample was 5 cm, and with adding a space for the two coils of  $\sim 4$  cm (at least 2 cm for each coil and their support to be hold in place), it seems that the minimum possible gap width would be 9 cm. Herein comes the next two factors, the MF strength and the MF gradient. Minimum MF strength and MF gradient found with the 9, 11 and 13 cm gap widths were 0.463 T and 6.15 mT/mm, 0.365 T and 6.32 mT/mm and 0.29 T and 6.24 mT/mm, respectively. The three MF gradient values are very close and do not look to be significantly different; however, there is a significant difference in the minimum MF intensities. The MF intensity of 0.463 T could be the most appealing in terms of saturation of the MNPs. However, it is most challenging for the coil. Practically, it could be very challenging for a lab-made ordinary coil within the setup dimensions to generate enough strong MF to affect a MF intensity near 0.5 T. So that, we choose a less challenging gap width at 11 cm between the two permanent magnets blocks with a minimum MF intensity of 0.365 T.

It isn't possible to finally decide on the optimum gap width without knowing the MF strength that could be generated by the coil. Therefore, the gap width in the actual setup will be designed to be modifiable according to the need using screws as would be clarified later. So the choice of the 11 cm gap width should not be considered as an irreversible one and could be modified and reconsidered after the coils design.

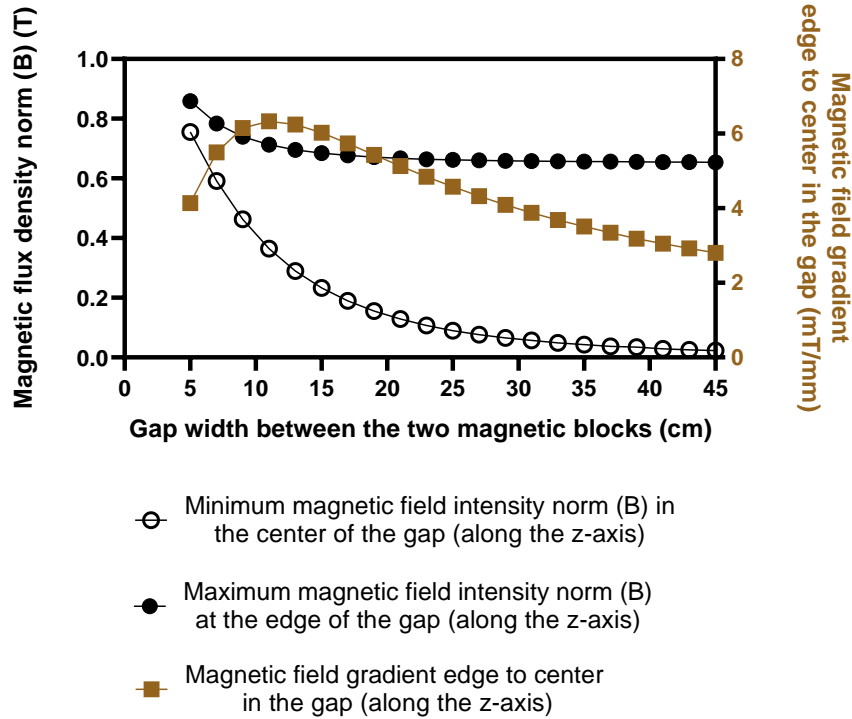


Figure 8: COMSOL® simulation results for optimizing the gap width between the two magnetic blocks through investigating the effect of increasing the gap width between the two permanent magnets block on the MF strength and gradient along the z-axis in the center on the gap.

### III.2. Optimization of the coils parameters

The aim of the two coils is to generate oppositely directed weaker, yet sufficiently strong, and higher gradient MF compared to the MF generated by permanent magnets. So that, the MF generated by the coils can change the MF distribution generated by the two magnetic blocks to have the highest MF intensity in a middle position in the gap away from the MF sources. The coils dimensions were firstly optimized followed by their number of turns and the current.

#### A) Establishing the coil dimensions

Within the initially determined 11 cm gap width between the two magnetic blocks, the coil dimensions were established to fit in. The coils were chosen by default to be cylindrical. The coils width was chosen to be 1 cm and to be initially positioned 1.5 cm away from the permanent magnet block surfaces. The 1.5 cm left between the coil and the permanent magnets blocks surface was to account for the coils support as would be described later. Consequently, there would be 6 cm remaining distance along the z-plane for placing the sample, 1 cm well above the minimal targeted final gap width (Figure 9).

The external coils diameter was fixed to be exactly half of the magnets length (i.e., 5 cm) and to be centered in the middle of the magnets blocks surface. At this diameter and position, the MF distribution generated by the coils would be concentrated in the middle of the MF created by the permanent magnets but with higher gradients. Therefore, the MF distribution created by the permanent magnets can be inverted to have the highest intensity in the center of the gap. The internal coil diameter was selected to be 1 cm to account for any possible needed coil cooling, such as by forced air-circulation as per our experiences with other setups that would be described later. Afterwards, according to Equation 1, it is required to determine the current times number of wire turns value in order to generate an optimum MF that is able to invert the MF distribution generated by the permanent magnets blocks.

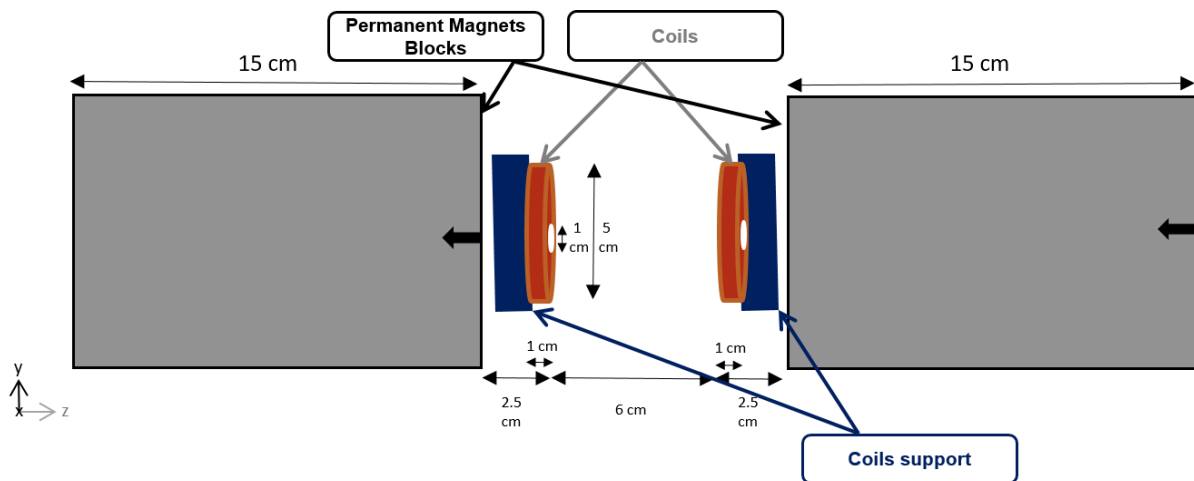


Figure 9: Illustration of the established coils dimensions within the initially determined 11 cm gap width between the two magnets blocks. The coils width was chosen to be 1 cm and to be initially positioned 1.5 cm away from the permanent magnets blocks surface to allow a space for the coils support. There is a remaining 6 cm distance along the z-plane for placing the sample. The external coils diameter was fixed to be exactly half of the magnet length (i.e., 5 cm) and the internal coil diameter was selected to be 1 cm.

## B) Optimizing the number of turns and the current

For concluding on the optimum number of turns and coils, their effect on the coil characteristic (wire resistance, coil power consumption and heating) was firstly clarified. Afterwards, the number of turns and wire diameter was determined. Thereafter, the current value was optimized to have the highest MF intensity area in the center of the gap. Finally, varying the highest MF intensity area through changing the currents in the coils was investigated.

*i. The effects of the number of turns and the current on the coil characteristic (wire resistance, coil power consumption and heating)*

The number of turns in the coil and the current would affect the generated MF and, simultaneously, the wire resistance, coil power consumption and heating. The CVI program was used to understand these effects. When specifying the coil dimensions (internal and external radii and length) and the wire diameter, the software first calculates the number of turns and the wire resistance. After feeding the software with the used current, the software is able to predict the generated MF strength of the coil along the z axis and its power consumption. Finally, the temperature of the coil is predicted by the software using the room temperature value and the heat transfer coefficient value between the coil surface and the environment. Since building and testing a coil is resource- and time-consuming, the CVI software was a valuable tool for understanding the effects of the previous factors.

Within the specified coil dimensions (external diameter of 5 cm, internal diameter of 1 cm and length of 1 cm), arbitrarily chosen wire diameters of 2, 1 and 0.5 mm were used with corresponding currents to generate the same MF intensity. The wire temperature used was the room temperature, and the convection heat transfer coefficient was equivalent to air convection cooling without any forced cooling effect ( $10 \text{ W}\cdot\text{m}^{-2}\cdot\text{K}^{-1}$ ). The chosen wire diameters, currents and convection heat transfer coefficient here are not the final used ones, but we will use them to illustrate the effects of wire diameter on the coil functioning.

Results in table 1 showed that decreasing the wire radius by half results in increasing the number of turns of the coil by a factor of 4 and a huge increase in the coil resistance by a factor of 16. However, it needs only quarter the amount of current to get the same MF intensity with almost the same coil heating and power consumption.

Consequently, it was concluded that a thicker wire with less number of turns could be better to avoid the high resistance of the coil. Under these conditions, high currents would be needed.

Table 1: CVI software results for investigating the effects of the wire diameter on wire resistance, coil heating and power consumption. Within the specified coil dimensions (external diameter of 5 cm, internal diameter of 1 cm and length of 1 cm), arbitrarily chosen wire diameters of 2, 1 and 0.5 mm were used with corresponding currents to generate the same MF intensity. The used wire temperature was the room temperature and the convection heat transfer coefficient was equivalent to air convection cooling without any forced cooling effect ( $10 \text{ W}\cdot\text{m}^{-2}\cdot\text{K}^{-1}$ ).  $r_{\text{ext}}$  is the external coil diameter (m),  $r_{\text{int}}$  is the internal coil diameter (m),  $L$  is the coil length(m),  $r_{\text{wire}}$  is the radius of the wire,  $N$  is the number of turns,  $I$  is the current (A),  $H_{\text{max}}$  is the maximum MF generated at the center of the coil (T),  $T$  is the coil temperature (K),  $R$  is the wire resistance ( $\Omega$ ), and  $P$  is the coil power consumption (W).

$r_{\text{ext}}$ (m)	$r_{\text{int}}$ (m)	$L$ (m)	$r_{\text{wire}}$ (m)	$N$	$R$ ( $\Omega$ )	$I$ (A)	$H_{\text{max}}$ (T)	$T$ (K)	$P$ (W)
0.025	0.005	0.01	<b>0.001</b>	<b>50</b>	<b>0.0299</b>	<b>32</b>	0.08	<b>1925</b>	<b>30.6</b>
0.025	0.005	0.01	<b>0.0005</b>	<b>200</b>	<b>0.44</b>	<b>8</b>	0.08	<b>1803</b>	<b>28</b>
0.025	0.005	0.01	<b>0.00025</b>	<b>800</b>	<b>6.8</b>	<b>2</b>	0.08	<b>1743</b>	<b>27.7</b>

ii. *Selecting the current range and the number of turns (wire diameter)*

As shown that for our setup, a power supply with the ability to generate high currents would be a better choice. Within the commercially available power supplies, the selected one was able to generate a current up to 30 A and a voltage up to 32 V (BK PRECISION, 1901B, SWITCHING MODE POWER SUPPLY, 1-32 VDC 30 A).

Afterwards, the CVI program was used to select the number of turns of the coil and the wire diameter. To get the strongest MF possible from the coil (that could be tuned later), the current selected for this CVI simulation was 30 A (the maximum one could be generated by the power supply). Different wire diameters within the established coil dimensions were fed into the CVI program with 30 A current, and the resulting output here was the wire resistance and the coil power. The optimum output is to get a wire resistance of  $\sim 1 \Omega$  in order to obtain the largest possible power from the power supply. A wide range of wires with different related diameters available in the lab was selected for this simulation, and it was as follows: 2, 1.6, 1, 0.75, 0.6 and 0.5 mm.

The CVI program predicted that a wire diameter of 1 mm would result in a  $0.44 \Omega$  coil and a consumed power of  $\sim 398 \text{ W}$ , while the 0.75 mm wire diameter would result in  $1.3 \Omega$  and a power of  $\sim 1184 \text{ W}$  (Table 2).

Table 2: CVI software results for selecting an optimum wire diameter using the established coil dimensions and a current of 30 A. The effect of different wire diameters on the wire resistance and the coil power consumption was compared.  $r_{ext}$  is the external coil diameter (m),  $r_{int}$  is the internal coil diameter (m),  $L$  is the coil length(m),  $r_{wire}$  is the radius of the wire,  $N$  is the number of turns,  $I$  is the current (A),  $H_{max}$  is the maximum MF generated at the center of the coil (T),  $T$  is the wire temperature (K),  $R$  is the wire resistance ( $\Omega$ ), and  $P$  is the coil power consumption(W).

$r_{ext}$ (m)	$r_{int}$ (m)	$L$ (m)	$r_{wire}$ (m)	$N$	$R$ ( $\Omega$ )	$I$ (A)	$H_{max}$ (T)	$T$ (K)	$P$ (W)
0.025	0.005	0.01	<b>0.001</b>	<b>50</b>	<b>0.0299</b>	30	0.075	<b>1728</b>	<b>26.9</b>
0.025	0.005	0.01	<b>0.008</b>	<b>78.125</b>	<b>0.066</b>	30	0.155	<b>3474</b>	<b>59.8</b>
0.025	0.005	0.01	<b>0.0005</b>	<b>200</b>	<b>0.44</b>	30	0.442	<b>21438</b>	<b>398.4</b>
0.025	0.005	0.01	<b>0.000375</b>	<b>355.5</b>	<b>1.3</b>	30	0.8	<b>63164</b>	<b>1184</b>
0.025	0.005	0.01	<b>0.0003</b>	<b>555.5</b>	<b>3.25</b>	30	0.76	<b>155680</b>	<b>2928</b>
0.025	0.005	0.01	<b>0.00025</b>	<b>800</b>	<b>6.8</b>	30	1.05	<b>325140</b>	<b>6122</b>

Herein, the wire diameter of 0.75 mm was selected as its resistance was near an optimum of  $1 \Omega$  so a maximum power can be obtained from this coil and the coil heating was planned to be handled with more efficient cooling, as it would be discussed later. For the used wire diameter of 0.75 mm within the coil dimensions, the number of turns is calculated to be  $\sim 355$ .

### iii. Studying the effect of current on the generated MF

Keeping in mind that the two coils function is to generate a weaker, yet sufficiently strong, and higher gradient MF compared to the permanent magnets. So that, the MF generated by the coils can change the MF distribution generated by the two magnetic blocks to have the highest MF intensity in a middle position in the gap away from the MF sources. To this end, the coil dimensions were established, the wire diameter of the 0.75 mm was selected, and a current up to 30 A can be used. However, before building the coils, COMSOL<sup>®</sup> was used to investigate if the selected coil parameters would allow inverting the MF distribution of the two permanent magnets blocks and to have the highest MF intensity at the center of the gap.

For this simulation, the established coils dimensions (external diameter of 5 cm, internal diameter of 1 cm and length of 1 cm) with a wire diameter of 0.75 mm were used. The coils were placed 1.5 cm away from the magnets surface. Afterwards, the current passing in the coils was increased gradually till inverting the MF distribution generated by the permanent magnets. Although the coil with the optimized dimensions can accommodate up to  $\sim 355$  turns of the 0.75 mm wire under ideal mechanical mounting conditions, it could be challenging to fit them perfectly in a real situation

due to possible turns disorders. So that, in the COMSOL® simulations, a lower number of turns of 300 was the selected for the number of turns of the 0.75 mm wire. This lower number of turns could be easily fitted in the coil dimensions mechanically.

In these simulations, the MF intensity norm along the z, y and x-axes (6 cm) at the center of the gap were used as output (Figure 10).

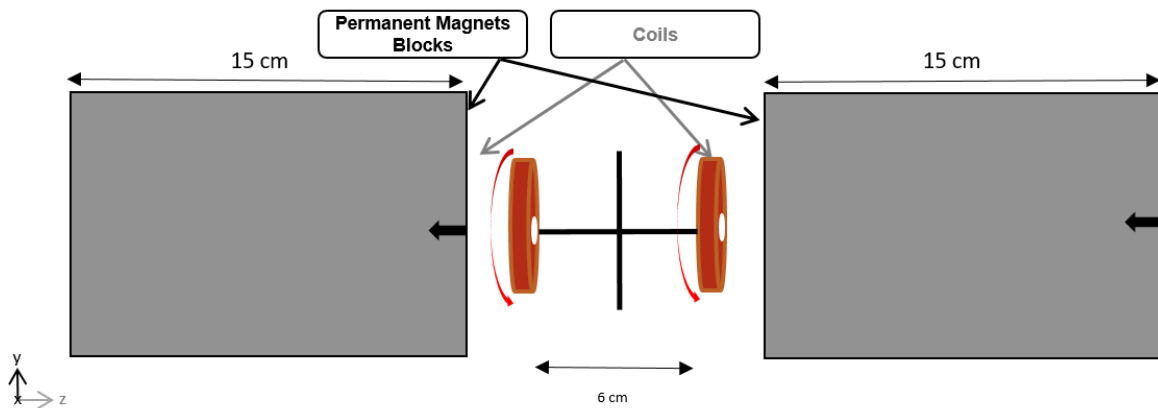


Figure 10: Illustration of the axes (x, y and z) and their lengths (6 cm) along which the MF intensity norm was simulated using COMSOL® in order to optimize the current of the coils to have the focusing area in the middle of the gap. Coils with the established dimensions (external diameter of 5 cm, internal diameter of 1 cm and length of 1 cm) with a wire diameter of 0.75 mm and 300 turns were used. The coils were placed 1.5 cm away from the magnets surface. The current in the coils was increased gradually until inverting the MF distribution generated by the permanent magnets blocks and having the focusing area initially in the middle of the gap away from the MF sources.

The evolution of the MF intensity norm (B) distribution along the z, y and x-axes in the center gap between the coils with increasing current intensities is shown in figure 11.

Increasing the current in the coils, thus its generated MF, resulted in gradual compensation of the MF generated by the permanent magnets along the z-axis till inverting it to have the highest MF intensity in the center of the gap. On the other hand, along the y and x- axes, the MF generated by the permanent magnets starts to have less gradients upon increasing the current in the coils.

The current of 25 A was optimum to get the highest MF intensity in the center of the gap in the three planes with MF gradient of 4.4 mT/mm edge to center along the z-axis and of 0.75 mT/mm edge to center along the y and x-ones. The minimum MF intensity in the gap was 194 mT at the edges along the z-axis and the maximum one was 326 mT in the center of the gap along the three axes.

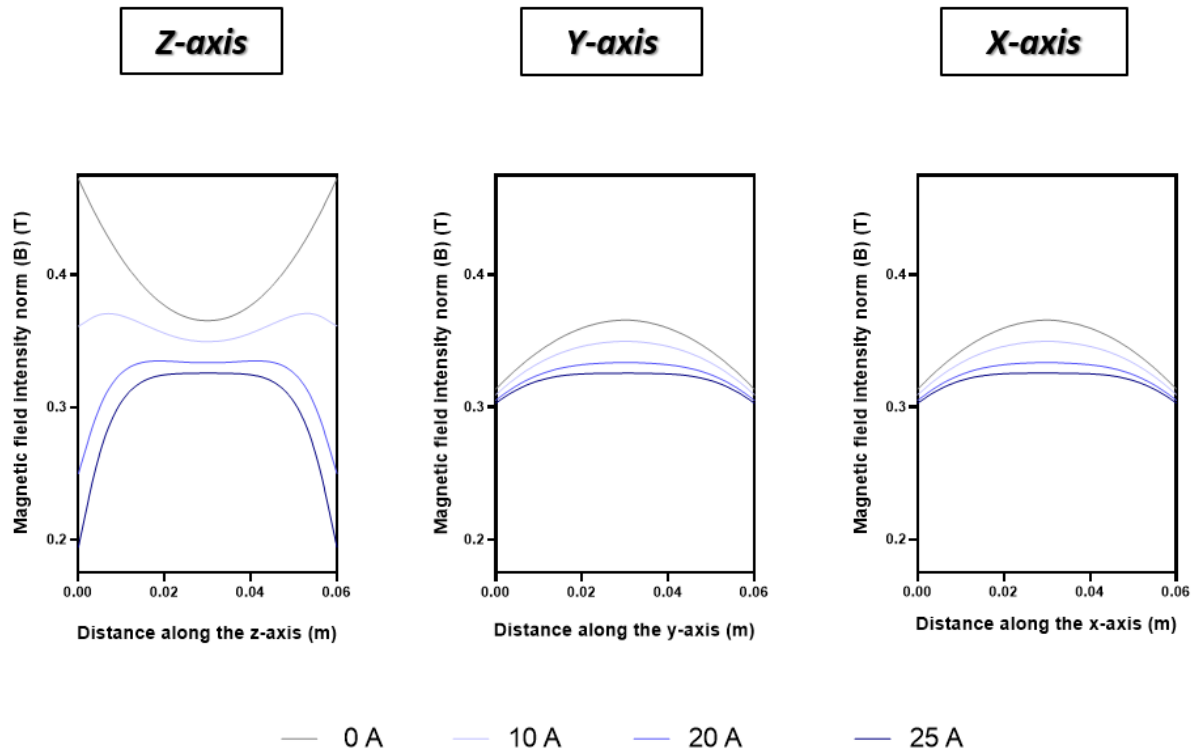


Figure 11: COMSOL® simulation results for optimizing the current in the coils (1 cm length, 5 cm external diameter and 1 cm internal diameter, 0.75 mm wire diameter and 300 turns) investigated through increasing current till inverting MF distribution generated by the permanent magnets blocks. The MF distribution of the permanent magnets only (0 A), its gradual change with increasing the current (10 A, 20 A) until being inverted (at 25 A) to have the highest MF away from the MF sources are shown.

It was also noticed that the highest MF intensity along the gap was toward a specified area in three dimensions z, y and x that could be corresponded to the targeted area. In an ideal situation for MNP focusing, having MF gradient to a specific point in the gap (corresponding to the center of the tumor) rather than towards an area could be better to help in the MNP tumor penetration after their accumulation. So that, a simulation was done with higher currents in the coils in a trial to get a MF gradient towards a specific point in the gap. Although the selected power supply in the lab can produce up to 30 A only, the higher currents used in the simulations were to understand the evolution of MF distribution in the gap and the feasibility of getting the ideal MF distribution.

Compared to using 25 A, higher currents passing in the coils resulted in a steeper gradient of the generated MF in the gap along the z-axis and the focusing started to be toward a specific point in the center of the gap. However, the highest MF intensity that was obtained in the center of the gap along the y- and x-axis, at 25 A, started to be lost with the higher currents where a well appeared in the center along these axes (Figure 12).

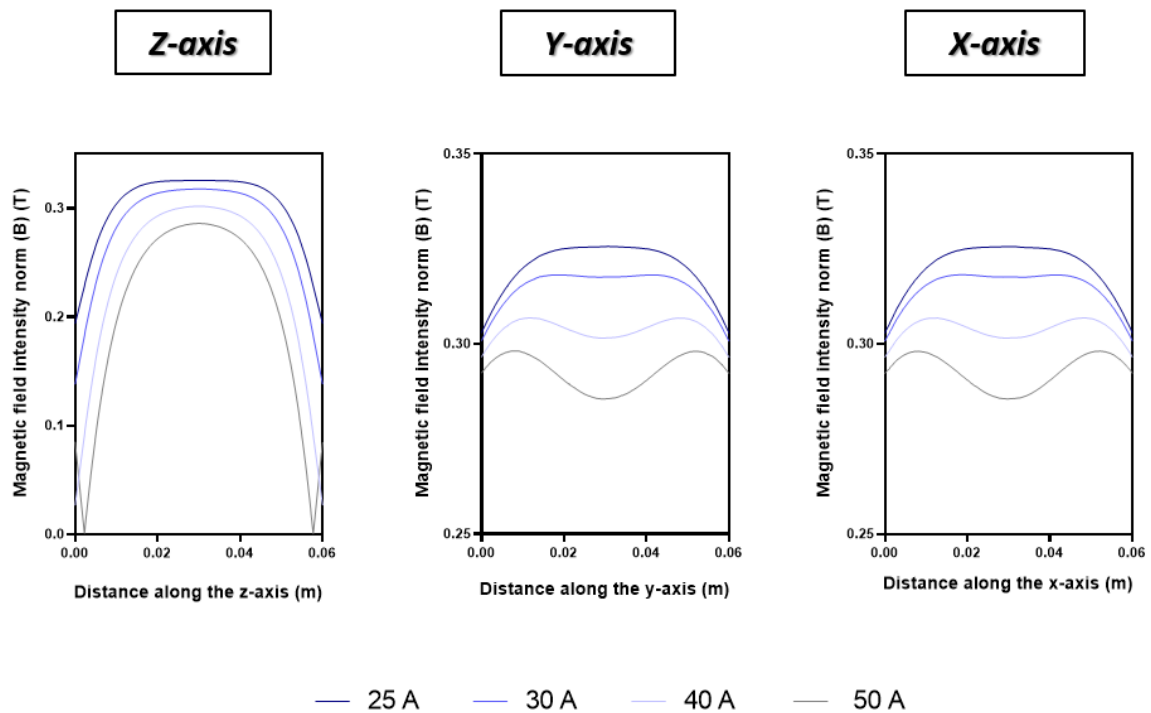


Figure 12: COMSOL® simulation results of the evolution of MF distribution in the gap by increasing the current of the coils more than 25 A in a trial to have a MF gradient towards a specific point in the gap.

Therefore, a current of 25 A was initially chosen as the optimum value for the setup to have MNP focusing toward a specific area away from the MF sources that could correspond to a deeply-seated tumor, taking into consideration the dimensions of the targeted area with respect to the whole gap width.

Hence, COMSOL® simulations showed that using the selected parameters of optimized permanent magnets blocks (10 cubic neodymium magnets (10\*10\*1.5 cm), 11 cm apart) and the oppositely magnetized coils (5 cm external diameter, 1 cm internal diameter, 1 cm width of 0.75 mm copper wire diameter (300 turns), 1.5 cm away from the magnets blocks surface), it was possible to have the highest MF intensity at the center of the gap away from the MF sources along the 3 planes upon passing an optimum current of 25 A in the coils.

iv. *Tuning the highest magnetic field intensity area position by changing the currents in the coils*

A major potential advantage of this setup design is the possibility to change the highest MF intensity position through varying the current in the coils. COMSOL® simulations were done to investigate the MF distribution in the gap when 25 A current was passed in the right side coil, and different currents were passed in the left side one (coils positions are shown in Figure 10).

It was found that upon gradually decreasing the current passing in the left side coil with the same current passing in the right side one, it was possible to shift the highest MF intensity position gradually to the right side of the gap along the z-axis (Figure 13). Interestingly, the highest MF intensity was towards one point, not an area, along the z-plane which could allow a narrower focusing of the MNPs along it. So that, the setup could enable having the MNP focusing position in an off-center position still away from the MF sources in the gap along one axis. In addition, the ability to vary the highest MF intensity position simply by tuning the current passing in the coils could be applied to magnetic guidance, upon coupling with imaging, to gradually shift the MNP accumulation from one position to another [10, 18].

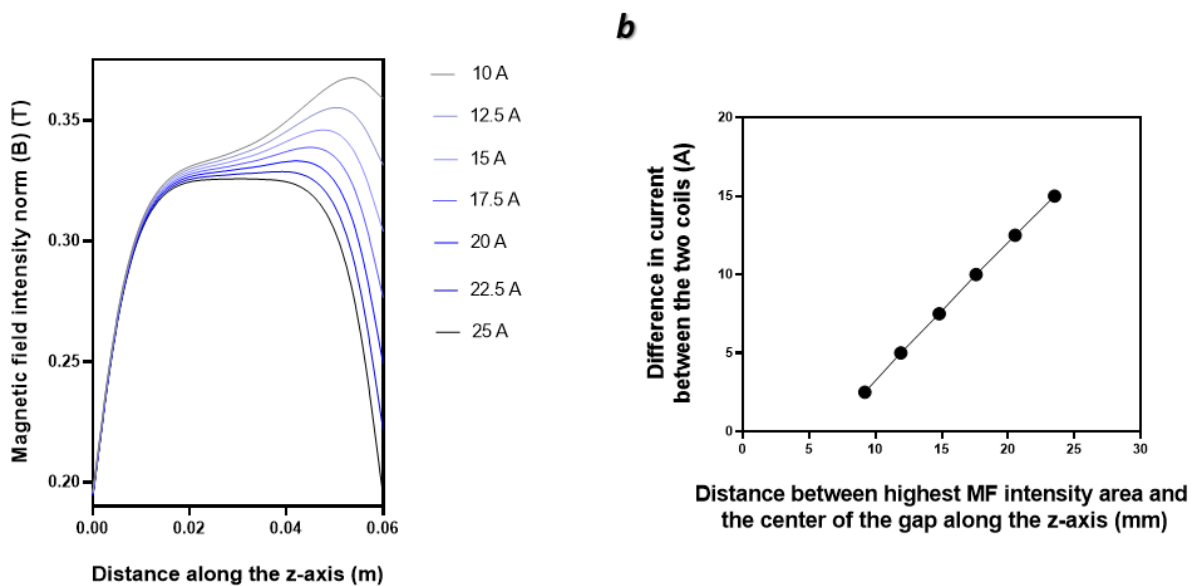


Figure 13: COMSOL® simulation results for investigating the possibility of shifting the focusing area along the z-axis upon changing the current in the coils of the optimized parameters. A) The evolution of the MF distribution along the z-axis in the center of the gap when a current of 25 A was always passed in one coil on the right of the z-axis and different currents, 25 A, 22.5 A, 20 A, 17.5 A, 15 A, 12.5 A and 10 A, were passed in the coil on the z-axis left side. B) Graph showing the shift in the accumulation position along the z-axis according to the difference in the currents between the two coils.

It was noticed that using the optimum parameters of the magnets blocks and coils to get highest MF intensity in the center of the gap, there was higher generated MF gradient in the z-axis (4.4 mT/mm) and lower gradients were present along the x and y-axes (0.75 mT/mm). Having higher MF gradients along more than one axis could be interesting. To do that, a perpendicular replicate of the two permanent magnets blocks and the two coils were added on the y-axis, and the MF intensity distribution was simulated in the gap between them when passing different currents in the coils (figure 14).

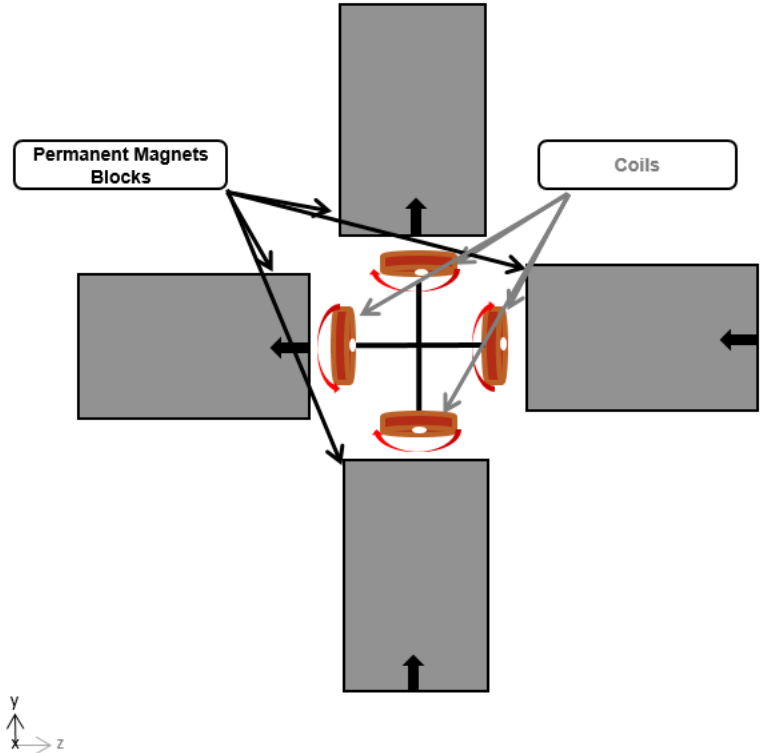


Figure 14: Illustration of the configuration of two perpendicular sets of permanent magnets blocks and coils with the optimized parameters to allow getting high MF gradient along the y-axis in addition to the z-one.

The simulation results of the MF intensity in the gap between the two perpendicular sets of permanent magnets blocks and coils when passing different currents in the coils are shown in Figure 15. A similar evolution of the MF distribution along the z- and y- axes was noticed upon increasing the current passing in the coils. Similar to the setup design with only two permanent magnets blocks and two coils, a current of 25 A was the optimum one to have the highest MF intensity in the center of the gap along the three axes. However, adding an extra perpendicular set of permanent magnets blocks and coils along the y-axis enabled getting higher MF gradients edge to center of 3.33 mT/mm along two axes (z- and y-ones), compared to a gradient of 1 mT/mm along the x-axis. The minimum MF

intensity in the gap was 359.6 mT at the edges along the z- and y-axes and the maximum one was 460 mT in the center of the gap along the three axes.

Compared to the setup configuration with only two sets of permanent magnets blocks and coils, the duplicate setup configuration resulted in  $\sim 2.5x$  higher gradient along the y-axis accompanied with  $1.25x$  higher gradient along the x-axis and  $1.25x$  less gradient along the z-axis. In addition, it enabled generating  $1.85x$  and  $1.41x$  stronger MF intensities minimum and maximum, respectively, in the gap compared to the setup configuration with only two sets of permanent magnets blocks and coils. Moreover, the duplicate perpendicular setup configuration could allow tuning the targeting area along two axes, z and y, not only one.

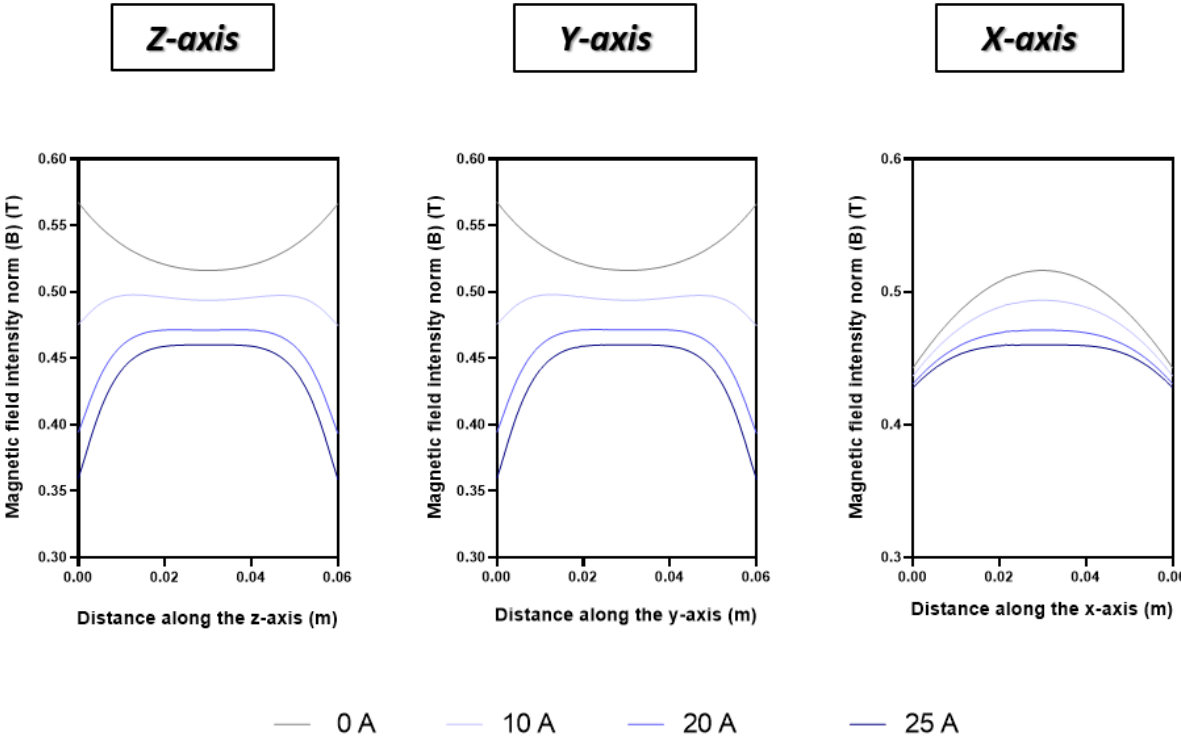


Figure 15: : COMSOL® simulation results for investigating the possibility of getting high MF gradient along the y-axis, in addition to the z-axis, upon having two perpendicular sets of the optimized permanent magnet and coils along the z and y-axes and passing different currents in the coils.

Adding a setup configuration copy along a third axis could achieve a more favorable MF distribution in the gap; however, it is not a practical option as there should be at least one free axis for inserting and removing the sample.

For the current proof-of-concept study, we aimed to construct a setup composed of two permanent magnets blocks and two ordinary coils.

### III.3. Experimental development of the coils

The setup ordinary coils and their support were built in the lab. In a CVI program simulation, it was found that a coil with optimized parameters (5 cm outer diameter, 1 cm inner diameter, 1 cm length, 0.75 mm wire diameter (300 turns) and 25 A) would have power consumption of ~803 W. Therefore, there is an expected coil heating that would be needed to be managed. From COMSOL® simulations, the optimized coils should be able to generate MF intensity as strong as 280 mT at the center of their surface for eventually being able to inverse the MF distribution pattern generated by the permanent magnets blocks to have the highest MF intensity area in the middle of the gap. The MF intensity at the center of the coil surface was the one chosen here to express of the strength of MF generated by the coil. The reason was that the center of the coil surface is easily accessible position where a gaussmeter probe can be accurately positioned to measure the MF intensity generated by the coil. So that, the ability to generate MF intensity of 280 mT at the center of the surface of coil to be developed was set as a target.

To confront the expected heating challenge in a step-by-step manner, thicker wires with fewer turns were investigated at the beginning with the same optimized coil dimensions (5 cm outer diameter, 1 cm inner diameter, 1 cm length). A thick wire of 1.6 mm diameter was first investigated, followed by a medium wire of 1 mm diameter, before trying with the optimum 0.75 mm diameter wire. In these trials, a maximum current of 30 A was always tried to be passed in the coils using the power supply. The temperatures of the wires were recorded using a thermal infrared camera (Testo 885-2, 33 Hz, Germany). In addition, the actual current level in the coil was noted on the power supply screen in order to get another indication about the coil heating. If the coil heating was not managed and its temperature was increasing, the wire resistance would increase which could be noticed in decreasing the actual current in the coil. Finally, the MF intensity at the center of the coils surface was measured using a gaussmeter (GM08, Hirst Magnetic Instruments, United Kingdom) upon stabilization of the wires' temperature and the passing current.

The used coils supports were constructed using an UltiMaker 2+ 3D printer fed with PLA (polylactic acid) polymer. The initial coil support was adapted for having forced air-cooling where the air would enter from the coil central hole (1 cm inner diameter) upon its suction from four external tubes (see Figure 16a).

Firstly, using a thick wire of 1.6 mm diameter (~60 turns), a current of 30 A generated by the power supply was passed to the coil under forced air-cooling. The coil temperature slightly increased a few degrees above the room temperature until stabilizing at ~309 K. Consequently, the current level

in the coil slightly decreased to  $\sim 27.7$  A (Figure 16b). Upon stabilization of the coil temperature and the current level, the MF intensity generated by the coil was measured using the gaussmeter at the center of the surface of the coil, and it was 45 mT. Hence, the heating of the thick wire coil was managed with forced air-cooling and it was possible to generate a MF intensity of 45 mT at the center of its surface.

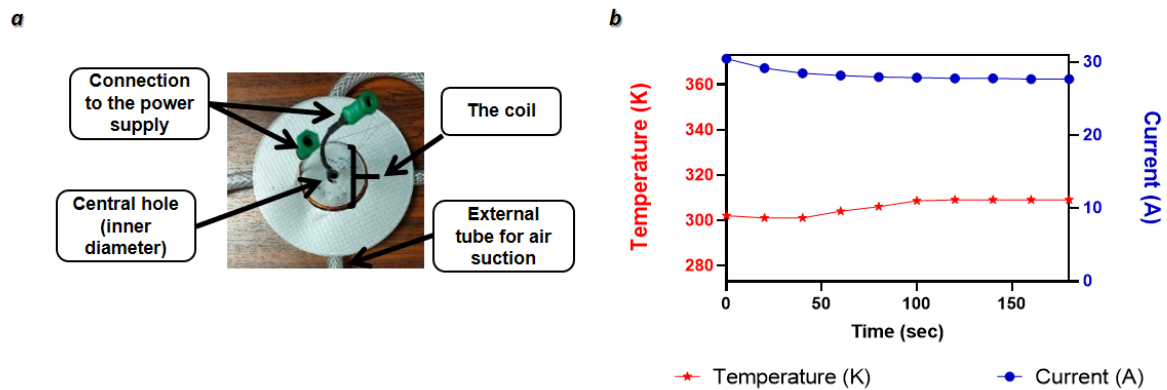


Figure 16: A) Photograph of the coil support initially used in the study where it had a central hole (1 cm inner diameter) through which the air enters upon suction from the four external tubes. B) A graph shows the time evolution of the temperature and of the current in the thick wire coil (1.6 mm wire diameter and  $\sim 60$  turns) are represented.

Afterwards, the same forced air-cooling approach for the coil support was applied to the medium wire. Using the medium wire of 1 mm ( $\sim 126$  turns) with forced-air cooling, it was not possible to manage the coil heating. After starting to pass the current of 30 A, the coil temperature passed 363 K very rapidly (in less than 2 min) causing a large decrease in the current down to  $\sim 15$  A (Figure 17b).

Alternatively, a better coil support design was used to enhance the forced air-cooling efficiency. In this new design, the coil support was perforated to allow the air to additionally come in from the sides of the coil, not only from the central hole (Figure 17a). With the perforated design of the coil support, the coil temperature was managed at  $\sim 316$  K, and the current was stabilized at  $\sim 23$  A, generating 65 mT at the center of the surface of the coil (Figure 17b).

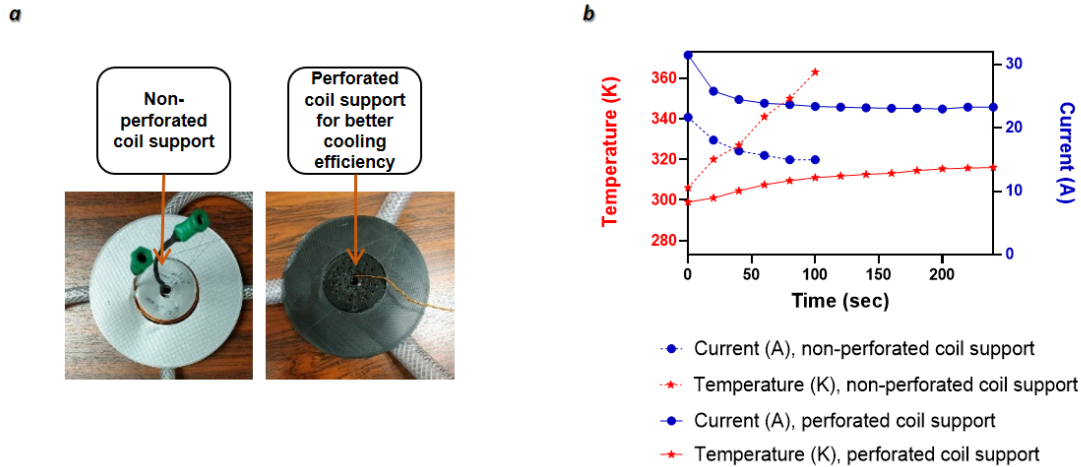


Figure 17: A) A photograph of both the non-perforated coil support (left) and the perforated coils support (right). The perforated coil support was used in order to have better forced air-cooling. B) A graph shows the time evolution of the temperature and current upon using medium wire of 1 mm (~126 turns) with forced air cooling on non-perforated coil support compared to the perforated one.

The final step was to fabricate a coil with a 0.75 mm in diameter wire, which was the optimum one based on the simulations. Using the thin wire of 0.75 mm diameter (~300 turns) with perforated coil support and air-cooling, it was not possible to manage the coil heating. After starting to pass the current of 30 A, the coil temperature passed 339 K rapidly, which caused a significant decrease in the current down to ~6.6 A (Figure 18b). Herein, the water cooling was the alternative, more efficient approach to allow managing the coil heating. In order to allow the water cooling of the coil, the coil and its perforated coil support were placed inside a jacket with the water coming in from one side (connected to a water tap) to pass through the whole coil and comes out from its other surface to a waste container (Figure 18a).

Using the water cooling of the coil, it was possible to manage the coil heating where its temperature was stable at ~302 K, and the current at ~21 A (Figure 18b). It is worth noting that these results go in line with the CVI software simulations of the coil resistance. In the CVI software, the expected coil resistance was 1.3  $\Omega$ , which was expected to decrease the current level by ~23%, i.e., to ~23.1 A instead of 30 A. Upon turning on the coil supply, the initial current level was at 23 A (Figure 18b), similar to the expected one from the CVI program. Due to the slight heating of the coil, the current level was slightly reduced to ~21 A.

At the stabilized current level of ~21 A in the coil, the resulted MF intensity at the center of the surface of the coil was 158.5 mT.

Hence, a coil with the optimized coil dimensions and wire diameter was built, and it was able to generate a MF intensity as high as  $\sim 158$  mT at the center of its surface.

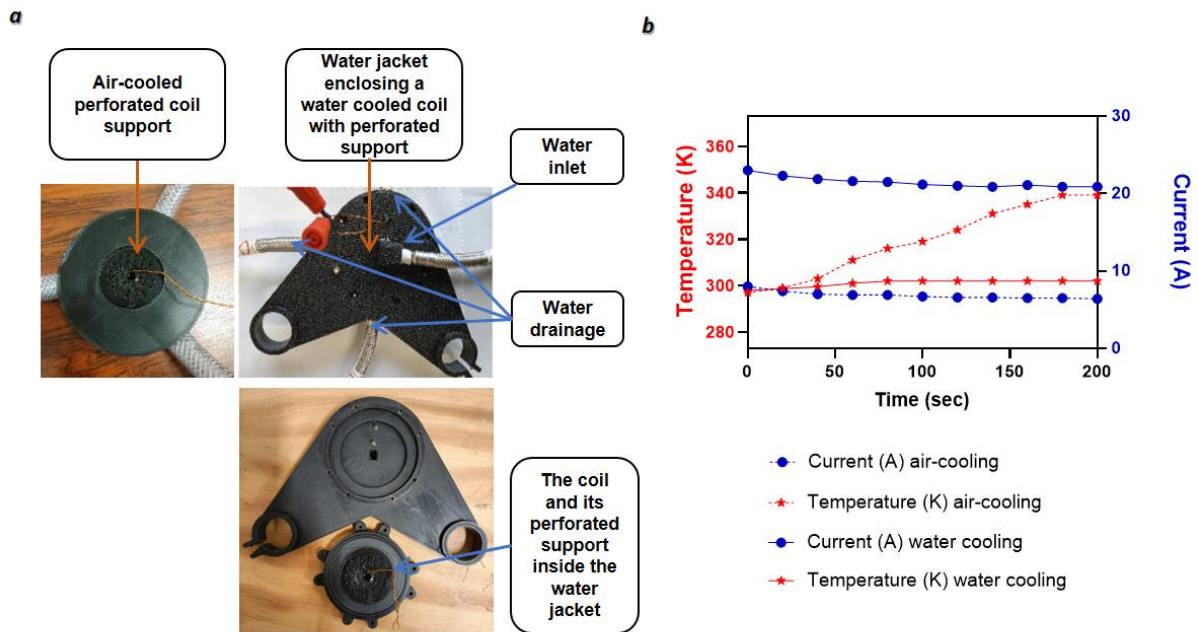


Figure 18: A) Photography of both the forced air-cooled perforated coil support (left) and the water-cooled perforated coil support (right) that was enclosed inside a water jacket where the water enters from one side at its center, passes through the coil and exits from the peripheries of the other side. B) A graph shows the time evolution of temperature and current upon using the optimum thin wire of 0.75 mm diameter ( $\sim 300$  turns) with forced air-cooling on perforated coil support compared to the jacketed and water-cooled perforated coil design.

Although the targeted MF intensity value was 280 mT, it could still be possible to benefit from the generated MF intensity of  $\sim 158$  mT to build the setup to make the proof-of-concept.

The aim of the coils is to generate, compared to the permanent magnets blocks, a lower MF intensity in the gap with a higher gradient to inverse the MF distribution created by the two magnets blocks. However, the lower MF intensity should still be sufficient to compensate the MF intensity generated by the two permanent magnets blocks. The MF intensity generated by the developed coil was lower than the targeted one from simulations. So that, COMSOL<sup>®</sup> simulation was done to assess the MF intensity distribution in the gap using all the optimized parameters for the two magnets blocks and coils, except to generate  $\sim 158$  mT (got by the designed coil), instead of 280 mT, at the center of the coil surface.

First, the two permanent magnets blocks were eliminated in COMSOL<sup>®</sup> and the current in the two coils was gradually decreased until generating 158 mT at the center of their surface. The current value to generate the 158 mT was found to be at 14.1 A. Afterwards, the two permanent magnets

blocks were added again in COMSOL® and the resulting MF distribution in the gap was simulated. It was found that the ~158 mT generated by the coil under the simulation parameters, was not enough to inverse the MF intensity generated by the two permanent magnets blocks along the z-axis (Figure 19).

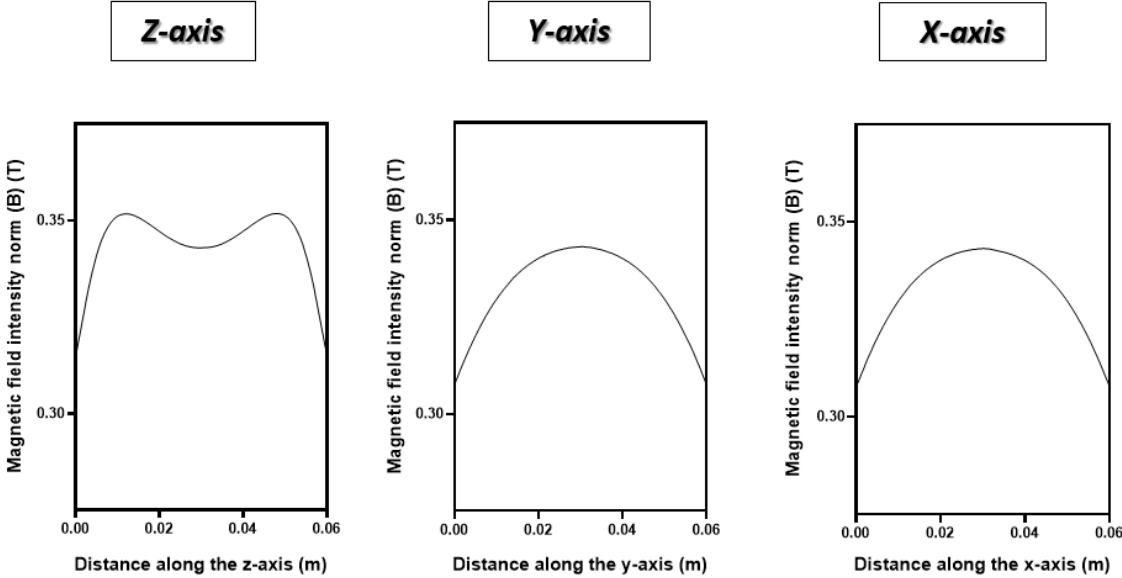


Figure 19: COMSOL® simulation results investigating the MF intensity distribution in the gap between the two coils when generating a maximum of ~158 mT at the center of their surface (using 14.1 A current).

To overcome this challenge, the MF intensity generated by the two permanent magnets blocks in the gap was needed to be reduced to allow reversing its distribution by the designed coils. This can be obtained by increasing the distance between the two permanent magnets blocks, as was shown in Figure 8. As it was previously explained during the optimization of the distance between the two permanent magnets blocks, it wasn't possible to definitely conclude its optimum value without knowing the MF intensity that could be generated by the coils. Thus COMSOL® simulations were performed to increase the distance between the two permanent magnets blocks (in a 1 cm increment) to gradually decrease their generated MF intensity until being possible to be reversed by the developed coils (generating 158 mT) (Figure 20).

It was found that increasing the distance between the blocks of the permanent magnets resulted in inverting the MF intensity distribution in the gap until getting the highest MF intensity in the center. Also, the MF intensity distribution along the y- and x-axes in the center of the gap was changed in a pattern of decreasing the MF gradient with increasing the distance between the two permanent magnets blocks. The optimum distance between the two permanent magnets blocks was 13 cm, at which the highest MF intensity was obtained in the center of the gap along the three axes.

Increasing the distance between the two permanent magnets blocks more than 13 cm resulted in a higher gradient along the z-axis towards a central point; however, a well with a minimal MF intensity value started to form in the center of the gap along the y-and x-axes. A similar effect on the MF distribution along the 3-axes was noticed upon increasing the current in the coils (Figure 12).

With the 13 cm distance between the two permanent magnets blocks, the MF gradient was 2.4 mT/mm edge to center along the z-axis and 0.4 mT/mm along the y-and x-axes in the center of the gap. The generated minimum MF intensity in the gap of the setup was 138.4 mT at the edges along the z-axis, and the maximum one was 211 mT in the center of the gap along the three axes. According to a simulation published by Blümner [18], MF gradients of 1-10 mT/mm could enable a speed of 1 mm/s of the magnetic particles of 100 nm to 1 μm size in human body, if all other parameters (such as the magnetic particles shape and saturation magnetization) were optimized. Also, as previously mentioned, it was reported that a MF intensity of 65 mT was able to saturate 40-50% of the ferumoxytol® superparamagnetic iron oxide nanoparticles [8]. So that, the generated MF intensity and gradients could be suitable for MNP focusing in terms of enabling MNP saturation and having a reasonable focusing speed.

Hence, suitable ordinary coils were successfully built with the ability to inverse the MF intensity distribution of the permanent magnets blocks and get the highest MF intensity in the center of the gap.

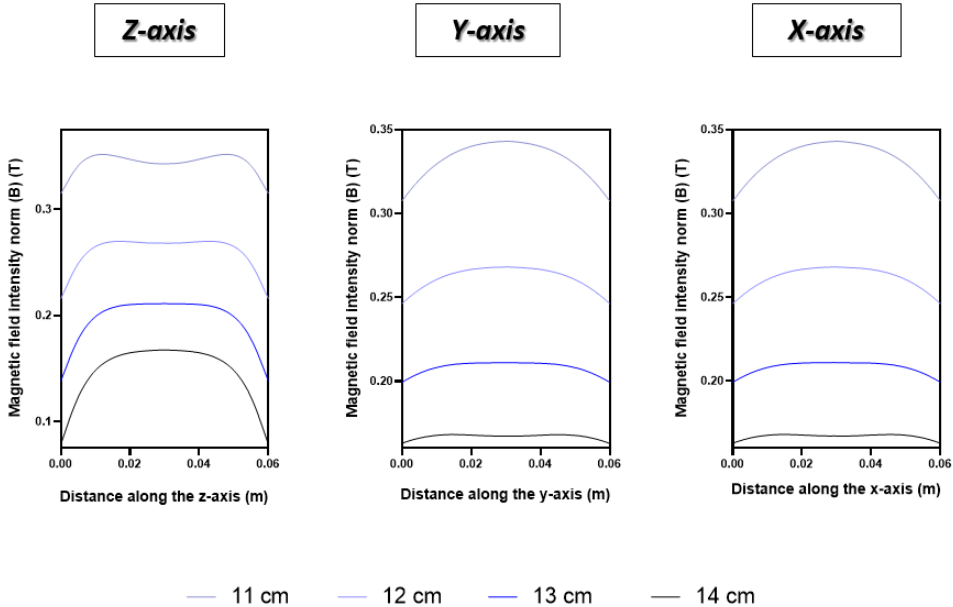


Figure 20: COMSOL® simulation results investigating the effect of increasing the distance between the two magnetic blocks on the MF intensity distribution in the gap between the two coils when generating a maximum of ~158 mT at the center of their surface (using 14.1 A passing current). The initial MF intensity distribution when having 11 cm distance between the two magnetic blocks and its gradual change until having 14 cm distance between the two magnetic blocks are shown.

### III.4. Experimental development of the setup

The permanent cubic neodymium magnets (10\*10\*1.5 cm) were purchased from their supplier (Ingeniera Magnetica Aplicada SL, Spain). The ordinary coils were built in the lab with the optimized parameters (1 cm internal diameter, 5 cm external diameter, 1 cm width) of 0.75 mm diameter copper wire and 300 turns. The perforated coil support was 3D printed in PLA. The water jacket of the coil was decided to be made of aluminum instead of the previously used PLA one (Figure 21). A major limitation of the PLA water jacket was the recurrent leakage at the points of contact with the wires and water connections. Trials to seal it with glue did not succeed in solving the problem. As a consequence, an aluminum water jacket with dedicated sealed ports for the coil wires and for the cooling water was developed. The aluminum water jacket was also varnished from inside to isolate it electrically from the coil. Finally, an additional palladium temperature sensor was added to constantly monitor the coil temperature. The aluminum jacketed water-cooled coil had a width of 3 cm. Hence, each coil (3 cm) can be placed 0.5 cm in front of each of the two permanent magnets blocks (separated by the optimum gap of 13 cm) to get at the end the initially targeted 6 cm space for the sample.

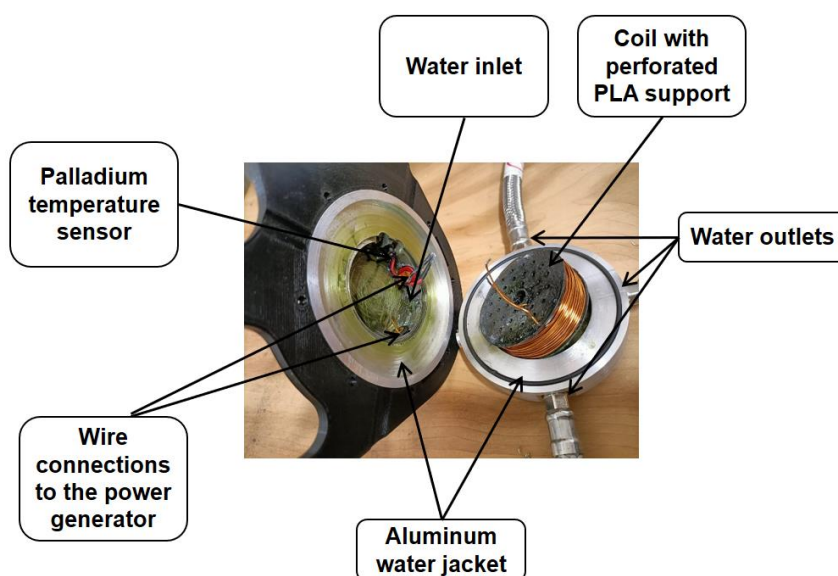


Figure 21: A photograph of the optimized coil inside the aluminum water jacket with dedicated sealed ports for the wires and water connections.

The final setup is composed of an aluminum base plate with two vertical magnets support plates made of magnetic inox. So that, the permanent magnets would be homed on the surface of their magnetic support plates to form the two magnet blocks. The position of the magnets on their support plates would be adjusted in the right position thanks to previously-fixed two non-magnetic

aluminum pieces surrounding the magnet adhering to the support plate (Figure 22 a). The magnets support plates can be move along two aluminum guiding columns. The distance between the two magnets blocks can be changed using a screw bar of nonmagnetic inox. The maximum distance the setup can achieve between the two magnets blocks is selected to be 50 cm. It was noticed that a MF intensity as low as  $\sim 22$  mT in the center of gap was achieved upon having 45 cm between the two permanent magnets blocks (Figure 6). So that at the 50 cm distance, there would be very low attraction between the two permanent magnets blocks when the setup is not in use. Dedicated 3D-printed PLA pieces were developed to place the coils on the two guiding columns in front of the two permanent magnets blocks. A schematic diagram of the setup configuration is illustrated in Figure 22a, and a photography of the developed setup at the current stage is shown in Figure 22b.

Final pieces of gears to drive the screw bar for changing the distance between the two permanent magnets blocks are being developed.

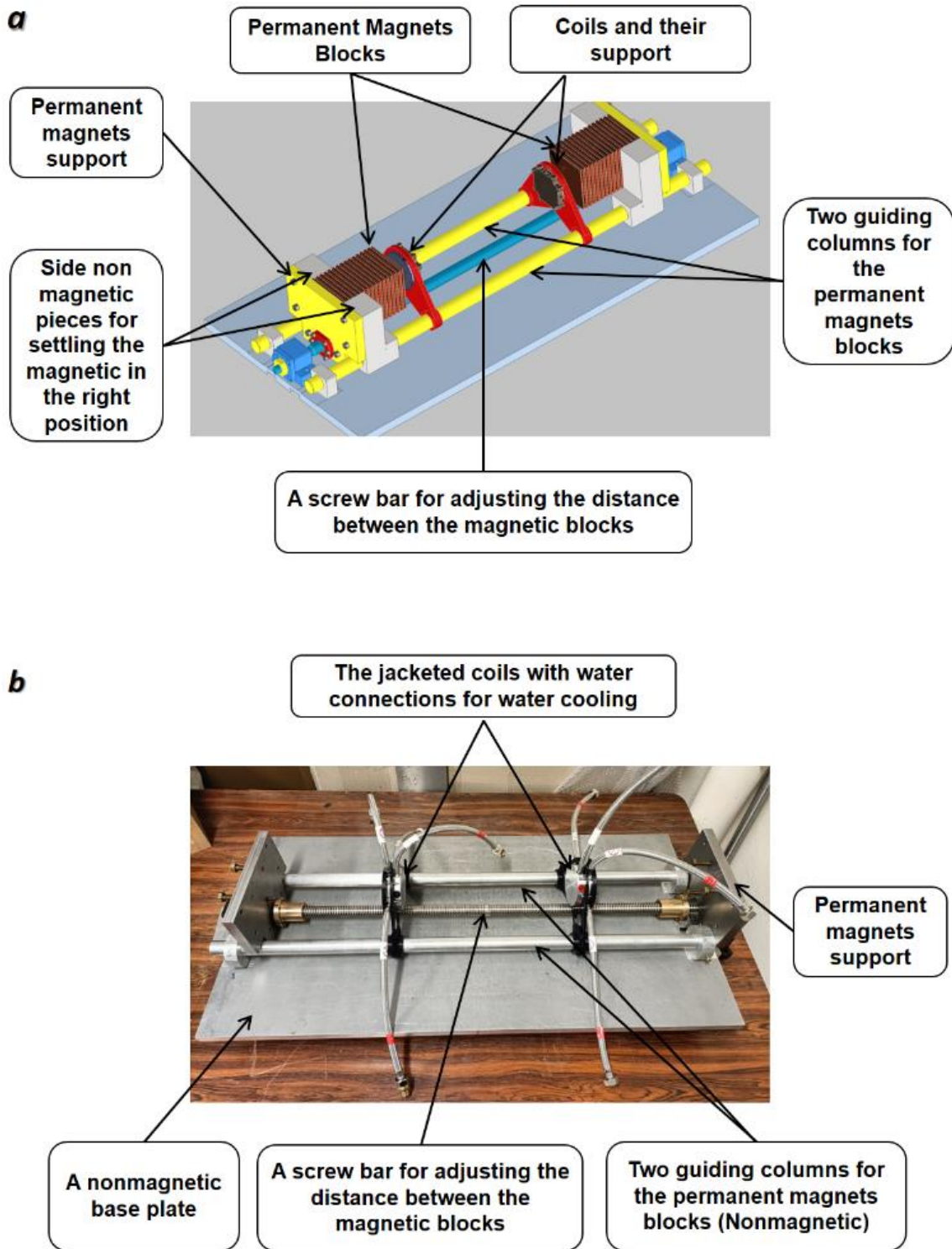


Figure 22: A) Illustration of configuration of the two permanent magnets blocks and coils on the setup. Magnets (in brown) adhere to two magnetic metal supports (in yellow) that can move along the two guiding columns (in yellow). The magnets would be settled on the magnet support pieces and surrounded by side nonmagnetic pieces (in grey) for homing the magnetic in the right position. The distance between the permanent magnets blocks can be controlled through a middle screw bar (in turquoise) that can be moved through connecting external gears. The coils were enclosed inside an aluminum water jacket (in black) and installed on the two guiding columns with a special support in red. B) A photograph of the actual setup with its components (without collecting the magnets).

A special protocol was developed for collecting the strong magnets to form the two blocks in a smooth way and manage their attraction forces. The main principle of the protocol is to allow gradual approaching and sticking of the magnetic parts. After mounting the setup components in place, the first magnet would be placed on the surface of the supporting plate with the help of three nonmagnetic screws (figure 23). The function of the screws is to allow the magnet to settle firstly on them due to its attraction to the magnetic supporting plate, then, the gradual dismantling of the three screws would allow the magnet to gradually come closer to the plate till be homed smoothly in its place.



*Figure 23: The magnetic support piece composed of magnetic inox material and have three nonmagnetic screws for collecting the first magnet.*

The next magnets would be added using a dedicated triangular wooden piece that would be placed at its large base on the first magnet. Then, the second magnet would be placed on the other side of the wooden piece that would be gradually withdrawn to allow gradual sticking between the two magnets. The side nonmagnetic pieces for homing the first magnet in the right position were adjusted to have a smaller thicknesses than the magnet itself to allow using the triangular wooden piece (Figure 24). The other magnets would be added in a similar way to the second magnet.

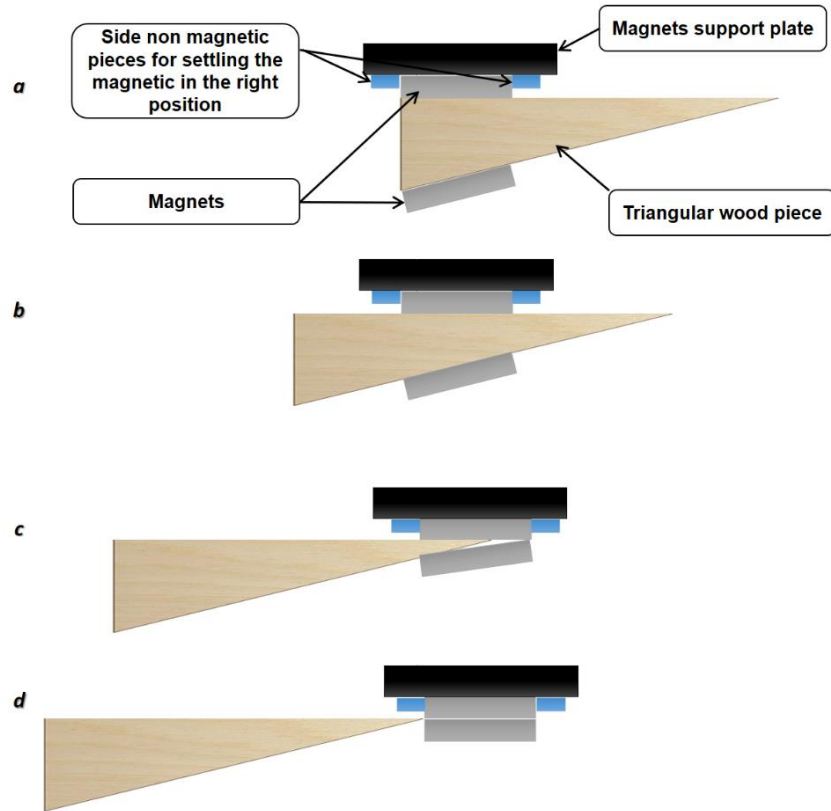


Figure 24: Schematic illustration for collecting two magnets smoothly and avoid collision between them with the help of a triangular piece of wood.

## VI. Conclusions and perspectives

In our study, we presented a new setup design that relied on using two permanent magnets blocks in order to generate a strong and homogenous MF in the gap between them, i.e., gaining the major advantage of strong MF generated by the permanent magnets. Afterwards, ordinary coils generating oppositely directed higher gradient and less strong MF were added between the two permanent magnets blocks, i.e., gaining the strong MF gradient and MF tuning advantages of the ordinary coils. Consequently, the net MF generated had the highest intensity in one area in the center of the gap away from the MF sourced that could be corresponded to a deep-seated tumor.

Simulations softwares were used to initially optimize the setup parameters after identifying them. The simulation results showed the possibility of creating the highest MF intensity area in the middle of the gap for 3D focusing of MNPs away from the MF sources. Moreover, it was possible to have a shift in this highest MF intensity position on the z-axis by tuning the current of the coils.

Afterwards, ordinary coils were successfully built in the lab and were able to generate up to 158 mT in the center of their surface. Although it was less than the targeted MF intensity, it was possible to re-optimize the setup parameters to still obtain the highest MF intensity area in the middle of the gap. From COMSOL® simulations, the final optimized setup design would allow a MF gradient of 2.4 mT/mm edge to center along the z-axis and 0.4 mT/mm along the y- and x-axes in the center of the gap. In the gap of the setup, the minimum MF intensity would be 138.4 mT at the edges along the z-axis, and the maximum one would be 211 mT in the center of the gap along the three axes.

The coils and setup components were built in the lab. Final piece of the setup to enable changing the distance between the two magnets blocks is being developed before collecting the magnets. After fully mounting the setup, the proof-of-concept experiments would be done on a cell culture plate using MNPs. Also, changing the MNP accumulation position along the z-axis in the cell culture plate by tuning the current in the coils would be investigated. In addition, 3D cell cultures based on polymers, as collagen, with embedded cells would be placed in the gap to investigate the 3D focusing of the MNPs. The relatively large MNP focusing area of the setup, when doing 3D targeting, would be taken into consideration to have proportionally large-sized samples that allow the proof-of-concept study.

In addition, MNP stepwise guidance and targeting would be investigated. This would be done by firstly having a highest MF intensity in the center of the gap along the 3 planes to direct the MNPs to a specific area in the center. Afterwards, the MF distribution would be changed either by passing more currents in the coils using more powerful power generators or by increasing the distance between the two permanent magnets blocks. This change (as shown in Figures 12 and 20) could result in a higher MF intensity in a specific sharp point in the center of the gap along the z-axis, although focusing to the center could be lost in the other two y- and x- axes. Under this situation, the MNPs previously accumulated in the central area (corresponding to a deep-seated tumor) could be directed along the z-axis to a central point (corresponding to the tumor center), allowing a narrower focusing and potential tumor penetration. However, it is also expected that other MNPs could be directed off-center in the other y- and x-axes. These effects would be firstly investigated using ferrofluid emulsions in water beaker that can be easily followed by eye, before being investigated using MNPs in 3D cell cultures.

The developed optimized setup design could allow getting a compromise to harness the advantages of both the permanent magnets as well as ordinary coils to allow MNP focusing in a position away from the MF sources with tunable targeting area along one plane. The challenges of the

ordinary coil heating was managed through water cooling. The permanent magnets would be collected with a specially developed protocol to manage their attraction forces.

The upgrade of the setup to get a tunable targeting area along two dimensions, not only one, was also described by adding a perpendicular set of permanent magnets and coils. The focusing of MNP-based nanomedicines formulations to a tunable area away from the MF sources could allow their preferential targeting to a deep-seated tumor in a noninvasive way. Therefore, it could offer higher tumor accumulation, deeper penetration, enhanced efficacy and reduced side effects, leading to better therapeutic outcomes of the targeted formulations.

## V. References:

1. Meng, Z., et al., *Functional metal–organic framework-based nanocarriers for accurate magnetic resonance imaging and effective eradication of breast tumor and lung metastasis*. Journal of Colloid and Interface Science, 2021. **581**: p. 31-43.
2. Denny, I.S., et al., *Nanotheranostics for Image-Guided Cancer Treatment*. Pharmaceutics, 2022. **14**(5): p. 917.
3. Xiong, X.Y., et al., *Enhanced effect of folated pluronic F87-PLA/TPGS mixed micelles on targeted delivery of paclitaxel*. International Journal of Biological Macromolecules, 2017. **103**: p. 1011-1018.
4. Lübke, A.S., et al., *Clinical experiences with magnetic drug targeting: a phase I study with 4'-epidoxorubicin in 14 patients with advanced solid tumors*. Cancer Res, 1996. **56**(20): p. 4686-93.
5. Liu, J.F., et al., *Use of Oppositely Polarized External Magnets To Improve the Accumulation and Penetration of Magnetic Nanocarriers into Solid Tumors*. ACS nano, 2020. **14**(1): p. 142-152.
6. Zhou, Z., Z. Shen, and X. Chen, *Tale of Two Magnets: An Advanced Magnetic Targeting System*. ACS Nano, 2020. **14**(1): p. 7-11.
7. Krzyminiewski, R., et al., *Focusing of Fe<sub>3</sub>O<sub>4</sub> nanoparticles using a rotating magnetic field in various environments*. Physics Letters A, 2018. **382**(44): p. 3192-3196.
8. Oberdick, S.D., et al., *Iron oxide nanoparticles as positive T1 contrast agents for low-field magnetic resonance imaging at 64 mT*. Scientific Reports, 2023. **13**(1): p. 11520.
9. Kummer, M.P., et al., *OctoMag: An electromagnetic system for 5-DOF wireless micromanipulation*. IEEE Transactions on Robotics, 2010. **26**(6): p. 1006-1017.
10. Baker, R.R., et al., *Image-Guided Magnetic Thermoseed Navigation and Tumor Ablation Using a Magnetic Resonance Imaging System*. Advanced Science. **n/a**(n/a): p. 2105333.
11. Dahmen, C., et al. *Threedimensional actuation of small ferromagnetic objects in MRI*. in *2012 International Symposium on Optomechatronic Technologies (ISOT 2012)*. 2012.
12. Kósa, G., et al., *MRI driven magnetic microswimmers*. Biomedical Microdevices, 2012. **14**(1): p. 165-178.
13. Muthana, M., et al., *Directing cell therapy to anatomic target sites in vivo with magnetic resonance targeting*. Nature Communications, 2015. **6**(1): p. 8009.
14. Liu, Y.-L., et al., *A review of magnet systems for targeted drug delivery*. Journal of Controlled Release, 2019. **302**: p. 90-104.
15. Diller, E., J. Giltinan, and M. Sitti, *Independent control of multiple magnetic microrobots in three dimensions*. The International Journal of Robotics Research, 2013. **32**(5): p. 614-631.
16. Perlo, J., F. Casanova, and B. Blümich, *Ex Situ NMR in Highly Homogeneous Fields: Spectroscopy*. Science, 2007. **315**(5815): p. 1110-1112.

17. Qian, T., et al., *Simpler optimized stellarators using permanent magnets*. Nuclear Fusion, 2022. **62**(8): p. 084001.
18. Blümler, P., *Magnetic Guiding with Permanent Magnets: Concept, Realization and Applications to Nanoparticles and Cells*. Cells, 2021. **10**(10): p. 2708.

# Conclusions and perspectives

This study enabled exploration of the magnetic properties and cellular interaction of magnetic nanoparticles@metal-organic frameworks (MNPs@MOFs) nanocomposites towards their development as magnetic fields (MF)-responsive drug delivery systems. Published research in this area is rare, which could be due to the need for specialized competencies in the synthesis of these nanocomposites as well as their physicochemical and magnetic characterization. It also needs expertise in the cellular studies of MNP-induced intracellular events upon MF exposure. Thanks to the HeatNMof project, it was possible to have collaborative research teams with these experiences. Three innovative areas were explored in this project, and they were as follows:

## **1) Intracellular MF-induced cargo release from the MNPs@MOFs nanocomposites induced by the MNP heating or mechanical actuation**

In this part, we used magnetic nanocomposites that consisted of superparamagnetic iron oxide magnetic nanoparticles (IONPs) cores and nano-zeolitic imidazolate framework-8 (ZIF-8) MOF shells (IONP@ZIF-8). The magnetic nanocomposites were loaded with cresyl violet (CV) fluorescent probe and coated with an amphiphilic polymer. The latter enabled the stabilization of the nanocomposites in aqueous environments, cell culture media as well as artificial lysosomal fluid.

The magnetic characterization revealed superparamagnetic properties of the IONP cores, that were not affected by the ZIF-8 shell growth. This finding could indicate the potential of the prepared nanocomposites for being used as magnetic contrast agents for biomedical imaging applications. In addition, the bare IONP had a saturation magnetization of  $73.7 \text{ Am}^2/\text{kg Fe}$  that almost did not change after being inside the nanocomposites. This preservation of the magnetic properties of the IONP could be related to the mild conditions of the ZIF-8 shell growth, indicating the versatility of the ZIF-8 MOFs for developing multifunctional drug delivery platforms.

The nanocomposites were biocompatible on MiaPaCa2 pancreatic cancer cells, and cancer-associated fibroblasts (CAF), up to 1 pM and 72 h of incubation with main accumulation inside the lysosomes. The intracellular MF-induced release studies revealed the efficiency of both the alternating high-frequency MF (AMF) and the rotating low-frequency MF (RMF) in triggering the CV cargo release from the nanocomposites in 2D culture models and 3D spheroids (Figure 1). These findings indicate that a controlled on-demand release from the developed IONPs@ZIF-8 nanocomposites could be achieved in response to IONP cores heating or mechanical movement. The CV release with AMF and

IONP heating could be related to thermodiffusion mechanisms, while its release with RMF and IONP movement could be related to magneto-mechanical induced diffusion.

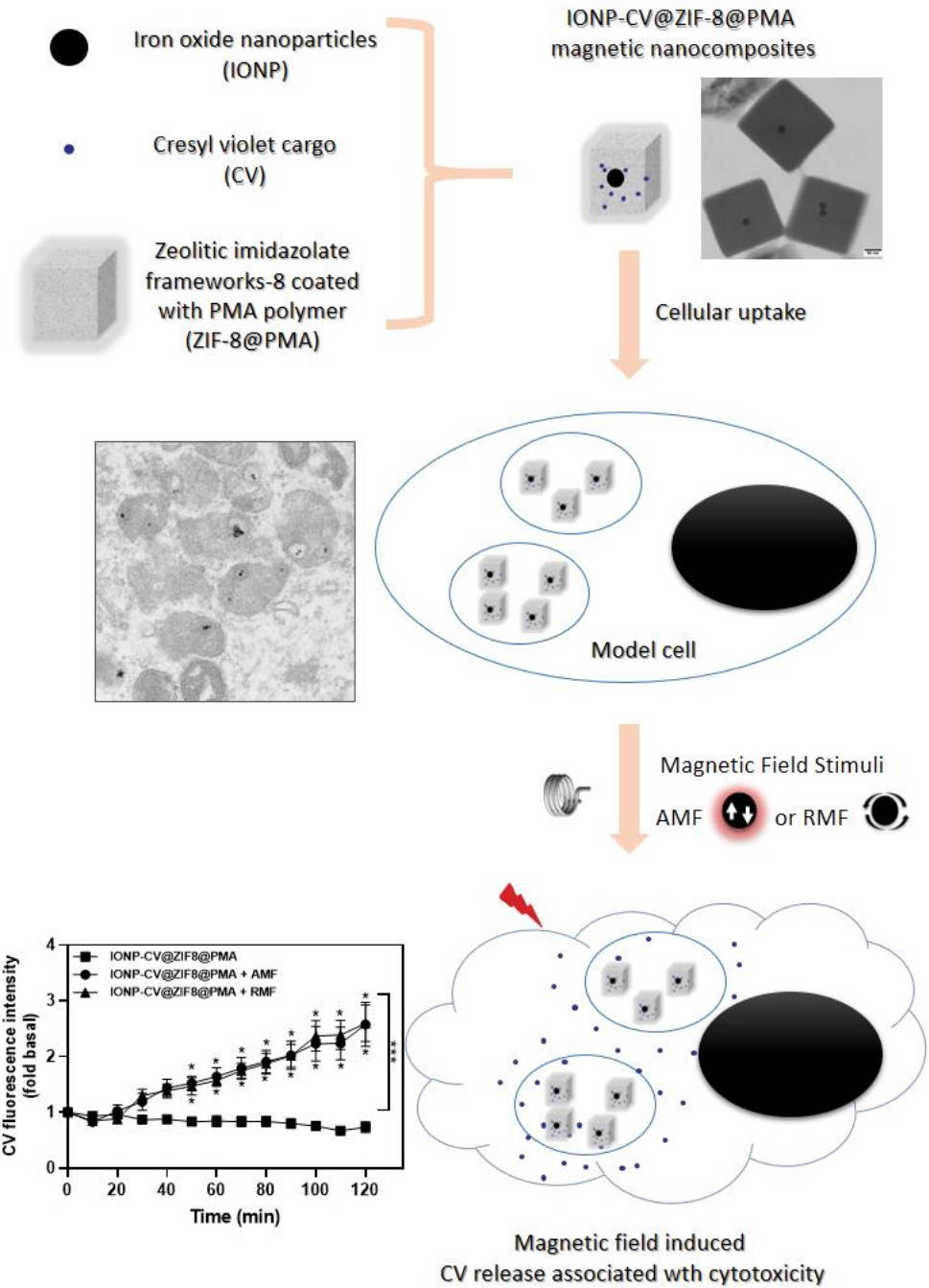


Figure 1: Schematic illustration of the prepared magnetic nanocomposites, their cellular uptake and MF-induced intracellular release in model cells in response to AMF and RMF.

Although it was not possible to get more details about the CV release mechanisms, we had interesting observations that enabled comparisons between the efficiencies of the two release strategies. First, we observed that a second AMF exposure enhanced CV release from the nanocomposites in MiaPaCa2 and CAF cells compared to the RMF. Also, the efficacy of the AMF-induced CV release in inhibiting MiaPaCa2 and CAF cell viability after repeated exposures was higher compared to the RMF. Hence, the IONP cores heating had a superior efficacy in inducing the CV release from the developed nanocomposites compared to the IONP mechanical movement.

It is worth noting that the RMF and mechanical movement could still be a promising strategy that could need to be optimized. For instance, MNP cores with high magneto-mechanical induced responses, such as anisotropic MNPs, could be suitable for allowing more efficient MF-induced cargo release.

In addition, there was a higher efficacy for the repeated AMF-induced CV release in inhibiting the MiaPaCa2 cell viability compared to CAF. Moreover, the repeated RMF-induced CV release induced cell inhibition in MiaPaCa2 only and not CAF. This difference highlights the need for developing therapeutic strategies that could act on the more resistant tumor microenvironment cells to enable effective cancer treatment.

Additionally, using the hemolysis assay on mice, rats and human blood, we proved hemocompatibility of the nanocomposites at concentrations up to 10-fold higher than the ones used for cellular studies, indicating their suitability for intravenous administration.

These results indicated the promise of the developed MOF-based magnetic nanocomposite platforms for developing MF-responsive anticancer theranostics. Further studies using chemotherapeutic drugs loaded nanocomposites could enable further investigations on the MF-induced intracellular cargo release and its associated cytotoxic effects.

## **2) Synthesis of chemotherapeutic drug-loaded MOF magnetic nanocomposites**

In this part of the study, we succeeded in synthesizing nanocomposites of ZIF-8 shells on the surface of magnetic cores of superparamagnetic iron oxide ( $\text{Fe}_3\text{O}_4$ ) nanocubes of 16 nm. In addition, the growth of the ZIF-8 shells on the surface of larger-sized MNP cores of different shape (flower) or composition (Zn–ferrite) was also assessed. However, they formed loops or aggregates, possibly due to having remanent magnetization, and the ZIF-8 shells grew on their surface. Therefore, they did not enable the formation of single core-shell MNP@ZIF-8 nanocomposites. These observations indicate the importance of studying the magnetic properties of the MNP cores used for the nanocomposites preparation. Also, it could indicate the importance of having superparamagnetic MNP cores for

synthesizing the core-shell MNP@MOF nanocomposites. Moreover, it was possible to tune the nanocomposites size by varying the ZIF-8 shell growth time.

In addition, it was feasible to load the nanocomposites of the iron oxide nanocubes (16 nm) cores and ZIF-8 shells with doxorubicin or 5-fluorouracil. Each drug was loaded by two approaches: either the one-pot *in-situ* method to allow its loading inside the ZIF-8 pores, or through the post-synthesis impregnation to load it on the ZIF-8 surface. During the one-pot synthesis of the doxorubicin-loaded nanocomposites, a high concentration of doxorubicin did not allow the ZIF-8 shells growth which could be attributed to interactions between the drug and the Zn<sup>2+</sup> cations of the ZIF-8 MOFs. Hence, the compatibility between the loaded drugs and the MOF synthesis conditions should be considered when choosing the drugs to be loaded using the one-pot approach. Finally, we noticed that doxorubicin could lead to the formation of mesopores inside the ZIF-8 shells with the one-pot synthesis approach. This could indicate that the loaded drugs inside the ZIF-8 pores could change their porous architecture.

Further studies to coat the prepared nanocomposites to stabilize them in aqueous media could allow their use in cellular studies. Studying the MF-induced drug release kinetics from the nanocomposites (surface *versus* pore loading) in response to the heating (by AMF) or movement (by RMF) could allow more insights into their release mechanisms. Furthermore, investigating the effects of different release behaviors on the nanocomposites antitumor efficacy *in vitro* (on cancer or tumor microenvironment cells or their 3D spheroids) and *in vivo* could help in the development of optimized MF-responsive magnetic MOF nanocomposites for cancer treatment applications.

### **3) Development of MNP focusing setup with tunable targeting area**

In this part, we investigated the development of a setup for 3D focusing of MNP-based nanomedicines. A novel setup design based on permanent magnets and ordinary coils was optimized using simulations to have the highest MF intensity area in the center of the gap of the setup away from the MF sources. Consequently, MNPs could be focused towards this highest MF intensity area that could be corresponded to a deep-seated tumor.

The ordinary coils of the setup were successfully fabricated in the lab with the optimum parameters. Also, using an efficient water-cooling strategy with a specially designed support, it was possible to generate up to 158 mT in the center of the coils surface. With the MF intensity generated by the coils, the setup would allow a relatively high MF intensity (minimum of ~138 mT and maximum of ~211 mT) that could enable high efficiency of MNP saturation. It would also generate a MF gradients

of 2.4 mT/mm along the z-axis and 0.4 mT/mm along the y- and x-axes, edge to center in the gap. These gradients could allow getting focusing speed in the range of 1 mm/s for the MNPs. Moreover, simulations showed that it could be possible to shift the highest MF intensity area position, corresponding to the targeting area, along one plane in a simple way by manipulating the current in the coils.

Further experimental work to finalize the setup mounting, would allow its testing on 3D cell cultures, based on polymers as collagen, that would be placed in the gap. In addition, it would allow the investigation of the setup ability to change the MNP accumulation position along one plane in a cell culture plate by tuning the current in the coils.

The setup design allowed to combine the advantages of the strong MF of the permanent magnets with the higher gradients that can be generated by the ordinary coils. We overcame the ordinary coils heating challenge through water-cooling. Also, we proposed a protocol that we would follow upon collecting the permanent magnets to manage their attraction forces. So that the proposed setup design have a relatively simple design, strong MF with high gradient, relatively large gap, reasonable cost, and feasible manipulation and upgrading. However, we obtained a 3D MF distribution with the highest intensity in a central area in the gap instead of a central sharp point. Overcoming this challenge through stepwise guidance of the MNP would be investigated to allow better MNP targeting towards smaller areas that could help in MNP tumor penetration.

Future investigations of the versatile biocompatible ZIF-8 MOF-based magnetic nanocomposites could allow a step further toward their clinical translation as cancer nanotheranostics. Using the 3D MNP focusing setup design, the nanocomposites accumulation in the targeted deep-seated tumor could be examined. Moreover, using drug-loaded nanocomposites, the anticancer triggered events after a pulsatile on-demand MF-induced drug release can be investigated *in vitro* and *in vivo*, thermally (by AMF) or mechanically (by RMF). In addition, the nanocomposites use as magnetic contrast agents could be studied using magnetic resonance or magnetic particle imaging. Finally, the versatility of the MF stimuli and the MOF-based magnetic nanocomposites could enable their exploitation for the development of targeted nanotheranostic platforms to achieve better therapeutic outcomes in cancer treatment.